

Optical Frequency Division via  
Periodically-Poled-LiNbO<sub>3</sub>-Based Nonlinear  
Optics

by

Phillip Tsefung Nee

Submitted to the Department of Electrical Engineering and  
Computer Science

in partial fulfillment of the requirements for the degree of

Doctor of Philosophy


at the

MASSACHUSETTS INSTITUTE OF TECHNOLOGY

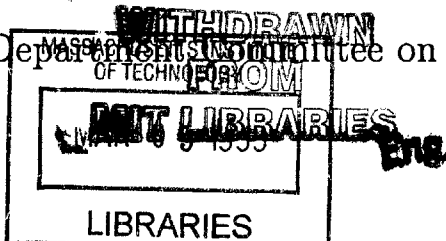
February 1999

© Massachusetts Institute of Technology 1999. All rights reserved.

Author .....  
Department of Electrical Engineering and Computer Science  
January 15, 1999

Certified by .....  
  
Dr. N.C. Wong  
Research Scientist  
Thesis Supervisor

Accepted by .....  
Arthur C. Smith  
Chairman, Departmental Committee on Graduate Students



**Optical Frequency Division via  
Periodically-Poled-LiNbO<sub>3</sub>-Based Nonlinear Optics**

by

Phillip Tsefung Nee

Submitted to the Department of Electrical Engineering and Computer Science  
on January 15, 1999, in partial fulfillment of the  
requirements for the degree of  
Doctor of Philosophy

**Abstract**

Nonlinear optical techniques are utilized in recent proposals of optical-to-microwave frequency chains to obtain exact frequency ratios that can be used to phase-lock an optical frequency to a microwave frequency standard. These new schemes hold a major advantage over conventional optical-to-microwave frequency chains in that frequency conversion is restricted to the near-IR spectral region where advanced lasers, detectors, and nonlinear materials are available.

This thesis investigates the implementation of nonlinear-optics-based optical frequency division through the use of periodically poled lithium niobate (PPLN). 3-to-1 optical frequency division of 532 nm was experimentally demonstrated in a double-grating PPLN crystal. In addition, successful operation of a continuous-wave, nearly-degenerate, doubly resonant optical parametric oscillator (OPO) pumped at 798 nm was achieved using a Brewster-cut PPLN crystal. This nearly-degenerate Brewster-cut PPLN OPO serves as a precursor to the implementation of a novel 3-to-1 optical frequency divider based on a dual-cavity Brewster-cut double-grating PPLN OPO.

Thesis Supervisor: Dr. N.C. Wong

Title: Research Scientist

## Dedication

To Stephanie:

*for her unwavering faith in me, in my capabilities, and in our marriage. Her love, encouragement, and understanding, especially during the past year when my coming home late at night became the norm rather than the exception, have made the rigors of doctoral study that much more bearable and my accomplishments that much more satisfying than they would be otherwise.*

## Acknowledgments

I'm grateful to Dr. Franco Wong for providing me with the opportunity to work on this thesis project and for helping me develop my experimental and analytic skills over the past few years. It's been a rewarding experience to work with and learn from a true expert in the field of nonlinear and quantum optics who is never short of new and clever ideas. He always offered helpful suggestions and insights in all aspects of my thesis work whenever I needed them. I'm also very appreciative of the time and effort he spent in providing thorough comments and suggestions to my thesis draft.

I'd like to acknowledge Professor Jeff Shapiro for his insightful comments and suggestions on many aspects of my thesis work during the group seminars. I'd also like to thank him for his helpful comments on my thesis draft.

I want to thank Dr. Lenny Johnson at Lincoln Lab for providing me with the facility and resources to carry out the fabrication portion of my thesis work, and Dr. Gary Betts for clearing up many questions I had regarding the processing of lithium niobate devices and optical damage issues in lithium niobate. I'd also like to thank Gary for loaning me the beam profiler which allowed me to characterize the MOPA diode laser beam.

A special thanks to Kevin Ray for training me in the photolithography process and for teaching me how to operate the various pieces of equipment in the C400 clean room at Lincoln Lab. I'd also like to acknowledge Skip Hoyt, from whom I learned how to cut and polish the PPLN samples, and other current and former members of Group 83 at Lincoln Lab: Bob Bailey, Fred O'Donnell, Dan Mull, Rich Polluci, Doug Hoyt, Sam Choi, John Twichell, and Dick Williamson for their generosity in offering assistance whenever I needed it.

I want to express my heartfelt thanks to Elliott Mason, who over the past year has helped me tremendously in fabricating PPLN samples and in setting up the PPLN OPO experiment.



I would also like to thank other current and former members of the group on campus: Jeff Bounds, Reggie Brothers, Jennifer Kleinman, Dicky Lee, Elisa Pasquali, and Joe Teja for their help in various experiments and for the stimulating conversations in lab.

I would like to say thanks to my good friends at MIT: Mike Chou, Cynthia Chuang, and Ralph Lin, for all the fun times we had and their lifetime friendship.

Finally, I would like to dedicate this thesis to my family: my father Tsu-Wei, my mother Soe-Mie, my wife Stephanie, and my sister Jocelyn, for their love and support.

# Contents

<b>1</b>	<b>Introduction</b>	<b>15</b>
1.1	Background . . . . .	15
1.2	Nonlinear Optical 3-Wave Mixing . . . . .	16
1.2.1	Phasematching . . . . .	17
1.2.2	Quasi-phasematching . . . . .	18
1.2.3	QPM nonlinear optical frequency conversion applications . . .	20
1.3	Motivation . . . . .	21
1.3.1	Applications of nonlinear optics to frequency metrology . . . .	21
1.3.2	3-to-1 optical frequency division . . . . .	24
1.4	Contributions of This Research . . . . .	25
1.5	Thesis Organization . . . . .	26
<b>2</b>	<b>Theory of QPM Nonlinear Interactions</b>	<b>28</b>
2.1	Overview of Quasi-Phasematching . . . . .	29
2.2	QPM Period and Conversion Efficiency . . . . .	32
2.3	Quasi-Phasematched Difference-Frequency Generation . . . . .	35
2.4	Quasi-Phasematched Optical Parametric Oscillation . . . . .	38
2.4.1	The OPO threshold . . . . .	41
2.4.2	Above-threshold OPO output . . . . .	44
2.4.3	OPO cavity resonances . . . . .	47
2.5	Calculation of QPM Grating Period . . . . .	49
2.6	Wavelength and Temperature Bandwidths . . . . .	50
2.6.1	Spectral bandwidth . . . . .	51

2.6.2	Temperature bandwidth . . . . .	52
2.7	Novel Features of QPM Nonlinear Optics . . . . .	54
2.7.1	Use of multiple parallel gratings for OPO tuning . . . . .	54
2.7.2	Multiple gratings in series . . . . .	56
2.7.3	Bandwidth engineering . . . . .	59
2.7.4	Chirped QPM gratings . . . . .	60
2.7.5	Spatial beam profile engineering . . . . .	63
2.8	Nonidealities . . . . .	63
2.8.1	Sub-optimal duty cycle . . . . .	63
2.8.2	Random duty-cycle error . . . . .	67
2.8.3	Missing domain reversals . . . . .	68
<b>3</b>	<b>Fabrication and Characterization</b>	<b>70</b>
3.1	QPM Materials–Choice of Lithium Niobate . . . . .	71
3.2	Methods of Preparing Domain-reversed Lithium Niobate Crystal . . . . .	71
3.3	E-field Poling Method . . . . .	75
3.4	Fabrication of PPLN . . . . .	81
3.5	Characterization of PPLN . . . . .	88
<b>4</b>	<b>Relevant Work By Others</b>	<b>93</b>
4.1	Early Work . . . . .	93
4.2	QPM Second Harmonic Generation in PPLN . . . . .	96
4.3	QPM Difference-Frequency Generation in PPLN . . . . .	98
4.4	QPM Optical Parametric Oscillation in PPLN . . . . .	99
4.5	Devices Based On Other Periodically-Poled Materials . . . . .	103
4.5.1	Periodically-poled LiTaO <sub>3</sub> . . . . .	104
4.5.2	Periodically-poled KTP and RTA . . . . .	106
<b>5</b>	<b>The Master Oscillator/ Power Amplifier Diode Laser System</b>	<b>108</b>
5.1	Introduction . . . . .	108
5.2	Background . . . . .	110

5.3	The Master Laser . . . . .	111
5.3.1	Operating principle . . . . .	111
5.3.2	Physical layout . . . . .	113
5.3.3	Current control . . . . .	115
5.3.4	Temperature control . . . . .	115
5.3.5	Alignment and tuning . . . . .	117
5.4	The Slave Laser . . . . .	120
5.4.1	Operating principles . . . . .	121
5.4.2	Current source and TE cooler . . . . .	123
5.4.3	Astigmatism compensation . . . . .	123
5.4.4	Laser output . . . . .	125
5.5	Frequency Stabilization of Laser Output . . . . .	128
5.6	Summary . . . . .	129
<b>6</b>	<b>Three-to-One Optical Frequency Division Experiment</b>	<b>131</b>
6.1	The Optical-to-Microwave Frequency Chain . . . . .	131
6.1.1	2:1 optical frequency division . . . . .	132
6.1.2	3:1 optical frequency division . . . . .	132
6.2	The Double-Grating PPLN Crystal . . . . .	136
6.2.1	Grating design and fabrication . . . . .	136
6.2.2	Characterization . . . . .	140
6.3	Experimental Setup . . . . .	143
6.3.1	532 nm laser system . . . . .	143
6.3.2	798 nm laser system . . . . .	143
6.3.3	Optics . . . . .	145
6.3.4	Detection system . . . . .	147
6.4	Frequency Stabilization . . . . .	151
6.5	Results . . . . .	153
6.6	Discussion . . . . .	155
6.7	Summary . . . . .	158

<b>7</b>	<b>Brewster-Angle PPLN OPO</b>	<b>159</b>
7.1	Brewster-Cut-PPLN-Based OPO . . . . .	159
7.2	Grating Design and Fabrication . . . . .	162
7.3	OPO Cavity Design . . . . .	165
7.4	Experimental Setup . . . . .	166
7.4.1	798 nm laser system . . . . .	166
7.4.2	1596 nm laser system . . . . .	166
7.4.3	Optics for pump laser system . . . . .	167
7.4.4	Optics for probe laser system . . . . .	168
7.4.5	Finesse measurements . . . . .	169
7.4.6	Single-pass DFG measurement . . . . .	170
7.5	Results . . . . .	172
7.5.1	OPO threshold estimate . . . . .	172
7.5.2	OPO threshold/output . . . . .	173
7.5.3	Optical damage . . . . .	176
7.6	Summary . . . . .	182
<b>8</b>	<b>Conclusion</b>	<b>184</b>
8.1	Summary . . . . .	184
8.2	Future Work . . . . .	184

# List of Figures

1-1	A traditional optical-to-microwave frequency chain. . . . .	23
1-2	Optical-to-microwave frequency chain based on optical frequency division. . . . .	24
2-1	Difference-frequency generation in a $\chi^{(2)}$ nonlinear medium. . . . .	30
2-2	Effect of phasematching of DFG output power as a function of distance in a nonlinear medium with nonlinear coefficient $d$ . . . . .	31
2-3	Profile of the effective nonlinear coefficient in a 1st-order QPM interaction. . . . .	34
2-4	An optical parametric oscillator. . . . .	39
2-5	Tuning of a QPM OPO by multiple grating periods. . . . .	56
2-6	PPLN OPO with a fan-out grating pattern. . . . .	57
2-7	Simultaneous phasematching of 2 nonlinear interactions in a QPM nonlinear crystal. . . . .	58
2-8	Building block for discrete approximation to the synthesis of an arbitrary effective nonlinear coefficient. . . . .	60
2-9	Synthesized SHG tuning curves using the discrete approximation method shown in Fig. 2-8 in a structure of length $Nl_c$ with $m = 3$ . . . . .	61
2-10	Time-domain representation of pulse compression during SHG in aperiodic QPM gratings. . . . .	62
2-11	Effect of spatially-varying QPM grating length on generated second harmonic beam profile for a Gaussian fundamental beam profile. . . . .	64
2-12	Effect of missing domain reversal on DFG conversion efficiency. . . . .	69

3-1	Ferroelectric domain reversal by titanium in-diffusion. . . . .	72
3-2	Ferroelectric domain reversal by electron beam writing. . . . .	74
3-3	Periodic domain reversal of LiNbO <sub>3</sub> by electron beam writing. . . . .	74
3-4	Molecular structure of LiNbO <sub>3</sub> . . . . .	76
3-5	Schematic of an electric field poling apparatus using metal grating. . . . .	77
3-6	Schematic of an electric field poling apparatus using liquid electrolyte. . . . .	78
3-7	Schematic of an electric field poling apparatus using metal grating and liquid electrolyte. . . . .	79
3-8	Liquid electrolyte poling fixture. . . . .	83
3-9	High voltage circuitry for electric field poling of LiNbO <sub>3</sub> . . . . .	84
3-10	Current and voltage monitors during electric field poling. . . . .	85
3-11	Photograph of the +z face of a double-grating periodically poled LiNbO <sub>3</sub> sample. . . . .	89
3-12	Spectral tuning of DFG conversion efficiency. . . . .	91
3-13	Temperature tuning of DFG conversion efficiency. . . . .	92
4-1	Stacked coherence length plates. . . . .	94
4-2	Temperature tuning curve for 1064-nm-pumped Q-switched PPLN OPO with a 31- $\mu$ m grating period. . . . .	100
4-3	OPO tuning curve as a function of grating period for a 1064-nm- pumped Q-switched OPO at room temperature (25°C). . . . .	101
5-1	Extended-cavity diode laser (ECDL) in the Littmann configuration. . . . .	112
5-2	Schematic of ECDL construction. . . . .	114
5-3	Output power vs. injection current of AR-coated Sharp LT017 laser diode. . . . .	115
5-4	Schematic of temperature control system. . . . .	116
5-5	Diode laser power vs. injection current. . . . .	118
5-6	Plot of output power vs. injection current of AR-coated LTO17 laser diode in extended cavity configuration. . . . .	119
5-7	Setup for injection locking the slave laser by the master laser. . . . .	121

5-8	Output power vs. injection current for slave laser with and without injection from the master diode laser. . . . .	122
5-9	Output power vs. emission wavelength for slave laser at fixed injection current settings. . . . .	124
5-10	Collimation of slave laser output. . . . .	125
5-11	Typical MOPA beam profile at various distances from beam waist locations. . . . .	126
5-12	Focused and collimated MOPA beam profiles. . . . .	127
5-13	Frequency stabilization scheme for the MOPA diode laser. . . . .	128
5-14	Locking electronics for servo-controlling the current source and the PZT.	129
5-15	Residual frequency noise of frequency-stabilized MOPA diode laser. .	130
6-1	3-to-1 optical frequency division schemes. . . . .	134
6-2	Temperature tuning curves for the two DFG interactions in the double-grating PPLN crystal. . . . .	138
6-3	Multiple duty cycle QPM grating design. . . . .	139
6-4	Schematic of second harmonic ring cavity for frequency-doubling 1064 nm Nd:YAG laser. . . . .	144
6-5	Experimental setup for 3-to-1 optical frequency divider using a double-grating PPLN crystal. . . . .	145
6-6	Schematic of detection system for $3\delta$ beat signal. . . . .	147
6-7	Frequency stabilization scheme for $3\delta$ beat signal. . . . .	152
6-8	Single-shot trace of frequency-stabilized $3\delta$ beat signal. . . . .	153
6-9	100-trace average of frequency-stabilized $3\delta$ beat signal. . . . .	154
6-10	An OPO-based 3-to-1 optical frequency divider. . . . .	157
7-1	A Brewster-angle-cut-PPLN-based dual-cavity OPO. . . . .	161
7-2	Temperature turning curve of a nearly degenerate PPLN-based OPO pumped at 798.4 nm with a 20.2 $\mu\text{m}$ grating period. . . . .	163
7-3	Reflectivity of air-LiNbO <sub>3</sub> interface as a function of angle of incidence.	164
7-4	Brewster-angle refraction at the air-LiNbO <sub>3</sub> interface for $\lambda= 1596$ nm.	164



7-5	Cavity design for nearly degenerate Brewster-angle-cut PPLN OPO. .	165
7-6	Experimental setup for nearly degenerate OPO based on Brewster-cut PPLN. . . . .	167
7-7	Optics for probe laser system. . . . .	169
7-8	Temperature tuning of single-pass DFG efficiency between the pump laser at 798 nm and probe laser output at 1596 nm. . . . .	171
7-9	Trace of OPO output vs. scanned cavity length. . . . .	173
7-10	Increase in round-trip cavity loss vs. temperature at 1596 nm after 15-minute illumination with 150 mW of pump. . . . .	176
7-11	8th-order QPM SHG of 798.4 nm as a function of $\Delta l$ , the deviation from the ideal 50/50 duty cycle. . . . .	177
7-12	Simulated second harmonic output power as a function of temperature deviation from the peak phasematching temperature. . . . .	179
7-13	Degradation of single-pass DFG output vs. time for 110 mW of con- stant illumination with pump laser. . . . .	180

# List of Tables

3.1	Processing procedure for patterning metal grating on LiNbO <sub>3</sub> . . . . .	82
6.1	Quasi-phasematching for double-grating PPLN . . . . .	137
7.1	Mirror reflectivities of the OPO cavity mirrors at 1593 nm . . . . .	170
7.2	Measured average duty cycle error $\Delta l$ and random duty cycle error $\sigma_l$ for different sections along the length of the 10-mm PPLN sample with $\Lambda = 20.2 \mu\text{m}$ . . . . .	178

# Chapter 1

## Introduction

### 1.1 Background

One of the most important technological inventions this century has been the laser, which provides coherent electromagnetic radiation covering the spectrum from the ultraviolet to the far infrared. Since the invention of the laser in 1958, many types of lasers have been developed, covering a wide range of output powers and output wavelengths. Today, lasers are applied to many essential applications in our society. In telecommunications, diode lasers produce information-carrying signals that are carried via optical fibers around the globe. Medical applications of lasers include their use as surgical and imaging tools. Industrial applications include the use of lasers for cutting, alignment, scribing, heating, etc. Lasers are also essential in a number of commercial products such as bar-code scanners, compact disc players, laser printers, and display. The most longstanding use of the laser has been in the scientific community where many new types of lasers have been developed over the years and have been used for a variety of scientific applications, among them are spectroscopy, remote sensing, the study of material properties, the study of chemical interactions, and many others. Today many types of lasers are available commercially, from high-powered gas lasers such as CO<sub>2</sub> lasers to efficient solid state lasers such as Nd:YAG lasers, and to compact and low-cost semiconductor diode lasers. Although together these lasers cover a broad spectral range, most do not offer the broad tuning range on

the order of tens of nanometers or more that is desirable in many scientific applications such as high-resolution spectroscopy, remote sensing, and quantum optics. While tunable lasers such as dye lasers and Ti:Sapphire lasers do offer excellent tuning ranges over selected spectral regions, there remains a vast collection of spectral regions in which tunable sources do not exist.

## 1.2 Nonlinear Optical 3-Wave Mixing

For years since its inception in 1961, nonlinear optics has been used to generate coherent radiation at new optical frequencies that are inaccessible otherwise. The most common way of generating new optical frequencies has been the use of three-wave mixing interactions in which power is transferred between a higher frequency field at  $\omega_1$  and two lower frequency fields at  $\omega_2$  and  $\omega_3$  through the second-order  $\chi^{(2)}$  nonlinearity of a nonlinear material, subject to the energy conservation requirement  $\omega_1 = \omega_2 + \omega_3$ . The various three-wave mixing processes include sum-frequency generation (SFG), in which two input fields at  $\omega_2$  and  $\omega_3$  generate an output at a higher frequency  $\omega_1 = \omega_2 + \omega_3$ ; difference-frequency generation (DFG), in which two input fields at  $\omega_1$  and  $\omega_2 (< \omega_1)$  generate an output field at  $\omega_3 = \omega_1 - \omega_2$ ; and optical parametric oscillation, in which an input field at  $\omega_1$  produces two outputs at frequencies  $\omega_2$  and  $\omega_3$  subject to the energy conservation requirement  $\omega_2 + \omega_3 = \omega_1$ . The non-deterministic nature of the output frequencies  $\omega_2$  and  $\omega_3$  of an optical parametric oscillator (OPO) suggests that an OPO can be used as a tunable source of coherent radiation by adjusting the physical properties of the nonlinear medium. Besides its use in generating new frequencies and providing a tunable coherent source, nonlinear optical three-wave mixing interactions also find applications in other areas such as the generation of squeezed states of light and optical frequency division for applications in frequency metrology and ultra-high precision measurements. This thesis aims to advance the state of the art in optical frequency metrology through nonlinear three-wave mixing interactions based on periodically-poled lithium niobate.

### 1.2.1 Phasematching

To achieve efficient power conversion in a three-wave mixing process, a nonlinear optical material must possess a reasonably large  $\chi^{(2)}$  nonlinearity and also satisfy the phasematching condition. The phasematching condition is a requirement that the relative phase among the interacting waves must be preserved throughout the medium in which the nonlinear interaction takes place. Because of phase velocity dispersion in which the index of refraction of a material is a function of wavelength, a three-wave mixing interaction is usually not phasematched unless special steps are taken to appropriately manipulate the refractive indices at one or more of the three interacting wavelengths. For most of the three decades since the inception of nonlinear optics, phasematching has been accomplished through the birefringent phasematching technique which takes advantage of the natural birefringence found in many anisotropic nonlinear materials. Phasematching in an isotropic material is in general not possible because of the monotonic dispersion relationship (refractive index vs. wavelength) for a given material. In a birefringent nonlinear material, where there are two sets of dispersion relationships corresponding to the ordinary and extraordinary polarized fields, one can accomplish phasematching through the judicious choice of the polarizations of the interacting fields. While many materials possess the requisite nonlinearity for efficient three-wave mixing interactions, only a selected few are considered practical for birefringent phasematching because most nonlinear materials have either too little or too much birefringence to phasematch a particular nonlinear interaction at the user-desired wavelengths of interest. In many cases a potentially practical nonlinear optical frequency conversion application is deemed infeasible simply because there does not exist a nonlinear material with the desirable properties to efficiently phasematch the interacting wavelengths of interest. Still, a number of nonlinear crystals suitable for birefringent phasematching of various three-wave mixing interactions in different spectral regions have been developed since 1961. Among them are potassium dihydrogen phosphate (KDP), potassium titanyl phosphate (KTP), beta barium borate (BBO), lithium triborate (LBO), silver thiogallate ( $\text{AgGaS}_2$ ), lithium iodate

(LiIO<sub>3</sub>), lithium niobate (LiNbO<sub>3</sub>), potassium niobate (KNbO<sub>3</sub>), rubidium titanyl arsenate (RTA), and cesium titanyl arsenate (CTA).

### 1.2.2 Quasi-phasematching

An alternative way of phasematching nonlinear interactions is the quasi-phasematching (QPM) technique. In QPM the relative phase mismatch of the three interacting fields is compensated by introducing a 180° phase shift among the interacting fields at periodic intervals. This periodic phase shift of 180° can be accomplished by a periodic reversal of the sign of the  $\chi^{(2)}$  nonlinearity. The period at which the 180° phase shift is introduced is determined by the indices of refraction at the interacting wavelengths and the temperature of the crystal. The most attractive feature of a quasi-phasematched nonlinear interaction rests in the freedom of the user to control the periodicity at which the 180° phase shift is introduced, which effectively allows the user to engineer the phasematching properties of the nonlinear material.

The concept of QPM was proposed independently by Bloembergen *et al.* [1] and by Franken and Ward [2] in 1961. QPM has been studied by many researchers using a number of nonlinear materials and techniques. Early efforts in the late 60's and early 70's sought to realize QPM by stacking together a number of coherence-length plates with alternating orientations of the spontaneous polarization vector. These efforts proved unsatisfactory because of excessive losses at the interfaces between adjacent plates [3][4][5][6][7]. This prevented the widespread use of QPM for efficient nonlinear optical frequency generation. Instead, for the past three decades since the discovery of nonlinear optics, birefringent phasematching has been the principal method used for phasematching nonlinear optical interactions. A revival of interest in the use of QPM occurred over the past 10 years as methods were developed to periodically reverse the sign of the optical nonlinearity of nonlinear optical materials such as lithium niobate (LiNbO<sub>3</sub>), lithium tantalate (LiTaO<sub>3</sub>), and potassium titanyl phosphate (KTP), by reversing their ferroelectric domain orientation. These ferroelectric domain-reversal methods include the use of titanium in-diffusion into a lithium niobate substrate, which worked well with waveguide devices and, more recently, the use of electric field

poling, which produced efficient bulk QPM materials. With these methods, low-loss QPM devices have been fabricated. Furthermore, the use of photolithography and the associated planar processing techniques allow this new generation of quasi-phasematched nonlinear optical devices to be fabricated inexpensively.

There are several distinct advantages in QPM over conventional birefringent phase-matching. In general, birefringent phase-matching for a given material can be utilized only in a very limited range of wavelengths. Furthermore, in cases where birefringent phase-matching is possible at a given wavelength, it often involves operation at inconvenient temperatures, or it requires the use of critical phase-matching geometry in which the propagation direction of the incident fields is not along any of the principal axes of the nonlinear crystal. Critically phase-matched geometry can lead to Poynting vector walk-off among the interacting fields and thus limits the effective interaction length. QPM, on the other hand, offers an engineerable approach to phase-matching in which the phase mismatch among the interacting waves at any wavelength and temperature can be compensated by specifying the proper domain-reversal period. This allows QPM nonlinear optical materials to be quasi-phasematched over the entire transparency region of the nonlinear optical material and at any user-specified temperature. Another advantage QPM has over birefringent phase-matching is that the user can choose the optimal set of polarizations for the interacting fields in order to utilize the largest nonlinear coefficient of the nonlinear crystal. In birefringent phase-matching one of the interacting fields must be orthogonally polarized relative to the other two. QPM, on the other hand, permits the three interacting fields to be co-polarized so that the “diagonal” elements of the nonlinear optical tensor can be accessed, which are in general larger than the “off-diagonal” elements to which birefringent phase-matching is restricted. In lithium niobate, for example, the largest effective nonlinear coefficient ( $d_{33}$ ) is approximately 4.5 times larger than the largest nonlinear coefficient ( $d_{31}$ ) accessible by birefringent phase-matching. This would produce an enhancement in conversion efficiency of 20 times compared to that for the case with birefringent phase-matching, all other things being equal.

### 1.2.3 QPM nonlinear optical frequency conversion applications

The inherent advantages of QPM, together with inexpensive and reliable fabrication of low-loss QPM materials, have fueled intense research in the use of QPM devices for a variety of nonlinear optical frequency mixing experiments over the past several years.

As an illustration of its practical applications, we provide two specific examples in which QPM nonlinear optical materials have been utilized to produce light sources with important commercial usage. One application is the production of coherent blue light from commercial near-infrared diode lasers. Blue-green laser sources have wide commercial applications such as displays, bar code scanners, and compact disc readers. Most of the high power and mature diode lasers in existence today are based on III-V semiconductor compounds, with operating wavelengths that are concentrated in the red to near-IR wavelength region, from approximately 635 to 980 nm and from 1300 to 1500 nm. Blue-green diode lasers, which are based on either III-V or II-VI compounds, have not matured to the point of being commercially available. However, the blue-green wavelength region can be accessed by direct frequency doubling of available near-infrared diode lasers. In principle, one can use GaAlAs and InGaAs diode lasers which operate between 800 nm and 1000 nm to double the optical frequency in a QPM material. Periodically poled lithium niobate (PPLN) has been used to generate hundreds of milliwatts of blue-green light from these high-power diode lasers which have outputs on the order of 1 W. Pruneri *et.al.* [8] generated 450 mW of blue light at 473 nm by frequency doubling a 1.07-W diode-pumped 946-nm Nd:YAG laser in a 6-mm-long PPLN crystal.

A second application for QPM materials is to produce a tunable source in the 1–5  $\mu\text{m}$  mid-infrared spectrum for applications in fiber-optic chemical sensors, spectroscopy, industrial process monitoring, and atmospheric and environmental monitoring. For these applications, there is a need to have a coherent source that can be tuned continuously across a wide wavelength region. One way to generate such a



tunable source is to use OPO's that are pumped by a near-infrared diode laser. In an OPO, the pump source is converted into two coherent outputs, the signal and the idler, the sum of whose frequencies is equal to the pump frequency. Myers *et al.* [9] demonstrated a Nd:YAG-pumped QPM OPO whose output wavelength is tunable from 1 to 5  $\mu\text{m}$ . Similar tuning ranges have also been achieved with other types of pump lasers as well [10][11].

## 1.3 Motivation

### 1.3.1 Applications of nonlinear optics to frequency metrology

In the field of frequency metrology there has been an immense interest in recent years in developing ultra-stable frequency references in the visible and near-IR spectral regions with fractional uncertainties (ratio of the line-center uncertainty to the transition frequency) that approach or even exceed the  $10^{-13}$  fractional uncertainty of the primary cesium frequency standard at 9.2 GHz. These ultra-stable frequency references are desirable for precision frequency measurements at visible and near-IR wavelengths. Ultra-high precision frequency measurements are important in quantum electrodynamics for determining the value of fundamental physical constants such as the Rydberg constant or the 1S-2S transition frequency of hydrogen. Ultra-stable frequency references also find potential applications in optical communications. For instance, a frequency-doubled diode laser output that is phase-locked to a rubidium transition at 778.1 nm can serve as an ultra-stable frequency reference for 1.55- $\mu\text{m}$ -based optical communications networks [12].

The realization of practical ultra-stable frequency references in the visible and near-IR regions has been greatly encouraged by the rapid development in recent years of high-power, compact, energy-efficient, narrow-linewidth, and low-noise solid-state and semiconductor lasers which can be frequency stabilized to these ultra-stable transitions.

Many potential visible and near-IR frequency references have been studied over the past few years. These include rf-trapped ions [13][14][15][16], magneto-optically-trapped Ca atoms [17], and various narrow-linewidth molecular transitions [18][19][20][21]. Like any other frequency reference, these potential optical frequency references must be calibrated to the primary cesium frequency standard via an optical-to-microwave frequency chain. Up until now, all existing optical-to-microwave frequency chains involve a cumbersome and complicated array of phase-locked IR and far-IR lasers and microwave oscillators. Figure 1-1 shows an example of a traditional optical-to-microwave frequency chain connecting a potential optical frequency standard of a Ca atomic transition at 445 THz to the cesium standard at 9.2 GHz [17]. Two modern schemes for implementing an optical-to-microwave frequency chains have been proposed recently. These schemes hold a major advantage over conventional frequency chains in that they require only laser oscillators in the visible and near-IR where there are excellent sources, detectors, and nonlinear materials for implementing frequency conversion. These schemes also eliminate the need for the array of transfer oscillators from the microwave up to the mid-IR spectral regions that make up the bulk of the traditional optical-to-microwave frequency chain. The frequency bisection scheme, proposed by Telle *et al.*, involves phase-locking the second harmonic of a laser to the sum frequency of two other lasers, thereby halving the difference frequency between the latter two lasers [22]. This frequency-halving procedure is then repeated until the difference frequency is sufficiently low to be measured by conventional means that are compatible with electronics. The other proposal, by Wong, relies on the use of optical frequency division by 2 and by 3 to implement an optical-to-microwave frequency chain [23][24][25], as illustrated in Fig. 1-2. Optical frequency division involves the precise generation and determination of frequency ratios between optical frequencies. Optical frequency division can also be applied to the establishment of secondary frequency markers that are related to their respective primary optical frequency references by precise ratios.

The basic idea behind the scheme proposed by Wong involves the use of a small number of 2:1 and 3:1 optical frequency dividers to reduce the task of measuring

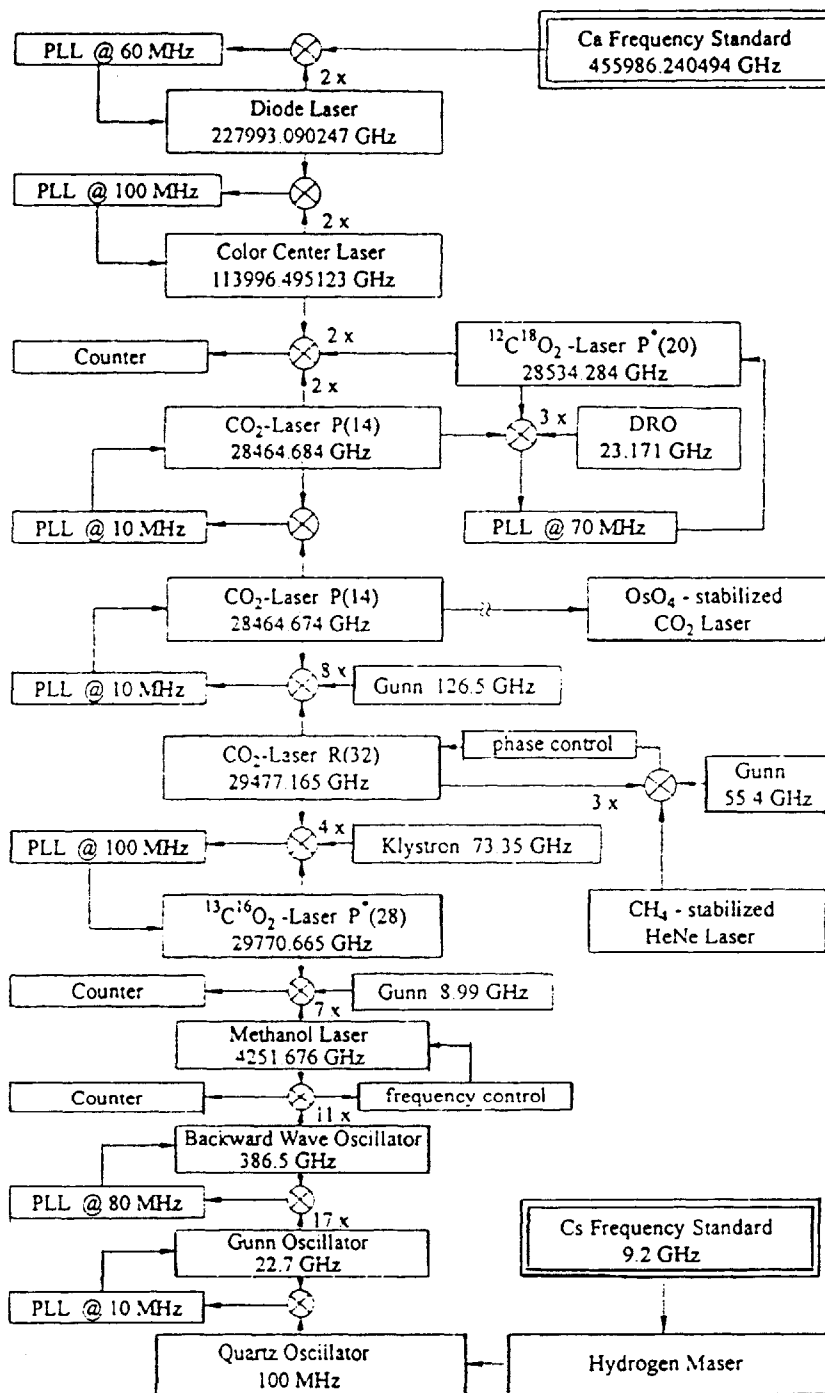


Figure 1-1: A traditional optical-to-microwave frequency chain. (Schnatz *et al.*, *Physical Review Letters* 76(1), pp. 18-21, 1996)

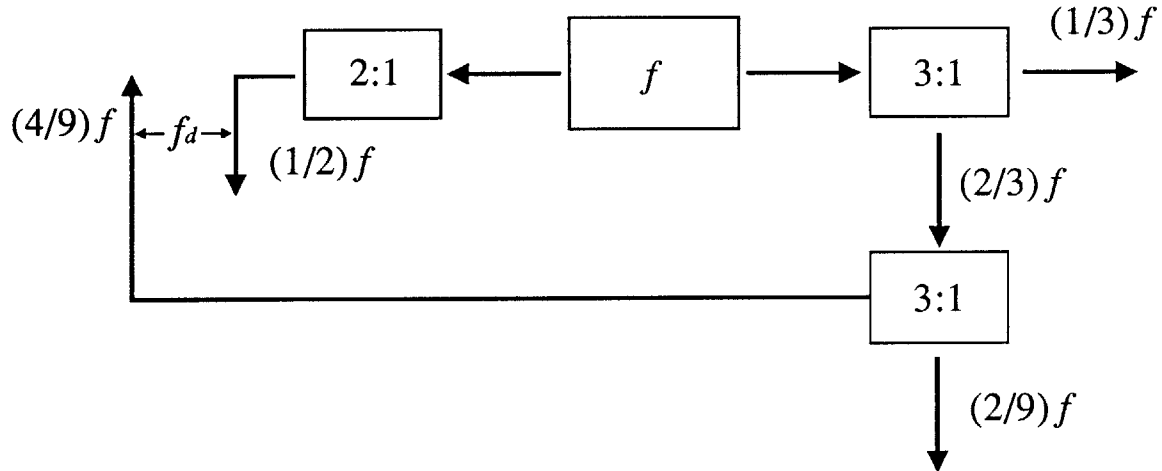


Figure 1-2: Optical-to-microwave frequency chain based on optical frequency division.

an optical frequency  $f$  in the visible and near-IR to that of measuring a difference frequency which is only a small fraction of  $f$  and which can be measured by methods compatible with electronics such as a multi-terahertz optical frequency comb generator. A more detailed discussion of the optical-to-microwave frequency chain is provided in Chapter 6. A 2:1 optical frequency divider can be implemented with a degenerate OPO in which the output frequencies are exactly  $1/2$  of the input frequency. Relevant work in 2:1 optical frequency division is discussed in Chapter 6.

### 1.3.2 3-to-1 optical frequency division

Compared to a 2:1 optical frequency divider, whose output frequencies are degenerate, a 3:1 optical frequency divider involves non-degenerate output frequencies in a 2:1 ratio. Therefore, its implementation requires an additional nonlinear frequency conversion stage to convert the optical frequency of one of the outputs to that of the second output such that phase/frequency locking can be performed.

3:1 optical frequency dividers have been demonstrated by Pfister *et al.* and Touahri *et al.* in 1996 and 1997, respectively. Each of these implementations rely on the use of two separate nonlinear crystals in birefringently phasematched DFG and SHG interactions to accomplish the 3:1 frequency connection. Detailed descriptions of these implementations are provided in Section 6.1.2.

As opposed to using two separate nonlinear crystals to phasematch the two nonlinear interactions, this research explored the feasibility of integrating the two nonlinear interactions in a single piece of nonlinear crystal, thereby simplifying the system configuration enormously and also reducing facet losses. In order to achieve high conversion efficiency for 2 nonlinear interactions in a single nonlinear crystal, both interactions must be simultaneously phasematched with well-overlapped temperature acceptance bandwidths. A natural candidate that satisfies the requirement of simultaneous phasematching is a double-grating PPLN in which two grating periods are defined to phasematch two separate nonlinear interactions on the same piece of nonlinear crystal at the same temperature.

In addition to possessing the engineered phasematching properties discussed in Section 1.2.2, PPLN also offers the added advantages of high nonlinearity via the  $d_{33}$  nonlinear coefficient of  $\text{LiNbO}_3$ , non-critical phasematching at user-defined temperatures, and low material cost compared to other nonlinear materials.

## 1.4 Contributions of This Research

This research has demonstrated the use of a single piece of periodically-poled  $\text{LiNbO}_3$  (PPLN) with a double-grating design to efficiently implement a dual-DFG-based 3-to-1 optical frequency divider of 532 nm. The choice of PPLN as the nonlinear material is based on PPLN's ability to be efficiently phasematched anywhere in its 0.35-5  $\mu\text{m}$  transparency range. This flexibility is an important consideration in the implementation of a practical optical-to-microwave frequency chain where any potential optical frequency reference in the visible and near-IR (up to 1.6  $\mu\text{m}$ ) spectral region can be frequency-divided-by-3 using PPLN.

This research also demonstrated for the first time the implementation of multiple nonlinear optical frequency interactions in a single piece of PPLN material. The general methodology can be extended to other applications requiring multiple nonlinear frequency synthesis. A discussion of the proposed optical-to-microwave frequency chain and the experimental implementation of the 3-to-1 frequency divider in

a double-grating PPLN will be provided in Chapter 6.

As will be discussed in Chapter 6, a 3:1 optical frequency divider can be implemented with much greater efficiency with an OPO/SHG-based scheme instead of the dual-DFG-based scheme by taking advantage of the much higher nonlinear conversion efficiency of an OPO compared to a single-pass DFG process. For this purpose, this research has also demonstrated a nearly-degenerate cw doubly-resonant OPO with a PPLN crystal with Brewster-angle-cut facets. This work demonstrates the use of Brewster-angle facets as a low-cost, low-loss alternative to multi-wavelength antireflection coatings in intra-cavity nonlinear optical frequency mixing applications and serves as a precursor to a 3:1 optical frequency divider based on a dual-cavity Brewster-cut double-grating PPLN OPO.

## 1.5 Thesis Organization

This thesis describes the use of PPLN-based devices that are fabricated via the electric field poling technique to investigate their use for applications in optical frequency metrology. Chapter 2 reviews the theory of QPM interactions. It outlines the basic derivations that lead to expressions for the QPM period, conversion efficiency, and wavelength and temperature bandwidths which are essential in characterizing a QPM nonlinear material. A review of the pertinent theory of DFG and OPO operation is also presented here. In addition, this chapter also discusses the effects of non-ideal fabrication on the conversion efficiency of the QPM interaction, followed by a discussion of a number of novel engineerable features of QPM interactions which are not available with the conventional birefringent phasematching. Chapter 3 addresses various aspects in the fabrication of PPLN, which is the nonlinear material used throughout the work described in this thesis. Included is a brief discussion of the various materials and methods that can be used for achieving periodic domain reversal. Characterization of the device quality of the fabricated PPLN samples is also presented here. Chapter 4 provides a summary of the relevant published work by others in nonlinear optical experiments using QPM materials fabricated by electric

field poling. Chapter 5 provides a detailed discussion of the master-oscillator/ power amplifier (MOPA) diode laser system which serves as a pump source for the experimental work discussed in Chapters 6 and 7. Chapter 6 presents the experimental work in realizing a 3-to-1 optical frequency divider of 532 nm by consecutive DFG interactions in a double-grating PPLN sample. A nearly degenerate cw doubly-resonant OPO based on a Brewster-cut PPLN crystal is discussed in Chapter 7. A summary of the current work and directions for future research is discussed in Chapter 8.

# Chapter 2

## Theory of QPM Nonlinear Interactions

This chapter describes the theory for quasi-phasematched (QPM) nonlinear optical interactions and discusses the design and characterization of QPM nonlinear optical devices.

Section 2.1 presents a conceptual description of quasi-phasematching. Section 2.2 derives the basic expressions for the QPM grating period and the effective nonlinearity of a QPM nonlinear interaction. QPM difference-frequency generation (DFG) is presented in Section 2.3, while QPM optical parametric oscillation (OPO) is discussed in Section 2.4. Section 2.5 treats the calculation of the QPM grating period for periodically-poled  $\text{LiNbO}_3$  using the Sellmeier's equation. In Section 2.6 the expressions for the spectral and temperature phasematching bandwidths for QPM DFG interactions are derived. In Section 2.7 a number of novel engineerable features unique to QPM nonlinear optical interactions will be described. Section 2.8 discusses a number of non-idealities associated with the fabrication of QPM devices that need to be considered when characterizing the performance of a QPM nonlinear optical material.



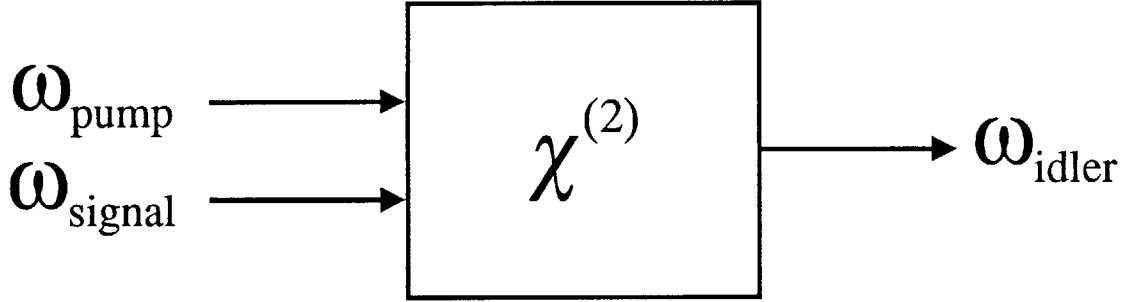
## 2.1 Overview of Quasi-Phasematching

In this section a conceptual description of QPM is presented. We illustrate the concept with the general three-wave mixing process in which two fields at frequencies  $\omega_1$  and  $\omega_2$  interact via the  $\chi^{(2)}$  optical nonlinearity of the medium to produce a third field at  $\omega_3$ , where  $\omega_3$  is either the sum- or difference-frequency  $\omega_3 = \omega_1 \pm \omega_2$  of the two input fields (assuming  $\omega_1 > \omega_2$ ). Conservation of energy requires that the sum of the photon energies of the lower-frequency fields equals the photon energy of the highest-frequency field. In keeping with the notation used for optical parametric amplifiers and oscillators, the highest-frequency field is denoted as the pump field and the lower-frequency fields as the signal and idler fields, respectively. Since the photon energy of a photon is equal to  $\hbar\omega$  where  $\omega$  is the optical frequency, the energy conservation requirement can be stated as

$$\omega_p = \omega_s + \omega_i \quad (2.1)$$

where the subscripts  $p$ ,  $s$ , and  $i$  denote the pump, signal, and idler fields, respectively. In a nonlinear 3-wave mixing process the input fields induce a nonlinear polarization at the sum- or difference-frequency. The polarization in turn radiates an output field at the same optical frequency. For efficient power conversion to the output field, the nonlinear optical interaction must also conserve linear momentum. Conservation of momentum requires that the relative phase between the output field and the polarization which drives the output field must be zero. That is,  $\sum_i \bar{k}_i = \bar{0}$  where  $\bar{k}_i$  is the wave-vector of the  $i^{\text{th}}$  interacting field.

The nonlinear interaction is said to be phasematched when the momentum conservation requirement is satisfied. Consider the case for difference-frequency generation (DFG), illustrated in Fig. 2-1. In DFG power is converted from the pump field to the signal and idler fields, subject to the condition that the idler field and the idler polarization are in phase. Figures 2-2 (a) and (b) illustrate the growth of the idler output power as a function of distance for a non-phasematched interaction, a perfectly phase-matched interaction, and a quasi-phasematched interaction. In a non-phasematched interaction, as is the case in general because of dispersion of the index of refraction



$$\omega_{\text{idler}} = \omega_{\text{pump}} - \omega_{\text{signal}}$$

Figure 2-1: Difference-frequency generation in a  $\chi^{(2)}$  nonlinear medium.

for a given nonlinear medium, this relative phase simply undergoes phase sweeps from 0 to  $2\pi$  repeatedly over the length of the crystal. The idler field would grow when the relative phase is between 0 and  $\pi$  and then decay when the relative phase is between  $\pi$  and  $2\pi$ . The distance over which the relative phase changes by  $\pi$  is called the coherence length. This is also the distance over which power exchange between the pump and the idler can remain in one direction. In a perfectly phasematched interaction, as is the case for birefringent phasematching, zero relative phase is maintained throughout the length of the crystal, resulting in a quadratic growth of the DFG output power as long as the DFG output power remains small compared to the input powers.

The concept of quasi-phasematching (QPM) is to preserve the direction of power flow from the pump to the signal and idler by alternating the sign of the  $\chi^{(2)}$  nonlinearity. The reversal in the sign of the nonlinearity is equivalent to a  $\pi$  phase change in the relative phase between the field and the polarization at the idler frequency. By changing the sign of the  $\chi^{(2)}$  nonlinearity every coherence length, one effectively resets the relative phase to zero every time the relative phase slips by  $\pi$ . With QPM, the nonlinear interaction is not strictly phasematched between points at which the relative phase is reset by  $\pi$ , since a perfectly phasematched interaction requires zero relative phase at all points. With the phase correction every coherence length, how-

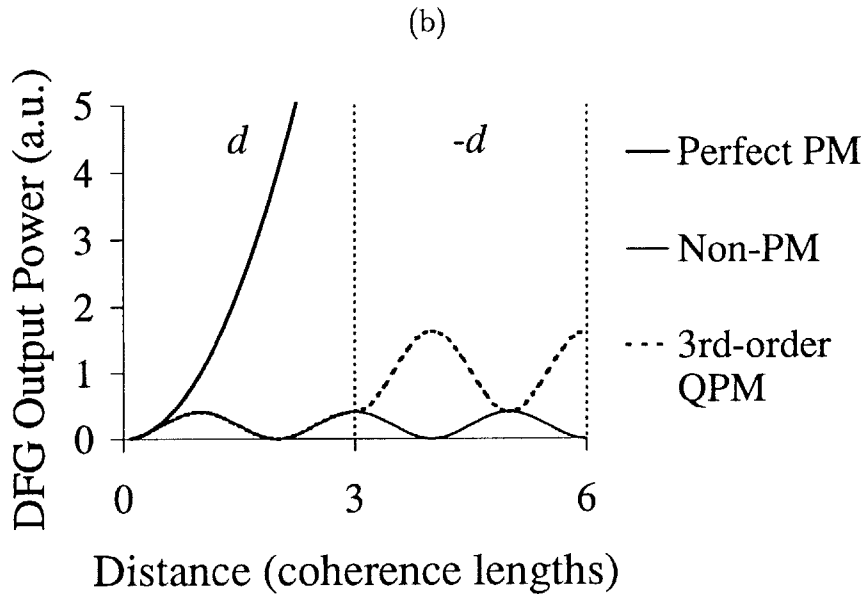
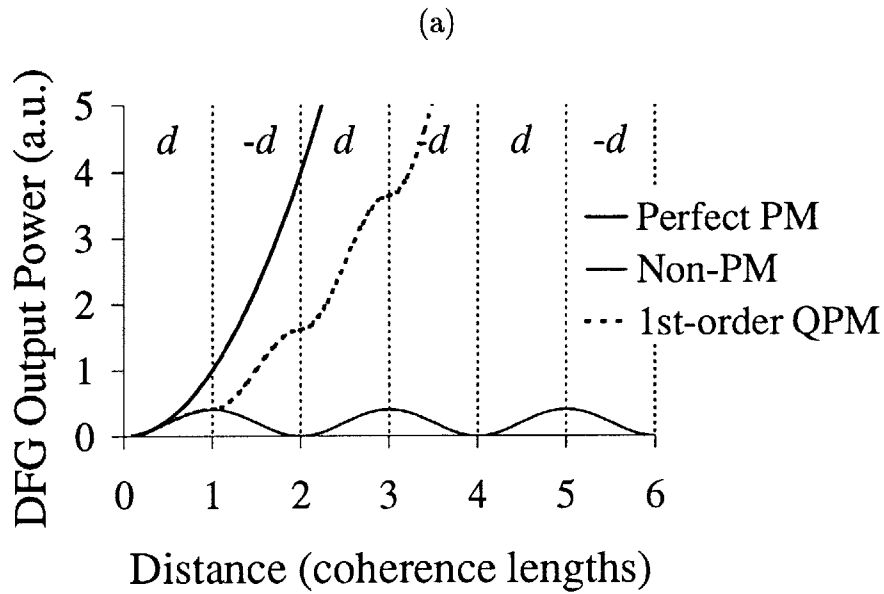


Figure 2-2: Effect of phasematching of DFG output power as a function of distance in a nonlinear medium with nonlinear coefficient  $d$ . This plot assumes non-depleted input powers and a plane-wave interactions. In a non-phasematched interaction, the output power oscillates with a period  $2l_c$ ,  $l_c$  being the coherence length of the nonlinear interaction. In a perfectly phasematched interaction, the output power grows quadratically versus distance. In a quasi-phasematched interaction (QPM), the nonlinear coefficient  $d$  alternates in sign to compensate for the phase velocity mismatch among the interacting fields. In a 1st-order QPM interaction (a), the nonlinear coefficient changes sign every  $l_c$ , while in a 3rd-order QPM (b), the sign change occurs every  $3l_c$ .

ever, the fields never become more than  $\pi$  out of phase, and the direction of power flow would be maintained in one direction, leading to the accumulation of power at the difference frequency  $\omega_i$ . The case where the sign of the nonlinear optical coefficient reverses every coherence length is called first-order QPM, as shown in Fig. 2-2a. It is also possible to achieve quasi-phasematching by reversing the sign of the nonlinear optical coefficient every 3, 5, 7..... coherence lengths, corresponding to third, fifth, seventh ..... order QPM. In these cases the overall conversion efficiency is reduced relative to that for first-order QPM because a reversal of power flow does occur over parts of the nonlinear medium. A third-order QPM is illustrated in Fig. 2-2b. Compared to a perfectly phasematched interaction, a QPM interaction is less efficient by a factor of  $(2/m\pi)^2$ ,  $m$  being the order of the QPM interaction. Thus, everything else being equal, the conversion efficiency for a first-order QPM interaction is  $\sim 40\%$  compared to a perfectly phasematched interaction.

## 2.2 QPM Period and Conversion Efficiency

In this section the derivations that lead to the expressions for the QPM period and the conversion efficiency are outlined. Here we assume difference-frequency generation (DFG), but the results apply equally well to any 3-wave mixing process such as sum-frequency generation (SFG), second harmonic generation (SHG), optical parametric amplification (OPA), and optical parametric oscillation (OPO). The optical fields are in the form:

$$E_j = \mathcal{E}_j(z)e^{-ik_j z}, \quad (2.2)$$

where  $E_j$  denotes the electric field with a wave-vector  $\bar{k}_j$  along the  $z$  direction, and  $\mathcal{E}_j$  is the slowly varying envelope function of the field  $E_j$ . The equation of motion for the idler field at frequency  $\omega_i$  is given by [1]

$$\frac{d\mathcal{E}_i}{dz} = i\frac{\omega_i}{n_i c}d(z)\mathcal{E}_p\mathcal{E}_s^* \exp(i\Delta k' z). \quad (2.3)$$

The above equation assumes no power loss inside the nonlinear medium and collinear interaction among the three fields. Furthermore, it is also assumed that the power accumulation at the idler frequency is much lower than the pump and signal power levels, and, therefore, there is no power depletion in the pump and signal fields as a function of distance. That is,

$$E_p(z) = E_p(z = 0),$$

and

$$E_s(z) = E_s(z = 0).$$

Here,  $\Delta k'$  is the wavenumber mismatch among the three fields and is given by

$$\Delta k' = k_p - k_s - k_i.$$

$d(z)$  is the nonlinear optical coefficient for the 3-wave mixing process and is a function of the distance  $z$ . Letting  $\Gamma = i \frac{\omega_i}{n_{ic}} \mathcal{E}_p \mathcal{E}_s^*$ , the output idler field can be expressed as

$$\frac{d\mathcal{E}_i(z)}{dz} = \Gamma d(z) \exp(i\Delta k' z). \quad (2.4)$$

In a quasi-phased-matched nonlinear medium the sign of the effective nonlinear coefficient  $d_{eff}$  is periodically modulated with a period  $\Lambda$ , as shown in Fig. 2-3 [26]. That is,

$$d(z) = \begin{cases} d_{eff} & n\Lambda < z < (n + \frac{1}{2})\Lambda \\ -d_{eff} & (n + \frac{1}{2})\Lambda < z < (n + 1)\Lambda \end{cases} \quad (2.5)$$

where  $n$  is an integer and  $\Lambda$  is the QPM grating period ( $\Lambda = 2l_c$  for 1st-order QPM). Let's define a normalized function  $g(z)$  such that  $g(z) = d(z)/d_{eff}$ . The field amplitude  $\mathcal{E}_i$  at a distance  $l$  can be expressed by the following integral:

$$\mathcal{E}_i(z = l) = \Gamma d_{eff} \int_0^l g(z) \exp(i\Delta k' z) dz. \quad (2.6)$$

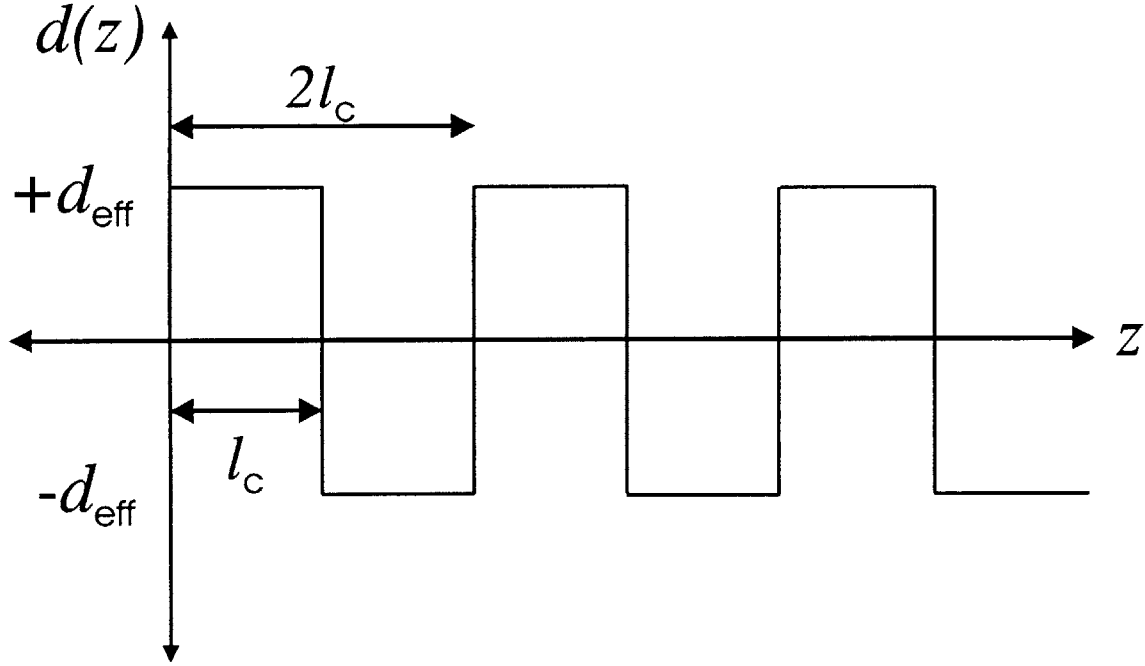


Figure 2-3: Profile of the effective nonlinear coefficient in a 1st-order QPM interaction where sign of the nonlinear coefficient alternates with a periodicity equal to twice the coherence length.

Since  $g(z)$  is a function periodic in  $z$  with period  $\Lambda$ , it can be represented as a Fourier series:

$$g(z) = \sum_{m=-\infty}^{m=+\infty} G_m \exp(-iK_m z), \quad (2.7)$$

where

$$K_m = \frac{2\pi m}{\Lambda}.$$

For the particular pulse train shown in Fig. 2-2, the Fourier coefficient  $G_m$  takes the form

$$G_m = \frac{2}{\pi m}, m = \text{odd integer}. \quad (2.8)$$

Substituting (2.8) into (2.6), we obtain

$$\mathcal{E}(z=l) = \Gamma d_{eff} \sum_{m=-\infty}^{m=+\infty} G_m \int_0^l \exp\{i(\Delta k' - K_m)z\} dz. \quad (2.9)$$

Let's assume that the  $m^{\text{th}}$  harmonic term  $K_m$  is close to  $\Delta k'$  such that the integral

is dominated by the  $m^{th}$  harmonic term. Evaluating the integral gives

$$\mathcal{E}(z = l) = \Gamma l d_{eff} \frac{2}{\pi m} \exp\left(i \frac{\Delta k l}{2}\right) \text{sinc}\left(\frac{\Delta k l}{2}\right), \quad (2.10)$$

where

$$\Delta k = \Delta k' - K_m = k_p - k_s - k_i - K_m.$$

According to (2.10),  $\mathcal{E}(z)$  is maximized if the wavenumber mismatch  $\Delta k'$  is set equal to  $K_m$ , or equivalently, if

$$\Lambda = \frac{2\pi m}{k_p - k_s - k_i}. \quad (2.11)$$

Equation (2.11) gives the period at which the nonlinear  $d_{eff}$  coefficient needs to be modulated to quasi-phasematch a nonlinear interaction with a wave-vector mismatch  $\Delta k'$ . The parameter  $m$  in equation (2.11) refers to the order of the QPM interaction. For first-order QPM interaction, the required QPM period is

$$\Lambda_1 = \frac{2\pi}{k_1 - k_2 - k_3}. \quad (2.12)$$

Likewise, for a third-order QPM interaction, the QPM period is

$$\Lambda_3 = \frac{6\pi}{k_1 - k_2 - k_3} = 3\Lambda_1. \quad (2.13)$$

## 2.3 Quasi-Phasematched Difference-Frequency Generation

In this section we present a brief review of the basic concepts of difference frequency generation (DFG) and some of the equations for analysis.

In a DFG interaction the outputs of two coherent optical sources are combined and sent through a  $\chi^{(2)}$  nonlinear optical medium. The  $\chi^{(2)}$  nonlinearity results in the generation of an output field at the frequency difference between the input optical frequencies. As illustrated in Fig. 2-1, the energy conservation requirement for DFG is

$$\omega_i = \omega_p - \omega_s. \quad (2.14)$$

Again, as discussed in Section 2.1, in keeping with the terminology used for OPO analysis, we call the difference-frequency output the idler field, the higher-frequency input the pump field, and the lower-frequency input the signal field. The momentum conservation, or phasematching, condition is typically expressed as

$$\bar{k}_p = \bar{k}_s + \bar{k}_i. \quad (2.15)$$

where  $\bar{k}_p$ ,  $\bar{k}_s$ , and  $\bar{k}_i$  are the wave-vectors for the pump, signal, and idler fields, respectively. For the special case where all three fields are collinear, one can express the phasematching condition in terms of the refractive indices and wavelengths of the interacting fields:

$$\frac{n_p}{\lambda_p} = \frac{n_s}{\lambda_s} + \frac{n_i}{\lambda_i}. \quad (2.16)$$

where  $n_s$ ,  $n_i$ , and  $n_p$  are the refractive indices at the signal, idler, and pump wavelengths. In QPM the phasematching condition is modified to take the following form:

$$\frac{n_p}{\lambda_p} = \frac{n_s}{\lambda_s} + \frac{n_i}{\lambda_i} + \frac{1}{\Lambda}. \quad (2.17)$$

where  $\Lambda$  is the QPM period for the DFG interaction. In general, the refractive indices are functions of temperature, and therefore the phasematching condition is also a function of temperature. For a given QPM period, efficient conversion is possible only within a specified temperature range. The intensity of the idler output is given as

$$I_i = \frac{1}{2} n_i c \epsilon_o E_i E_i^* = \frac{1}{2} n_i c \epsilon_o |\mathcal{E}_i|^2. \quad (2.18)$$

Likewise, the intensities of the pump and signal fields are expressed as

$$I_p = \frac{1}{2} n_p c \epsilon_o |\mathcal{E}_p|^2 \quad (2.19)$$



and

$$I_s = \frac{1}{2} n_s c \epsilon_o |\mathcal{E}_s|^2. \quad (2.20)$$

Substituting (2.10), (2.19), and (2.20) into (2.18), we obtain the DFG output intensity:

$$I_i = \frac{8\pi^2 d_Q^2 l^2}{\epsilon_o c n_i n_p n_s \lambda_i^2} I_p I_s \text{sinc}^2 \left( \frac{\Delta k l}{2} \right), \quad (2.21)$$

where  $d_Q = \frac{2}{\pi m} d_{eff}$  is the effective nonlinear coefficient for a QPM interaction. The above expression applies to plane waves. For Gaussian beams, the total power is the more relevant quantity. Let's define the output powers for the pump, signal, and idler fields as

$$P_p \equiv I_p A_p, P_s \equiv I_s A_s, P_i \equiv I_i A_i,$$

where  $A_p$ ,  $A_s$ , and  $A_i$  are the effective beam areas of the respective fields. It is straightforward to show that for Gaussian beams the effective beam area is related to the  $1/e^2$  beam radius as follows:

$$A_p = \frac{\pi}{2} w_p^2, A_s = \frac{\pi}{2} w_s^2, A_i = \frac{\pi}{2} w_i^2.$$

The idler output power expression thus becomes

$$P_i = \frac{16\pi d_Q^2 l^2}{\epsilon_o c n_i n_p n_s \lambda_i^2} P_p P_s \frac{1}{w_s^2 + w_p^2} \text{sinc}^2 \left( \frac{\Delta k l}{2} \right). \quad (2.22)$$

The above expression is valid in the limit of a loosely focused Gaussian beam in which the confocal parameter of the beam, defined as  $b = 2\pi n \omega_o^2 / \lambda$  is large compared to the interaction length of the nonlinear medium.  $\omega_o$  is the  $1/e^2$  waist radius of the beam. In the case when the confocal parameter is comparable to or less than the interaction length, the above expression needs to be modified to include the effect of the strong focusing. Taking into account the effect of strong focusing, as analyzed by Boyd and

Kleinman [27], the expression for the output idler power becomes

$$P_i = \frac{16\pi d_Q^2 P_p P_s l \bar{h}_m(B, \zeta)}{c \epsilon_0 n_p n_s n_i \lambda_i^2 \left( \frac{1}{k_p} + \frac{1}{k_s} \right)} \text{sinc}^2 \left( \frac{\Delta k l}{2} \right). \quad (2.23)$$

Here  $\bar{h}_m(B, \zeta)$  is the so-called reduction factor. The variable  $B$  takes into account the effect of double-refraction in an anisotropic medium, and  $\zeta = l/b$  is the interaction length normalized to the confocal parameter of the Gaussian beam. The reduction factor  $\bar{h}$  is maximized with respect to  $B$  when  $B=0$ , corresponding to non-critical phasematching in which the direction of propagation is along one of the principal axes of the nonlinear medium, and therefore there is no reduction in conversion efficiency due to Poynting vector walk-off among the interacting fields. Unlike birefringently phasematched interactions, which can seldom be non-critically phasematched, QPM interactions can always be designed to be non-critically phasematched at the user-desired temperature by specifying the proper QPM grating period. This constitutes a major advantage of QPM over birefringent phasematching. Under the optimal focusing condition in which  $\zeta = 2.28$ , and  $B = 0$ ,  $\bar{h}_m(B, \zeta) = 1.08$ . In the loosely focusing limit we find  $\bar{h}_m(B, \zeta) \rightarrow \zeta$ , and equation (2.23) becomes identical to equation (2.22).

## 2.4 Quasi-Phasematched Optical Parametric Oscillation

In optical parametric oscillation the nonlinear medium is placed inside an optical cavity that resonates one or both of the signal and idler fields, as shown in Fig. 2-4. There exists a threshold power level for the pump field which must be reached before the signal and idler fields begin to build up power. Physically, the gain at the signal and idler frequencies is provided by the pump beam. The more power the pump delivers to the gain medium (i.e. the nonlinear crystal), the larger the gain experienced by the signal and idler fields. Below the threshold pump power, the losses at the signal and idler frequencies due to the output coupling of the mirrors and intra-cavity losses exceed the gain provided by the pump over one cavity round-trip,

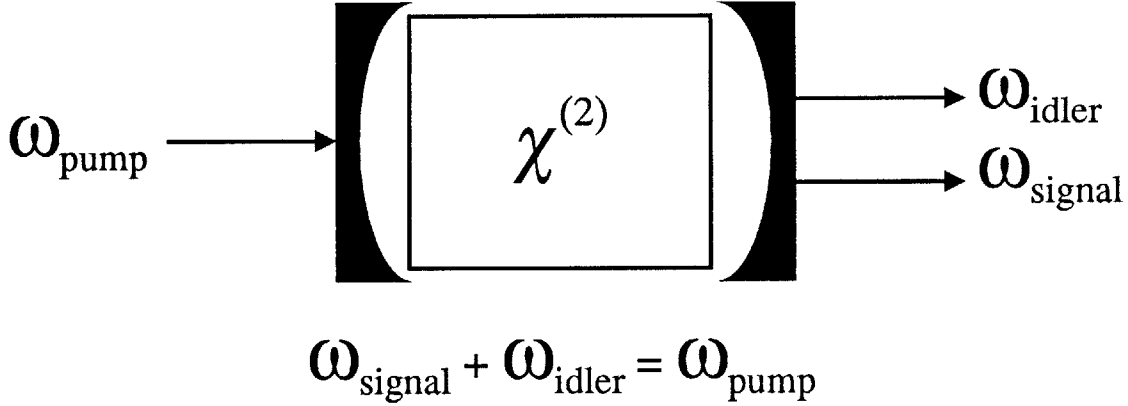


Figure 2-4: An optical parametric oscillator.

and therefore no power buildup is possible at the signal and idler frequencies. At the threshold pump power, the gain at the signal and idler fields matches the total loss, leading to non-decaying signal and idler fields over one resonator round-trip. Further increase in the pump power results in increasing power levels in the signal and idler fields. In a singly-resonant optical parametric oscillator (OPO), only the signal field is resonant inside the cavity; the cavity is highly lossy at the idler wavelength. In a doubly-resonant OPO, both the signal and idler fields are resonant.

The energy conservation and phasematching requirements for an OPO are analogous to those for DFG but with one important distinction. In a DFG interaction the interacting frequencies are fixed with the conversion efficiency of the idler output determined by the phasematching conditions. In an OPO the signal and idler output frequencies are determined directly by the phasematching conditions, which can be varied to tune the OPO output frequencies. Hence an OPO is effectively a coherent tunable source and serves as an attractive alternative to tunable lasers.

The energy conservation requirement for an OPO stipulates that the pump frequency equals the sum frequencies of the signal and idler fields. That is,

$$\omega_p = \omega_s + \omega_i. \quad (2.24)$$

In terms of the free space wavelengths  $\lambda$  of the interacting optical fields, the energy conservation requirement is

$$\frac{1}{\lambda_p} = \frac{1}{\lambda_s} + \frac{1}{\lambda_i}. \quad (2.25)$$

The energy conservation requirement determines the allowed signal-idler wavelength pairs (of which there are an infinite number) for a given pump wavelength. Just as in the case for any nonlinear optical interaction, the phasematching condition must also be satisfied in an OPO in order to obtain efficient power conversion from the pump to the signal and the idler. As already seen in Section 2.3 for the case of DFG, the phasematching condition for an OPO stipulates that the wave-vector of the pump field must be equal to the vector sum of the wave-vectors of the signal and idler fields:

$$\bar{k}_p = \bar{k}_s + \bar{k}_i. \quad (2.26)$$

Again, for the special case where the fields are collinear, the phasematching condition can be expressed in terms of the refractive index and the wavelength:

$$\frac{n_p}{\lambda_p} = \frac{n_s}{\lambda_s} + \frac{n_i}{\lambda_i}, \quad (2.27)$$

where  $n_p$ ,  $n_s$ , and  $n_i$  are the refractive indices at the pump, signal, and idler wavelengths, respectively. Just as for the case of DFG, the QPM phasematching condition is

$$\frac{n_p}{\lambda_p} = \frac{n_s}{\lambda_s} + \frac{n_i}{\lambda_i} + \frac{1}{\Lambda}. \quad (2.28)$$

The refractive indices are functions of both wavelength and temperature, and in general the output signal and idler wavelengths are determined by the pair of  $n_s$  and  $n_i$  that most closely satisfy the phasematching condition. Furthermore, because of the temperature dependence of the refractive indices, tuning the temperature of the crystal changes the phasematching condition and thus tunes the wavelength of the output signal and idler fields. It should be pointed out that the cavity resonances for the signal idler field also play an important role in determining the exact output wavelength of the OPO. The OPO cavity resonances will be discussed in Section 2.4.3.

### 2.4.1 The OPO threshold

In this section we derive the expression for the threshold pump power necessary to achieve oscillation in an OPO. We take the case of a doubly resonant OPO since the experimental devices to be discussed in Chapter 7 are based on a doubly-resonant OPO.

The equations of motion for the signal, idler, and pump fields, are, under the slowly varying field envelope approximation,

$$\frac{d\mathcal{E}_s}{dz} = i \frac{\omega_s d_Q}{n_s c} \mathcal{E}_p \mathcal{E}_i^* \exp(+i\Delta kz) \quad (2.29)$$

$$\frac{d\mathcal{E}_i}{dz} = i \frac{\omega_i d_Q}{n_i c} \mathcal{E}_p \mathcal{E}_s^* \exp(+i\Delta kz) \quad (2.30)$$

$$\frac{d\mathcal{E}_p}{dz} = i \frac{\omega_p d_Q}{n_p c} \mathcal{E}_p \mathcal{E}_s \exp(-i\Delta kz), \quad (2.31)$$

where  $\Delta k = k_p - k_s - k_i - K_m$  and  $d_Q = \frac{2}{m\pi} d_{eff}$ . If we consider the fact that the polarization waves at the three wavelengths do not have the same beam size as that defined by the cavity, we need to modify equations (2.29) to (2.31) to include only those components of the polarization waves that are supported by the resonator modes for the three interacting fields. After taking this effect into account, the equations of motions become

$$\frac{d\mathcal{E}_s}{dz} = i \frac{\omega_s d_Q}{n_s c} \frac{2w_p^2 w_i^2}{w_p^2 w_s^2 + w_p^2 w_i^2 + w_s^2 w_i^2} \mathcal{E}_p \mathcal{E}_i^* \exp(+i\Delta kz) \quad (2.32)$$

$$\frac{d\mathcal{E}_i}{dz} = i \frac{\omega_i d_Q}{n_i c} \frac{2w_p^2 w_s^2}{w_p^2 w_s^2 + w_p^2 w_i^2 + w_s^2 w_i^2} \mathcal{E}_p \mathcal{E}_s^* \exp(+i\Delta kz) \quad (2.33)$$

$$\frac{d\mathcal{E}_p}{dz} = i \frac{\omega_p d_Q}{n_p c} \frac{2w_s^2 w_i^2}{w_p^2 w_s^2 + w_p^2 w_i^2 + w_s^2 w_i^2} \mathcal{E}_p \mathcal{E}_s \exp(-i\Delta kz). \quad (2.34)$$

We now define normalized variable  $\mathcal{A}_m(z)$  such that  $|\mathcal{A}_m(z)|^2$  is the number of photons per second of each field, we obtain

$$\frac{d\mathcal{A}_s}{dz} = \Gamma \mathcal{A}_p \mathcal{A}_i^* \exp(+i\Delta kz) \quad (2.35)$$

$$\frac{d\mathcal{A}_i}{dz} = \Gamma \mathcal{A}_p \mathcal{A}_s^* \exp(+i\Delta kz) \quad (2.36)$$

$$\frac{d\mathcal{A}_p}{dz} = -\Gamma \mathcal{A}_p \mathcal{A}_s \exp(-i\Delta kz) \quad (2.37)$$

where

$$\mathcal{A}_m(z) = -i \left( \frac{\epsilon_o n_m \lambda_m \pi w_m^2}{4h} \right)^{\frac{1}{2}} \mathcal{E}_m(z) \quad (2.38)$$

and

$$\Gamma = \frac{2w_p w_s w_i}{w_p^2 w_s^2 + w_p^2 w_i^2 + w_s^2 w_i^2} \left( \frac{16\pi h d_Q^2}{\epsilon_o n_p n_s n_i \lambda_p \lambda_s \lambda_i} \right)^{\frac{1}{2}} \quad (2.39)$$

According to the analysis of Boyd and Kleinmann [27], optimum conversion efficiency occurs when

$$\frac{1}{w_p^2} = \frac{1}{w_s^2} + \frac{1}{w_i^2}$$

In this case the parametric gain coefficient  $\Gamma$  becomes

$$\Gamma = \left[ \frac{16\pi h d_Q^2}{\epsilon_o n_p n_s n_i \lambda_p \lambda_s \lambda_i (w_s^2 + w_i^2)} \right]^{\frac{1}{2}} \quad (2.40)$$

Integrating the normalized equations of motion (2.35) through (2.37) from  $z = 0$  to  $z = l$  and assuming that the field amplitudes do not change appreciably over the length  $l$ , one obtains

$$\mathcal{A}_p(l) - \mathcal{A}_p(0) = -l\chi^* \mathcal{A}_s(0) \mathcal{A}_i(0) \quad (2.41)$$

$$\mathcal{A}_s(l) - \mathcal{A}_s(0) = +l\chi \mathcal{A}_p(0) \mathcal{A}_i^*(0) \quad (2.42)$$

$$\mathcal{A}_i(l) - \mathcal{A}_i(0) = +l\chi \mathcal{A}_p(0) \mathcal{A}_s^*(0), \quad (2.43)$$

where

$$\chi = \Gamma l \exp(-i\Delta kl/2) \frac{\sin(\Delta kl/2)}{(\Delta kl/2)},$$

and

$$|\chi|^2 = \Gamma^2 l^2 \frac{\sin^2(\Delta kl/2)}{(\Delta kl/2)^2} = \frac{16\pi h d_Q^2 l^2}{\epsilon_o n_p n_s n_i \lambda_p \lambda_s \lambda_i (w_s^2 + w_i^2)} \frac{\sin^2(\Delta kl/2)}{(\Delta kl/2)^2}.$$

Including the effects of focusing,  $|\chi|^2$  becomes

$$|\chi|^2 = \frac{16\pi h d_Q^2 l \bar{h}_m(B, \xi)}{\epsilon_o n_p n_s n_i \lambda_p \lambda_s \lambda_i (\frac{1}{k_s} + \frac{1}{k_i})} \frac{\sin^2(\Delta kl/2)}{(\Delta kl/2)^2}. \quad (2.44)$$

We now derive the threshold power for optical parametric oscillation. Setting gain equal to loss for the respective fields inside the oscillator at resonance, we obtain the following coupled equations:

$$\kappa_p \mathcal{A}_p = t_p e_p - \chi^* \mathcal{A}_s \mathcal{A}_i \quad (2.45)$$

$$\kappa_s \mathcal{A}_s = \chi \mathcal{A}_p \mathcal{A}_i^* \quad (2.46)$$

$$\kappa_p \mathcal{A}_i = \chi \mathcal{A}_p \mathcal{A}_s^*. \quad (2.47)$$

Here,  $\kappa_p$ ,  $\kappa_s$ , and  $\kappa_i$  are the dimensionless round-trip total field loss and are defined as

$$\kappa_m = 1 - r_m(1 - \alpha_m), \quad (2.48)$$

where  $\alpha_m$  is the field amplitude loss due to crystal absorption and  $r_m$  is the effective field amplitude loss from the cavity mirrors. In Eq. (2.45)  $e_p$  is the external pump field amplitude and  $t_p$  is the transmission coefficient of the input coupler. By multiplying (2.47) by the conjugate of (2.46), one gets

$$|\mathcal{A}_p|^2 = \frac{\kappa_s \kappa_i}{|\chi|^2}.$$

Using (2.45), with the condition  $|\mathcal{A}_s|, |\mathcal{A}_i| \ll |\mathcal{A}_p|$  at threshold, one obtains

$$|e_{p,th}|^2 = \frac{\kappa_p^2 \kappa_i \kappa_s}{t_p^2 |\chi|^2}.$$

where  $|e_{p,th}|^2$  is the threshold pump power in units of photons per second. The

threshold pump power in watts is

$$P_{th} = \frac{hc}{\lambda_p} |e_{p,th}|^2 = \frac{hc \kappa_p^2 \kappa_i \kappa_s}{\lambda_p t_p^2 |\chi|^2}. \quad (2.49)$$

The above analysis has assumed that the pump field is resonant inside the cavity. For the special case where the pump is non-resonant and makes a single pass through the nonlinear medium with unity transmission at the input coupler, we can set  $\kappa_p = 1$  and  $t_p = 1$ , in which case the threshold pump power is

$$P_{th} = \frac{hc \kappa_i \kappa_s}{\lambda_p |\chi|^2}. \quad (2.50)$$

In Eq. (2.50), the signal and idler losses  $\kappa_s$ ,  $\kappa_i$  refer to the round-trip attenuation of the signal and idler fields. Assuming that the losses are small, that is  $\kappa_s \ll 1$  and  $\kappa_i \ll 1$ , we can approximate the round-trip power loss  $a_s$ ,  $a_i$  as  $a_s \sim 2\kappa_s$  and  $a_i \sim 2\kappa_i$ . Furthermore, by substituting (2.44) into (2.50), we obtain an expression for  $P_{th}$  that is similar to that for the DFG output power (2.23):

$$P_{th} = \frac{c\epsilon_o n_p n_s n_i \lambda_s \lambda_i (1/k_s + 1/k_i)}{64\pi d_{eff}^2 L \bar{h}_m} \left[ \frac{\sin^2(\Delta k L/2)}{(\Delta k L/2)^2} \right]^{-1}. \quad (2.51)$$

Under phasematched condition,  $\Delta k = 0$ , and (2.51) reduces to

$$P_{th} = \frac{c\epsilon_o n_p n_s n_i \lambda_s \lambda_i (1/k_s + 1/k_i)}{64\pi d_{eff}^2 L \bar{h}_m}. \quad (2.52)$$

As mentioned in the previous section, the absence of walk-off among the interacting fields in a non-critically angle-phasematched interaction results in a more efficient single-pass conversion efficiency and thus a higher nonlinear gain  $|\chi|^2$  and therefore a lower pump threshold power compared to that for critical angle-phasematching that is unavoidable in most birefringently phasematched interactions.

## 2.4.2 Above-threshold OPO output

We now derive the expression for the signal and idler output power for the case where the pump power is above threshold for a doubly-resonant OPO. The coupled



equations above threshold are

$$\kappa_p \mathcal{A}_p = -\chi^* \mathcal{A}_s \mathcal{A}_i + t_p e_p \quad (2.53)$$

$$\kappa_s \mathcal{A}_s = \chi \mathcal{A}_p \mathcal{A}_i^* \quad (2.54)$$

$$\kappa_p \mathcal{A}_i = \chi \mathcal{A}_p \mathcal{A}_s^*. \quad (2.55)$$

By substituting (2.55) into (2.53) we obtain an expression for  $\mathcal{A}_p$ ,

$$\mathcal{A}_p \left( 1 + \frac{|\chi|^2 |\mathcal{A}_s|^2}{\kappa_p \kappa_i} \right) = \frac{t_p e_p}{\kappa_p}.$$

Taking the magnitude squared, one gets

$$|\mathcal{A}_p|^2 \left( 1 + \frac{|\chi|^2 |\mathcal{A}_s|^2}{\kappa_p \kappa_i} \right)^2 = \frac{t_p^2 |e_p|^2}{\kappa_p^2}. \quad (2.56)$$

Because of the oscillation condition that gain equals to loss at the signal and idler wavelengths, the internal pump power inside the resonator is clamped at the threshold level when pumping above threshold. That is,

$$|\mathcal{A}_p|^2 = |\mathcal{A}_{p,th}|^2 = \frac{\kappa_s \kappa_i}{|\chi|^2}. \quad (2.57)$$

Substituting the above expression into (2.56), one obtains

$$\left( 1 + \frac{|\chi|^2 |\mathcal{A}_s|^2}{\kappa_p \kappa_i} \right)^2 = \frac{|\chi|^2 t_p^2}{\kappa_p^2 \kappa_s \kappa_i} |e_p|^2 = \frac{|e_p|^2}{|e_{p,th}|^2}. \quad (2.58)$$

Note that the term  $|e_p|^2/|e_{p,th}|^2$  is simply the ratio between the external pump power and the threshold pump power. The signal power inside the cavity (in units of photon per second) is

$$|\mathcal{A}_s|^2 = \frac{\kappa_p \kappa_i}{|\chi|^2} \left( \sqrt{\frac{P}{P_{th}}} - 1 \right). \quad (2.59)$$

Likewise, the idler output power inside the cavity is

$$|\mathcal{A}_i|^2 = \frac{\kappa_p \kappa_s}{|\chi|^2} \left( \sqrt{\frac{P}{P_{th}}} - 1 \right). \quad (2.60)$$

The signal and idler output powers outside the cavity are determined by multiplying (2.59) and (2.60) by the power transmission  $T_s$ ,  $T_i$  of the output coupler at the signal and idler wavelengths. The expressions for the signal and idler output power becomes

$$|\mathcal{A}_s|^2_{out} = \frac{\kappa_p \kappa_i}{|\chi|^2} T_s \left( \sqrt{\frac{P}{P_{th}}} - 1 \right) \quad (2.61)$$

$$|\mathcal{A}_i|^2_{out} = \frac{\kappa_p \kappa_s}{|\chi|^2} T_i \left( \sqrt{\frac{P}{P_{th}}} - 1 \right). \quad (2.62)$$

Making use of (2.44), the expressions for the signal and idler output power in units of watts become

$$P_{s,out} = \frac{\lambda_p}{\lambda_s} \frac{t_p^2}{\kappa_p \kappa_s} T_s P_{th} \left( \sqrt{\frac{P}{P_{th}}} - 1 \right) \quad (2.63)$$

$$P_{i,out} = \frac{\lambda_p}{\lambda_i} \frac{t_p^2}{\kappa_p \kappa_i} T_i P_{th} \left( \sqrt{\frac{P}{P_{th}}} - 1 \right). \quad (2.64)$$

Again, if we assume a single-pass pump geometry and unity pump transmission through the cavity, we can set  $\kappa_p = 1$  and  $t_p = 1$ . Furthermore, by substituting  $a_s = 2\kappa_s$  and  $a_i = 2\kappa_i$ , the signal and idler output powers become

$$P_{s,out} = \frac{2\lambda_p T_s}{\lambda_s a_s} P_{th} \left( \sqrt{\frac{P}{P_{th}}} - 1 \right) \quad (2.65)$$

$$P_{i,out} = \frac{2\lambda_p T_i}{\lambda_i a_i} P_{th} \left( \sqrt{\frac{P}{P_{th}}} - 1 \right). \quad (2.66)$$

Sometimes it is useful to describe the performance of the OPO in terms of the total conversion efficiency  $\eta$ , defined as the ratio between the sum of the signal and idler output powers and the input pump power. From (2.65) and (2.66), we obtain

$$\eta = \frac{P_{s,out} + P_{i,out}}{P} = 2\lambda_p \left( \frac{1}{\lambda_s} \frac{T_s}{a_s} + \frac{1}{\lambda_i} \frac{T_i}{a_i} \right) \frac{P_{th}}{P} \left( \sqrt{\frac{P}{P_{th}}} - 1 \right). \quad (2.67)$$

For degenerate OPO outputs where  $\lambda_s = \lambda_i$ ,  $a_s = a_i = a_{s,i}$ , and  $T_s = T_i = T_{s,i}$ , the

expression for  $\eta$  can be further reduced to

$$\eta = 2 \frac{T_{s,i}}{a_{s,i}} \frac{P_{th}}{P} \left( \sqrt{\frac{P}{P_{th}}} - 1 \right). \quad (2.68)$$

### 2.4.3 OPO cavity resonances

In a doubly-resonant OPO the signal and idler output frequencies are determined by a combination of the requirements for the conservation of energy, the minimum threshold pump power for oscillation (which, in turn, is a function of phasematching, round-trip cavity losses, etc.), and the double-resonance condition. A typical OPO can operate on a large number of discrete oscillation frequencies within the phasematching bandwidth. For PPLN, the phasematching bandwidth for a degenerate OPO pumped at 798 nm is  $\sim 150$  nm for a 10-mm interaction length. In general, the OPO oscillates at frequencies that are on or very close to the cavity resonances at the signal and idler wavelengths. Let's define the signal/idler axial mode numbers as  $m_s = 2L_s/\lambda_s$  and  $m_i = 2L_i/\lambda_i$ , where  $L_s$  and  $L_i$  are the optical path lengths of the cavity and  $\lambda_s$ ,  $\lambda_i$  are the free space signal/idler wavelengths. There are two types of mode spacings for the signal/idler outputs. The first type, called the axial mode spacing, are the frequency changes associated with integral changes of the mode numbers  $m_s$  and  $m_i$ . A signal/idler mode pair differs from an adjacent pair by a change of +1 in  $m_s$ , in conjunction with a change of -1 in  $m_i$ , or vice versa, such that the total mode number  $m = m_s + m_i$  remains unchanged.

The change in the signal/idler frequency  $\Delta f = \Delta f_s = -\Delta f_i$  for adjacent mode pairs is given approximately by the cavity free spectral range:

$$\Delta f \sim \delta f = \frac{c}{2L}.$$

A detailed analysis such as those given by Eckardt *et al.* [28] and Lee *et al.* [29] shows that the actual oscillation frequencies may differ slightly from the cavity resonance frequencies in order to satisfy the condition of energy conservation. In such cases the precise frequency separation between adjacent signal/idler axial mode pairs also

depends on the cavity finesse for the signal and idler fields. A straightforward way to tune the OPO signal and idler outputs is by changing the total cavity length  $L$ , where

$$L = L_{\text{freespace}} + nL_{\text{crystal}} \quad (2.69)$$

with  $n$  being the refractive index. The change in  $\Delta L$  that corresponds to a frequency separation  $\Delta f$  between adjacent signal/idler axial mode pairs can be shown to be [29]

$$\Delta L = L_{\text{crystal}}(n_s - n_i + \alpha_s f_s - \alpha_i f_i) \frac{\Delta f}{f_p} \quad (2.70)$$

where  $\alpha_s \equiv \Delta n_s / \Delta f_s$  and  $\alpha_i \equiv \Delta n_i / \Delta f_i$  are the linear dispersion coefficients, and  $f_p$  is the pump frequency. In general, as a tuning variable, say the cavity length or temperature, is varied, an adjacent signal/idler mode pair may better satisfy the energy conservation requirement and/or yield a lower pump threshold than the original pair. It then becomes advantageous for the oscillation frequencies to hop to the adjacent signal/idler mode pair. Such a change in the signal/idler oscillation frequency is called mode hopping.

The second type of mode spacing is called the cluster mode spacing and corresponds to integral change in the mode number  $m = m_s + m_i$ . The frequency spacing between adjacent clusters is given as [28]

$$\Delta f_{\text{cluster}} = \frac{\delta f_s \delta f_i}{\delta f_s - \delta f_i} \quad (2.71)$$

where  $\delta f_s$  and  $\delta f_i$  are the free spectral ranges of the cavity at the signal and idler frequencies. In general  $\Delta f_{\text{cluster}} \gg \Delta f_{\text{axial}}$ . If the gain bandwidth of the OPO interaction is large enough to support more than one frequency cluster, the signal/idler frequency pairs from different frequency clusters occupy the same cavity position. That is  $\Delta L = 0$  for corresponding signal/idler mode pairs from different frequency clusters. This situation can lead to unpredictable mode hops between the clusters under small perturbations.

## 2.5 Calculation of QPM Grating Period

As discussed in Section 2.1, a quasi-phasematched interaction involves a periodic reversal of the sign of  $d_{eff}$  to compensate for phase velocity dispersion. Let's consider the case of difference-frequency mixing and optical parametric oscillation that we discussed in the previous two sections. From (2.17) and (2.28) the phasematching condition for a collinear interaction can be expressed as

$$\frac{n_p}{\lambda_p} = \frac{n_s}{\lambda_s} + \frac{n_i}{\lambda_i} + \frac{1}{\Lambda}, \quad (2.72)$$

where  $\Lambda$  is the period of the sign reversal. From now on we shall refer to the sign reversal period  $\Lambda$  as the grating period.

In general the refractive index of any nonlinear material is a function of both wavelength (dispersion) and temperature. For LiNbO<sub>3</sub> normal dispersion results in

$$\frac{n_p}{\lambda_p} > \frac{n_s}{\lambda_s} + \frac{n_i}{\lambda_i}$$

over the entire transparency region of the material. The phasematching condition can thus be expressed as

$$\frac{n_p(\lambda_p, T)}{\lambda_p} = \frac{n_s(\lambda_s, T)}{\lambda_s} + \frac{n_i(\lambda_i, T)}{\lambda_i} + \frac{1}{\Lambda}. \quad (2.73)$$

The grating period is thus given by

$$\Lambda = \left[ \frac{n_p(\lambda_p, T)}{\lambda_p} - \frac{n_s(\lambda_s, T)}{\lambda_s} - \frac{n_i(\lambda_i, T)}{\lambda_i} \right]^{-1}. \quad (2.74)$$

Very accurate Sellmeier's equations for LiNbO<sub>3</sub> are available that facilitates the design of the proper grating period  $\Lambda$  necessary for quasi-phasematching any interaction within the transparency region of 0.33 - 5  $\mu\text{m}$ . The temperature-dependent Sellmeier's equations used in this work is derived by Edwards and Lawrence [30]. In interactions utilizing the  $d_{33}$  coefficient, as is true for all work described in this thesis, all three fields are polarized as extraordinary waves. The extraordinary refractive index is

given as

$$n_e^2 = A_1 + \frac{A_2 + B_1 F}{\lambda^2 - (A_3 + B_2 F)^2} + B_3 F - A_4 \lambda^2, \quad (2.75)$$

where  $A_1 = 4.5820$ ,  $A_2 = 0.09921$ ,  $A_3 = 0.21090$ ,  $A_4 = 0.021940$ ,  $B_1 = 5.2716 \times 10^{-8}$ ,  $B_2 = 4.9143 \times 10^{-8}$ ,  $B_3 = 2.2971 \times 10^{-7}$ , and  $F = (T - 24.5)(T + 570.5)$ . The wavelength  $\lambda$  is in units of  $\mu\text{m}$ , and the temperature  $T$  is expressed in  $^\circ\text{C}$ .

The grating period itself is a function of temperature as a result of thermal expansion of the  $\text{LiNbO}_3$ . The coefficient of expansion  $\alpha$  for  $\text{LiNbO}_3$  is  $1.5 \times 10^{-5}/\text{K}$

## 2.6 Wavelength and Temperature Bandwidths

In this section we derive expressions for the spectral and temperature bandwidths for quasi-phasematched nonlinear optical interactions. This is particularly important because the phasematching condition is a very sensitive function of the refractive indices of the interacting waves which are, in turn, sensitive functions of both wavelength (dispersion) and temperature.

Equation (2.10) shows that the conversion efficiency for a DFG interaction is proportional to  $\text{sinc}^2[(\frac{\Delta k}{2})l]$  where  $\Delta k$  is the wavenumber mismatch from phasematched condition. The conversion efficiency drops to 1/2 of its peak when  $\text{sinc}^2[(\frac{\Delta k}{2})l] = 0.5$ , or when  $\Delta k l = 2.783$ . Assuming that the length  $l$  is fixed, the full-width-half-max (FWHM) bandwidth is given by

$$(\delta \Delta k)_{FWHM} = 5.566/l. \quad (2.76)$$

We first derive a general expression for the phasematching bandwidth associated with an arbitrary physical observable  $x$  near  $x_o$ . Let  $\Delta k$  be a function of  $x$  and assume that the interaction is phasematched at  $x = x_o$  such that  $\Delta k(x = x_o) = 0$ . By expanding  $\Delta k$  in a Taylor series around  $x_o$  and keeping just the first-order term, we obtain

$$\Delta k(x) = (x - x_o) \frac{\delta \Delta k}{\delta x} \Big|_{x=x_o}. \quad (2.77)$$

The conversion efficiency drops to 1/2 when  $\Delta k = (\delta x) \left( \frac{\delta \Delta k}{\delta x} \right) = 2.783/l$ . This gives

$$(\delta x)_{FWHM} = (5.566/l) \left( \frac{\delta \Delta k}{\delta x} \right)^{-1} \quad (2.78)$$

### 2.6.1 Spectral bandwidth

Based on equation (2.75), the expression for the FWHM spectral bandwidth is

$$(\delta \lambda_m)_{FWHM} = (5.566/l) \left( \frac{\delta \Delta k}{\delta \lambda_m} \right)^{-1} = (5.566/l) \left( \frac{\delta \Delta k'}{\delta \lambda_m} \right)^{-1} \quad (2.79)$$

Recall that  $\Delta k = k_p - k_s - k_i - K_m$  and  $\Delta k' = k_p - k_s - k_i$ . Here  $m = p, s, i$  refers to the pump, signal, and idler, respectively. The above expression can be rewritten in terms of the interacting wavelengths and the corresponding refractive indices:

$$(\delta \lambda_m)_{FWHM} = (0.886/l) \left[ \frac{\delta}{\delta \lambda_m} \left( \frac{n_p}{\lambda_p} - \frac{n_s}{\lambda_s} - \frac{n_i}{\lambda_i} \right) \right]^{-1} \Big|_{\lambda_m = \lambda_{m,o}} \quad (2.80)$$

As an illustration of typical spectral bandwidths associated with LiNbO<sub>3</sub> nonlinear interactions, consider a QPM LiNbO<sub>3</sub> parametric interaction via the  $d_{33}$  nonlinearity with a pump wavelength of 1064 nm. Let's consider two cases. In the first case, the signal and idler outputs are non-degenerate with  $\lambda_s = 1596$  nm and  $\lambda_i = 3192$  nm. In the second case, the signal and idler outputs are degenerate with  $\lambda_s = \lambda_i = 2128$  nm. Let's further assume that the pump wavelength is fixed because we are interested in the spectral bandwidth of the signal field. According to Myers *et al.* [31], the spectral bandwidth based on calculations using the Sellmeier's equations [30] for a 1-cm-long interaction length is 11 nm for the non-degenerate interaction and 322 nm for the degenerate interaction.

## 2.6.2 Temperature bandwidth

Based on Eq. (2.78) the expression for the FWHM temperature bandwidth is

$$(\delta T)_{FWHM} = (5.566/l) \left( \frac{\Delta k}{\delta T} \right)^{-1}. \quad (2.81)$$

However, in this case the crystal length  $l$  is also a function of temperature. (2.78) should then be modified to

$$(\delta T)_{FWHM} = (5.566) \left[ \frac{\delta}{\delta T} (\Delta kl) \right]^{-1} \Big|_{T=T_0}. \quad (2.82)$$

The temperature dependence of the phasematching condition contains two parts: the change in the refractive index as a function of temperature, and the change in the grating period as a result of thermal expansion of the crystal.

$$\frac{\delta}{\delta T} (\Delta kl) = l \frac{\delta \Delta k}{\delta T} + \Delta k \frac{\delta l}{\delta T} = l \left( \frac{\delta \Delta k'}{\delta T} - \frac{\delta K_m}{\delta T} \right) + \Delta k \frac{\delta l}{\delta T} \quad (2.83)$$

The first term on the right hand side of (2.83) is

$$l \frac{\delta \Delta k'}{\delta T} = 2\pi l \left( \frac{1}{\lambda_p} \frac{\delta n_p}{\delta T} - \frac{1}{\lambda_s} \frac{\delta n_s}{\delta T} - \frac{1}{\lambda_i} \frac{\delta n_i}{\delta T} \right). \quad (2.84)$$

The second term on the right hand side of (2.83) is

$$-l \frac{\delta K_m}{\delta T} = -l \frac{\delta}{\delta T} \left( \frac{2\pi m}{\Lambda} \right) = l \frac{2\pi m}{\Lambda^2} \frac{\delta \Lambda}{\delta T} = K_m l \frac{1}{\Lambda} \frac{\delta \Lambda}{\delta T}. \quad (2.85)$$

The thermal expansion coefficient is given by

$$\alpha \equiv \frac{1}{\Lambda} \frac{\delta \Lambda}{\delta T} = \frac{1}{l} \frac{\delta l}{\delta T},$$

such that (2.85) becomes

$$-l \frac{\delta K_m}{\delta T} = \alpha K_m l. \quad (2.86)$$



The third term on the right hand side of (2.83) is

$$\Delta k \frac{\delta l}{\delta T} = \Delta k' \alpha l - K_m \alpha l = \alpha l \left( \frac{n_p}{\lambda_p} - \frac{n_s}{\lambda_s} - \frac{n_i}{\lambda_i} \right) - K_m \alpha l. \quad (2.87)$$

We then obtain the following expression for the FWHM bandwidth:

$$(\delta T)_{FWHM} = (0.886/l) \left[ \frac{\alpha}{2\pi} \left( \frac{n_p}{\lambda_p} - \frac{n_s}{\lambda_s} - \frac{n_i}{\lambda_i} \right) + \left( \frac{1}{\lambda_p} \frac{\delta n_p}{\delta T} - \frac{1}{\lambda_s} \frac{\delta n_s}{\delta T} - \frac{1}{\lambda_i} \frac{\delta n_i}{\delta T} \right) \right]^{-1} \quad (2.88)$$

The dependence of the index of refraction  $n$  on both wavelength and temperature can be estimated from the Sellmeier's equations [30]. If either the temperature or the wavelength is tuned,  $\Delta k$  would deviate from 0, and the reduction in conversion efficiency would be given by equation (2.23).

As we have done in the previous section, let's again consider a 1064-nm-pumped  $d_{33}$  QPM parametric interaction in a 1-cm-long LiNbO<sub>3</sub> at T= 25°C for the non-degenerate ( $\lambda_s = 1596$  nm,  $\lambda_i = 3196$  nm) and the degenerate ( $\lambda_s = \lambda_i = 2128$  nm) cases [31]. The temperature bandwidths are 22°C for the non-degenerate interaction and 19°C for the degenerate interaction based on calculations using Sellmeier's equations [30]. Furthermore, it is interesting to compare the temperature bandwidths for QPM interactions with parallel-polarized fields and the orthogonally-polarized birefringently phasematched interactions in LiNbO<sub>3</sub>. In LiNbO<sub>3</sub> the temperature bandwidth of a parallel-polarized QPM interaction is determined primarily by the temperature dependence of dispersion and to a lesser extent by the thermal expansion of the crystal length and grating period. For a birefringently phasematched interaction which must be orthogonally polarized, the temperature bandwidth is determined by a combination of the temperature dependence of dispersion and of the birefringence between the ordinary and extraordinary indices, and also to a lesser extent by the thermal expansion of the crystal. Because the temperature dependence of the birefringence is greater than that of dispersion in LiNbO<sub>3</sub>, the temperature bandwidth is larger for parallel-polarized interactions. For the same 1064-nm-pumped parametric interactions described above but using the  $d_{31}$  nonlinearity, where the in-

teracting fields are orthogonally polarized, the temperature bandwidth would be 1.0°C for birefringent phasematching and 2.8°C for QPM for both the non-degenerate and degenerate cases.

## 2.7 Novel Features of QPM Nonlinear Optics

The user-chosen phasematching conditions that are possible with quasi-phasematched materials such as periodically-poled lithium niobate (PPLN) have made it possible to incorporate, on a single piece of nonlinear material, novel functionalities which were previously unattainable with the use of birefringently phasematched nonlinear materials.

### 2.7.1 Use of multiple parallel gratings for OPO tuning

One of the unique features of QPM is the ability to integrate multiple functional blocks on a single piece of nonlinear material such as PPLN by defining different grating periods on different parts of the material. One important application of multi-grating PPLN involves the use of multiple parallel grating sections to realize discrete wavelength tuning of the signal and idler outputs of an OPO. Consider an OPO with input frequency  $\omega_p$  and signal and idler outputs at  $\omega_{s0}$  and  $\omega_{i0}$ . Suppose one would like to access another pair of signal-idler output pair at  $\omega_{s1}$  and  $\omega_{i1}$ . To accomplish this feat one needs to alter the phasematching conditions for the new interaction. Consider the phasematching condition for the original interaction (interaction 0):

$$\Delta k_0 = k_p - k_{s0} - k_{i0} - K_0 = 0. \quad (2.89)$$

However, without altering any of the physical properties of the material, the new interaction (interaction 1) would not be phasematched because of dispersion. That is,

$$\Delta k_1 = k_p - k_{s1} - k_{i1} - K_0 \neq 0. \quad (2.90)$$

One method to phasematch the new interaction is to alter the indices of refraction for the pump, signal, and idler fields such that

$$\Delta k_1'' = k_p'' - k_{s1}'' - k_{i1}'' - K_0 = 0. \quad (2.91)$$

This can typically be accomplished by changing the temperature of the material or by applying a voltage across the crystal using the electro-optic effect. An alternative way to achieve phasematching for the new interaction is to use a different grating period such that a new grating vector  $K_1$  satisfies the phasematching condition

$$\Delta k_1 = k_p - k_{s1} - k_{i1} - K_1 = 0. \quad (2.92)$$

Thus for each pair of signal and idler output frequencies  $\omega_{sn}$  and  $\omega_{in}$  that one would like to access, there would be a corresponding grating period  $\Lambda_n$  such that the phase-matching condition

$$\Delta k_n = k_p - k_{sn} - k_{in} - K_n = 0 \quad (2.93)$$

can be satisfied. In a practical application such as an OPO, the tuning of the output frequencies of the OPO can be achieved by defining a number of grating sections in parallel, with each section having a slightly different grating period from its adjacent section. To provide full spectral coverage, the phasematching bandwidths of the adjacent sections must overlap partially. To tune the output frequencies up or down, one would translate the nonlinear crystal laterally to the section with the proper grating period to satisfy the phasematching condition, as illustrated in Fig. 2-5. The use of multiple grating sections to tune the output frequencies of an OPO has been demonstrated by Myers *et al.* in 1996 [32]. In that work a PPLN with 25 parallel grating sections with grating periods ranging from 28.7  $\mu\text{m}$  to 32.1  $\mu\text{m}$  was used to discretely tune the idler output of an OPO pumped at 1.064  $\mu\text{m}$  from the degenerate wavelength at 2.128  $\mu\text{m}$  to 4.83  $\mu\text{m}$ . The corresponding signal tuning range was from 2.128  $\mu\text{m}$  to 1.36  $\mu\text{m}$ . Note that the discrete tuning using multiple grating periods can be combined with continuous frequency tuning methods such as temperature tuning

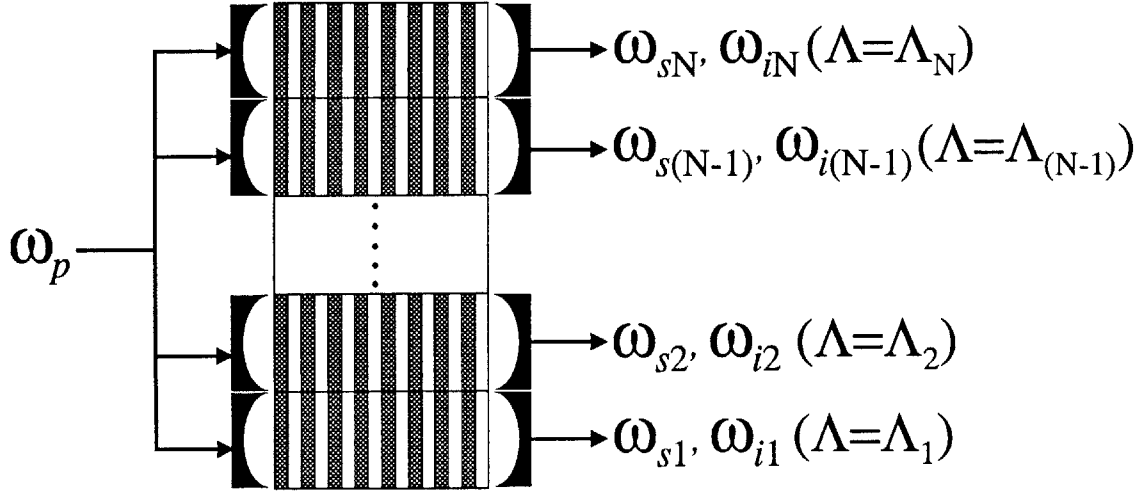


Figure 2-5: Tuning of a QPM OPO by multiple grating periods. By defining a series of QPM gratings in parallel, each with a slightly different grating period from the adjacent gratings, one can tune the signal/idler output frequencies by choosing the section with the desired signal/idler output frequencies.

to offer a full wavelength coverage over a very wide spectral region. It is also possible to implement continuous wavelength tuning of an OPO using a nonlinear material with a continuously varying grating period, as shown in Fig. 2-6. In this scheme the output of an OPO can be continuously tuned by simply translating the crystal laterally. The use of a continuously variable grating period eliminates the need for temperature tuning. Such a design was experimentally demonstrated by Powers *et al.* in which a cw OPO pumped at  $1.064 \mu\text{m}$  was continuously tuned from  $1.53 \mu\text{m}$  to  $1.62 \mu\text{m}$  for the signal output at  $150^\circ\text{C}$  by using a PPLN sample with a continuously varying grating period from  $29.3 \mu\text{m}$  to  $30.1 \mu\text{m}$  [33].

### 2.7.2 Multiple gratings in series

Another class of applications of multiple-grating QPM material involve integrating multiple nonlinear interactions in series on a single piece of nonlinear material. There are a number of applications of nonlinear optics which requires the use of 2 or more nonlinear frequency mixing stages in series. One example is a 3-to-1 optical frequency divider, which requires 2 nonlinear frequency mixing stages in series. The 3-to-1 optical frequency divider will be discussed in Chapter 6. Conventionally, such

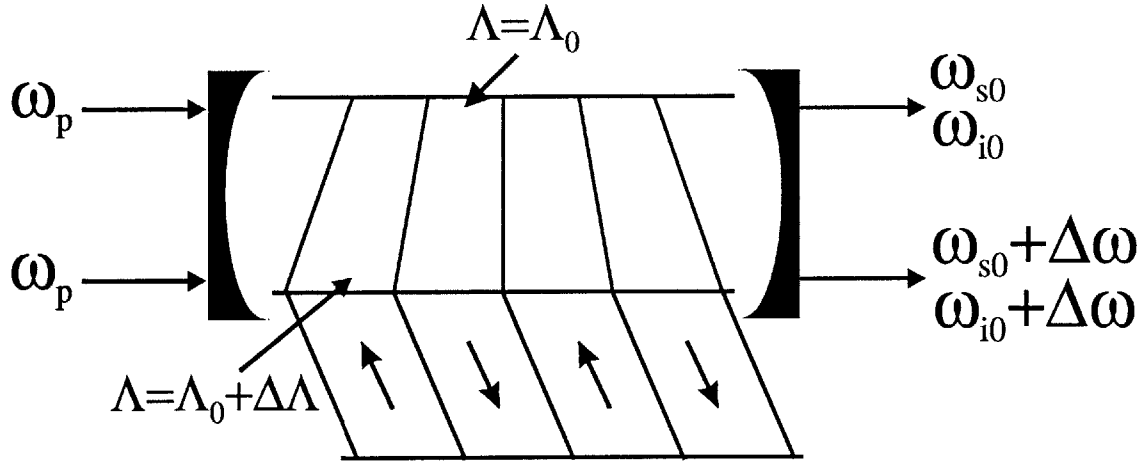


Figure 2-6: PPLN OPO with a fan-out grating pattern. The side of the crystal indicates the poling direction. The grating period changes continuously along the  $y$ -direction, phasematching a continuous range of signal and idler output frequencies. (Powers *et al.*, *Optics Letters* 23(3), pp. 159-161, 1997).

an application would require the use of 2 separate nonlinear crystals for the 2 nonlinear interactions. The severe restrictions for conventional birefringent phasematching imply complicated setup for both frequency-mixing stages. Furthermore, it is often difficult, if not impossible, to find two nonlinear crystals that will phasematch the exact wavelengths involved in the 2 nonlinear interactions. However, one can integrate the 2 nonlinear interactions on a single piece of material by simply partitioning the sample into two functional blocks in series, with each functional block having its own grating period necessary to phasematch the corresponding interaction. Figure 2-7 (a) illustrates the concept behind the use of multiple gratings to realize multiple nonlinear interactions. The beauty of this concept is that one can design the grating period in such a way that the two interactions will phasematch at the same temperature, as illustrated in Fig. 2-7 (b). The application of this principle can be extended to more than 2 functional blocks, making such devices useful for applications in optical signal processing. The design of the grating periods for our double-grating 3-to-1 optical frequency division will be discussed in more detail in Chapter 6.

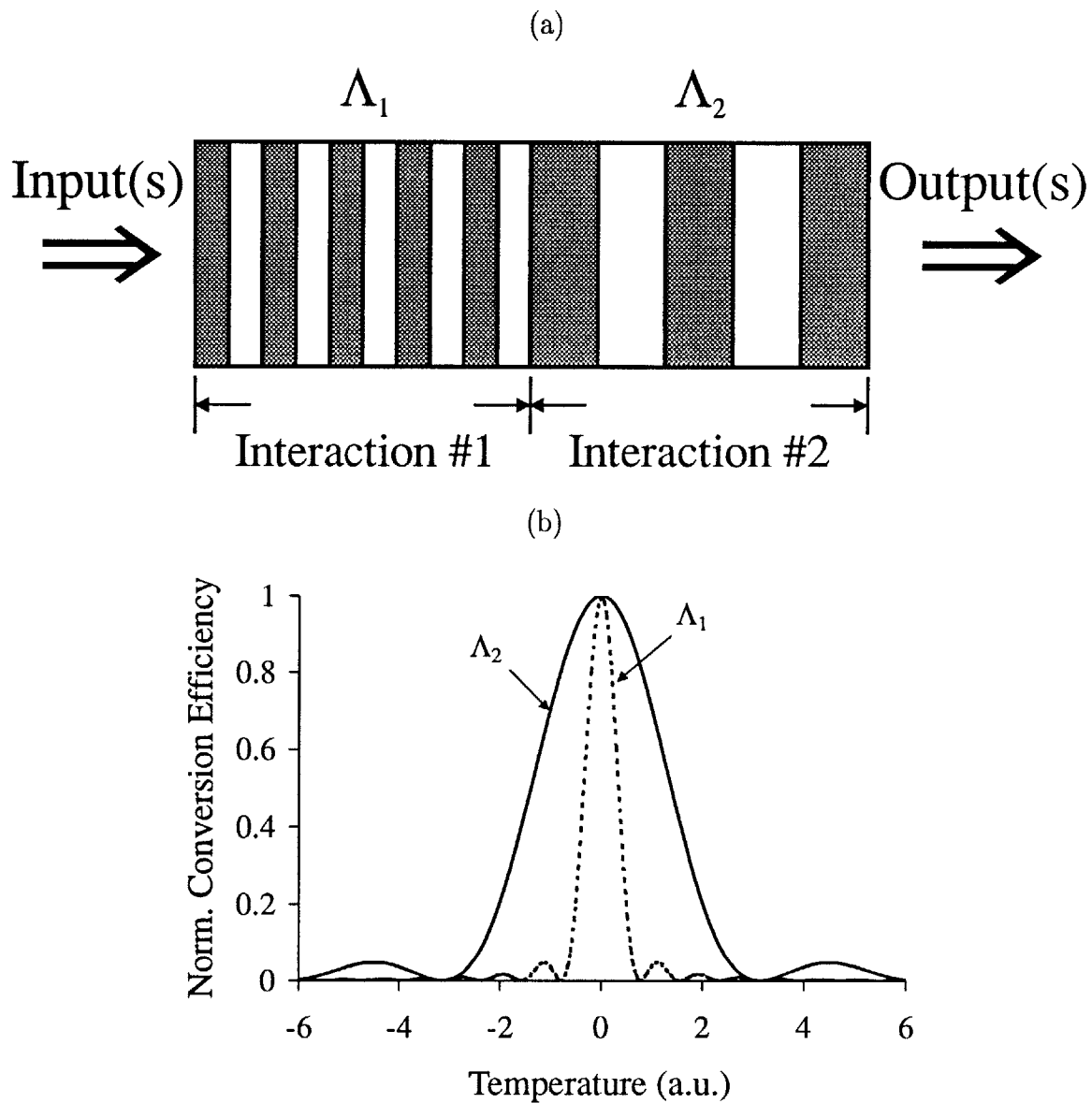


Figure 2-7: Simultaneous phasematching of 2 nonlinear interactions in a QPM nonlinear crystal. In (a), 2 different grating periods are used to phasematch the different nonlinear interactions. In (b), the grating periods are chosen such that the peak phasematching temperatures of the 2 interactions coincide.

### 2.7.3 Bandwidth engineering

In addition to the unique features of integrating multiple functionalities on a single piece of QPM material by defining multiple grating periods for different parts of the sample, there are several other features unique to the use of QPM nonlinear optics not found in birefringently phase-matched interactions. One such feature is the possibility of bandwidth engineering using aperiodic grating structures. Consider the normal case of quasi-phase-matched interaction with the regular periodic nonlinear coefficient profile as shown in Fig. 2-3. For the case of difference-frequency generation, the  $k$ -space tuning curve of the DFG output profile is, according to equation (2.23), the Fourier transform of the spatial profile of the nonlinear coefficient. In principle, we can phase-match a nonlinear interaction with any arbitrary tuning curve by using a nonlinear coefficient profile which is the inverse Fourier transform of the desired tuning curve. This, however, most often requires a continuously spatially varying nonlinear coefficient profile which is in general not readily available. For instance to produce a “flat top” tuning curve requires a  $\sin x/x$  nonlinear coefficient profile. Fejer *et al.* was able to demonstrate that one can approximate the desired nonlinear coefficient profile by the use of a discrete approximation to the nonlinear coefficient [26]. The approximation consists of using a building block of length  $L = 2ml_c$  where  $m$  is the order the QPM interaction. The block consists of 2 sections, as shown in Fig. 2-8. The first section of length  $l$  has a nonlinear coefficient equal to  $+d_{eff}$ , whereas the second section of length  $(L - l)$  has a nonlinear coefficient equal to  $-d_{eff}$ . The effective nonlinear coefficient over this building block can be shown to be

$$d_Q = \frac{2d_{eff}}{m\pi} \sin\left(\frac{\Delta kl}{2}\right) \exp\left(-i\frac{\Delta kl}{2}\right)$$

where  $\Delta k = k_p - k_s - k_i - K_m$ . By varying the ratio between  $l$  and  $L$  along the length of the crystal, which is user-controlled via the lithographic mask, one can construct a QPM grating structure with a close approximation of the desired tuning curve. Figures 2-9 (a) and (b) show the synthesized flat top and triangular tuning curves obtained by using the nonlinear coefficient profiles  $d_{Qj} = \left(\frac{2d_{eff}}{m\pi}\right) \sin\left(\frac{24\pi j}{N}\right) / \left(\frac{24\pi j}{N}\right)$  and

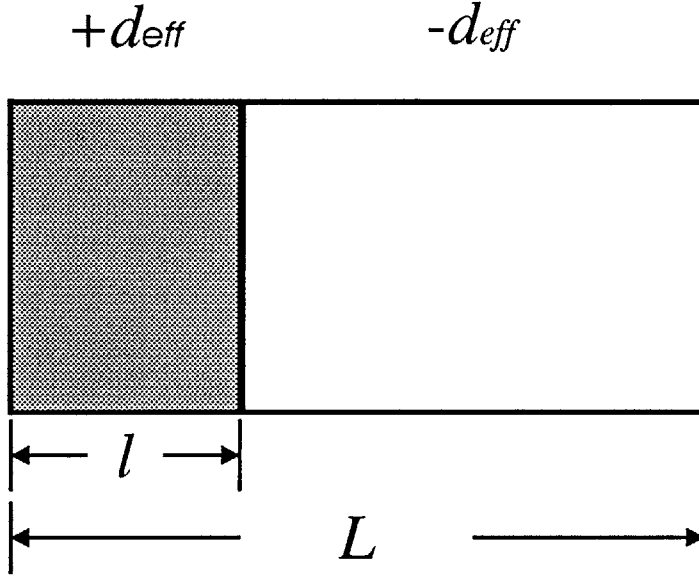


Figure 2-8: Building block for discrete approximation to the synthesis of an arbitrary effective nonlinear coefficient. For  $L = 2ml_c$ , where  $l_c$  is the coherence length and  $m$  is the order of the QPM, the effective nonlinear coefficient is  $d_Q = \frac{2d_{eff}}{m\pi} \sin\left(\frac{\Delta kl}{2}\right) \exp\left(-i\frac{\Delta kl}{2}\right)$ .

$d_{Qj} = \left(\frac{2d_{eff}}{m\pi}\right) \sin^2\left(\frac{24\pi j}{N}\right) / \left(\frac{24\pi j}{N}\right)^2$ , respectively, where  $j = 1, 2, \dots, N$ . The reader is referred to Reference 26 for a more detailed discussion.

#### 2.7.4 Chirped QPM gratings

Besides bandwidth engineering, aperiodic QPM gratings also find potential applications in the stretching or compression of ultrashort laser pulses [34]. Arbore *et al.* has demonstrated the novel use of a chirped QPM grating for generating compressed second harmonic output from chirped fundamental input pulses [35]. Figure 2-10 shows a schematic of a chirped QPM grating consisting of a grating structure with continuously varying QPM periods along the length of the grating. The different QPM periods are designed to phasematch the different spectral components of the chirped input pulse. The chirped input pulse can be considered as possessing different frequency components for different temporal intervals of the pulse, as illustrated in Fig. 2-10. That is, the front of a chirped pulse has a higher optical frequency than the tail of the pulse, or vice versa. The chirp compression scheme is based on the effects of



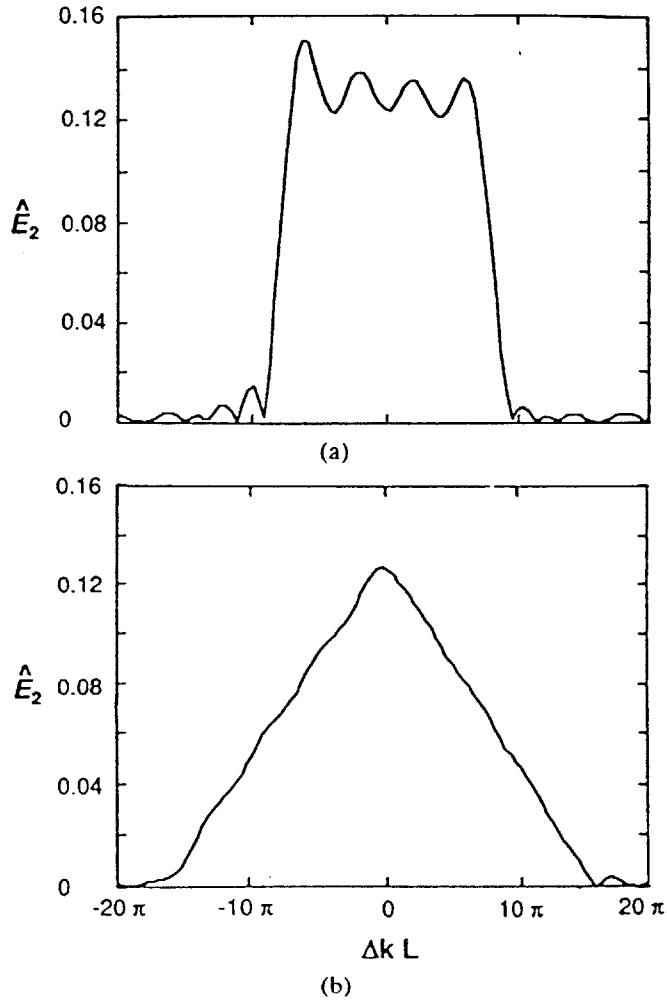


Figure 2-9: Synthesized SHG tuning curves using the discrete approximation method shown in Fig. 2-8 in a structure of length  $Nl_c$  with  $m = 3$ . (a) shows a flat-top tuning curve synthesized using  $d_{Qj} = \left(\frac{2d_{eff}}{m\pi}\right) \sin\left(\frac{24\pi j}{N}\right) / \left(\frac{24\pi j}{N}\right)$ ,  $j = 1, 2, \dots, N$ . (b) shows a triangular tuning curve synthesized using  $d_{Qj} = \left(\frac{2d_{eff}}{m\pi}\right) \sin^2\left(\frac{24\pi j}{N}\right) / \left(\frac{24\pi j}{N}\right)^2$ .  $\hat{E}_2$  denotes the second harmonic field amplitude normalized to the peak of the tuning curve for an ideal 3rd-order ( $m = 3$ ) QPM structure with  $|d_{Qj}| = \frac{2}{m\pi}$  and the same total length  $L$ . (Fejer *et al.*, *IEEE Journal of Quantum Electronics* 28(11), pp. 2631-2654, 1992)

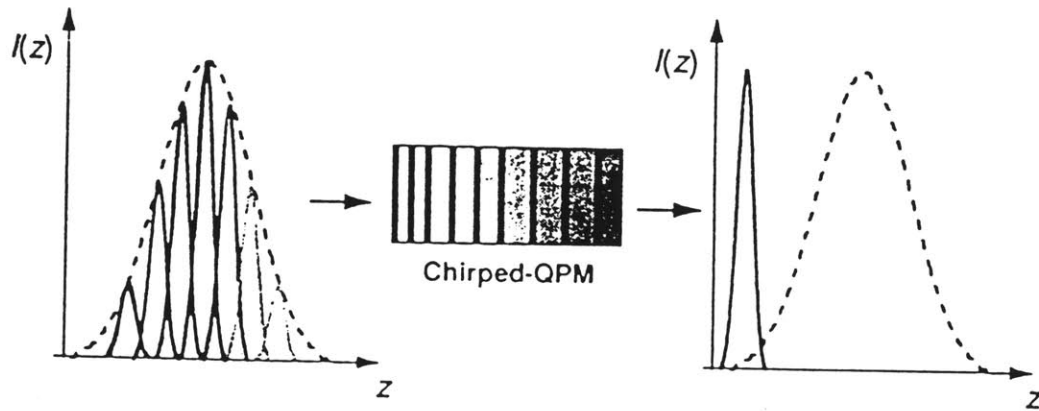


Figure 2-10: Time-domain representation of pulse compression during SHG in aperiodic QPM gratings. Different shadings correspond to the optical frequency of each temporal slice of the fundamental pulse (dashed curve) and to the optical frequency for which SHG is quasi-phased-matched in each spatial region of the aperiodic QPM grating. (Arbore *et al.*, *Optics Letters* 22 (17), pp. 1341-1343, 1997)

group-velocity mismatch between the fundamental and second harmonic wavelengths in the nonlinear material and the spatial localization of second harmonic conversion for the different spectral components that is due to the chirped QPM grating. As a result of group velocity dispersion inside the nonlinear material, the generated second harmonic pulse will lead or lag the fundamental pulse. Because of the chirped QPM grating different frequency components which make up the input pulse will phase-match at different positions along the length of the QPM grating. For a chirped input pulse this is equivalent to the statement that the different temporal slices of the chirped input pulse will generate second harmonic outputs in different regions of the grating and therefore experience different lead or lag times relative to the center of the fundamental input pulse. If the “chirp” of the QPM grating is designed such that the second harmonic outputs of the different spectral components coincide at the same time in space, the resulting second harmonic output will be chirp-compensated and greatly compressed, as shown in Fig. 2-10 for a chirped PPLN, where the second harmonic pulse lags the fundamental pulse. Arbore *et al.* has demonstrated a 110-fs second harmonic output pulse from a 17-ps chirped input pulse at 1560 nm in a chirped-PPLN sample with grating periods ranging from 18.2  $\mu\text{m}$  to 19.8  $\mu\text{m}$  [35].

## 2.7.5 Spatial beam profile engineering

The engineering properties of QPM nonlinear materials can also be extended to controlling the spatial beam profile of the generated nonlinear output beam. Consider the grating design shown in Figs. 2-11 (a) and (b). For Gaussian beam inputs the structure in Fig. 2-11 (a) would produce an output with the same Gaussian beam profile. Now consider the grating structure shown in Fig. 2-11 (b). The center of the beam which has the highest intensity, sees the shortest grating length, and thus has the lowest conversion efficiency in the nonlinear output. As we move outwards from the center of the input beam, the grating length becomes correspondingly longer, thereby increasing the conversion efficiency. For instance, one can design the structure in such a way that the output beam has a flat top intensity profile as demonstrated by Imeshev *et al.* and shown in Fig. 2-11 (b) [36].

## 2.8 Nonidealities

Several types of nonidealities associated with the fabrication of quasi-phasematched devices contribute to potential reduction in conversion efficiency. This section discusses several of the most commonly encountered types of fabrication nonidealities in the electric field poling technique that will be discussed in Chapter 4.

### 2.8.1 Sub-optimal duty cycle

We define the duty cycle of a QPM grating as

$$D = l_{(+d_{eff})}/\Lambda$$

which is the ratio of the length of the sections with  $d = +d_{eff}$  to the QPM grating period  $\Lambda$ . In equation (2.10) it was assumed that the relative lengths of sections with positive and negative signs of  $d_{eff}$  are equal. That is,  $D = \frac{1}{2}$ . We now derive an expression for the reduction in the effective nonlinearity for deviations from the optimum duty cycle of 50%.

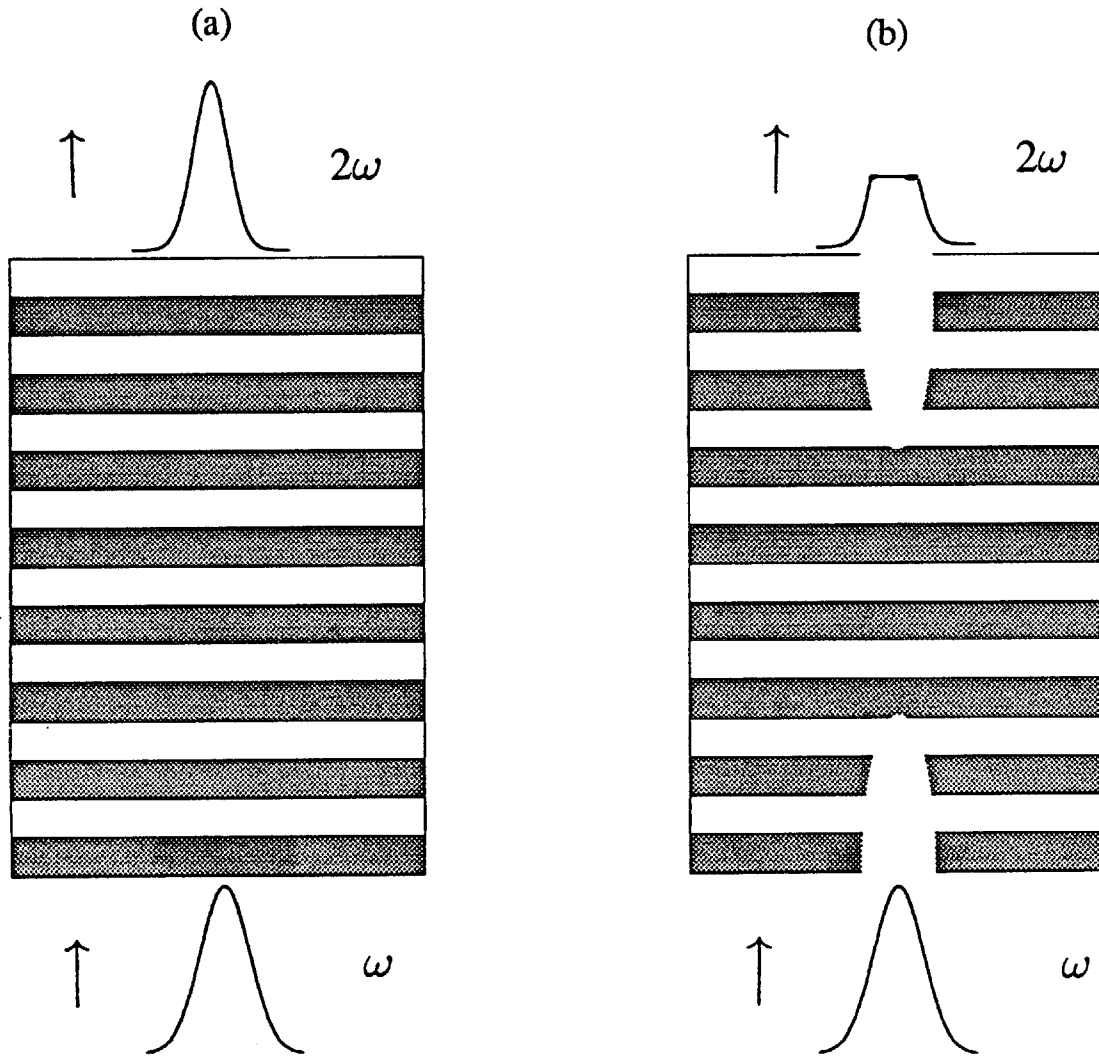


Figure 2-11: Effect of spatially-varying QPM grating length on generated second harmonic beam profile for a Gaussian fundamental beam profile. In (a), a uniform grating structure produces a Gaussian second harmonic output beam profile. A non-uniform grating structure shown in (b) produces a flat-top second harmonic output beam profile.

Recall from Section 2.2 the normalized conversion efficiency is defined as  $g(z) = d(z)/d_{eff}$ . For the ideal QPM grating structure with the optimum 50/50 duty cycle,

$$g(z) = \begin{cases} +1 & n\Lambda < z < (n + \frac{1}{2})\Lambda \\ -1 & (n + \frac{1}{2})\Lambda < z < (n + 1)\Lambda \end{cases}$$

If the duty cycle is allowed to deviate from the optimal 50/50 ratio such that

$$g(z) = \begin{cases} +1 & n\Lambda < z < (n + D)\Lambda \\ -1 & (n + D)\Lambda < z < (n + 1)\Lambda \end{cases}$$

where  $0 < D < 1$ , the Fourier coefficient  $G_m$  in equation (2.9) becomes

$$G_m = \frac{2}{\pi m} \sin(\pi m D), \quad (2.94)$$

and, in the case of difference-frequency generation, the expression of the output field becomes

$$\mathcal{E}(z = l) = \Gamma d_{eff} \frac{2}{\pi m} \sin(\pi m D) \exp\left(i \frac{\Delta k l}{2}\right) l \sin\left(\frac{\Delta k l}{2}\right). \quad (2.95)$$

Based on the above expression, one can incorporate the effects of non-50/50 duty cycle into the effective nonlinear coefficient  $d_Q$  defined in Eq. (2.14) such that

$$d_Q = \Gamma d_{eff} \sin(\pi m D) \quad (2.96)$$

The above expression also proves that the effective nonlinear coefficient  $d_Q$  is maximized for a 50/50 duty cycle in which  $D = \frac{1}{2}$  and the  $\sin(\pi m D)$  term becomes unity.

Let's define  $\Delta l$  as the deviation of the length of the  $+d_{eff}$  domain segment from the coherence length  $l_c$ . That is,  $\Delta l = l_{(+d_{eff})} - l_c$ . The duty cycle is then  $D = \frac{1}{2} + \Delta l / 2l_c$ . The ratio between the idler output power with a non-50/50 duty cycle to that with

the ideal 50/50 duty cycle ( $\Delta l = 0$ ) is

$$\frac{|\mathcal{E}_i(z=l)|^2|(D \neq \frac{1}{2})}{|\mathcal{E}_i(z=l)|^2|(D = \frac{1}{2})} = \sin^2 \left[ \pi \left( \frac{l_c + \Delta l}{2l_c} \right) \right] = \cos^2 \left( \frac{\pi \Delta l}{2l_c} \right) \quad (2.97)$$

Based on this expression, a 50% reduction of the conversion efficiency results when  $\Delta l = \frac{1}{2}l_c$ .

As will be described in Chapter 3, the spreading of reversed ferroelectric domains during electric field poling of the nonlinear crystal leads to a final grating structure with a non-50/50 duty cycle. To illustrate the effects of a non-50/50 duty cycle on the conversion efficiency for common QPM applications, let's consider two nominal cases. The first case corresponds to frequency doubling of a Nd:YAG laser output at  $\lambda = 1064$  nm with a grating period of  $\Lambda = 6.8$   $\mu\text{m}$ . Let's assume that, due to the spreading of the reversed ferroelectric domains, the final width of the reversed domains is  $2\mu\text{m}$  beyond the design width of  $3.4$   $\mu\text{m}$ . That is,  $\Delta l = 2$   $\mu\text{m}$  and  $l_c = 3.4$   $\mu\text{m}$ . The resulting normalized conversion efficiency is

$$\frac{|\mathcal{E}_i(z=l)|^2|(D \neq \frac{1}{2})}{|\mathcal{E}_i(z=l)|^2|(D = \frac{1}{2})} = 0.36. \quad (2.98)$$

That is, the resulting conversion efficiency is only 36% of that for a grating with a 50/50 duty cycle. The second case corresponds to a degenerate OPO pumped at 1064 nm, yielding signal and idler outputs at 2128 nm. The grating period for this interaction is  $31.7$   $\mu\text{m}$ , corresponding to a coherence length  $l_c = 15.85$   $\mu\text{m}$ . Again, let's assume a final reversed domain width that is  $2$   $\mu\text{m}$  beyond the design width of  $15.85$   $\mu\text{m}$ . That is,  $\Delta l = 2$   $\mu\text{m}$  and  $l_c = 15.85$   $\mu\text{m}$ . Equation (2.97) gives

$$\frac{|\mathcal{E}_i(z=l)|^2|(D \neq \frac{1}{2})}{|\mathcal{E}_i(z=l)|^2|(D = \frac{1}{2})} = 0.96. \quad (2.99)$$

The resulting conversion efficiency is only reduced by 4% compared to the case with a perfect 50/50 duty cycle. The above examples illustrate the different sensitivity of the conversion efficiency to a fixed deviation from 50/50 duty cycle for different grating periods.

## 2.8.2 Random duty-cycle error

In the actual fabrication of QPM devices based on the use of photolithographic techniques, the period of the QPM grating structure is defined by the photolithographic mask. However, the boundary positions of the interfaces between  $+d_{eff}$  domains and  $-d_{eff}$  domains may deviate from their ideal locations. This type of error is called the random duty cycle error. It assumes that the overall periodicity of the grating structure is a constant but the individual lengths of the domain sections have a random variation around the design value. Let's assume a grating structure with the optimum 50/50 average duty cycle but with random duty cycle errors such that the standard deviation of the domain lengths is  $\sigma_l$ . The effect of Gaussian random duty-cycle error on the effective nonlinear coefficient  $d_Q$  has been theoretically analyzed by Fejer [26] and is given by

$$\frac{d_{Q\sigma=\sigma_l}^2}{d_{Q\sigma=0}^2} \approx \exp\left(-\frac{\pi^2\sigma_l^2}{2l_c^2}\right), \quad (2.100)$$

under the assumption that the number of periods in the grating is large. We find that for a 50% reduction in conversion efficiency,  $\sigma_l = 0.375l_c$ .

As an example, let's again consider the two cases with  $\Lambda = 6.8\mu\text{m}$  and  $\Lambda = 31.7\mu\text{m}$  discussed in the previous section. Let's assume that  $\sigma_l = 1\mu\text{m}$ . For the case where  $\Lambda = 6.8\mu\text{m}$  and  $l_c = 3.4\mu\text{m}$ , (2.100) gives

$$\frac{d_{Q\sigma=\sigma_l}^2}{d_{Q\sigma=0}^2} \approx 0.65. \quad (2.101)$$

For the second case where  $\Lambda = 31.7\mu\text{m}$  and  $l_c = 15.85\mu\text{m}$ , (2.100) gives

$$\frac{d_{Q\sigma=\sigma_l}^2}{d_{Q\sigma=0}^2} \approx 0.98. \quad (2.102)$$

The above examples show that random duty cycle errors have a much more pronounced effect on the conversion efficiency for interactions using short grating periods than those using long grating periods.

### 2.8.3 Missing domain reversals

As will be discussed in Chapter 3, a typical way to prepare the structures with alternating signs of the nonlinear coefficient  $d_{eff}$  is to periodically reverse the ferroelectric domain orientation of a single-domain ferroelectric material. The reversal of the ferroelectric domain orientation corresponds to a reversal in the sign of the nonlinear coefficient. In many instances due to imperfections of the fabrication process missing reversals may occur. Figures 2-12 (a) and (b) illustrate the effect of a missing domain. In Fig. 2-12 (a), each domain reversal represents a sign flip in the nonlinear coefficient and thus adds a  $\pi$  phase shift to the relative phase of the interacting waves to reset the accumulated phase slip to zero. A missing domain, as shown in Fig. 2-12 (b), however, has the effect of letting the total phase slip accumulate for another  $2\pi$  radians before the next domain reversal resets the relative phase to zero. The net effect of a missing domain reversal is to reduce the effective number of domains by 2. The reduction in the effective nonlinear coefficient  $d_Q$  due to M missing domain reversals in a QPM grating with N periods is shown by Fejer *et al.* [26] to be

$$\frac{|d_Q(\text{M missing domains})|^2}{|d_Q(\text{ideal})|^2} = (1 - M/N)^2 \quad (2.103)$$

As an example, consider a QPM nonlinear material with a length of 10 mm and a grating period of  $20 \mu\text{m}$  such that the total number of periods is  $N= 500$ . The effect of 1 missing reversal, according to Eq. (2.106), is to reduce the conversion efficiency by 0.4%.



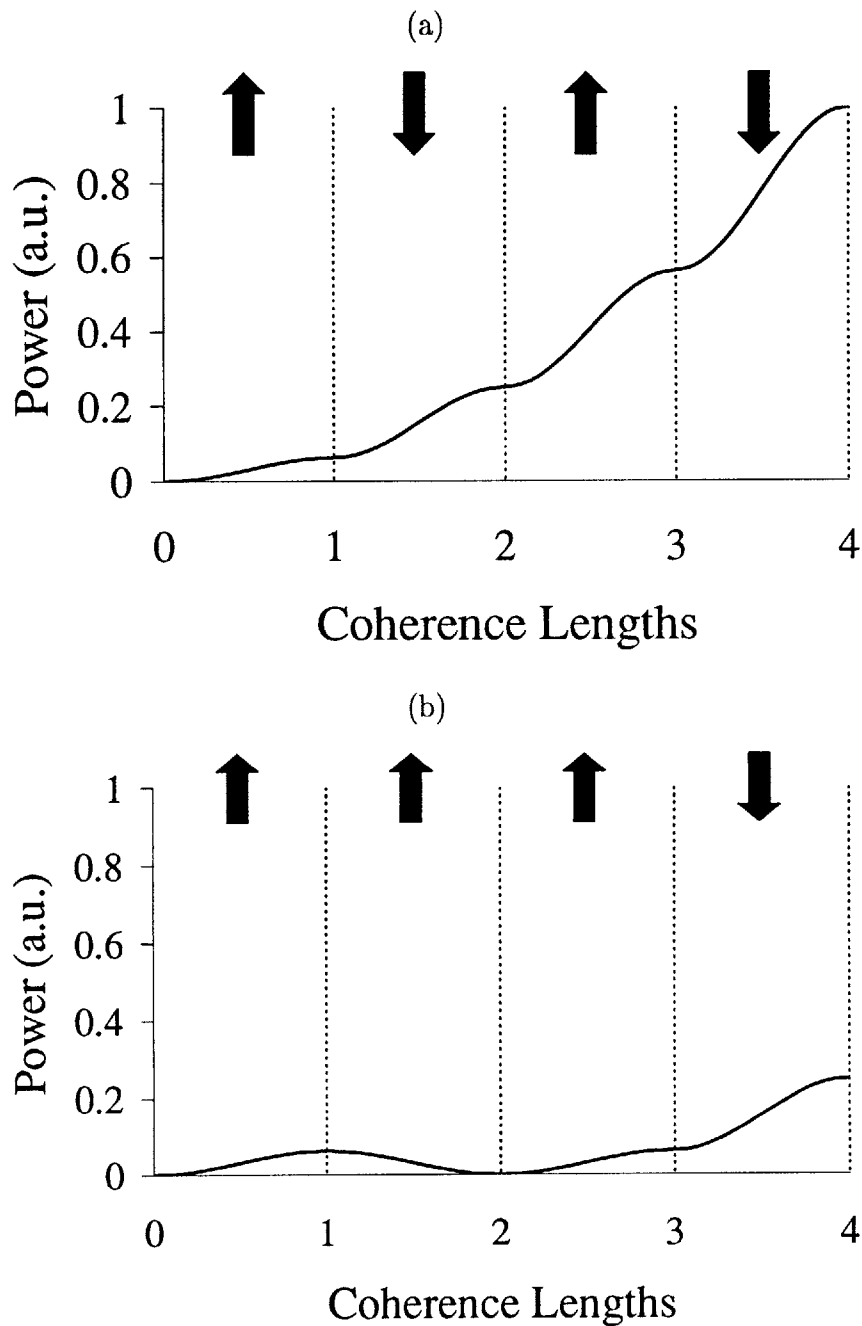


Figure 2-12: Effect of missing domain reversal on DFG conversion efficiency. In (a), the orientation of the domains alternates every coherence length, leading to continued power growth of the DFG output. In (b), a missing reversal at the second domain segment results in a reversal of power flow over the length of the missing domain and thus contribute to reduce the overall conversion efficiency.

# Chapter 3

## Fabrication and Characterization

This chapter deals with the fabrication of QPM nonlinear optical materials. As discussed in preceding chapters, the phase mismatch among the interacting fields in a nonlinear interaction can be compensated by a switch in the sign of the nonlinear  $d$  coefficient with a periodicity that is an integer multiple of twice the coherence length for the nonlinear interaction. In practice, the switch in the  $d$  coefficient of the medium can be accomplished by a periodic reversal in the orientation of the ferroelectric domains of the nonlinear optical material. As mentioned in Chapter 1, in the early days this was realized by stacking a series of nonlinear optical crystal “plates” with alternating ferroelectric domain orientations, which was severely hampered by losses at the interfaces from one plate to another, resulting in low conversion efficiencies [3][4][5][6][7]. In recent years, QPM materials have been fabricated by periodic ferroelectric domain reversal that is introduced directly on a single piece of single-domain nonlinear optical crystal.

In the following sections, discussions will center on the many ways of fabricating periodically domain-reversed single crystals. Section 3.1 discusses the choice of lithium niobate ( $\text{LiNbO}_3$ ) as the nonlinear material for this work. Section 3.2 summarizes three selected methods for preparing periodically domain-reversed nonlinear crystals. Section 3.3 reviews the various setups in which an electric field is used to domain-reverse the ferroelectric domains. This method, called electric field poling, is used in this work to fabricate QPM devices. Section 3.4 details the procedures and

hardware for fabricating periodically poled lithium niobate (PPLN). Finally, Section 3.5 describes the characterization of the fabricated samples.

### 3.1 QPM Materials—Choice of Lithium Niobate

To date ferroelectric domain reversal has been accomplished in several nonlinear optical materials using a variety of methods. These materials include lithium niobate ( $\text{LiNbO}_3$ ), potassium titanyl phosphate (KTP), rubidium titanyl arsenate (RTA), and lithium tantalate ( $\text{LiTaO}_3$ ). Of these,  $\text{LiNbO}_3$  is chosen for the work described by this thesis mainly because of its large nonlinear  $d$  coefficient compared to the others, its low cost, high optical quality, and the fact that  $\text{LiNbO}_3$  has been extensively studied and widely used. Many of its physical properties are well known, and high quality crystals are readily available at very reasonable prices.

### 3.2 Methods of Preparing Domain-reversed Lithium Niobate Crystal

In recent years ferroelectric domain reversal in  $\text{LiNbO}_3$  has been accomplished using a variety of methods, each with its advantages and disadvantages. In this section we present a brief discussion of three representative methods developed for domain-reversal in  $\text{LiNbO}_3$ , namely, titanium in-diffusion, electron beam writing, and, electric field (E-field) poling.

#### (1) Titanium In-diffusion

In titanium in-diffusion, ferroelectric domain reversal takes place when a layer of titanium is diffused into the  $-z$  face of the  $\text{LiNbO}_3$  crystal at a high temperature, as shown in Fig. 3-1 (a) and (b) [37][38]. One of the major advantages of using this method is that a periodic grating composed of titanium lines can be fabricated with standard lift-off lithography used in the microelectronics industry. The subsequent high temperature diffusion into the  $\text{LiNbO}_3$  substrate results in a periodically domain-reversed structure with a period and duty cycle that is precisely defined by

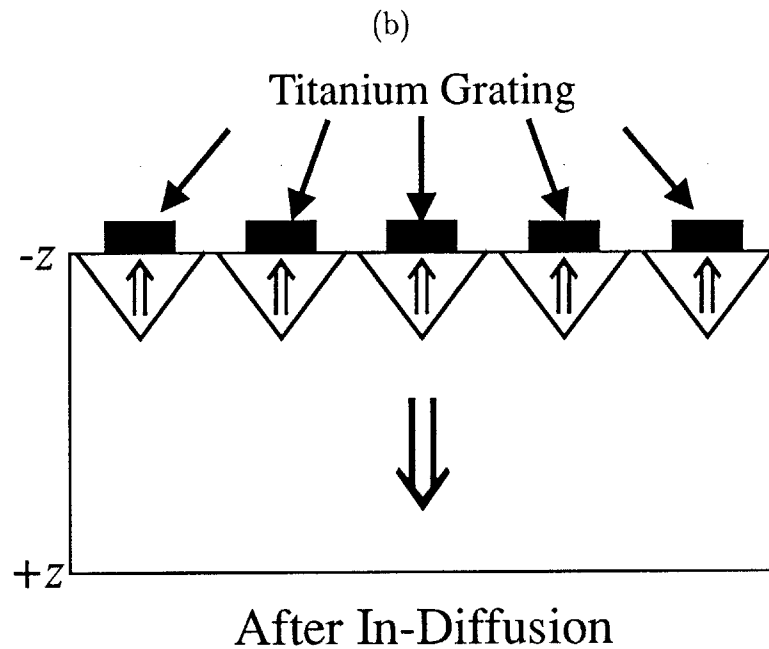
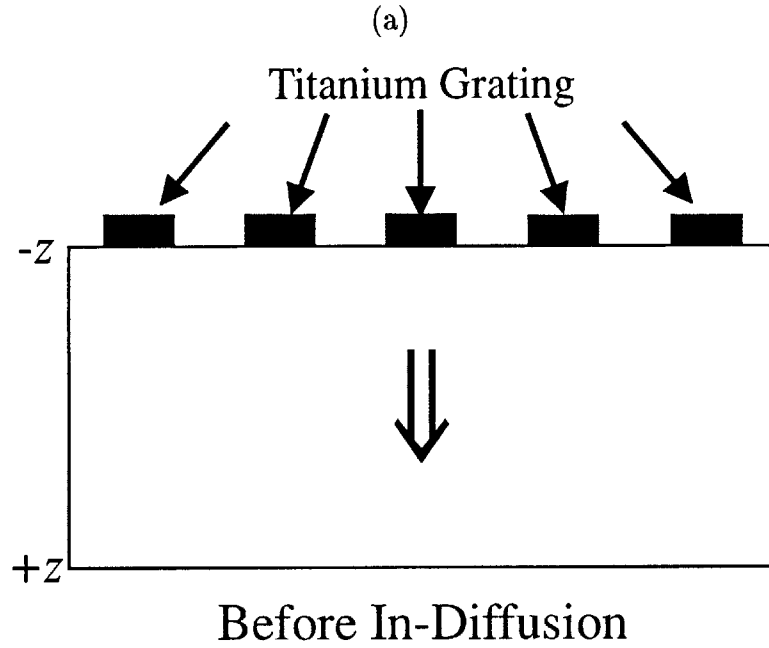


Figure 3-1: Ferroelectric domain reversal by titanium in-diffusion. In (a), a periodic grating pattern consisting of titanium is deposited onto the  $-z$  face of a  $\text{LiNbO}_3$  substrate. In (b), domain reversal takes place when the titanium is driven into the  $\text{LiNbO}_3$  substrate via high temperature diffusion. Only a shallow region near the surface is domain-reversed.

the lithographic mask. However, titanium in-diffusion has its limitations. For one, the domain reversal takes place only near the surface of the  $-z$  face of the  $z$ -cut crystal and is about a few tens of  $\mu\text{m}$  thick. This limits the use of titanium in-diffusion to mainly waveguide applications where the optical field is highly confined to a narrow region. Furthermore, as shown in Fig. 3-1 (b), the domain reversal profile takes on a triangular shape instead of the ideal rectangular shape, which produces non-optimal overlap between the guided modes along the domain-reversed grating, and thereby results in reduced conversion efficiency. Furthermore, the waveguide fabrication process can be time-consuming. Nevertheless, the fact that domain-reversal gratings can be fabricated using standard microfabrication procedures has resulted in widespread use of this method to fabricate QPM LiNbO<sub>3</sub> waveguide devices.

### (2) Electron Beam Writing

Domain reversal using direct electron beam writing was first reported by Yamada and Kishima [39]. In this method, the  $+z$  face of a thin piece (approximately 1 mm thick) of LiNbO<sub>3</sub> crystal is bombarded with an electron beam, and domain reversal takes place at the spot where the electron beam hits the sample (Fig. 3-2). The merit of this method lies in the fact that the reversed domains can traverse the entire thickness of the crystal, in principle making it suitable for bulk QPM applications. In practice, however, a number of non-idealities and other factors have prevented this method from becoming widespread. The first is that while electron beam is effective in producing domain-reversal in one spot, it does not work well when one tries to domain reverse a continuous grating-like region. Instead, the reversed domains occur in segmented regions, as illustrated in Fig. 3-3. Furthermore, the domain reversal was obtained in only a fraction of the overall area scanned by the e-beam [39]. These difficulties, coupled with the high cost and general inaccessibility of electron beam machines, have prevented the electron beam writing method from seeing widespread use.

### (3) Electric Field Poling

In electric field poling the ferroelectric domains of LiNbO<sub>3</sub> is reversed by applying a dc electric field above the coercive field of LiNbO<sub>3</sub> across the  $z$ -axis of a  $z$ -cut LiNbO<sub>3</sub>

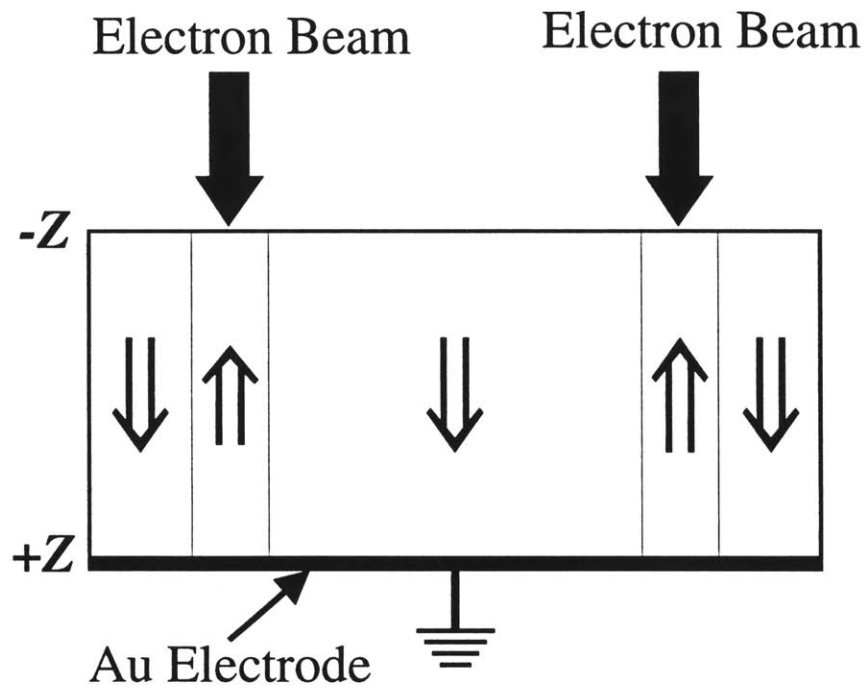


Figure 3-2: Ferroelectric domain reversal by electron beam writing.

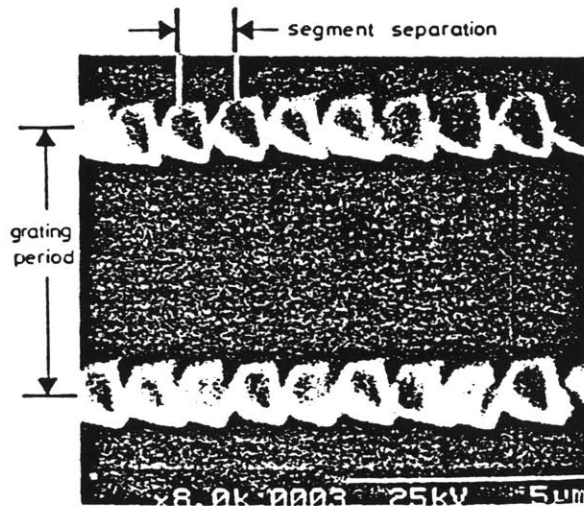


Figure 3-3: Periodic domain reversal of  $\text{LiNbO}_3$  by electron beam writing. Shown is a photograph of the  $+z$  face of a  $\text{LiNbO}_3$  sample domain-reversed by direct e-beam scanning on the  $-z$  face. Domain reversal occurred in segmented regions as opposed to a continuous line region. (Yamada *et al.*, *Electronics Letters* 28(8), pp. 721-722, 1992)

wafer. As in the case for titanium in-diffusion, photolithography is used to define a periodic grating where metal is patterned on one face of the wafer. A uniform conducting layer contacts the other face. The poling field is created by applying one or more high voltage pulses between the metallized portion of the grating on one face and the uniform conductor on the other face of the  $\text{LiNbO}_3$  crystal. One major advantage of the electric field poling method is that the reversed domains can reach very deep into the  $\text{LiNbO}_3$  sample. In practice 1-mm-thick samples have been successfully and reliably domain-reversed. Furthermore, the period of the grating pattern is precisely defined by the lithographic mask, just as in the case for titanium in-diffusion.

In some sense, the electric field poling method combines the virtues of the e-beam scanning method and the titanium in-diffusion method. With electric field poling, it is possible to inexpensively and reliably fabricate periodic domain-reversed gratings that extend from one face of the crystal to the other. However, the electric field poling method is not without its own set of problems. One of the major problems lies in the tendency of the reversed domains to spread laterally beyond the width defined by the lithographic mask. This lateral spreading gives rise to a non-optimal duty cycle of the reversed domains which reduces conversion efficiency. Furthermore, the domain-reversal spreading is typically nonuniform from one reversed domain to the next, resulting in a random duty cycle error. Fortunately, improvements in fabrication technology in recent years have reduced these problems significantly.

### **3.3 E-field Poling Method**

Domain reversal by electric field poling was first reported in 1992 by Yamada [40]. It had been well known for many years that ferroelectric domains can be reversed by application of a strong electric field for many ferroelectrics. A qualitative illustration of ferroelectricity in  $\text{LiNbO}_3$  is shown in Fig. 3-4 [41][31]. The polarity of a ferroelectric domain is determined by the offset of the metal ions either above or below the oxygen layers of  $\text{LiNbO}_3$ . Domain reversal involves changing the crystal from one

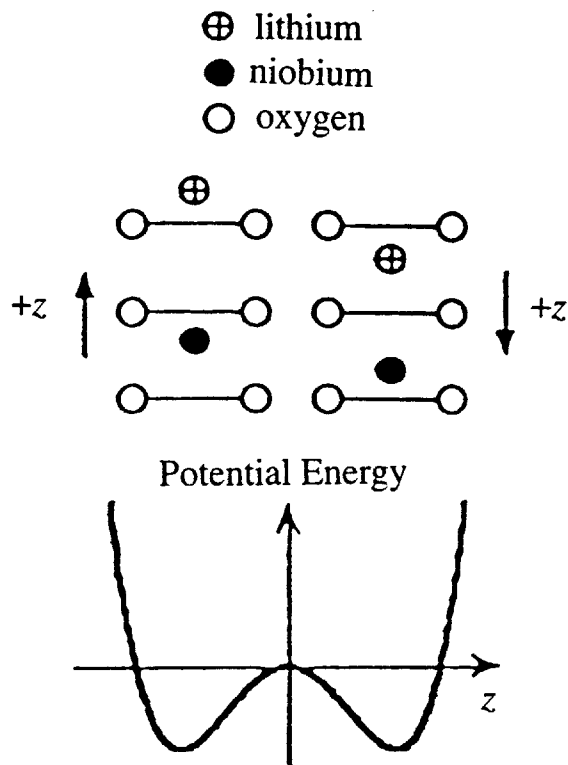


Figure 3-4: Molecular structure of  $\text{LiNbO}_3$ .  $\text{LiNbO}_3$  has 2 stable energy configurations, corresponding to anti-parallel domain orientations. The direction of offset of the lithium and niobium ions relative to the oxygen layer determines the domain orientation. The domain orientation can be reversed by an external field with sufficient activation energy to move  $\text{LiNbO}_3$  from one stable energy configuration to another.



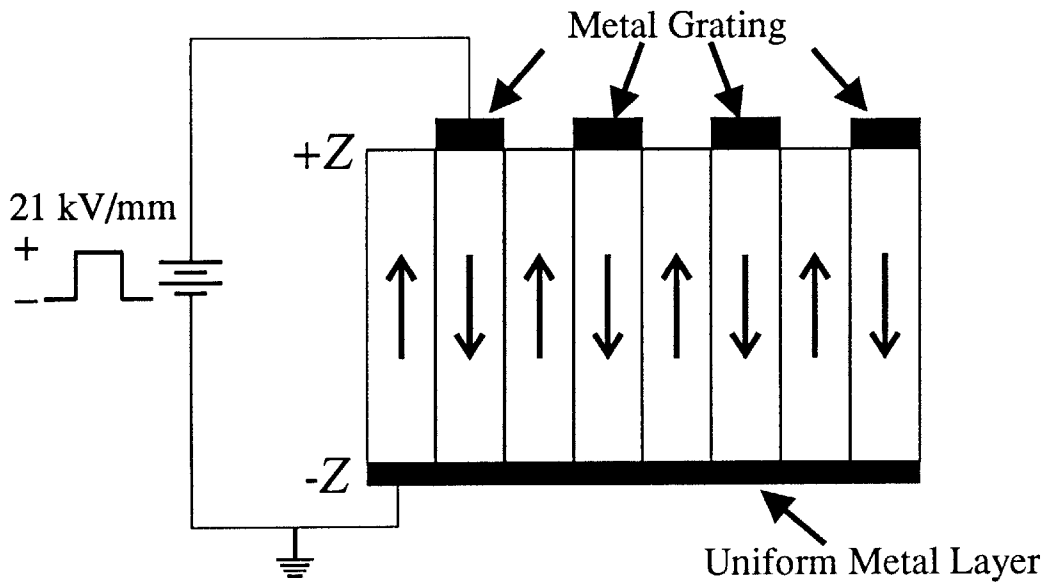


Figure 3-5: Schematic of an electric field poling apparatus using metal grating. A metal grating structure is patterned onto the  $+z$  face of the  $\text{LiNbO}_3$  substrate. The metal grating is contacted directly by the high voltage circuitry. The  $-z$  face is uniformly coated with metal. Domain reversal usually takes place inside oil to prevent voltage arcing between the metal pattern on the  $+z$  face and the uniform metal layer on the  $-z$  face.

stable energy configuration to the other. Domain reversal typically occurs when the applied field exceeds the so-called coercive field of the crystal, which for  $\text{LiNbO}_3$  is 21 kV/mm. For  $\text{LiNbO}_3$ , however, the sample tends to suffer dielectric breakdown well before domain reversal takes place. Yamada discovered that if the  $\text{LiNbO}_3$  sample was thin enough, domain reversal could take place at a voltage lower than the sample breakdown voltage. The first electric-field poled devices was domain-reversed by applying high voltages across a 0.25-mm-thick sample in an oil bath [40][42]. The use of oil was necessary to prevent voltage from arcing through the air path between the  $\pm z$  faces. Typically, a metal grating is defined on the  $+z$  face of the  $z$ -cut sample, while the  $-z$  face has a uniform metal film, as shown in Fig. 3-5.

E-field poling was later demonstrated [43] using liquid electrolytes instead of metal electrodes by Webjorn *et.al.* In this scheme the periodic grating structure was patterned by standard photolithography with a photoresist thickness of 1000 Å. The sample was then contacted on both sides by a solution of LiCl in De-ionized water.

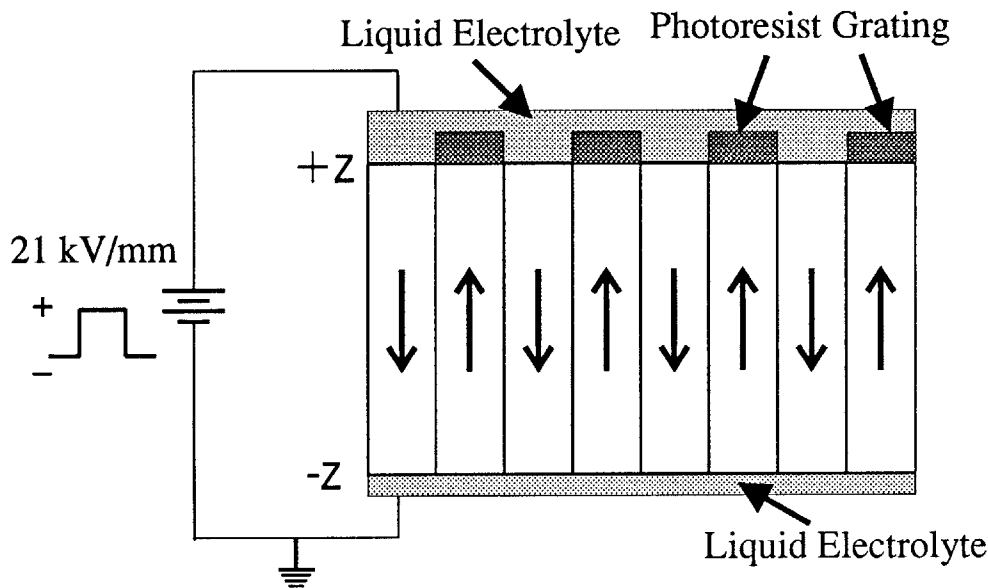


Figure 3-6: Schematic of an electric field poling apparatus using liquid electrolyte. A photoresist grating structure is patterned onto the  $+z$  face of the  $\text{LiNbO}_3$  substrate. The areas between the photoresist grating is contacted by a liquid electrolyte conductor. Domain reversal takes place in the areas contacted directly by the liquid electrolyte. The  $-z$  face is uniformly contacted with liquid electrolyte.

Physically, this was accomplished by sandwiching the  $\text{LiNbO}_3$  crystal between two filter papers soaked in  $\text{LiCl}$  solution. The  $\text{LiCl}$  solution was contacted on both sides of the sample to a high voltage pulser, and high voltage pulses were applied across the sample with the  $\text{LiCl}$  solution serving as the metal contacts. Figure 3-6 illustrates this domain reversal scheme. The photoresist in this case acted as an insulator, so that the areas covered by photoresist were not domain reversed.

A variant of the liquid electrolyte poling was demonstrated later by Myers *et al.* [9][31]. In this design, shown in Fig. 3-7, the lithium niobate sample was patterned with a metal grating on the  $+z$  face, much as in the design using oil as insulation. Photoresist was then deposited onto the  $+z$  face, covering most of the grating pattern except for the contact pads (not shown in Fig. 3-7) which were left exposed. The  $\text{LiNbO}_3$  sample was contacted on both sides by a solution of  $\text{LiCl}$ . This was realized by squeezing the sample between two O-ring chambers connected to a reservoir of the  $\text{LiCl}$  solution. The liquid electrolyte reservoirs were then connected to a high voltage

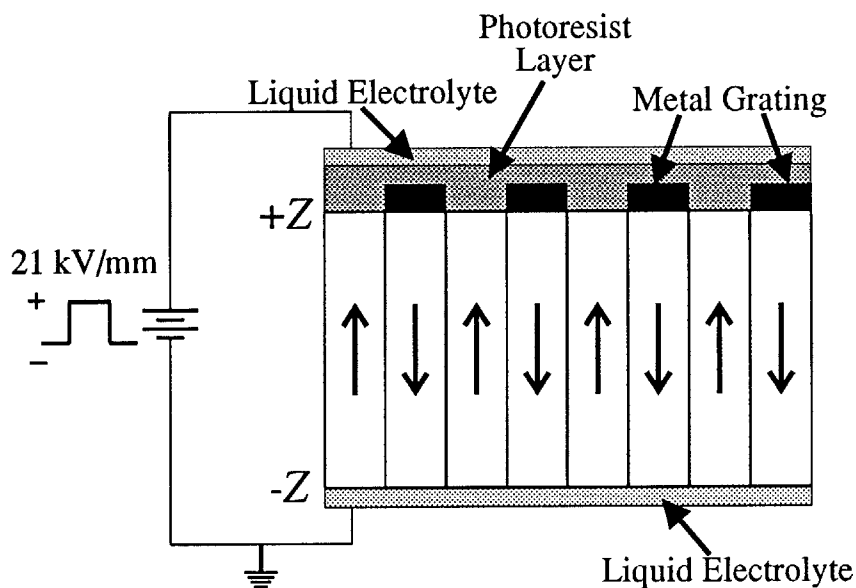


Figure 3-7: Schematic of an electric field poling apparatus using metal grating and liquid electrolyte. A metal grating structure is patterned onto the  $+z$  face of the  $\text{LiNbO}_3$  substrate. A layer of photoresist covers most of the metal grating pattern except for the contact pads (not shown), which are left exposed. Liquid electrolyte is then applied over the photoresist and contacts the metal grating pattern via the contact pads. Domain reversal takes place in the areas contacted by the metal grating. The  $-z$  face is uniformly contacted with liquid electrolyte.

source. Electrical contact was made via the liquid electrolyte to the exposed contact pads of the metal pattern on the  $+z$  face and to the bare  $\text{LiNbO}_3$  surface on the  $-z$  face. In this scheme, the photoresist again served as an insulator, preventing domain reversal from taking place between the metal lines. However, now the  $\text{LiNbO}_3$  surface is directly contacted by metal as opposed to liquid electrolyte. It was claimed that the metal lines provide better domain-reversal pattern fidelity than does the liquid electrolyte alone [31].

The liquid electrolyte method has several advantages versus the oil method. The oil method seems to be very sensitive to the high voltage pulse parameters. The correct voltage and pulse widths must be used to obtain reasonable results. Working pulse widths tend to be very short, ranging from  $100 \mu\text{s}$  to  $500 \mu\text{s}$ . Growth of the reversed domains along the  $z$  axis is essentially instantaneous. The duration of the pulse allows primarily lateral growth of the reversed domains under the areas defined by the electrodes. Additionally, there is a tendency for the reversed-domains to spread laterally beyond the defined electrode width if the poling field continues to be applied after a given area of the grating pattern has been domain-reversed. With long pulses the reversed domains in one part of the sample has time to spread while the other parts of the sample are being poled. With short pulses, however, the duration of the poling pulses are short enough that there is little time for excess lateral spreading of the reversed domains in any part of the sample. The liquid electrolyte method, on the other hand, is largely insensitive to the pulse length used or the exact poling voltage. Short as well as long pulses (up to a few seconds) can be used. The photoresist in the liquid electrolyte scheme acts as an effective insulator which suppresses fringing fields between adjacent electrodes. The tendency of the reversed domains to spread is hindered by the photoresist layer between the electrodes, therefore making it possible to use long pulses without having the grating structure “washed-out” by excessive lateral spreading of the reversed domains. Nevertheless, a moderate amount of excess lateral spreading of reversed domains of  $2 \mu\text{m}$  or more still exists in the liquid electrolyte poling scheme, and special care must be taken in domain-reversing samples with grating periods below  $\sim 10 \mu\text{m}$ . Furthermore, in

the liquid electrolyte scheme, the poling results also depend somewhat on the poling current, as lower current have been found to produce straighter domain walls [9][31].

It has been known that having the periodic pattern on the  $+z$  or  $-z$  face makes a difference in the poling results. Early poling studies based on the oil method have concluded that the periodic pattern should be on the  $+z$  face since the orientation of the dipoles causes the domain reversal to initiate from the  $+z$  face [40][42]. One could either ground the pattern on the  $+z$  face and apply negative pulses to the backside or apply positive pulses to the pattern and ground the backside. The poling method used by Myers *et al.* also follows this heuristical conclusion [9][31]. However, Webjorn *et al.* reported little difference between fabricating with the pattern on the  $+z$  face of the crystal and doing so on the  $-z$  face [43]. In fact, their devices were all fabricated with the pattern on the  $-z$  face. In this work the poling method will closely follow that described by Myers *et al.* where grating patterns are fabricated on the  $+z$  face [9][31].

### 3.4 Fabrication of PPLN

This section discusses the standard procedures and relevant issues in the fabrication of PPLN used in the work described by this thesis.

The first step in the fabrication of PPLN involves the patterning of electrodes with the desired grating periods on the  $+z$  face of a  $z$ -cut  $\text{LiNbO}_3$  sample. We used standard photolithographic techniques to pattern metal grating structures on the  $+z$  face of the  $\text{LiNbO}_3$  sample. Table 3.1 shows the standard procedure for patterning the metal pattern. The starting material was a  $z$ -cut 75-mm-diameter  $\text{LiNbO}_3$  wafer purchased from Crystal Technology. We typically cut out 1.5 cm x 1.5 cm or 2 cm x 2 cm square pieces from the 3" wafer to accommodate a typical grating pattern of 1 cm x 1 cm. In our earlier fabrication of 0.25-mm-thick PPLN, we used 1-mm thick starting wafers and lapped the individual square pieces down to 0.25 mm. In our subsequent fabrication of 0.5-mm-thick PPLN, we used 0.5-mm-thick starting wafers, and thus no lapping was necessary. The procedure for our most recent fabrication

Step	Procedure
1	Clean $z$ -cut $\text{LiNbO}_3$ sample with standard solvents: trichloroethylene, acetone, isopropanyl.
2	Spin Shipley 1430 photoresist on $+z$ face of sample: 30 sec at 4000 rpm, thickness $\sim 1.67 \mu\text{m}$ .
3	Soft bake sample with photoresist: $80^\circ\text{C}$ for 20 min
4	Expose grating pattern on photoresist. Exposure time: 6 sec.
5	Soak sample in chlorobenzene for 15 min.
6	Develop sample with photoresist in 7:1 Shipley 606 photoresist developer.
7	Deposit metal in e-beam evaporator: $100 \text{ \AA Ti} + 2000 \text{ \AA Au}$ .
8	Lift-off photoresist in acetone.

Table 3.1: Processing procedure for patterning metal grating on  $\text{LiNbO}_3$

of 0.75-mm-thick PPLN was identical to that for the 0.25-mm-thick PPLN with the exception of the 0.75 mm final thickness. After cleaning with standard solvents, the sample was placed in buffered hydrofluoric acid (BHF) for a few minutes to etch away any surface impurities that might be present. This improved the adhesion of the metal layer to the bare  $\text{LiNbO}_3$  surface in the subsequent metal deposition process. A  $1.6 \mu\text{m}$  thick layer of Shipley 1430 photoresist was deposited on the  $+z$  face of the sample. The sample was then held in contact with a glass mask with the desired grating pattern and exposed by ultraviolet (UV) light. The mask design was such that the areas to be occupied by the metal electrodes were exposed by the UV light. The exposure to UV light altered the chemical properties of the exposed photoresist such that subsequent immersion of the sample in a photoresist developer dissolved the exposed photoresist but left the UN-exposed photoresist intact.

After exposure and development we deposited a metal layer consisting of  $100 \text{ \AA}$  of titanium followed by  $2000 \text{ \AA}$  of gold via e-beam evaporation. The sample was then immersed in acetone to dissolve the photoresist and thereby “lifting off” the metal in areas where the metal layer had covered the photoresist. Following metal deposition we deposited another layer of photoresist over the entire grating pattern except for a portion of the grating area which was designed for contact with the liquid

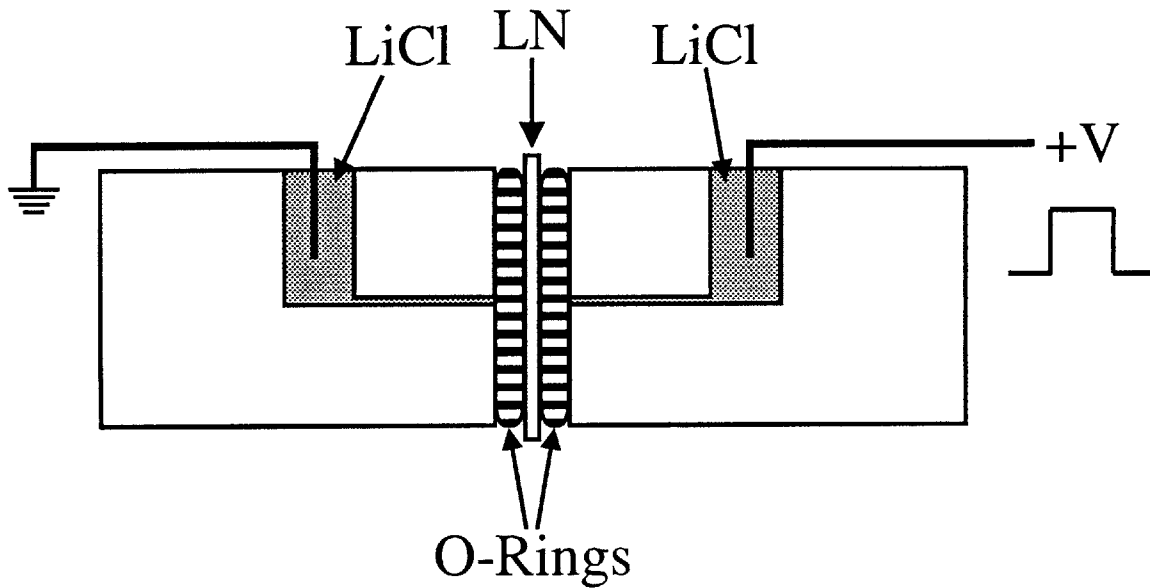


Figure 3-8: Liquid electrolyte poling fixture. A  $z$ -cut  $\text{LiNbO}_3$  substrate is squeezed between two O-ring chambers.  $\text{LiCl}$  solution contacts the two sides of the sample through the two O-ring chambers. The two reservoirs containing the  $\text{LiCl}$  solution are electrically connected to the high voltage circuitry via two wires.

electrolyte. Instead of using a metal contact for the  $+z$  face, one may also contact the  $+z$  face directly with liquid electrolyte. In this approach, the metal deposition step is eliminated. We generally prefer the use of metal grating because the metal seemed to form a better contact with the  $\text{LiNbO}_3$  which resulted in a lower threshold voltage for poling.

A schematic of the liquid electrolyte poling fixture is shown in Fig. 3-8. We sandwiched the  $\text{LiNbO}_3$  sample between two O-rings. Each O-ring was squeezed between the  $\text{LiNbO}_3$  sample on one side and a plexiglass block on the other side. The size of the O-rings was chosen such that the inner boundary of each O-ring was sufficient to enclose the entire grating pattern. The plexiglass block contained a liquid electrolyte reservoir which was connected to the O-ring chamber. After securing the  $\text{LiNbO}_3$  sample between the O-rings, the reservoirs in the plexiglass blocks were filled with liquid electrolyte consisting of a lithium chloride ( $\text{LiCl}$ ) solution. The  $\text{LiCl}$  solution was prepared by dissolving 50 g of  $\text{LiCl}$  in 100 ml of de-ionized water. We then filled the O-ring chambers with the liquid electrolyte by pumping the air out from the liquid

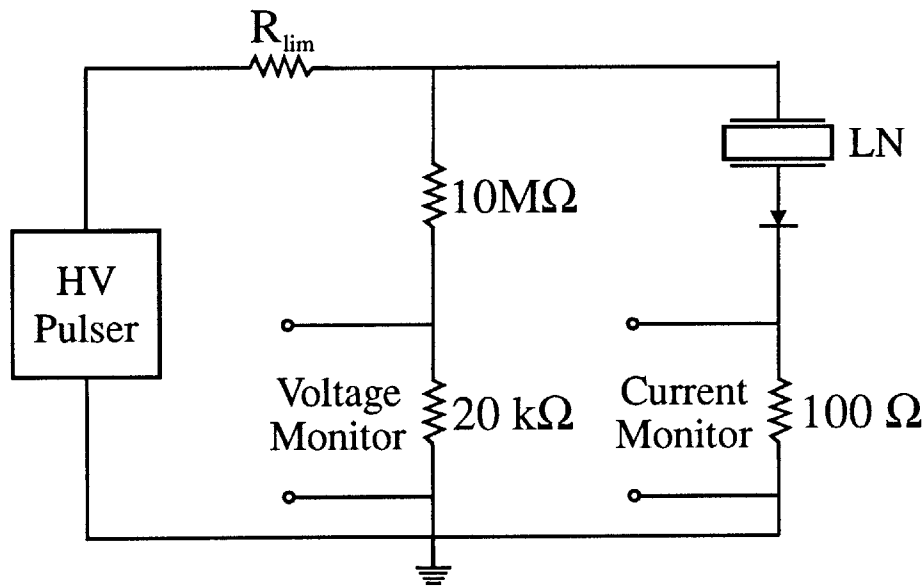


Figure 3-9: High voltage circuitry for electric field poling of LiNbO<sub>3</sub>.

electrolyte reservoir using vacuum. Electrical contacts were then established between the liquid electrolyte reservoirs and a high voltage pulse generator. A schematic of the high voltage domain-reversal setup is shown in Fig. 3-9. With the  $-z$  face of the LiNbO<sub>3</sub> sample grounded, high voltage pulses with positive polarity were applied to the  $+z$  face. An electric field strength exceeding the coercive field of 21 kV/mm for LiNbO<sub>3</sub> was required to initiate domain reversal. As shown in Fig. 3-9, the poling current through the sample was regulated by a current-limiting resistor and by the applied voltage. The voltage across the sample was monitored by a resistive voltage divider while the current through the sample was measured by an 100  $\Omega$  resistor. Domain-reversal was observed as the pulser voltage was ramped above a threshold voltage. Figure 3-10 shows plots of the voltage across the sample and the current through the sample as a function of time. As the voltage was raised beyond the threshold, current due to ferroelectric domain-reversal began to flow. The voltage across the sample was clamped at the threshold voltage while domain reversal took place, and the current was determined by the difference between the pulser voltage and the threshold voltage and by the current-limiting resistance. In general, the current was not quite constant because the threshold voltage typically varied somewhat



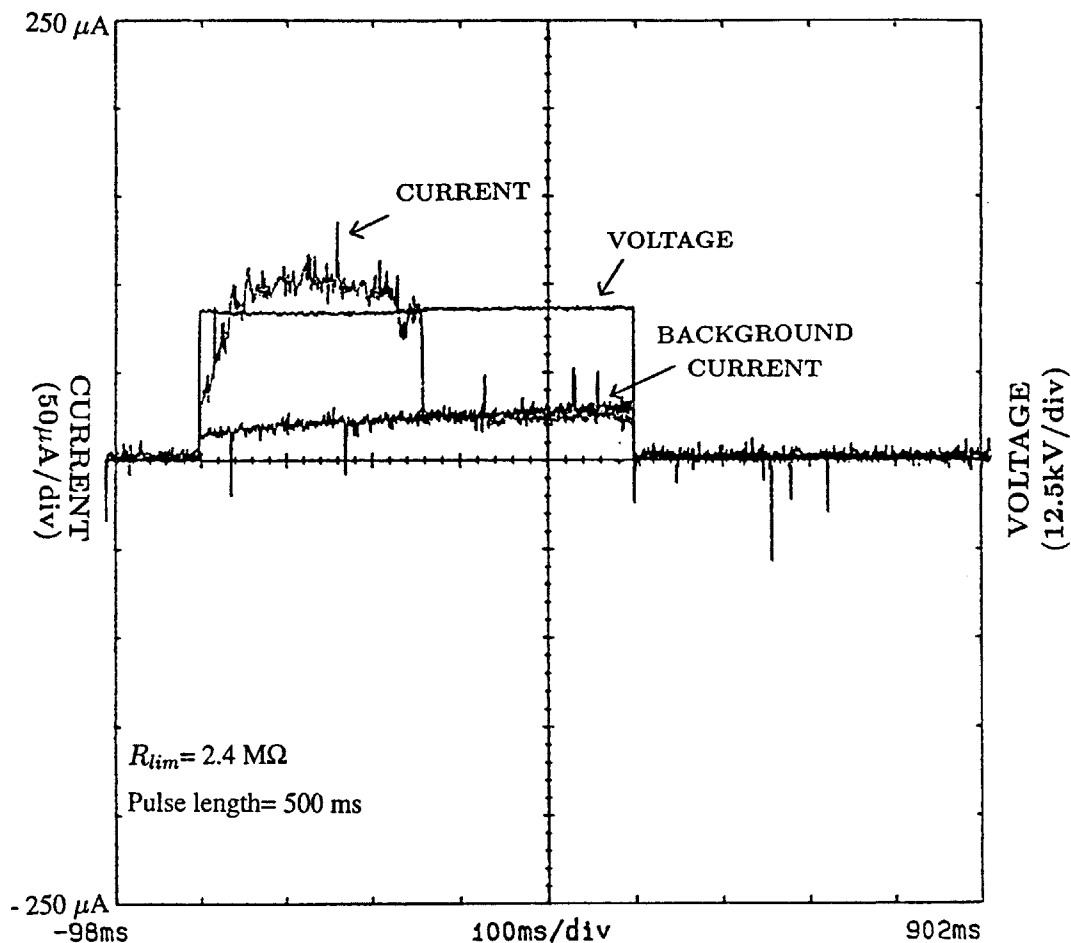


Figure 3-10: Current and voltage monitors during electric field poling. Ferroelectric domain reversal is monitored by the current flow due to the movement of free charges to compensate for the reversal of the permanent electric dipole moments of the material. Current flow ceases when the domain reversal process is completed. The current level is regulated by a current-limiting resistor  $R_{lim}$  positioned between the sample and the high voltage source (shown in Fig. 3-9).

from one part of the sample to another. The sample with the poling parameters shown in Fig. 3-10 was completely domain-reversed in a single pulse. After domain-reversal was completed, the current flow stopped, and the voltage across the sample reverted to the pulser voltage. One can calculate the total charge needed to pole a sample by determining the total area covered by the grating electrodes and the spontaneous polarization of  $\text{LiNbO}_3$ . The total charge required to pole a LN sample with poling area  $A$  is

$$\Delta Q = 2P_s A.$$

where  $P_s = 71 \mu\text{C}/\text{cm}^2$  is the spontaneous polarization. The current monitor allowed us to calculate the total amount of charge transferred after each pulse. In cases where the poling was to be completed in several pulses, one could thus keep a “running total” of the amount of charge to be transferred and thus determine whether additional pulses were needed, and if so, what the pulse length should be. There are a number of issues associated with the E-field poling process:

First, the  $z$ -cut LN samples were subject to dielectric breakdown if the applied voltage exceeded the threshold voltage by more than a few hundred volts. As a general rule of thumb, the thicker the sample, the smaller was the “poling window” between the poling threshold and the breakdown voltage. We have successfully poled samples with thicknesses of 0.25 mm, 0.5 mm, and 0.75 mm. As the thickness approaches 1 mm, the poling threshold and the breakdown voltage became roughly equal, which made it exceedingly difficult to completely pole a sample without dielectric breakdown.

Second, in general the domain reversal profile spread out laterally by at least  $2 \mu\text{m}$  or so from their defined widths. It is thus important that the voltage pulse was turned off after all areas under the electrodes had been completely poled. Leaving the voltage pulse on resulted in additional lateral spreading of the reversed domains. In our poling experience we found it difficult to predict exactly how much of the grating area would be poled in one single pulse. Therefore, we normally tried to pole the

sample in 3 or more pulses rather than a single pulse such that we could adjust the total number of pulses and/or the width of the pulses based on the amount of poling completed after the previous pulses.

Third, it was necessary to place a high-voltage diode in series with the  $\text{LiNbO}_3$  sample to prevent reversal of the ferroelectric domains back to its original configuration at the end of a pulse. According to Myers *et al.* domain reversal is permanent after roughly 50 ms [31]. If the voltage were abruptly turned off after 50 ms, domains that switched polarity in the last 50 ms would return to their original polarity, generating large “back reversal” current [31]. When the poling rate is fast, the amount of material that reverts to its original polarity may represent a significant portion of the domain-reversed region. By placing a diode in series with the  $\text{LiNbO}_3$  sample, one can effectively block the back-reversal current flow.

After poling the samples, we immersed the samples in hydrofluoric (HF) acid to remove the metal electrode and to delineate the reversed domain patterns on the  $+z$  and  $-z$  faces. The etch rate differs for the two domain orientations, thereby revealing the domain structure. On some samples, we also cut the samples along the  $x$ -direction and polished the  $\pm y$  faces. Observation under a microscope shows that the reversed domain pattern spread out laterally from the widths that were defined by the metal grating. Depending on the amount of over-poling, the lateral spreading can be as low as  $2 \mu\text{m}$  for samples with minimum spreading or as high as  $5 \mu\text{m}$  or more for severely over-poled samples. We also measured the random duty cycle error by sampling 20 periods over a certain segment of the poled samples and measuring the variation in the duty cycle (on the  $+z$  face) over the segment. The random duty cycle error typically ranges from  $0.6 \mu\text{m}$  to  $1.2 \mu\text{m}$ , given a  $21.5 \mu\text{m}$  grating period. By observing the  $+z$  and  $-z$  faces of the  $\text{LiNbO}_3$  sample we found that typically the domain reversal pattern uniformity was much better at the  $+z$  face, where the metal grating contacts the surface, than at the  $-z$  face. Furthermore, the amount of lateral spreading was always larger at the  $-z$  face than at the  $+z$  face. This confirms that the domain reversal process initiated from the  $+z$  face and propagated to the  $-z$  face, which was also observed for partially poled  $\text{LiNbO}_3$ .

### 3.5 Characterization of PPLN

Following E-field poling of  $\text{LiNbO}_3$  it was necessary to characterize each poled sample to determine the quality of the periodic domain reversal pattern. The first step in characterizing a particular poled sample was to delineate the domain-reversal grating pattern to assess the overall quality of the poled grating structure. By observing the delineated structure, one can often identify non-ideal features which can be detrimental to the nonlinear conversion efficiency and thus the usefulness of the device. Three of the most common types of non-ideal features are discussed below:

1. UN-poled grating regions. Frequently some portion of the grating structure failed to domain reverse. Sometimes one or more broken metal grating lines was the cause of the non-reversal. Many times a whole region of the grating pattern was UN-poled. This can be caused by the presence of air bubbles in the liquid electrolyte solution which contacts the samples inside the O-ring, which would lead to an undefined electric potential over parts of the grating pattern and results in an UN-poled region. The failure of a whole region to pole can also be due to the premature termination of the poling field. The net effect of the presence of UN-poled regions is the reduction in the effective length of the grating and thus a reduction in the effective interaction length.

2. Non-50/50 duty cycle. As discussed in Section 2.9, optimum conversion efficiency of a QPM interaction is obtained with a 50/50 ratio between the lengths of the reversed and UN-reversed domains. Figure 3-11 shows a photograph of the etched  $+z$  face of a typical PPLN sample. From Fig. 3-11 it is evident that the duty cycle is not the ideal 50/50 ratio. By measuring the widths of the reversed and UN-reversed domains from the etched  $+z$  and  $-z$  faces of the poled sample, one can determine the amount of deviation from a 50/50 duty cycle.

3. Random duty cycle errors. As discussed in Section 2.9, random variations in the positions of the domain boundaries contribute to random duty cycle errors, which results in reduced conversion efficiency as given by Eq. (2.97).

Based on the observation of the delineated domain reversal structure of the PPLN

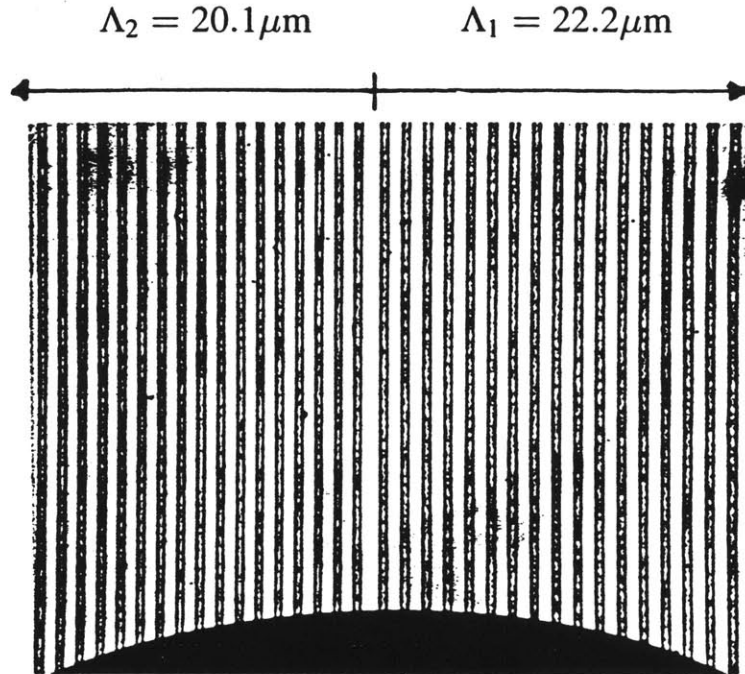


Figure 3-11: Photograph of the  $+z$  face of a double-grating periodically poled  $\text{LiNbO}_3$  sample that has been delineated by etching in hydrofluoric acid. The region on the left has a grating period of  $20.1 \mu\text{m}$  while the region on the right has a grating period of  $22.2 \mu\text{m}$ . The dark bands are the domain-reversed regions.

sample, samples which were deemed acceptable were then polished and then further characterized by optical means.

The real measure of the quality of a PPLN sample can be determined only by measurement of the conversion efficiency of the sample in an actual nonlinear frequency conversion experiment. We typically characterized our samples by measuring the conversion efficiency in a DFG interaction by measuring the following physical parameters:

1. Peak phasematching temperature. Recall from Section 2.6 that the design of the grating period for a particular nonlinear frequency conversion experiment was based on the published Sellmeier's equation [30], which provides approximate values of the refractive indices at the wavelengths of interest. Therefore, for a given grating period, one should not expect the actual peak phasematching temperature to coincide with that calculated from the Sellmeier's equation. Furthermore, the accuracy of the Sellmeier's equations depends on the wavelength of interest. Therefore, conclusions

about the accuracy of the Sellmeier's equations for a particular three-wave mixing interaction drawn from one set of interacting wavelengths cannot be applied to another set of interacting wavelengths.

2. Conversion efficiency. Recall from in Section 2.9 that two particular types of non-idealities, namely random duty cycle errors and a non-50/50 average duty cycle, contribute to reduced conversion efficiency. Measurement of the conversion efficiency can be used to experimentally determine the effective nonlinearity of a particular PPLN sample.

3. Temperature and Spectral Bandwidths. This measurement is used to determine the effective interaction length of a PPLN sample, which is often somewhat less than the physical length of the grating. Consider a DFG interaction. Based on equation (2.23) which expresses the reduction in conversion efficiency as a function of the wavenumber mismatch  $\Delta k$ , the conversion efficiency scales as  $\text{sinc}^2(\frac{\Delta k L}{2})$ . Since the refractive indices of  $\text{LiNbO}_3$  are functions of temperature and wavelength,  $\Delta k$  is also a function of temperature and wavelength of all three interacting fields. Therefore, based on the Sellmeier's equation one can determine the expected full-width-half-max (FWHM) spectral and temperature bandwidths. By measuring the actual FWHM bandwidth, which corresponds to

$$\delta(\Delta k L) = 5.566,$$

one can thus determine the effective interaction length  $L_{eff}$ . Several factors can contribute to an effective interaction length which is shorter than the physical interaction length. In temperature bandwidth measurements, the shorter effective interaction length can be due to a non-uniform temperature distribution across the PPLN crystal, resulting in a spread of the peak phasematching temperature across the sample.

Another source for the reduced interaction length can be attributed to the non-uniformity of the domain-reversed structure across the length of the grating structure. Based on the analysis of Section 2.9, a deviation of the average duty cycle from the ideal 50/50 ratio results in reduced conversion efficiency but does not affect the

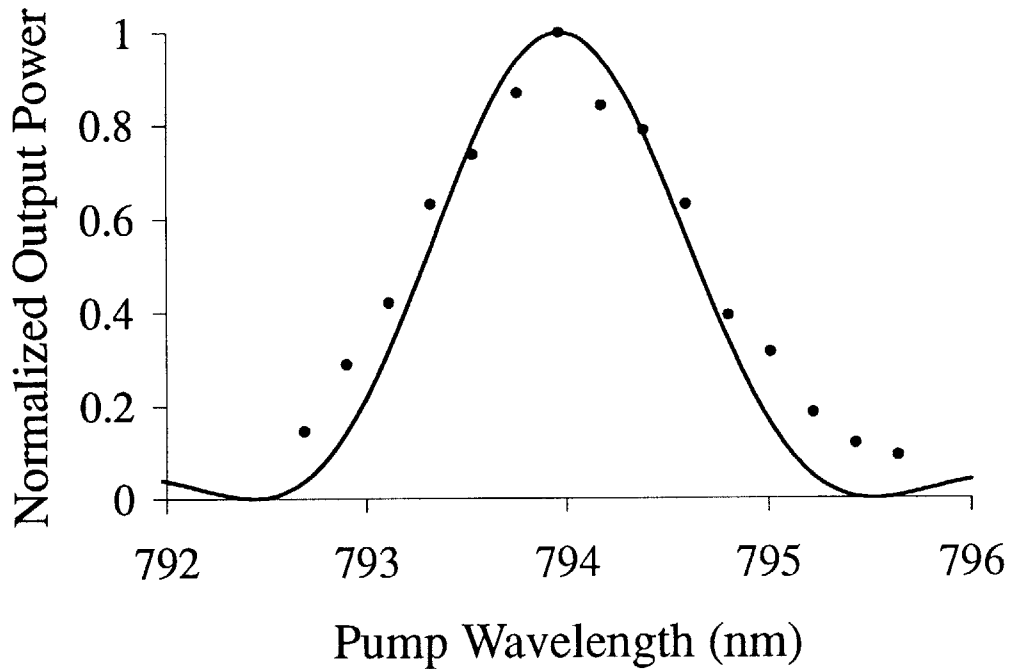


Figure 3-12: Spectral tuning of DFG conversion efficiency. Relative DFG output power from a 6-mm-long PPLN crystal with a  $21.5 \mu\text{m}$  grating period is plotted as a function of pump wavelength for a signal wavelength of 1064 nm at a crystal temperature of  $43.9 \text{ }^\circ\text{C}$ .

bandwidth and thus the effective length. Likewise, random errors in the duty cycle also reduce the the conversion efficiency without affecting the bandwidth. However, in most of the samples we fabricated, both average duty cycle and the random duty cycle error vary somewhat over the length of the grating due to the non-uniformity in the spreading of the reversed ferroelectric domains. This can result in increased temperature as well as spectral bandwidth and therefore an effective interaction length that's shorter than the physical grating length.

Figure 3-12 shows results of spectral bandwidth measurements for a QPM-DFG interaction between a Ti:Sapphire laser and a Nd:YAG laser at 1064 nm. The PPLN crystal has a grating period of  $21.5 \mu\text{m}$  and a physical grating length of 6 mm. As seen in Fig. 3-12, the experimental tuning curve has a FWHM bandwidth that's about 10% larger than the theoretically calculated curve based on the Sellmeier's equation. This suggests that the physical interaction length was only 5.4 mm instead

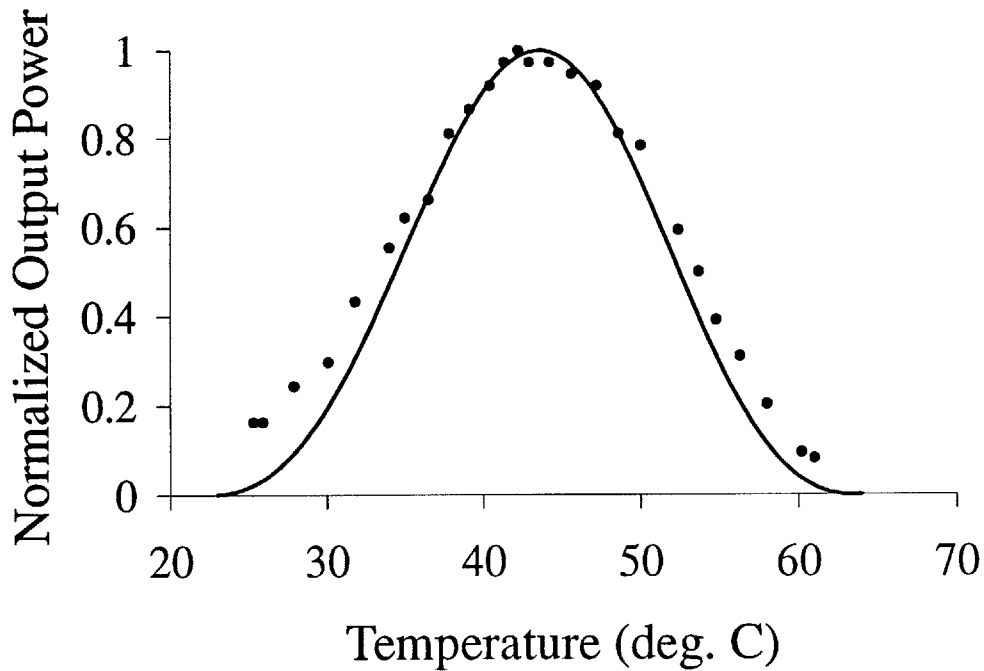


Figure 3-13: Temperature tuning of DFG conversion efficiency. Relative DFG output power from a 6-mm-long PPLN crystal with a  $21.5 \mu\text{m}$  grating period is plotted as a function of temperature for a pump wavelength of 794.0 nm and a signal wavelength of 1064 nm. The solid curve, calculated from the Sellmeier's equations by Edwards, is shifted by  $-9.0^\circ\text{C}$  to match the experimental data (filled circles).

of 6 mm. Figure 3-13 shows the results of the temperature bandwidth measurements for the same DFG interaction and PPLN crystal. Again, the FWHM bandwidth of the experimental tuning curve had a FWHM bandwidth that's roughly 10% larger than the theoretically calculated curve based on Sellmeier's equations. In addition, as a result of the limited accuracy of the Sellmeier's equations by Edwards [30], the calculated peak phasematching temperature was about  $9.0^\circ\text{C}$  higher than the experimentally measured values.



# Chapter 4

## Relevant Work By Others

This chapter aims to provide a summary of the numerous milestones over the past few years in the rapidly progressing field of quasi-phasematched nonlinear optics. Particular emphasis will be placed on applications based on periodically-poled lithium niobate (PPLN). Several of the pioneering works in establishing reliable means of fabricating PPLN for frequency doubling experiments are discussed in Section 4.1. Section 4.2 reviews the important milestones achieved in the use of PPLN for second harmonic blue and green light generation. Experiments in QPM difference-frequency generation of mid-IR outputs are discussed in Section 4.3, while relevant work in PPLN-based OPO's are described in Section 4.4. In Section 4.5 we examine recent device demonstrations based on periodically poled  $\text{LiTaO}_3$ ,  $\text{KTiOPO}_4$ , and  $\text{RbTiOAsO}_4$ .

### 4.1 Early Work

The concept of quasi-phasematching was first proposed by Armstrong *et al.*[1] and Franken and Ward [2] in 1961, which predates that for the conventional birefringent phasematching. Early experimental efforts involved stacking together a series of thin plates of single-domain nonlinear material such as GaAs with alternating crystal orientations along the  $z$ -axis of the crystal, as shown in Fig. 4-1[3][4][5][6]. However, dielectric losses at the interfaces and the difficulty in fabrication thin plates with thicknesses on the the order of a few tens of  $\mu\text{m}$  prevented widespread use of QPM

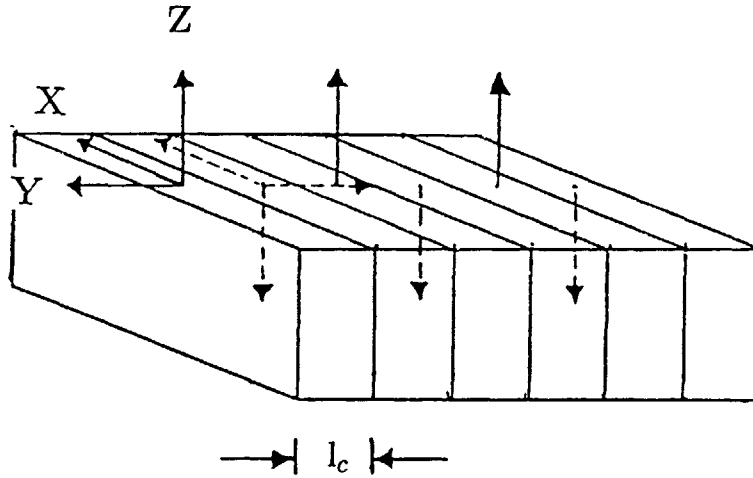


Figure 4-1: Stacked coherence length plates. Quasi-phasematching can be implemented by stacking together a series of thin crystal plates with a thickness of one coherence length. The plates have alternating orientations of the crystal  $z$ -axis, corresponding to alternating signs of the effective nonlinear coefficient.

materials prepared this way.

The advent of the use of lithographic patterning to periodically domain-reverse ferroelectric domains for QPM occurred in 1988 when Lim *et al.* achieved periodic ferroelectric domain reversal at the surface of a  $\text{LiNbO}_3$  sample by use of the titanium in-diffusion method discussed in Chapter 3 [38]. Lim *et al.* reported the first QPM nonlinear optical interaction by doubling the frequency of a Nd:YAG laser output in a third-order QPM second harmonic generation (SHG) with grating periods of  $15 \mu\text{m}$  to  $22 \mu\text{m}$  in a waveguide geometry [38].

Over the next few years numerous results in QPM SHG in  $\text{LiNbO}_3$  were reported. SHG into the blue spectral region was repeatedly demonstrated [37][38]. As fabrication techniques improved, devices with shorter QPM grating periods were successfully fabricated, making it possible to achieve first order QPM SHG into the green and blue wavelengths. However, because the ferroelectric domain-reversal occurred only in a shallow region beneath the surface of the  $\text{LiNbO}_3$  sample, QPM  $\text{LiNbO}_3$  nonlinear optics was limited only to waveguide applications where the field is tightly confined to the small domain-reversed region near the surface.

As mentioned in Chapter 3, the first successful QPM nonlinear frequency conversion interaction using electric-field poled technique was reported in 1993 by Yamada *et al.* [40] In that work, a 3-mm-long PPLN waveguide was used to double the frequency of a Ti:Sapphire laser output at a wavelength of 851.7 nm. From 196 mW of infrared input, 21 mW of blue light was generated in a first-order QPM interaction with a grating period of 2.8  $\mu\text{m}$ . This work demonstrated successfully the full potential of the E-field poling technique in creating short grating periods for efficient, cost effective nonlinear frequency conversion.

The first bulk QPM interaction using E-field-poled  $\text{LiNbO}_3$  was reported by Burns *et al.* in 1994 [42], who demonstrated second harmonic generation (SHG) of continuous-wave (cw) blue light from the output of a Ti:Sapphire laser at  $\lambda=936.8$  nm. The 6-mm-long, 230- $\mu\text{m}$ -thick PPLN samples had a grating period of  $\Lambda=13.4$   $\mu\text{m}$  designed for third-order QPM.

Webjorn *et al.* also demonstrated SHG of a near-IR source in bulk PPLN to produce blue light in 1994 with a liquid electrolyte poling setup as described in Chapter 3 [43]. Using third-order QPM, the output of an 832 nm Ti:Sapphire laser was frequency-doubled to produce about 20  $\mu\text{W}$  of blue output at a wavelength of 416 nm. The bulk PPLN samples had a grating period of 9  $\mu\text{m}$  and were 3.3 mm long and 200  $\mu\text{m}$  thick. This work demonstrated the alternative use of liquid electrolyte contacts with photoresist insulator for achieving periodic domain reversal as opposed to the use of metal grating with oil as insulator in Yamada's and Burn's work. For reasons already discussed in Chapter 3, over the past few year the use of liquid electrolyte contacts has become the dominant method for fabricating PPLN devices.

Note that in these "early days" the conversion efficiencies achieved were typically low because of a number of reasons. First, the lateral spreading of the ferroelectric domain inversion resulted in a grating with a non-50/50 duty cycle, and the random errors in the boundary positions also contributed to reduce the conversion efficiency. Second, the very short coherence lengths for interactions that produce visible light via SHG made it extremely difficult to fabricate first-order QPM gratings for bulk applications. Therefore, third-order QPM gratings were fabricated instead, but at a

penalty of nearly 1 order of magnitude reduction in the conversion efficiency.

## 4.2 QPM Second Harmonic Generation in PPLN

As discussed in Chapter 1, the main impetus behind the interest in QPM second harmonic generation is to produce coherent blue output from commercial diode lasers operating in the near-IR spectrum. With output power of 100 mW or more readily available from today's single-mode near-IR diode lasers, one can expect to generate tens of mW of blue output in a single-pass QPM-SHG using PPLN.

Research activities over the past few years have addressed two main issues related to the use of PPLN for highly efficient frequency doubling crystals. The first concerns the challenge of fabricating periodically poled LN samples with 3-5  $\mu\text{m}$  grating periods necessary for first-order QPM-SHG of blue light. With improvements in the electric field poling technique, such as optimizing the ratio between the conductor linewidth and the grating period to compensate for lateral spreading of the domain-reversal profile, improving processing techniques to ensure a good, uniform electrical contact between the grating conductor and the  $\text{LiNbO}_3$  surface, and optimizing poling parameters such as the poling current and pulse lengths, high quality short-grating-period PPLN devices were successfully fabricated for first-order QPM frequency doubling of near-IR sources. Webjorn *et al.* demonstrated first-order QPM SHG of 1064 nm Nd:YAG laser output to produce green at 532 nm in 1995 [44], using both cw and pulsed pump lasers. The grating period of the PPLN was 6.8  $\mu\text{m}$ , and the length of the sample was 4 mm. Shortly thereafter, first-order QPM frequency-doubling into the blue spectral region was demonstrated [8] [45] with successful fabrication of PPLN with grating periods less than 5  $\mu\text{m}$ . Pruneri *et al.* demonstrated a highly efficient first-order SHG of a cw Nd:YAG laser output at  $\lambda = 946$  nm to produce blue light at  $\lambda = 473$  nm [8]. The grating period of the PPLN sample was 4.6  $\mu\text{m}$ , the thickness was 200  $\mu\text{m}$ , and the length was 6 mm. A maximum of 49 mW of blue output power was produced from 1.07 W of input IR power, indicating a  $d_{eff}$  of 19 pm/V, which is quite close to the theoretical limit of 21 pm/V. This suggests that

the fabricated sample had a domain-reversal duty cycle close to the ideal 50% and that there was little random fluctuation in the domain positions. Comparison of the work by Pruneri *et al.* and that by Yamada shows that while waveguide PPLN devices produces higher conversion efficiency due to the confinement of optical fields inside the waveguides, bulk PPLN devices, with the high  $d_{33}$  nonlinearity and non-critical phasematching, offer reasonable conversion efficiencies and the potential for producing high-power single-pass second harmonic outputs. As will be discussed in the following paragraph, with scaling of the PPLN length and the pump power level, bulk PPLN devices have been shown to generate high-power second harmonic outputs with conversion efficiencies in excess of 40%.

The second main issue related to the use of PPLN for frequency-doubled visible generation concerns the scaling of the interaction lengths of PPLN devices and pump power levels to improve the single-pass conversion efficiency in order to generate high-power blue outputs. However, photorefractive effects which typically lead to distorted output beam profile and reduced conversion efficiency are frequently associated with frequency doubling into the blue spectral region with mW outputs. PPLN has been known to be much more immune to photorefractive damage compared to single-domain  $\text{LiNbO}_3$  due to the cancellation effects between adjacent domains. One common method to avoid photorefractive damage is to operate the crystal at an elevated temperature, typically  $100^\circ\text{C}$  or higher, where photorefractive effects are much less pronounced. In 1998, Ross *et al.* [46] extended the aforementioned work by Pruneri *et al.* [8] by the use of a thicker (0.5 mm) and longer (15 mm) PPLN to obtain a much higher SHG conversion efficiency with high-repetition-rate pulses. 450 mW average power of blue output at 473 nm was obtained from an average fundamental power of 1.13 W, yielding a conversion efficiency of 40%. The PPLN was maintained at an elevated temperature of  $140^\circ\text{C}$  to avoid photorefractive damage. This work demonstrated the capability of PPLN to be used for high-power blue generation with very high single-pass conversion efficiencies.

Likewise, Miller *et al.* demonstrated in 1997 42% single-pass conversion efficiency in the second harmonic generation of 532-nm radiation in a 53-mm long PPLN with

a grating period of  $6.5 \mu\text{m}$  [47]. The key to the high conversion efficiency was the long interaction length and the high input power of 6.5 W, which produced 2.7 W of frequency-doubled green output. The maximum output power of 2.7 W was limited by the onset of irreversible crystal damage at higher pump powers. At high input powers deleterious thermal loading effects such as thermal lensing became apparent, even at the elevated temperatures ( $\sim 200^\circ\text{C}$ ) the crystal was maintained to eliminate photorefractive effects. Miller's work demonstrated the potential for watt-level visible light generation in PPLN but also exposed the limitation to further power scaling due to thermal loading effects such as thermal lensing.

### 4.3 QPM Difference-Frequency Generation in PPLN

While producing blue and green light from frequency-doubling near-IR sources constitutes a major application for  $\text{LiNbO}_3$  QPM devices, research activity in the use of near-IR pump sources to produce tunable radiation in the mid-IR region has also been actively pursued for potential applications in remote gas sensing and environmental monitoring. Two approaches, one using difference-frequency generation (DFG) and the other using optical parametric oscillation, were taken to generate these tunable mid-IR sources.

In a typical DFG scheme, two near-IR sources are mixed inside a bulk PPLN sample and a difference-frequency output in the mid-IR wavelength region is generated. Goldberg *et al.* generated tunable mid-IR outputs from  $3.0 \mu\text{m}$  to  $4.1 \mu\text{m}$  by mixing the outputs from a Ti:Sapphire laser and a Nd:YAG laser inside a PPLN sample [48]. The Ti:Sapphire laser was tunable from 750 nm to 950 nm, while the Nd:YAG laser had a fixed wavelength of 1064 nm. The PPLN sample had three grating periods that were designed for phasematched idler wavelengths of  $3.0 \mu\text{m}$ ,  $3.5 \mu\text{m}$ , and  $4.0 \mu\text{m}$ . Tuning of the idler output wavelength was achieved by tuning the wavelength of the Ti:Sapphire laser and rotating the angle of the PPLN sample. This was the first reported use of multiple parallel gratings to extend the tuning range. Later Myers *et al.* also reported the generation of tunable mid-IR radiation from 3.6 to 4.3

$\mu\text{m}$  by difference-frequency generation between two near-IR diode lasers at 780 nm and 980 nm, each of which is tunable over tens of nm [49].  $\sim 7\mu\text{W}$  at 3.9  $\mu\text{m}$  was generated from input powers of 180 mW at 780 nm and 500 mW at 980 nm. This work demonstrated the potential for a compact tunable mid-IR source composed of two diode lasers and a PPLN chip.

## 4.4 QPM Optical Parametric Oscillation in PPLN

In applications requiring a more powerful tunable mid-IR source, the use of an optical parametric oscillator (OPO) is preferred, as it typically can generate tunable outputs with power levels comparable to the input pump power. In a typical OPO, a pump source at a near-IR wavelength is frequency down-converted into its signal and idler outputs, with the idler wavelength at 2-5  $\mu\text{m}$ .

The first PPLN-based OPO was reported by Myers *et al.* in 1995 [9][31]. 0.5-mm-thick *z*-cut  $\text{LiNbO}_3$  samples were successfully poled using a liquid electrolyte setup as discussed in Chapter 3. The ability to pole thicker samples was an important milestone since it made it possible to accommodate the larger idler beam sizes at the longer mid-IR wavelengths and to allow longer samples. The OPO was a singly-resonant Q-switched OPO pumped by a mode-locked Nd:YAG laser at  $\lambda = 1064$  nm. The sample had a grating period  $\Lambda = 31 \mu\text{m}$ . As shown in Fig. 4-2, temperature tuning was used to tune the wavelength of the signal and idler outputs from 1664 nm to 2951 nm.

As discussed in Chapter 2, one of the novel engineerable design features of using photolithographic techniques for patterning the periodic grating structure is the use of multiple grating periods in parallel to extend the tuning range of OPO's. Myers *et al.* [32] demonstrated such a grating-period tuned OPO, in which a singly-resonant Q-switched OPO pumped by a Nd:YAG laser at  $\lambda = 1064$  nm achieved a tuning range from 1.36  $\mu\text{m}$  to 4.83  $\mu\text{m}$ , as illustrated in Fig. 4-3. The grating structure consisted of 25 sections, each with a grating period spaced 0.25  $\mu\text{m}$  from that of an adjacent section. This work demonstrated the feasibility to extend the tuning range of an OPO

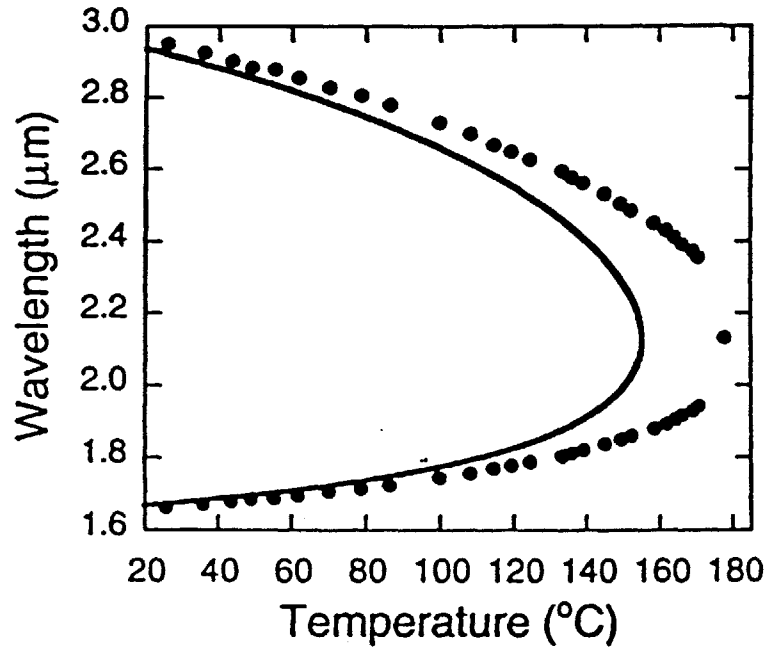


Figure 4-2: Temperature tuning curve for 1064-nm-pumped Q-switched PPLN OPO with a 31- $\mu\text{m}$  grating period. The calculated (solid) curve is based on the Sellmeier's equations and includes thermal expansion. (Myers *et al.*, *Optics Letters* 20(1), pp. 52-54, 1995)

by a combination of grating period tuning and temperature tuning.

The work by Powers *et al.* [33] mentioned in Chapter 2 on the use of a fan-out grating structure to continuously tune the signal and idler output wavelengths offered the possibility of continuous tuning of the OPO outputs without the need for temperature tuning, which tends to be a slow process and does not have the degree of control that the mechanical translation of the crystal along the fan-out grating offers.

The first continuous-wave (cw) OPO using PPLN was demonstrated in 1995 by Myers *et al.* in a nearly degenerate doubly-resonant configuration [50]. CW OPO's are important in applications requiring a narrow-linewidth source that is tunable over a large spectral region covering hundreds of nm to several  $\mu\text{m}$ . Compared to a singly-resonant OPO in which only the signal field is resonated, the doubly-resonant OPO, with both the signal and idler fields resonant, has a much lower threshold that is on the order of tens of mW that can be provided by commercial diode lasers with optical amplifiers. By comparison, singly-resonant OPO's in general have thresholds



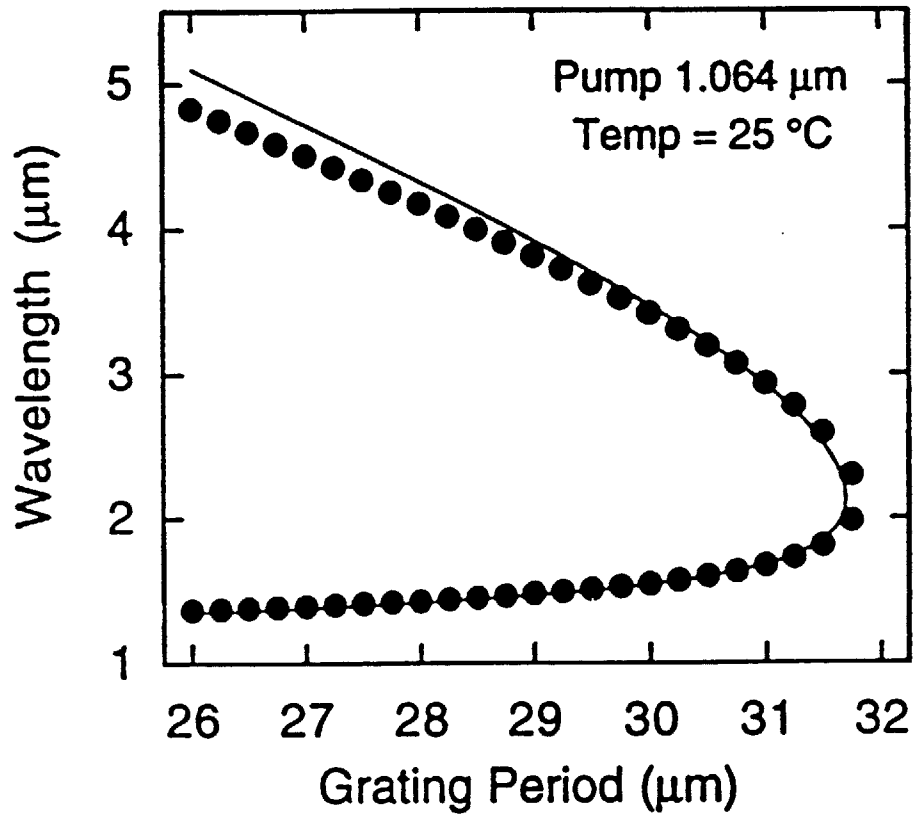


Figure 4-3: OPO tuning curve as a function of grating period for a 1064-nm-pumped Q-switched OPO at room temperature (25°C). The PPLN crystal is translated laterally through 24 different grating sections. The solid curve is calculated from Sellmeier's equations. (Myers *et al.*, *Optics Letters* 21(8), pp. 591-593, 1996)

on the order of 1 W or higher. The grating period of the 9.3-mm-long PPLN sample was  $28.5 \mu\text{m}$ , and the OPO was pumped by a 977.6 nm master oscillator/ power amplifier (MOPA) diode laser. Nearly-degenerate OPO operation with signal and idler wavelengths of 1955.2 nm was demonstrated. With an input power of 370 mW, 64 mW of output signal and idler power was measured.

Further progress in cw QPM OPO was made in 1996 when Myers *et al.* reported a cw singly-resonant OPO pumped by a high-powered Nd:YAG laser at  $\lambda=1064 \text{ nm}$  [51][52]. The grating period was  $\Lambda=29.75 \mu\text{m}$ , and the length of the sample was 50 mm long, suggesting further improvements in the fabrication technology of PPLN. Three different OPO cavity geometries were used: a two-mirror linear cavity, a four-mirror linear cavity, and a four-mirror ring cavity. 93% depletion of the pump power was demonstrated with the four-mirror ring cavity and the four-mirror linear cavity. Of these configurations the two-mirror linear cavity had the lowest threshold at 2.9 W. The two-mirror cavity also achieved a wavelength tuning range of  $3.11 \mu\text{m}$  to  $3.98 \mu\text{m}$  for the idler beam and  $1.45 \mu\text{m}$  to  $1.62 \mu\text{m}$  for the signal beam by using multiple gratings that phasematch different signal-idler pairs for the same pump wavelength. This work demonstrated the potential use of PPLN as a cw widely tunable high-power source.

Schneider *et al.* reported in 1997 a cw 1064-nm-pumped OPO which is resonant at the pump and signal wavelengths [10]. By resonating the pump field inside the OPO cavity, the external threshold power was reduced to 260 mW, compared to the 3.5 W threshold reported by Myers *et al.* in a single-pass pump configuration [52]. Unlike the singly-resonant OPO reported by Myers *et al.* [52] which was pumped by a multi-longitudinal mode laser, the pump source used in Schneider's work was a single-longitudinal-mode laser with good frequency stability. This resulted in a continuous OPO signal tuning range of 2 GHz without mode hops.

Batchko *et al.* reported in 1998 the first cw singly-resonant OPO pumped at 532 nm with signal and idler outputs tunable from 917 nm to 1266 nm [53]. The oscillation threshold was 930 mW internal to the PPLN crystal. This work extended the cw OPO tuning range to the near-IR spectral region. It should be noted that it

took considerably longer to demonstrate a 532-nm-pumped cw singly-resonant PPLN OPO than it did for a 1064-nm-pumped system [51][52]. The key to its successful implementation was the fabrication of a PPLN sample with both the short grating period needed for phasematching ( $\Lambda = 6.5 \mu\text{m}$ ) and the long interaction length (53-mm long grating) needed to obtain sub-watt level of threshold pump power.

One important aspect of the work by Batchko *et al.* involved the finding that at high enough pump power levels absorption of 532-nm pump radiation resulted in thermal lensing and beam-pointing instability of the transmitted pump and idler beams [53]. Such effects were also observed by Turnbull *et al.* [11] in a cw PPLN singly-resonant OPO pumped by an intra-cavity Ti:Sapphire laser with the intra-cavity laser power clamped at the OPO threshold of 8.8 W. Furthermore, Batchko *et al.* also reported that the 532-nm pump radiation induced absorption loss in the IR which resulted in increased pump threshold power [53].

Singly-resonant cw and Q-switched OPO in PPLN waveguide devices have also been demonstrated recently. Compared to bulk devices, waveguide devices offer the advantages of much higher conversion efficiencies as the interacting fields are tightly confined to the waveguide modes over long interaction lengths. However, waveguide devices require additional processing steps for patterning and fabricating the waveguides, and also suffer from the fact that single mode operation at the longer wavelength fields most often means that the shorter wavelength fields are multi-moded, thereby decreasing the overall conversion efficiency. The first QPM OPO in waveguide geometry was demonstrated in 1995 by Fejer *et al.* [54]. In that work the domain reversal was accomplished by the use of titanium in-diffusion.

## 4.5 Devices Based On Other Periodically-Poled Materials

By far most of the bulk QPM device demonstrations in recent years have been based on PPLN. As discussed in Chapter 3, the prevalence of the use of  $\text{LiNbO}_3$  as the

nonlinear material was due to its high nonlinearity, wide availability, low substrate cost, and the fact that its material properties have been extensively characterized such that accurate Sellmeier's coefficients are available to predict its phasematching behavior. However,  $\text{LiNbO}_3$  is not without its own problems and limitations. First, in SHG applications  $\text{LiNbO}_3$  is susceptible to photorefractive damage at visible and ultraviolet wavelengths even at second harmonic power levels of only a few mW. Photorefractive damage can be much reduced by operation at elevated temperatures, which may be an inconvenience for many applications in which room temperature operation is preferred. Second, the poling of  $\text{LiNbO}_3$  requires a high coercive field of 21 kV/mm, and practical devices have been limited to thicknesses of 1 mm, which may be insufficient for high-energy pulsed operations, as discussed by Missey *et al.* [55]. Finally, the power scaling of pump power for PPLN is limited by deleterious thermal effects such as thermal lensing and beam pointing instabilities for both up-conversion (i.e., SHG and SFG) [47] as well for down-conversion (i.e., DFG, OPA, and OPO) [11][53] interactions at several watts of continuous-wave pump power levels. These effects tend to defocus the pump beam and cause other instabilities that lower the conversion efficiency.

For the reasons mentioned above there has been growing interest in exploring other periodically-poled materials. To date periodical poling has been successfully achieved in lithium tantalate ( $\text{LiTaO}_3$ ), potassium titanyl phosphate (KTP), and rubidium titanyl arsenate (RTA).

#### 4.5.1 Periodically-poled $\text{LiTaO}_3$

$\text{LiTaO}_3$  is an isomorph of  $\text{LiNbO}_3$ . Prior to the advent of electric field poling technique,  $\text{LiTaO}_3$  was primarily used as electro-optic modulators but not for nonlinear frequency mixing because it does not have the proper amount of birefringence for birefringent phasematching over its transparency range, despite the fact that it has a reasonably large  $d_{33}$  nonlinear coefficient. The advent of periodical poling techniques made possible the use of quasi-phasematched  $\text{LiTaO}_3$  for efficient nonlinear optical frequency conversion.  $\text{LiTaO}_3$  has a coercive field of 25 kV/mm, similar to

the coercive field of 21 kV/mm for LiNbO<sub>3</sub>.

LiTaO<sub>3</sub> holds a few advantages over LiNbO<sub>3</sub> in short wavelength applications. LiTaO<sub>3</sub> has a transparency range that extends further into the ultraviolet than does LiNbO<sub>3</sub>. The transparency cut-off wavelength for LiTaO<sub>3</sub> is 280 nm, compared to 330 nm for LiNbO<sub>3</sub> [56]. This makes LiTaO<sub>3</sub> a better candidate for QPM second harmonic generation of ultraviolet radiation. The refractive index dispersion relationship for LiTaO<sub>3</sub> is similar to that for LiNbO<sub>3</sub> which requires very short grating periods for generating visible and ultraviolet light through frequency doubling. However, the propensity of the reversed ferroelectric domains to spread laterally is somewhat less than in LiNbO<sub>3</sub>, which allows the fabrication of grating periods as short as 1.7 μm [57].

One of the disadvantages of LiTaO<sub>3</sub> compared to LiNbO<sub>3</sub> is the fact that the  $d_{33}$  coefficient of 13.8 pm/V for SHG of 1064 nm, although large compared to the  $d_{33}$  coefficient of most other nonlinear materials, is a factor of 2 lower than that for LiNbO<sub>3</sub> of 27 pm/V [57]. Another disadvantage is that an accurate Sellmeier's equations for the wavelength and temperature dependence of the refractive index of LiTaO<sub>3</sub> were not available until recently [56]. In addition, the cost of LiTaO<sub>3</sub> remains high and it is not as readily available compared to that for LiNbO<sub>3</sub>. These factors have contributed to limit the widespread use of LiTaO<sub>3</sub> in nonlinear optical devices. But nevertheless, quasi-phasematched interactions such as SHG and OPO that have previously been demonstrated in PPLN have also been accomplished in periodically-poled LiTaO<sub>3</sub> (PPLT) as well.

The first nonlinear optical device based on PPLT was demonstrated in 1995 by Mizuuchi *et al.* [58] in which blue radiation at 425 nm was generated via frequency doubling of a Ti:Sapphire laser output in PPLT with a grating period of 3.8 μm. Mizuuchi *et al.* then reported, in 1997, generation of ultraviolet radiation at 342 nm by frequency doubling a red diode laser output in PPLT with a first-order grating period of 1.7 μm [57]. A Sellmeier's equation based on SHG experiments using PPLT at a number of wavelengths combined with refractive index data in literature was published by Meyn *et al.* in 1997 [56]. Based on this Sellmeier's equation, Klein *et al.*

demonstrated the first PPLT-based cw OPO. The pump- and signal-resonant OPO was pumped by an InGaAs MOPA diode laser with signal and idler outputs that were tunable from 1.55  $\mu\text{m}$  to 2.3  $\mu\text{m}$  by use of multiple parallel grating periods ranging from 27.3  $\mu\text{m}$  to 27.9  $\mu\text{m}$  and by temperature tuning [59]. The lowest threshold pump power achieved was 360 mW as a result of resonating the pump. An interesting feature from this work was the operation of the OPO at a pump wavelength where the nearly degenerate signal and idler wavelengths coincide with the wavelength where the second derivative of the index of refraction is zero, thus resulting in an extremely wide phasematching bandwidth, with a temperature tuning coefficient of 25.5 nm/ $^{\circ}\text{C}$  for the signal and idler output wavelengths.

#### 4.5.2 Periodically-poled KTP and RTA

Periodic poling of potassium titanyl phosphate (KTP) and rubidium titanyl arsenate (RTA) have also attracted attention as an alternative to PPLN for two main reasons. First as mentioned before, PPLN is prone to photorefractive damage at visible wavelengths unless it is operated at elevated temperatures and to thermal lensing effects at very high pump powers. KTP and RTA are known to be less susceptible to photorefractive damage at visible wavelengths and have also been shown to be much less susceptible to thermal lensing problems compared to PPLN. Second, the coercive field for poling KTP (2.6 kV/mm) and RTA (2 kV/mm) are about an order of magnitude lower than the 21 kV/mm coercive field for PPLN, which makes them much easier to pole. The disadvantages of KTP and RTA are their comparatively small  $d_{33}$  nonlinear coefficient compared to PPLN, their high material cost, and their low availability.

Successful fabrication of periodically-poled KTP and RTA crystals along with demonstration of second harmonic generation of visible blue radiation have been accomplished by several groups [60][61][62][63]. The greater transmission of RTA in the 4-5  $\mu\text{m}$  spectral region also makes it a suitable candidate for tunable mid-IR source by DFG or OPO. Reid *et al.* demonstrated the first OPO based on RTA pumped by a femtosecond self-mode-locked Ti:sapphire laser, generating femtosecond outputs that

could be temperature tuned from 1060 nm to 1225 nm (signal) and 2.67  $\mu\text{m}$  to 4.5  $\mu\text{m}$  (idler) using a QPM grating with a period of 30  $\mu\text{m}$  [64]. Subsequently, Edwards *et al.* reported the first continuous-wave OPO based on periodically poled RTA [65]. The singly-resonant OPO is located within a Ti-Sapphire laser cavity because of the high oscillation threshold of 15 W due to the limited interaction length of available PPRTA and lower nonlinearity compared to PPLN. The OPO was tuned from 1.13 to 1.27  $\mu\text{m}$  (signal) and 2.53 to 3.26  $\mu\text{m}$  (idler) by tuning the wavelength of the Ti:Sapphire pump laser. One important find of this work was the drastically reduced thermal lensing effects compared to a similar setup using PPLN [11].

# Chapter 5

## The Master Oscillator/ Power Amplifier Diode Laser System

This chapter provides a detailed review of the assembly and operation of the master oscillator/ power amplifier (MOPA) diode laser system that was employed as the pump laser source for both the 3-to-1 optical frequency division experiment and the 2-to-1 Brewster-angle OPO experiment discussed in Chapters 6 and 7, respectively.

Section 5.1 discusses the various requirements the pump laser must satisfy for the experiments. Section 5.2 briefly reviews the diode laser and discusses its relative merits. A full discussion of the extended-cavity master diode laser is provided in Section 5.3, while the power amplifier (slave laser) is discussed in Section 5.4.

### 5.1 Introduction

For the work described in this thesis, there are stringent demands on the pump laser system. The primary requirements are:

1. For frequency metrology applications, the spectral purity of the pump laser must be high, often with frequency uncertainties on the order of 1 kHz or less. Although such ultra-stable frequency lasers are not strictly necessary for our 3-to-1 frequency division demonstration, we nevertheless demand that our lasers have single longitudinal mode output and spectral linewidths on the order of 1 MHz or less such



that one may easily reduce the linewidth by electronic servo controls.

2. The laser must be continuously tunable. Since the 3:1 frequency division experiment discussed in the next chapter involves tuning the laser frequency to an exact fraction ( $2/3$ ) of another reference laser frequency and stabilizing the beat signal between the two lasers to within a 1-GHz detection bandwidth, the laser should be continuously tunable over a range such that the beat signal can be continuously tuned over 1 GHz. This requires that the laser frequency be continuously tunable over at least  $\sim 300$  MHz, since the beat note frequency is 3 times the frequency difference  $\delta$  between the laser frequency and  $2/3$  of the reference laser frequency.

3. The laser must have sufficient output power. High pump power is a necessary requirement for nonlinear optical frequency mixing experiments because the distributed nonlinearity over the typical length of a nonlinear crystal is usually quite weak. For practical nonlinear optical devices such as optical parametric oscillators, the threshold pump power range from a few tens of mW for doubly-resonant OPO's to a few W for singly-resonant OPO's. For 3:1 frequency division experiment discussed in the following chapter where we employ two consecutive difference-frequency generation (DFG) processes, the need for a high pump power is even more crucial since the converted outputs are typically 3 to 4 orders of magnitude lower in power compared to the pump. Since our laser serves as the pump laser for the doubly-resonant OPO discussed in Chapter 7, we demand that our laser can produce at least 100 mW of useful pump power going into the nonlinear crystals.

4. The laser must have good mode quality. In many applications requiring mode-matching the laser beam into an optical resonator such as an optical parametric oscillator, the eigenmodes of the resonator are Gaussian beams. Such devices act as a filter allowing lossless transmission for only the lowest order Gaussian mode ( $TEM_{00}$ ). It is thus highly desirable that the mode structure of the laser beam comprises predominantly of the  $TEM_{00}$  Gaussian mode. Furthermore, many laser beam parameters such as the beam diameter, radius of curvature, and beam waist, assumes a  $TEM_{00}$  Gaussian beam profile, which makes the analysis of the beam profiles much less complicated if the laser mode were a  $TEM_{00}$  Gaussian beam.

5. The laser should be compact and efficient.

## 5.2 Background

Diode lasers are prevalent in many applications because of their well known attributes: high reliability, miniature size, relative simplicity of use, and relatively low cost. In addition to commercial applications such as bar-code scanners, CD player, and communications lasers, diode lasers are also attractive candidates for use in scientific applications because of their unique capabilities such as tunability, high efficiency, useful power levels, reasonable coherence, and good modulation capabilities.

A diode laser wavelength is determined by the semiconductor material and structure, and is a function of both temperature and the injected carrier density. In a typical single-mode laser the wavelength increases monotonically with increasing temperature and then suddenly jumps to another mode at a longer wavelength with a typical mode spacing of 0.3 nm [66]. The typical temperature tuning coefficient for AlGaAs lasers, which is the type used in our experiments, is about 30 GHz/°C. The diode laser wavelength is also a function of the injection current of the diode laser, which also controls the laser output power. Typical tuning of a AlGaAs laser as a function of injection current is about 3 GHz/mA. Operating a diode laser at a precise wavelength such as an atomic or molecular transition usually requires iterative selection of injection current and temperature settings. However, for any given laser, the optimum tuning to a specific wavelength can never be guaranteed. One alternative is to use optical feedback techniques to control the wavelength of the laser. An extended-cavity diode laser is one type of diode laser which allows tuning of the diode laser to any wavelength within the bandwidth of the gain medium.

Output powers of typical single-frequency near-IR diode lasers are in the tens of mW range, which may be insufficient for applications requiring single-longitudinal-mode high-power lasers. To overcome the power deficiency, one may use the diode laser to injection lock a semiconductor optical amplifier with typical output powers on the order of a few hundred mW to a few W. Such a system is called a master

oscillator/ power amplifier (MOPA) diode laser system. The master oscillator and the power amplifier are typically referred to as the master and slave laser, respectively.

## 5.3 The Master Laser

This section provides a description of the operating principles of the extended-cavity diode laser and the associated electronics such as the current source and the thermoelectric cooler.

### 5.3.1 Operating principle

Tuning the wavelength of diode lasers and narrowing their linewidths can be accomplished using some form of dispersive optical feedback. Distributed feedback (DFB) and distributed Bragg reflector (DBR) lasers are diode lasers with wavelength-selective feedback elements integrated in the semiconductor material. Such lasers are also effective in narrowing the linewidth of the diode laser. Another type of diode laser with wavelength-selective capability is the extended cavity diode laser (ECDL). ECDL's can be constructed using many configurations. The particular type of ECDL used in this work employs the Littmann configuration, whose geometry is shown in Fig. 5-1. The output of a collimated diode laser output is reflected off a diffraction grating near grazing incidence. The diffracted output beam is retro-reflected and returned to the diode laser, providing feedback which can be used to tune the wavelength of the diode laser. The master grating relationship is given as [67]

$$\lambda = \frac{\Lambda_g}{m}(\sin \theta_0 + \sin \phi) \quad (5.1)$$

Here  $\lambda$  is the wavelength,  $\Lambda_g$  is the period of the diffraction grating,  $\theta_0$  is the incident angle, and  $\phi$  is the diffraction angle which also corresponds to the tuning angle of the tuning mirror about the pivot point. Tuning of the ECDL wavelength can be achieved by rotating the tuning mirror around the pivot as shown in Fig. 5-1, as this changes the feedback angle  $\phi$  at which the resonance condition is achieved. The laser

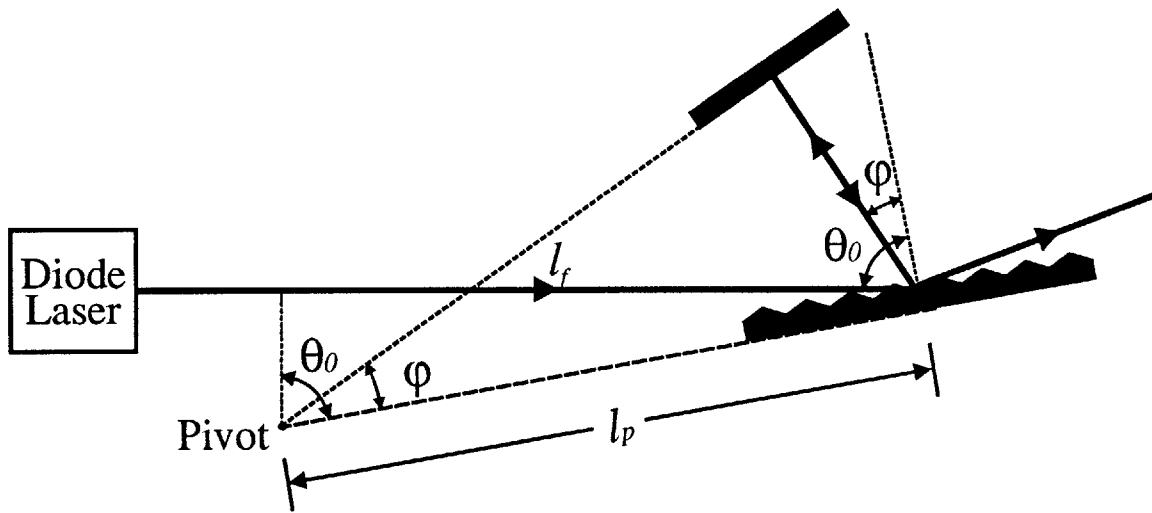


Figure 5-1: Extended-cavity diode laser (ECDL) in the Littmann configuration.  $\theta_0$  is the angle of incidence at the diffraction grating;  $\phi$  is the diffracted angle;  $l_d$  is the distance from the diode laser output to the grating; and  $l_p$  is the distance from the pivot point to the grating.

wavelength will adjust in such a way that the diffraction angle will coincide with the new feedback angle required for resonance.

In principle, the ECDL can be designed to achieve continuous single longitudinal mode tuning over many nm by synchronizing the tuning of the extended cavity length with the tuning of the feedback angle such that the cavity output remains in the same longitudinal mode during the course of the scan. Mathematically, we require that the cavity length corresponds to an integral number of half-wavelengths:

$$\lambda = \frac{2}{N} [l_f + l_p \sin(\phi)] \quad (5.2)$$

Here  $l_f$  is the distance from the back facet of the diode laser to the diffraction grating and  $l_p$  is the distance from the pivot point to the diffraction grating, as shown in Fig. 5-1.

Solving for  $l_f$  and  $l_p$  using Eqs. (5.1) and (5.2) gives the following conditions for single-mode tuning [67]:

$$l_f = \frac{N\Lambda_g}{2m} \sin(\theta_0) \quad (5.3)$$

$$l_p = \frac{N\Lambda_g}{2m} \quad (5.4)$$

Our ECDL design did not involve synchronizing the tuning of the ECDL's cavity length to the tuning of the feedback angle, as governed by Eqs (5.3) and (5.4). This resulted in limited tunability and mode hops for the cavity output.

ECDL designs that employ relatively high optical feedback power can have a large tuning range and be very stable. The overall tuning ranges can be as large as the gain bandwidth of the diode laser itself. Another important feature of ECDLs is their narrow linewidths. ECDLs have fast linewidths on the order of 50 kHz as opposed to a few tens of MHz for ordinary diode lasers.

### 5.3.2 Physical layout

The extended cavity diode laser used in this work is based on a design from the National Institute of Standards and Technology (NIST) [66]. For stable single longitudinal mode operation it is important that the ECDL be well isolated from mechanical vibrations, pressure fluctuations, and also temperature variations. Thus it is important to have a design that provides good mechanical and thermal stability. Our ECDL is enclosed inside a 12 cm long, 6 cm wide, and 4 cm deep copper enclosure. A copper base plate which rests inside the copper enclosure serves both as a rigid mount for the laser resonator and as the heat sink for the temperature control system. Figure 5-2 shows a schematic of the ECDL construction. The laser diode is mounted in a copper fixture that bridges the TE cooler and attaches to a copper laser base mount. The base mount is then rigidly attached to one end of the copper baseplate. A collimating lens is connected to the laser base mount by a stiff spring-steel flexure that is clamped in place after initial coarse alignment. An eccentric on the lens mount is used to adjust the vertical height of the collimated laser beam. The horizontal position of the laser is set by the transverse displacement of the laser on the base mount. Critical adjustment of the focus is done with a high quality fine-pitched screw that translates the lens against the restoring force provided by the flexure.

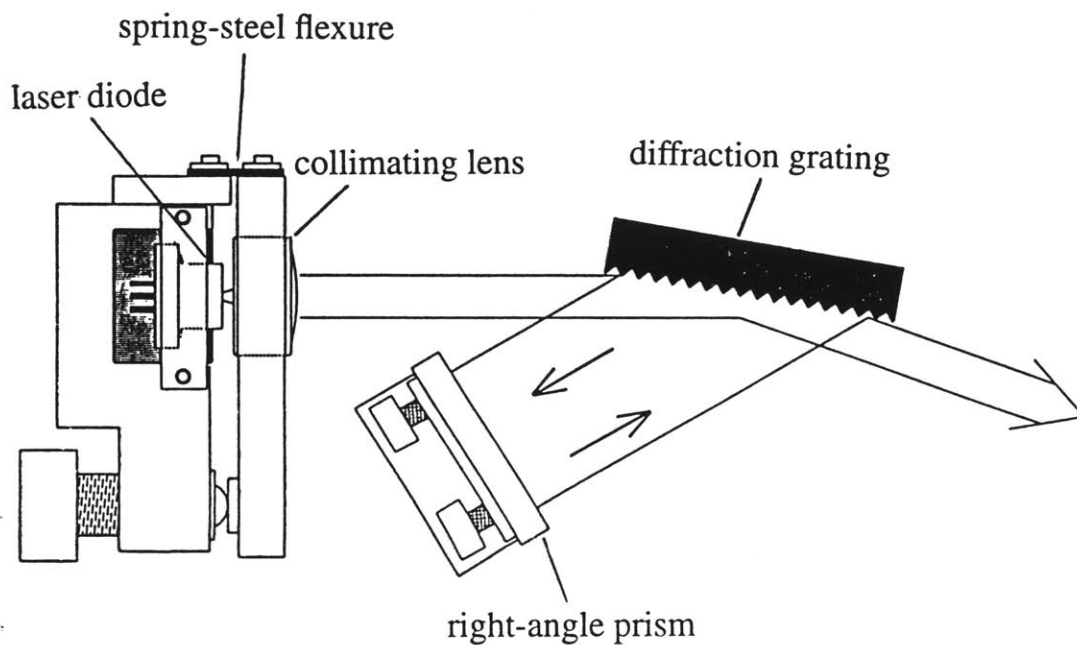


Figure 5-2: Schematic of ECDL construction. The laser diode is mounted in a copper fixture that bridges the TE cooler (not shown) and attaches to a copper base mount (not shown). A collimating lens is connected to the laser base mount by a stiff spring-steel flexure that is clamped in place after initial coarse alignment. The laser's output such that the beam is collimated over several meters. A diffraction grating is positioned such that the first-order diffracted beam reflects off a right-angle prism and returns to the laser via the diffraction grating.

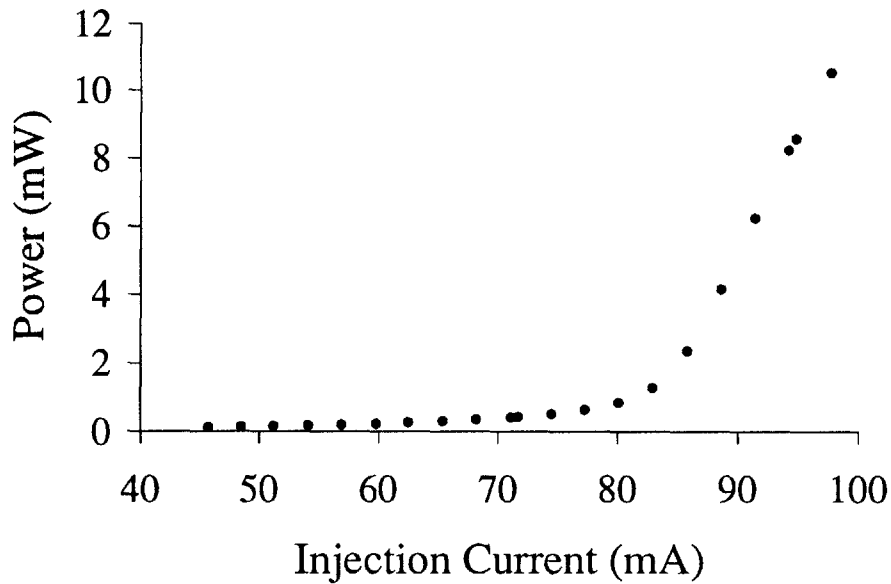


Figure 5-3: Output power vs. injection current of AR-coated Sharp LT017 laser diode.

### 5.3.3 Current control

The current source used in our ECDL is a NIST-designed system whose operation is based on a summing amplifier which balances the voltage drop across a sense resistor with a voltage supplied by a precision variable voltage source [66]. The current control system not only provides the necessary current to drive the laser but also includes protection circuitry located at the laser mount inside the copper enclosure to protect against power shutdown, electrostatic discharge, and excessive drive current. Our laser diode is a Sharp LT017 laser diode with a nominal output wavelength of 804 nm and a maximum output power of 50 mW. Figure 5-3 shows a plot of the injection current vs. output power of the Sharp LT017 laser diode. In addition, the current source also contains input ports which can be used to modulate and servo-control the diode laser output.

### 5.3.4 Temperature control

Since the diode laser frequency is temperature sensitive, it is also necessary to stabilize the diode laser temperature. Figure 5-4 shows a simplified schematic of the temper-

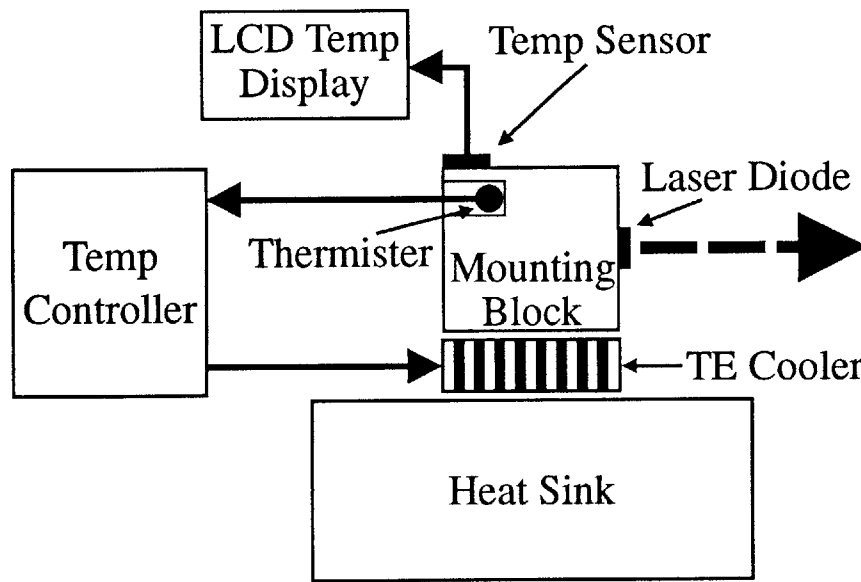


Figure 5-4: Schematic of temperature control system. The laser diode is mounted in a copper block which sits on a TE cooler. The temperature controller compared the user-defined temperature setting with the temperature sensed by a thermistor embedded in the copper block and generates an error signal which controls the TE cooler. A separate temperature sensor mounted on the copper block is used to control the LCD temperature display.

ature control system. The laser diode is mounted in a copper block which sits on a thermoelectric (TE) cooler. A thermistor which resides in the copper block senses the temperature of the copper block (and thus the temperature of the laser diode) and an error signal is generated by comparing the temperature sensed by the thermistor with the user-defined operating temperature. The error signal is then conditioned and fed to the TE cooler which either heats or cools the copper block until the preset temperature is reached. A separate temperature sensor mounted on the copper block produces a temperature-sensitive current signal which is then displayed on the LCD front panel. Typically the temperature of the diode laser is set at a nominal value of  $18^{\circ}\text{C}$  with a temperature stability of  $\pm 0.1^{\circ}\text{C}$ .



### 5.3.5 Alignment and tuning

As illustrated in Fig. 5-2, a collimating lens is centered on the laser's output such that the beam is collimated over a distance of several meters. A Spectrogen diffraction grating with 1800 grooves/mm is positioned such that the first-order diffracted beam reflects off a right-angle prism and returns to the laser via the diffraction grating. The right-angle prism is mounted on a 1-inch Lees mirror mount, which is used to fine-tune the alignment. With the diode laser current set at a level slightly below threshold ( $\sim 60$  mA), the diode laser injection current is modulated with a triangular current ramp. The Fresnel-reflected beam from the diffraction grating is reflected by a high reflector and exits the diode laser box through an AR-coated optical window and then detected by a large-area silicon photodetector. The detected signal is monitored on an oscilloscope synchronized to the triangular ramp wave. With the coarse alignment complete, one needs to adjust both the collimating lens and the alignment of the returned beam to the laser diode until evidence of feedback is observed. With no feedback from the extended cavity, the detected output waveform will show a classic diode laser power vs. intensity (P vs. I) curve as shown in curve A of Fig. 5-5. With feedback from the extended cavity, abrupt and discontinuous changes in the threshold behavior will give an output waveform as shown in curve B of Fig. 5-5. Under optimal alignment one expects to see a clean output signal from the detector, as shown in curve C of Fig. 5-5, which reproduces the modulating triangular wave.

Figure 5-6 shows plots of injection current vs. output power for the Fresnel-reflected beam from the grating with and without feedback to the laser diode. Without any feedback to the laser diode, the output power has a threshold current of about 80 mA. With the extended cavity in optimal alignment, the threshold is reduced to about 60 mA. Note that the maximum Fresnel-reflected output power from the extended cavity diode laser remains less than that of the direct laser diode output in Fig. 5-3. We typically operate the master laser at a current level at which the output power is saturated at around 6 mW. A typical driving current is 106 mA, with a current stability of  $\pm 1$  mA.

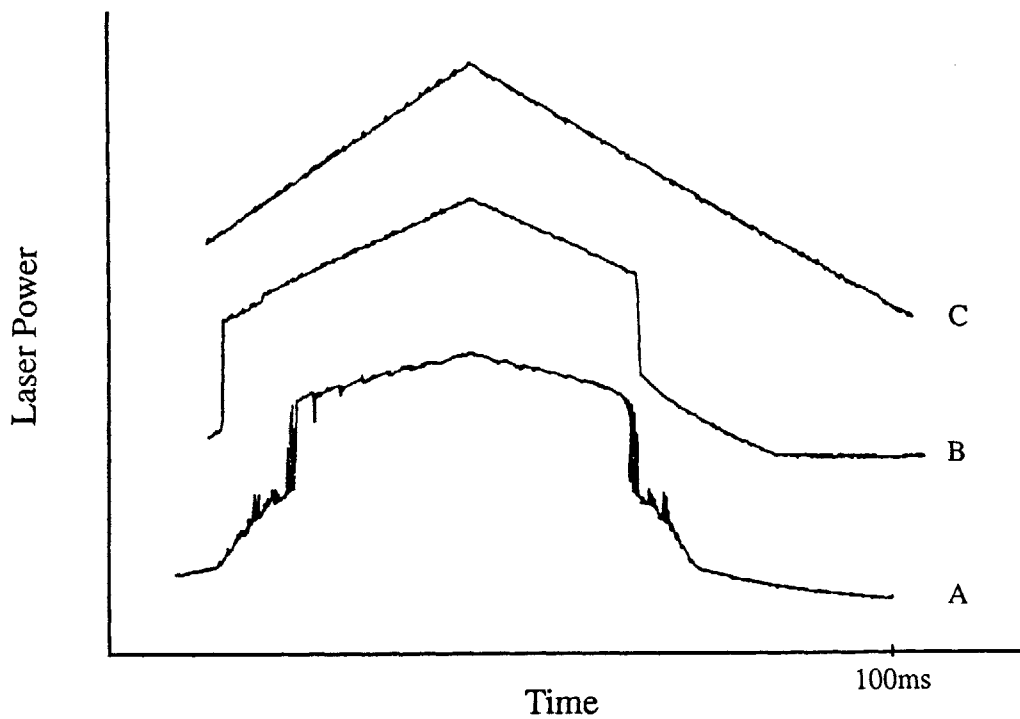


Figure 5-5: Diode laser power vs. injection current. The diode laser injection current set slightly below threshold and then modulated with a triangular current ramp. With no feedback from the extended cavity the detected output waveform is shown in trace A. The output waveform with feedback from the extended cavity is shown in trace B. The output waveform with optimal alignment is shown in trace C, where the output waveform reproduces the modulating triangular wave.

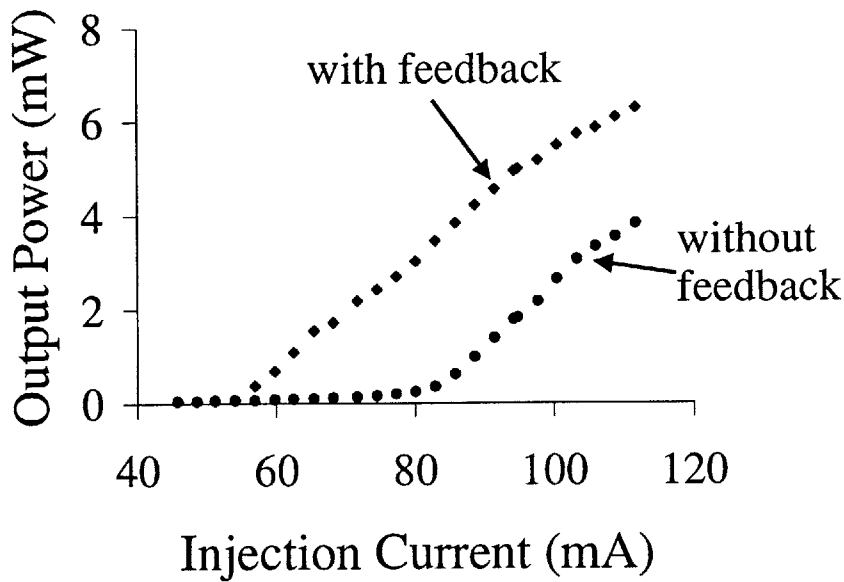


Figure 5-6: Plot of output power vs. injection current of AR-coated LTO17 laser diode in extended cavity configuration. The power measurement is taken for the Fresnel-reflected beam from the diffraction grating with and without feedback to the laser diode.

In order for the ECDL to operate in a stable manner, sufficient optical feedback must be returned to the diode laser waveguide mode. With insufficient optical feedback, there will be discontinuities in the ECDL wavelength tuning range in which the diode laser operates at its chip wavelength. The amount of optical feedback is controlled by the amount of power diffracted from the diffraction grating. In general, one may increase the amount of feedback from the diffraction grating by decreasing the angle of incidence away from grazing incidence at the expense of reducing the output power of the Fresnel-reflected output beam. Therefore, there is a tradeoff between output power and stability. A good rule-of-thumb is that the diffraction grating should be set such that the diffracted spot size fills roughly 1/3 of the total grating area that is 50 mm long and 12 mm wide. In our laser system, the maximum output power in the extended cavity configuration is roughly 6 mW, while the maximum output power in a straightforward emission from the laser diode easily exceeds 25 mW. Fortunately, the 6 mW of output power available from the master laser is sufficient to injection lock the slave laser, as will be discussed in Section 5.4.

The front facet of the diode laser must be anti-reflection coated such that its reflectance is on the order of  $10^{-3}$  or less. Under such conditions the maximum wavelength tuning range can be as large as the gain curve of the lasing material, which is approximately  $\pm 20$  nm for AlGaAs lasers. The laser diodes used in our system were coated at NIST. The resulting ECDL tuning range was approximately 15 nm (785 nm – 800 nm).

Coarse tuning of the ECDL wavelength is accomplished by turning the knob on the LEES mirror mount on which the right-angle prism is mounted. This adjusts the diffraction angle from the grating and therefore changes the output wavelength. A piezoelectric transducer (PZT) is inserted into the mirror mount for even finer wavelength tuning. However, note that as we adjust the mirror mount the ECDL cavity length also changes, which normally leads to mode hops unless care is taken to design the ECDL in such a way that the tuning of the extended cavity length is synchronized with the tuning of the feedback angle from the diffraction grating. Our ECDL could be continuously tuned over 100 MHz with a gap of  $\sim 150$  MHz between adjacent continuously tunable frequency regions.

Due to the rectangular dimensions of the active region, the output beam of the diode laser had an elliptical intensity profile with approximately a 3-to-1 aspect ratio between the vertical and horizontal dimensions. The ECDL frequency linewidth was determined to be  $\leq 430$  kHz, limited by the measurement resolution of the high-finesse Fabry-Perot cavity. The intrinsic linewidth of the ECDL is expected to be less than 50 kHz [66].

## 5.4 The Slave Laser

This section provides a general description of the operating principles of the SDL 8630-E power amplifier which is injection-locked by the master laser. The main associated electronics such as the current source and thermoelectric coolers will also be discussed.

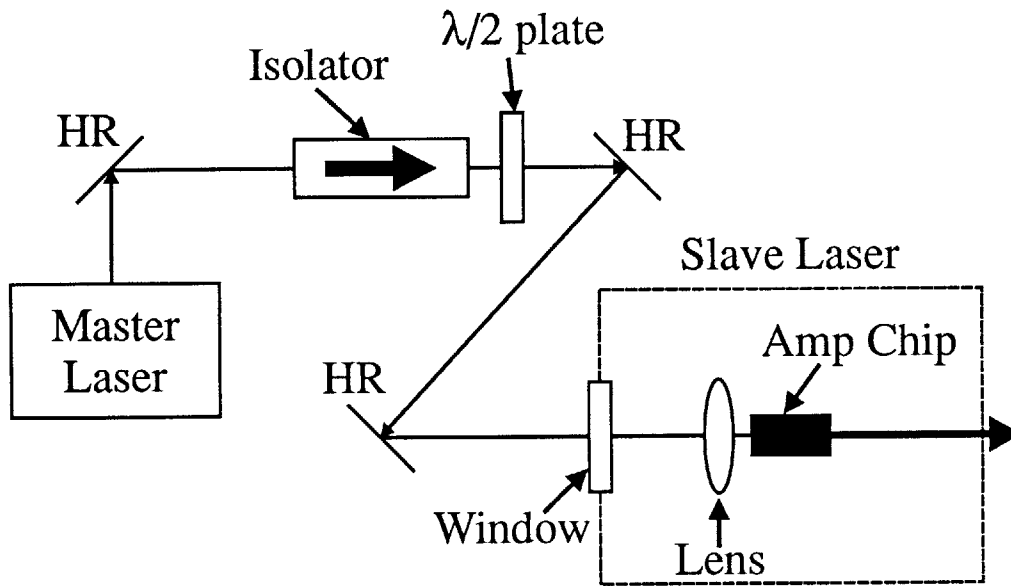


Figure 5-7: Setup for injection locking the slave laser by the master laser.

### 5.4.1 Operating principles

The purpose of the power amplifier is to produce a high-power laser beam that preserves the essential characteristics of the master laser, i.e. the wavelength and the spectral linewidth. Operating by itself, the power amplifier emits a broadband emission centered around the center of its gain curve. The power amplifier chip emits in both directions, with the majority of the power emitting from the front surface. To have the power amplifier reproduce the wavelength and spectral purity of the master laser, it is necessary to mode-match the master laser output into the power amplifier chip. Figure 5-7 shows a schematic of the setup for injection locking the power amplifier by the master laser. The master laser output is steered by three high reflectors into the power amplifier chip. An optical isolator is used to prevent the backward emission from the power amplifier from entering the master laser. A collimating lens at the back of the power amplifier chip is used to collimate the backward emission from the power amplifier chip as well as acting as a mode-matching lens for the injected master laser beam. Mode-matching between the master laser and the power amplifier requires overlapping the master laser beam profile with the backward propagating power amplifier beam profile. This requires the use of the mirror mount

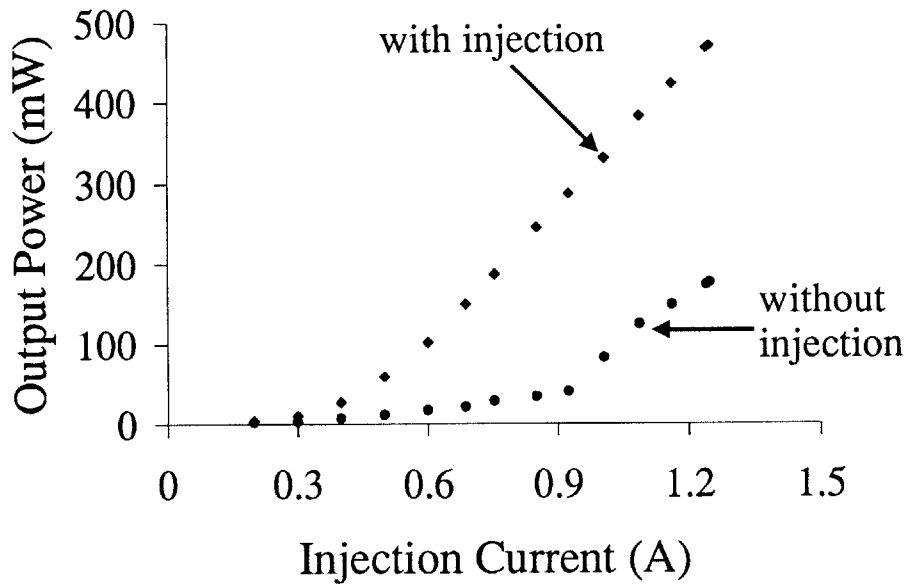


Figure 5-8: Output power vs. injection current for slave laser with and without injection from the master diode laser. The output emission wavelength, set by the master diode laser, is 790.0 nm. The temperature of the amplifier chip is 23°C.

controls to adjust the relative alignment between the two beams as well as adjustment of the collimating lenses for both lasers. By monitoring the front emission from the power amplifier using a silicon photodetector, one observes a sharp increase in output power when the two lasers are well aligned and mode-matched.

The output power of the slave laser is a function of both the injected power from the master laser and the injection current of the slave laser itself. Everything else being equal, the output power of the power amplifier saturates at a few mW of the injected master laser power. In general, the output power of the master diode laser is set at a level at which the slave laser output power saturates. The output power of the slave laser also saturates as a function of its own injection current. For our particular power amplifier chip the output power saturates at approximately 1300 mA of injection current. Figure 5-8 shows a plot of the output power of the slave laser as a function of injection current with and without injection from the master laser. The slave laser can generate a maximum output power of 490 mW at 790 nm, the center of the gain curve of the amplifier medium. The maximum output power decreases as the wavelength is tuned away from the center of the gain curve, dropping to 380

mW at 796.5 nm and to 280 mW at 798 nm. Figure 5-9 shows the manufacturer's measurement of the output power of the tapered amplifier emission without injection as a function of wavelength. The maximum output power drops off significantly at 797 nm compared to at its peak at 790 nm.

### 5.4.2 Current source and TE cooler

Just as in the case for the master ECDL laser, the power amplifier also contains a current source to control the injection current to the slave laser and a thermoelectric (TE) cooler for maintaining the chip temperature. The current source and the TE cooler are integrated in an ILX Lightwave LDC-3742B current source/temperature controller. The temperature of the power amplifier chip is monitored by a thermistor located inside the copper block on which the amplifier chip is mounted. Whereas in the master diode laser a TE cooler is sufficient to regulate the temperature of the laser diode, in the power amplifier the TE cooler alone was not sufficient to dissipate the heat generated by the power amplifier, necessitating the use of water cooling. Typically the temperature of the power amplifier chip is maintained at a nominal temperature of 23°C with a long-term ( $\leq 1$  hour) temperature stability of  $\pm 0.05^\circ\text{C}$ .

### 5.4.3 Astigmatism compensation

Because of the highly rectangular dimensions of the active region of the power amplifier, the output of the slave laser is highly elliptical and astigmatic. Figure 5-10 illustrates the optics necessary to collimate the output beam of the slave laser. A collimating lens with  $f = 2.5$  cm is positioned in front of the laser facet to collimate the output beam profile along the vertical axis. The output beam then exits the slave laser box through an AR-coated optical window. The beam is propagated until the horizontal component of the beam expands to the same size as the vertical component. A cylindrical lens with  $f = 30$  cm was then placed to collimate the horizontal component of laser beam. A spherical lens with  $f = 100$  cm was then used to focus the collimated laser beam through an optical isolator.

SDL 8630-E MOPA chip S/N: TD184  
Output Powers at Fixed Drive Current

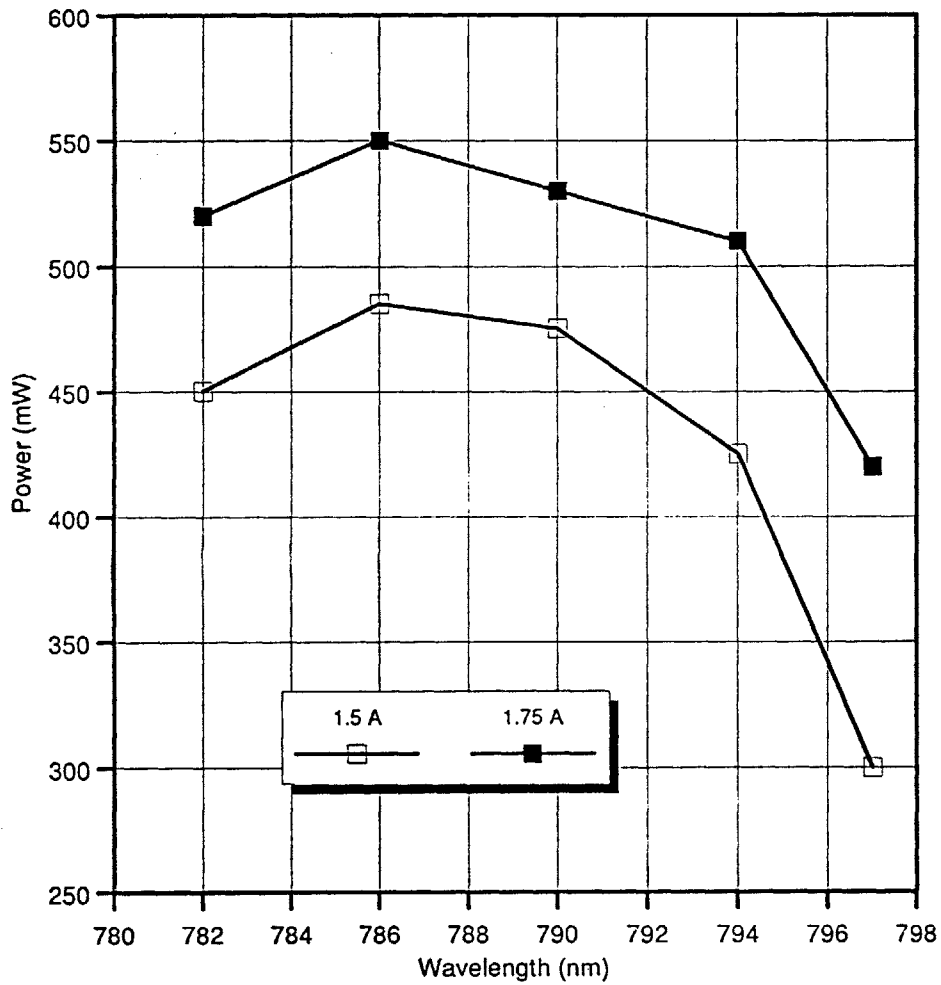


Figure 5-9: Output power vs. emission wavelength for slave laser at fixed injection current settings. The measurements were taken by the manufacturer prior to delivery.



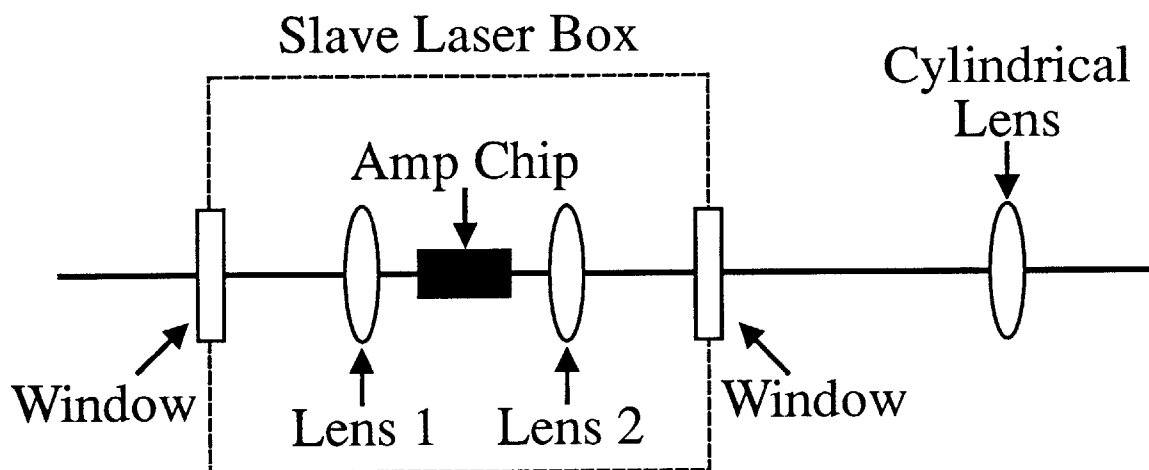


Figure 5-10: Collimation of slave laser output. The highly astigmatic output beam profile of the slave laser requires the use of cylindrical optics. Spherical lens (1 and 2) with  $f = 2.5$  cm collimates the input beam and the vertical component of the output beam. The horizontal component of the output beam is collimated by a cylindrical lens with  $f = 30$  cm.

#### 5.4.4 Laser output

Measurements of the laser beam profile using a beam profiler shows that the laser output is still somewhat astigmatic. The beam parameter of the laser beam after the 100 cm focusing lens has a vertical confocal parameter of  $b = 6.27$  cm but a horizontal confocal parameter of  $b = 12.30$  cm. The astigmatism of the laser output, although not a desirable characteristic, can be more or less compensated with either a cylindrical lens or a curved mirror to produce a circular beam profile.

A more disturbing behavior of the slave laser output is the distortion of the beam profile at a distance away from the beam waist. Figures 5-11 (a)–(d) and Figs. 5-12 (a) and (b) illustrate the beam profiles at various distances away from the beam waist.

The beam distortion suggests that the slave laser contains higher-order Gaussian modes in addition to the main  $TEM_{00}$  mode. The existence of higher-order modes effectively reduces the useful laser output power in applications requiring the coupling of the laser beam into an optical resonator such as an OPO, where higher-order modes are not supported by the resonator.

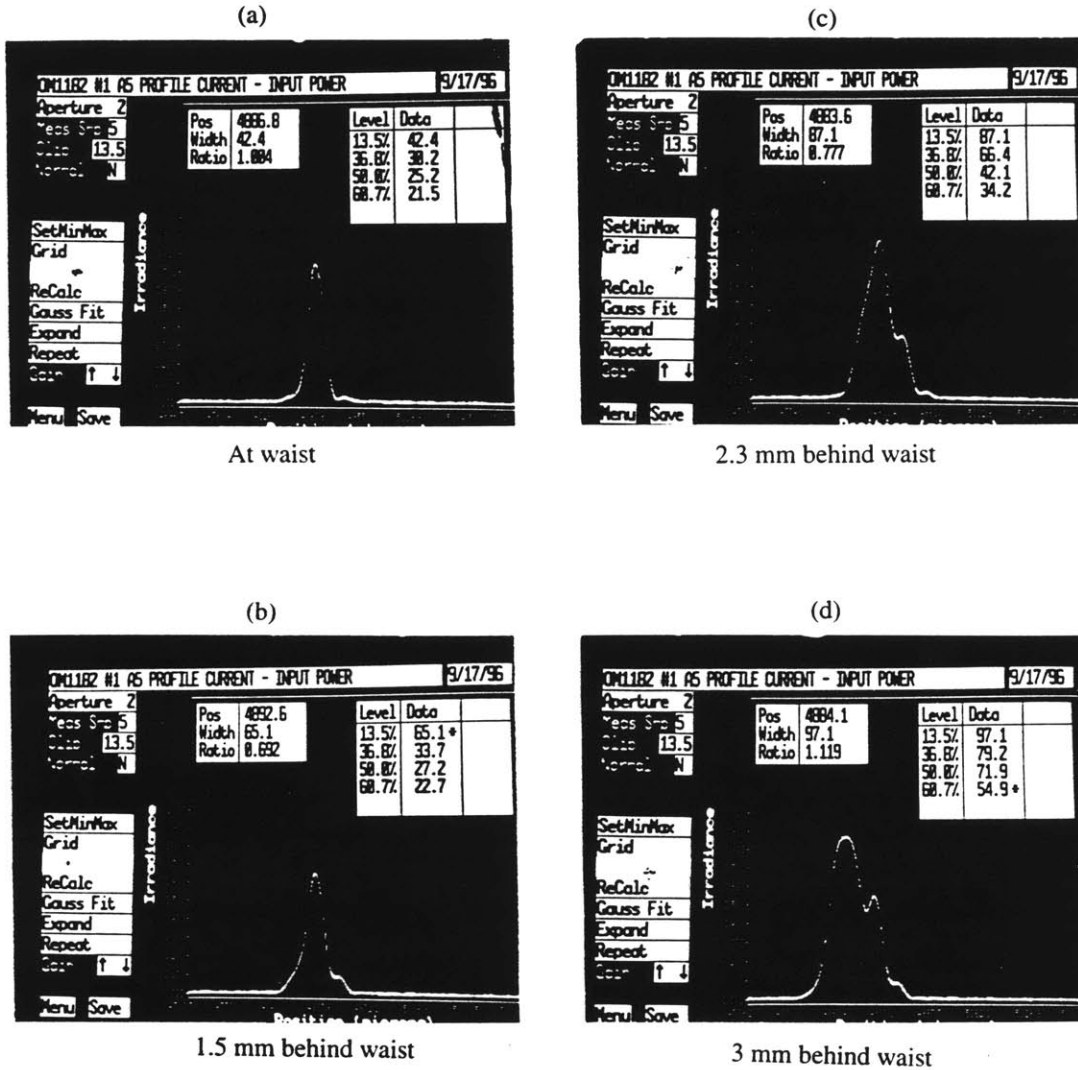
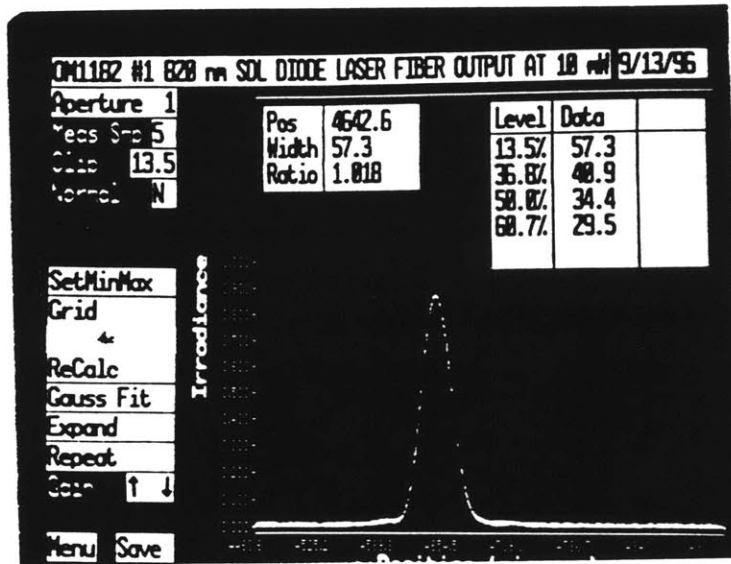


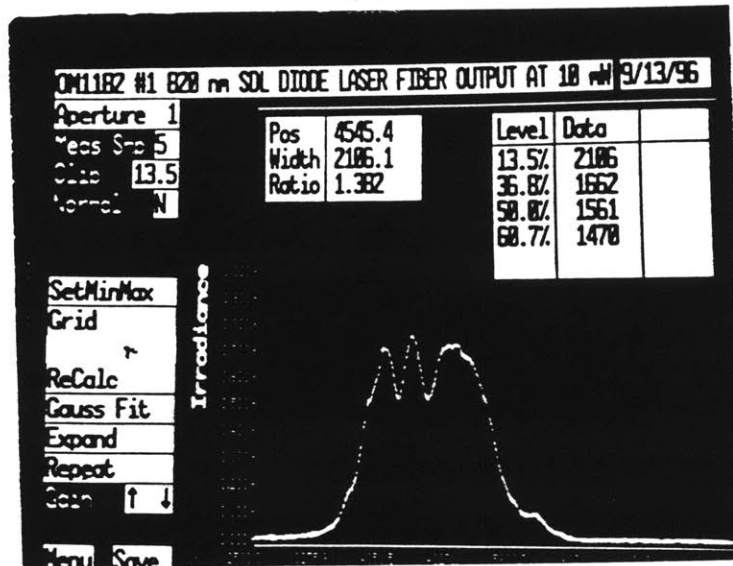
Figure 5-11: Typical MOPA beam profile at various distances from beam waist locations. (a) shows the beam waist with  $w_0 = 21.2 \mu\text{m}$  (confocal parameter  $b = 2.6$  mm). (b), (c), and (d) show the beam profiles at 1.5 mm, 2.3 mm, and 3 mm away from the waist location with  $1/e^2$  beam radii  $w$  of  $32.6 \mu\text{m}$ ,  $43.6 \mu\text{m}$ , and  $48.6 \mu\text{m}$ , respectively.

(a)



At waist

(b)



Far field pattern of collimated beam

Figure 5-12: Typical MOPA beam profile for (a) a focused beam with  $w_0 = 57.3 \mu\text{m}$  (confocal parameter  $b = 6.5 \text{ mm}$ ) at the beam waist and (b) a far-field collimated beam with  $w \sim 1 \text{ mm}$ .

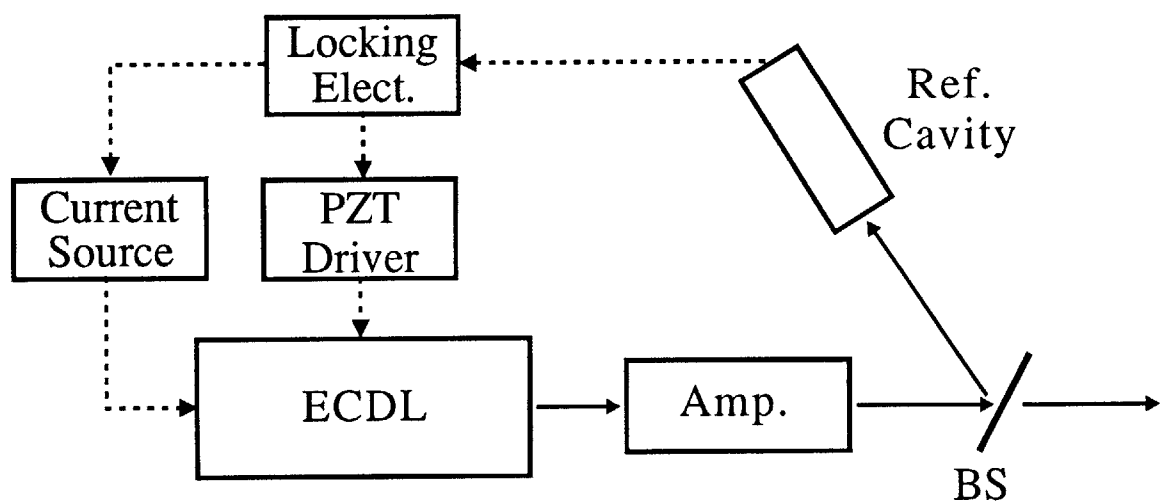


Figure 5-13: Frequency stabilization scheme for the MOPA diode laser using a side-locking technique. The reference cavity is set to the side of a transmission peak to provide an error signal.

## 5.5 Frequency Stabilization of Laser Output

Under free-running conditions the MOPA diode laser output has a peak-to-peak frequency jitter on the order of a few MHz. The frequency jitter of the master diode laser is the principal cause of the large frequency jitter of the detected beat signal in the 3-to-1 frequency division experiment to be discussed in Chapter 6. Therefore, it is necessary to implement an active servo loop to stabilize the frequency of the MOPA diode laser.

Figure 5-13 shows a schematic of the stabilization scheme for the MOPA diode laser. A small fraction of the MOPA output was split off and mode-matched into a Newport SR-140-C reference cavity which was set to the side of a transmission fringe. The hermetically sealed and temperature stabilized reference cavity has a cavity length of 25.4 mm and a finesse of 14000. The transmitted signal from the reference cavity was used as an error signal and fed back to the extended-cavity diode laser. Figure 5-14 shows a schematic of the locking electronics for servo-controlling the current source and the PZT. The transmitted signal from the reference cavity was first conditioned by a half-integrator followed by a full-integrator and then split into two parts. Part of the conditioned signal was sent directly to the current source

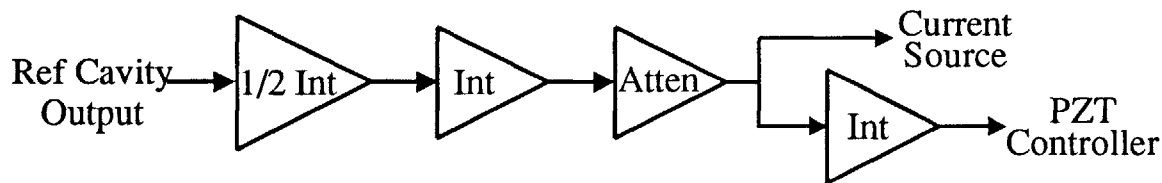


Figure 5-14: Locking electronics for servo-controlling the current source and the PZT. Int: integrator. 1/2 Int: half-integrator. Atten: attenuator.

for fast frequency control, while the rest of the signal was integrated again and then sent to the PZT controller. The frequency of the extended-cavity diode laser could be controlled by both the diode laser injection current and the PZT-mirror. The PZT had a much larger dynamic range that covers the entire continuous tuning range of the diode laser. However, the dynamic response of the PZT was slow, with a measured unity-gain frequency of 4.5 kHz. The diode laser injection current, on the other hand, had a much faster frequency response with a unity-gain frequency of  $\sim 40$  kHz. Its dynamic range, however, was limited. Therefore, the PZT was useful in tracking slow frequency drifts of the diode laser, while the current source was more effective in stabilizing the faster frequency jitters.

The frequency-stabilized MOPA laser had a residual frequency noise of 10 kHz rms as shown in Fig. 5-15. We were able to sustain the locking for about 2-3 minutes before the PZT runs out of dynamic range to track the frequency drift. Sometimes the MOPA would lose lock because of mode-hopping of the ECDL.

## 5.6 Summary

In summary, we have constructed a master-oscillator/power-amplifier diode laser system which satisfies the various requirements for linewidth, tunability, output power, and mode quality.

The diode laser output has an intrinsic linewidth of approximately 50 kHz. Although there exists a large peak-to-peak frequency jitter of about 1 MHz, active stabilization to a reference cavity reduced the peak-to-peak jitter to less than 80 kHz (15 kHz rms).

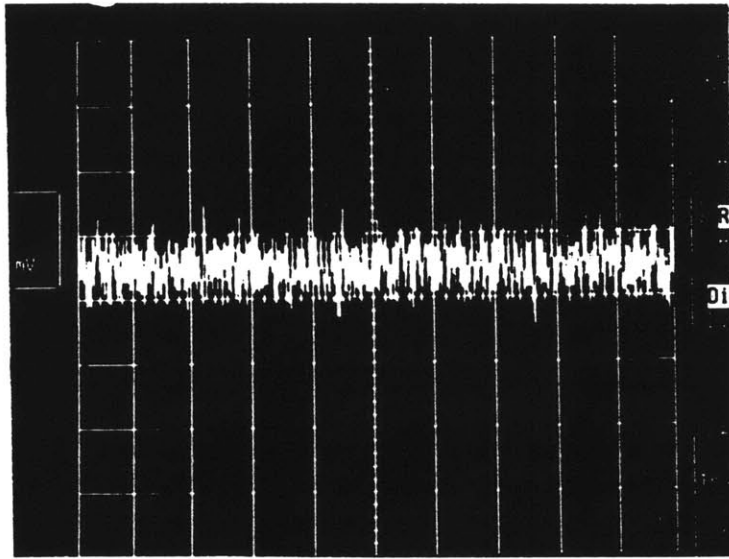


Figure 5-15: Residual frequency noise of frequency-stabilized MOPA diode laser. Vertical scale: 50 kHz/div. Horizontal scale: 1 ms/div.

The diode laser was continuously tunable over at least 100 MHz with frequency gaps between mode hops covering approximately 150 MHz. Although the continuous tuning range falls short of the desired tuning range of 300 MHz, it is nevertheless sufficient for the 3-to-1 optical frequency division experiment to be discussed in Chapter 6.

The diode laser was capable of producing 170 mW of useful output power at 798 nm after losses due to 2 Faraday isolators and other beam steering components are taken into account. The useful output power can be increased to about 220 mW at 796 nm. These output powers are sufficient to drive PPLN-based doubly-resonant OPO's with threshold pump powers on the order of tens of mW.

Finally, the mode quality of our diode laser, although far from ideal, is considered adequate. There exist significant amounts of astigmatism as well as some higher-order spatial modes. The astigmatism could be corrected with a cylindrical lens or with a spherical mirror. The amount of power present in the high-order Gaussian modes was judged to be only a small fraction ( $\leq 10\%$ ) of the total power based on measurements of the transmission spectrum from a reference cavity.

# Chapter 6

## Three-to-One Optical Frequency Division Experiment

This chapter describes the experiment that demonstrates 3-to-1 optical frequency division of 532 nm by using two difference-frequency generation (DFG) interactions in a double-grating PPLN crystal. In section 6.1 the optical-to-microwave frequency chain proposed by Wong is briefly summarized [23][24], followed by a description of the basic scheme of 3-to-1 optical frequency division by two DFG interactions. Important milestones and relevant work in experimental demonstration of 2:1 and 3:1 optical frequency division are also discussed here. The specific implementation of the double-DFG 3:1 frequency division scheme using a double-grating PPLN crystal is described in section 6.2. Section 6.3 describes the experimental setup. Experimental results including the detection and frequency stabilization of the beat signal are presented in Section 6.4. Section 6.5 compares our work with the 3:1 optical frequency division experiment by Pfister *et al.*, followed by summarizing remarks in Section 6.6.

### 6.1 The Optical-to-Microwave Frequency Chain

In Chapter 1 the optical-to-microwave frequency chain proposed by Wong was briefly discussed [23][24]. This section provides a more detailed description of the role of 2:1 and 3:1 optical frequency division as essential building blocks for the frequency chain.

The schematic of the basic scheme is shown in Fig. 1-1. Consider an optical frequency of interest  $f$  that is to be calibrated against the cesium clock frequency at 9.2 GHz. A 2:1 frequency divider yields an output at  $(1/2)f$ . Two 3:1 frequency dividers in series produce another output at  $(4/9)f$ . A difference-frequency measurement between the two outputs yields a signal at a frequency  $f_d=(1/18)f$ . Consider the 532 nm wavelength for a frequency-doubled Nd:YAG laser. In this case,  $f= 563$  THz, and  $f_d= 31$  THz. This frequency difference can then be accurately compared to a microwave frequency standard via a multi-THz-span optical frequency comb [68]. With such an optical-to-microwave frequency chain it is then possible to calibrate any optical frequency relative to the 9.2 GHz primary frequency standard.

### 6.1.1 2:1 optical frequency division

As mentioned in Section 1.3.2, a 2:1 optical frequency divider can be implemented with a degenerate OPO. 2:1 optical frequency division was first demonstrated by Nabors *et al.* in 1990 [69] in a cw self-phase-locked LiNbO<sub>3</sub> optical parametric oscillator (OPO) pumped at 532 nm. The degenerate self-phase-locked signal and idler outputs at 1064 nm automatically assured a 2:1 frequency ratio between the pump laser frequency and the signal/idler output frequency. In 1992 Lee *et al.* also demonstrated 2-to-1 optical frequency division in a cw 532-nm-pumped KTP OPO in which the beat note between the signal and idler outputs at 1064 nm was phase-locked to an external microwave oscillator [70][29]. A self-phase-locked KTP OPO, also pumped at 532 nm, was demonstrated by Mason *et al.* in 1996, again demonstrating 2-to-1 optical frequency division [71]. Note that in a 2-to-1 frequency divider where the outputs are degenerate in frequency, only a single stage of nonlinear optical interaction is required.

### 6.1.2 3:1 optical frequency division

As discussed in Section 1.3.2, implementation of a 3:1 optical frequency divider requires two nonlinear frequency conversion stages in order to convert the optical fre-



quency of one of the outputs to that of the second output such that phase-locking can be performed. Figures 6-1 (a) and (b) illustrate two possible implementations of 3:1 optical frequency division using two input sources. One implementation, shown in Fig. 6-1 (a), involves the use of a DFG stage in conjunction with a SHG stage to accomplish 3:1 frequency division. In this scheme the pump fields with an optical frequency of  $3f$  is mixed with the signal field at a frequency  $f+\delta$  to generate a difference-frequency output at  $2f-\delta$ . The signal field is simultaneously frequency-doubled via SHG to produce a signal at  $2f+2\delta$ . The two outputs at  $2f-\delta$  and  $2f+2\delta$  are then detected to yield a rf beat signal at  $3\delta$ . Tuning the frequency of the input source at  $f+\delta$  allows one to set  $\delta=0$  and achieve exact 3:1 optical frequency division. The second implementation, shown in Fig. 6-1 (b), employs two consecutive DFG stages to accomplish 3:1 frequency division. In this scheme the input sources have optical frequencies  $3f$  and  $2f+\delta$ . The first DFG interaction generates an output at frequency  $f-\delta$ . The UN-converted portion of the  $2f+\delta$  input is then mixed with the output at  $f-\delta$  to generate another difference-frequency output at  $f+2\delta$ . The DFG outputs at  $f-\delta$  and  $f+2\delta$  are then detected to yield a beat signal at  $3\delta$ . Again, tuning the optical frequency of the source at frequency  $2f+\delta$  allows one to set  $\delta=0$  to achieve exact 3:1 optical frequency division.

3:1 optical frequency division using the DFG/SHG scheme has been experimentally demonstrated by Pfister *et al.* in 1996 [72] and by Touahri *et al.* in 1997 [12]. The purpose of the work by Pfister *et al.* was to demonstrate the potential of connecting the methane-stabilized He-Ne mid-IR frequency reference at  $3.39 \mu\text{m}$  to the proposed  $\text{Hg}^+$ -based UV frequency reference at 282 nm in an exact 12:1 frequency ratio. The 12:1 ratio is accomplished by a 4:1 frequency connection between 1130 nm and 282 nm via successive second harmonic generation stages, in conjunction with a 3:1 optical frequency divider between  $3.39 \mu\text{m}$  and 1130 nm. The actual sources used in Pfister's work were a Nd:YAG laser at  $\lambda=1064 \text{ nm}$  and a CO overtone laser at 3192 nm, which were mixed inside a bulk  $\text{RbTiOAsO}_4$  (RTA) crystal to generate a DFG output at 1596 nm. Another output at 1596 nm was generated via SHG of the 3192 nm laser in a  $\text{AgGaSe}_2$  crystal. The two outputs at 1596 nm were then detected

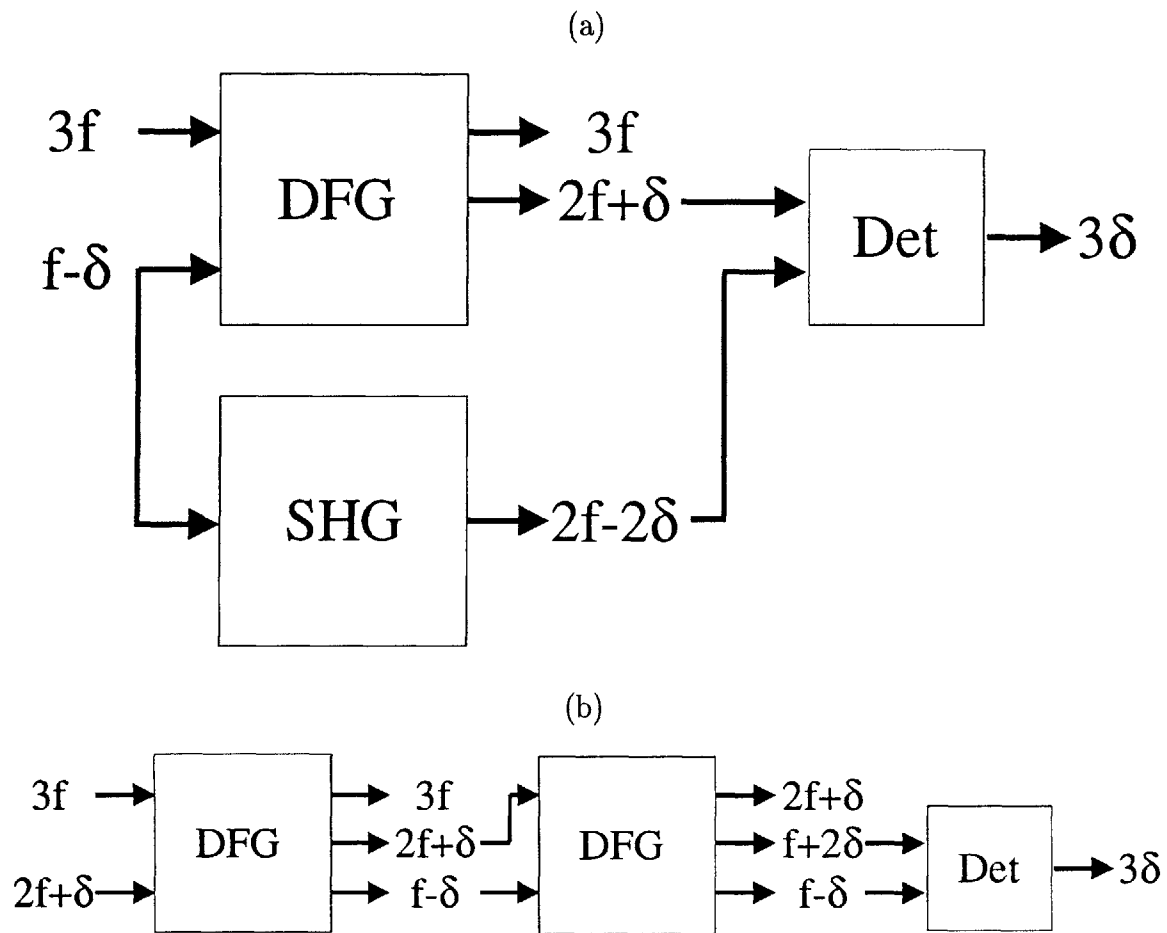


Figure 6-1: (a) 3-to-1 optical frequency division via the DFG/SHG scheme.  $\delta \ll f$  is the frequency separation from an exact 3:1 ratio between the input sources. The outputs at  $2f + \delta$  and  $2f - 2\delta$  are detected to yield a beat signal at  $3\delta$  which can then be used to control the input source at  $f - \delta$  such that  $\delta = 0$ . (b) 3-to-1 optical frequency division via the DFG/DFG scheme.  $\delta \ll f$  is the frequency separation from an exact 3:2 ratio between the input sources. The outputs at  $f + 2\delta$  and  $f - \delta$  are detected to yield a beat signal at  $3\delta$  which can then be used to control the input source at  $2f + \delta$  such that  $\delta = 0$ .

by an InGaAs PIN diode to generate a beat-note signal, which was then frequency stabilized to establish an exact 3:1 frequency connection between the 1064 nm and 3192 lasers. The frequency stabilized beat-note signal had a signal-to-noise ratio of  $\sim 40$  dB and a jitter linewidth of  $\sim 150$  kHz.

The work by Touahri *et al.* involved the measurement of the absolute frequency of the  $5S_{1/2}$  ( $F=3$ ) to  $5D_{5/2}$  ( $F=5$ ) two-photon transition in rubidium at  $\lambda = 778$  nm based on an optical-to-microwave frequency chain starting from a  $\text{CO}_2/\text{OsO}_4$  reference laser at  $\lambda = 10.3 \mu\text{m}$  [12]. A 3:1 frequency divider between 843 nm and 2528 nm was employed as part of the frequency chain which connected the transition frequency at  $\lambda = 778$  nm and the reference frequency at  $\lambda = 10.3 \mu\text{m}$ . In Touahri's 3:1 frequency divider the output from a KCl:Li color-center laser at 2528 nm was mixed with a diode laser at 843 nm in  $\text{AgGaSe}_2$  to generate a difference-frequency output at 1264 nm. Another output at 1264 nm was generated via SHG in another  $\text{AgGaSe}_2$  crystal. The 3:1 division was established by monitoring the beat notes between the 1264-nm outputs and an InGaAsP diode laser which served as a local oscillator. The rest of the 10.3- $\mu\text{m}$ -to-778-nm frequency chain was implemented by connecting the 10.3  $\mu\text{m}$   $\text{CO}_2$  reference laser to the 2528 nm laser in a 4:1 frequency ratio via a MIM diode. This connection established, in conjunction with the aforementioned the 3:1 frequency divider, the 843 nm laser frequency as the 12th harmonic of the 10.3  $\mu\text{m}$  reference. Finally, a sum frequency generation between the 10.3- $\mu\text{m}$  reference laser and the 843 nm laser produced an output at 778 nm. This 778-nm SFG output was then frequency locked to an ECDL at 778 nm that is used to measure the two-photon transition.

The work described in this chapter also demonstrates a 3-to-1 optical frequency division but differs from the work reported by Pfister *et al.* and Touahri *et al.* in 3 main respects:

1. We employed the DFG/DFG scheme in Fig. 6-1 (b) with input frequencies of  $3f$  and  $2f$  to establish a 3-to-1 frequency connection between the input and output fields, whereas the works by both Pfister *et al.* and Touahri *et al.* accomplished the 3-to-1 connection via the DFG/SHG scheme in Fig. 6-1 (a) with input frequencies of

$3f$  and  $f$ .

2. Whereas Pfister’s and Touahri’s experimental configurations involve 2 separate nonlinear crystals for the SHG and DFG interactions, our setup involves the use of a single PPLN sample with 2 domain-reversed gratings to phasematch the respective DFG interactions. This greatly simplified the complexity of the system because we only needed to align and mode-match our inputs through one nonlinear crystal instead of two. This resulted in the additional benefit that the two outputs generated from the two DFG interactions were automatically aligned, thus eliminating the need to recombine and align the output beams generated from two separate nonlinear crystals.

3. Because of the different applications between Pfister’s work, Touahri’s work, and our work, the specific wavelengths of interest were also different. Pfister’s work demonstrated optical frequency division of 1064 nm, whereas in Touahri’s work the pump wavelength was 843 nm. The work described in this thesis demonstrates optical frequency division of 532 nm.

## 6.2 The Double-Grating PPLN Crystal

### 6.2.1 Grating design and fabrication

We designed and fabricated a PPLN sample with two grating periods to phasematch the successive DFG interactions for implementing the 3-to-1 frequency division scheme described in Section 6.3. The 250- $\mu\text{m}$ -thick, 3-mm-wide PPLN sample was 1 cm long divided into two 5-mm-long sections of different grating periods. Our input sources had wavelengths at 532 nm and 798 nm and thus were in approximate 3:2 optical frequency ratio. The first QPM grating, with a grating period of 22.2  $\mu\text{m}$ , was designed to phasematch a third-order DFG interaction at a temperature of 72.1°C with the 532-nm and 798-nm inputs to generate an idler output at 1596 nm. The second QPM grating, with a grating period of 20.1  $\mu\text{m}$ , is designed to phasematch the DFG interaction at 68.3°C between the idler output from the first DFG interaction and the residual 798 nm input. The grating periods are calculated from Eq. (2.61),

Parameters	DFG1	DFG2
$\lambda_p$ (nm)	532.2	798.3
$n_{e,p}$	2.2370	2.1781
$\lambda_s$ (nm)	798.3	1596.6
$n_{e,s}$	2.1783	2.1384
$\lambda_i$ (nm)	1596.6	1596.6
$n_{e,i}$	2.1385	2.1384
$T_{PM}$ ( $^{\circ}\text{C}$ )	72.1	68.3
$2l_c$ ( $\mu\text{m}$ )	7.4	20.1
$\Lambda$ ( $\mu\text{m}$ )	22.2	20.1

Table 6.1: Quasi-phasematching for double-grating PPLN

and the relevant physical quantities used to calculate the grating periods for the two DFG interactions are listed in Table 6.1. The values for the refractive indices are determined from the published Sellmeier's equation by Edwards *et al.* [30] in Eq. (2.62).

Ideally, the grating periods for the two DFG interactions should be chosen to have the same peak phasematching temperature for optimal overall conversion efficiency. This would be possible only if one can define the grating periods with arbitrary accuracy. Since our mask vendor's stepping equipment which defines the exact positions of the grating lines is specified to an accuracy of  $0.1 \mu\text{m}$ , we were also limited to an accuracy of  $0.1 \mu\text{m}$  in specifying the grating periods. In order to optimize the efficiency of the double-DFG process, we searched for the pair of grating periods which minimizes the separation in the corresponding phasematching temperatures. We computed the phasematching temperatures for different pairs of grating periods and found that grating periods of  $\Lambda_1 = 22.2 \mu\text{m}$  and  $\Lambda_2 = 20.1 \mu\text{m}$  yield the pair of phasematching temperatures ( $T_{PM1} = 72.1^{\circ}\text{C}$  and  $T_{PM2} = 68.3^{\circ}\text{C}$ ) which are closest to each other. The calculated temperature phasematching curves for the first and second DFG interactions are plotted in Fig. 6-2 (a). The peak phasematching temperature for the first DFG interaction is calculated to be  $72.1^{\circ}\text{C}$ , with a FWHM bandwidth of  $5.5^{\circ}\text{C}$ . The calculated peak phasematching temperature for the second DFG interaction is  $68.3^{\circ}\text{C}$  with a FWHM bandwidth of  $15.8^{\circ}\text{C}$ . The peak phasematching temperatures of the two interactions are  $3.8^{\circ}\text{C}$  apart, which is well within the temperature bandwidths of

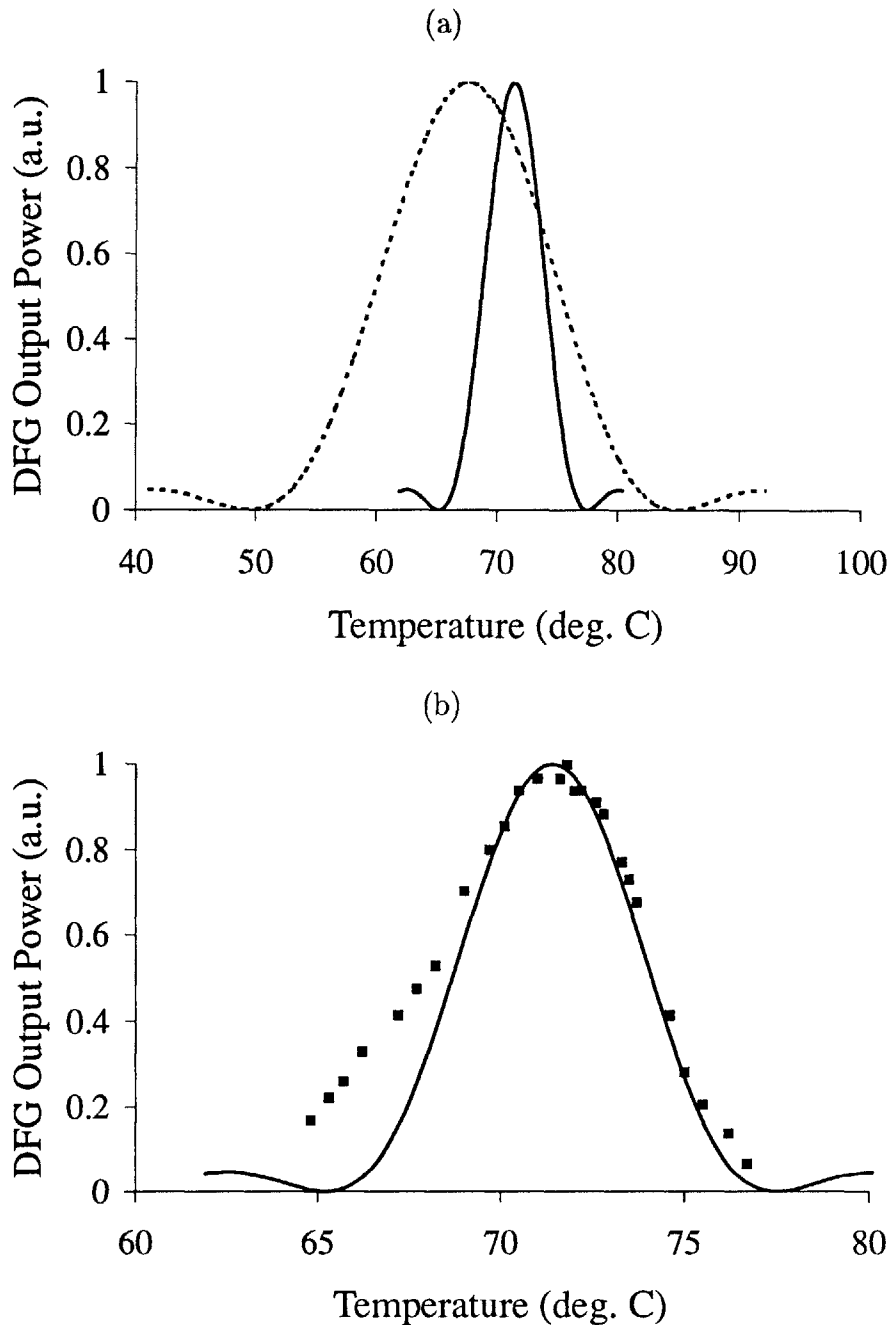


Figure 6-2: (a) Temperature tuning curves for the two DFG interactions in the double-grating PPLN crystal calculated from Sellmeier's equations. Solid curve corresponds to 3rd-order QPM DFG interaction between 532 nm and 798 nm with a  $22.2 \mu\text{m}$  grating period. Dashed curve corresponds to 1st-order QPM between 798 nm and 1596 nm. The length of each grating is 5 mm. (b) Temperature tuning curves of DFG interaction between 532 nm and 798 nm with a 3rd-order QPM grating period of  $22.2 \mu\text{m}$ . Solid curve is calculated from the Sellmeier's equations. The length of the grating is 5 mm.

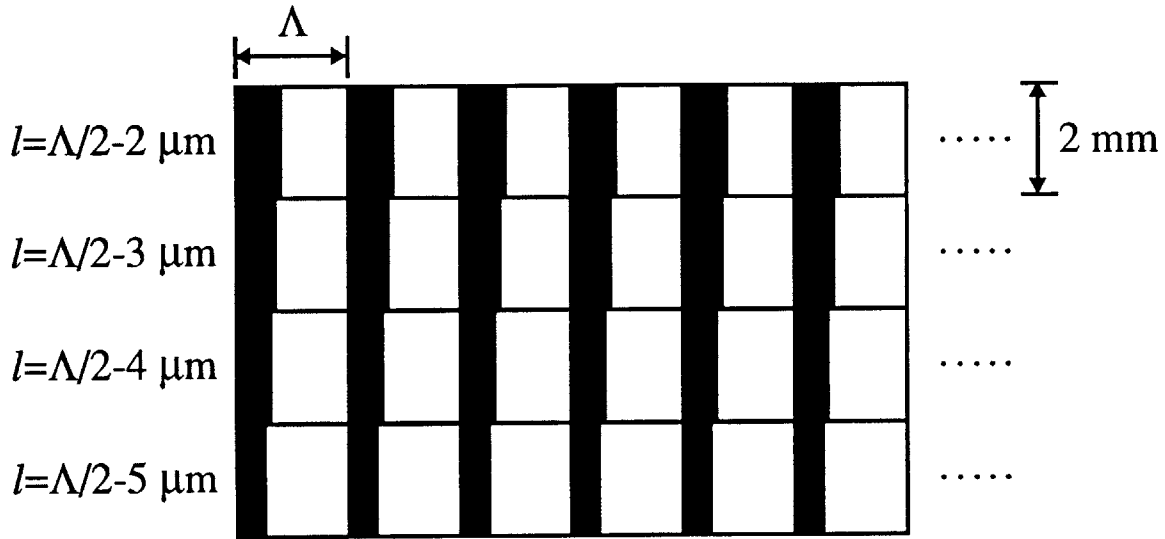


Figure 6-3: Multiple duty cycle QPM grating design. The grating pattern is partitioned into 4 2-mm-wide sections of different duty cycles. The domain lengths  $l$  of the reversed sections had duty cycles designed to compensate for domain spreadings of 2, 3, 4, and 5  $\mu\text{m}$ , respectively.

the two interactions. By setting the crystal temperature at the peak phasematching temperature of first DFG interaction, we expected a 15% reduction in the conversion efficiency for the second DFG interaction.

As shown in Fig. 6-3, the PPLN grating pattern is partitioned into 4 2-mm sections of different duty cycles along the width of the grating structure. The 4 sections have electrode linewidths designed to compensate for lateral domain spreading of 2  $\mu\text{m}$ , 3  $\mu\text{m}$ , 4  $\mu\text{m}$ , and 5  $\mu\text{m}$ , respectively. For instance, the grating pattern with a grating period of 22.2  $\mu\text{m}$  (DFG1) has sections with electrode linewidths of 9.1  $\mu\text{m}$ , 8.1  $\mu\text{m}$ , 7.1  $\mu\text{m}$ , and 6.1  $\mu\text{m}$ , respectively. In Chapter 3 we mentioned that the lateral spreading of domains during poling typically ranges from 2-5  $\mu\text{m}$ . Since it is usually difficult to precisely control the amount of spreading during poling, we designed our grating pattern to compensate for different amounts of spreading. In this fashion one may simply use the section with a resulting domain reversal duty cycle that is closest to the ideal 50/50 ratio.

Most of the details regarding the fabrication of PPLN has been described in Chapter 3. Following E-field poling, our double-grating PPLN samples was diced to its

final dimensions (10 mm long by 3 mm wide) and end-polished for normal incidence. Although our PPLN sample was designed for a total useful width of 8 mm, the final width of our sample was 3 mm because a portion of the sample cracked during dicing. Since no anti-reflection (AR) coatings were applied to the polished facets, we expect a  $\sim 14\%$  Fresnel loss at each facet.

## 6.2.2 Characterization

Following E-field poling, we inspected the double-grating PPLN sample and observed 4-6 missing reversals along the length of the grating structure. The 3-mm-wide sample consists of a 2-mm-wide section designed to compensate  $4 \mu\text{m}$  of domain spreading and a 1-mm-wide section designed to compensate  $5 \mu\text{m}$  of spreading. The 1-mm-wide section was used for our experiment because the measured DFG output power (first DFG interaction) was greater in this section. For the 1-mm-wide section, we measured by observing under a microscope the lengths of the domain-reversed sections over 20 consecutive grating periods on the  $+z$  face of the PPLN sample for both the  $\Lambda = 20.1 \mu\text{m}$  grating and the  $\Lambda = 22.2 \mu\text{m}$  grating. The average duty cycle was 51.0% for the  $\Lambda = 20.1 \mu\text{m}$  grating and 50.4% for the  $\Lambda = 22.2 \mu\text{m}$  grating. For the same sets of 20 consecutive grating periods standard deviation of the random duty cycle error  $\sigma_l$  was  $0.70 \mu\text{m}$  for the  $\Lambda = 20.1 \mu\text{m}$  grating and  $0.72 \mu\text{m}$  for the  $\Lambda = 22.2 \mu\text{m}$  grating. Based on Eqs. (2.85) and (2.88), we expect the conversion efficiency for the 1st DFG interaction ( $\Lambda = 20.1 \mu\text{m}$ ) to be reduced by 2.4% and that for the 2nd DFG interaction ( $\Lambda = 22.2 \mu\text{m}$ ) to be reduced by 2.1%.

In order to determine the peak phasematching temperature and to characterize the effective interaction length of our PPLN sample, we measured the idler output power from the first DFG interaction as a function of temperature. Figure 6-2 (b) shows the measured data vs. the calculated curve for the first DFG interaction based on Sellmeier's coefficients. The measured peak phasematching temperature is  $71.8^\circ\text{C}$ , which is in excellent agreement with the calculated value of  $72.1^\circ\text{C}$ . The measured FWHM temperature bandwidth of  $6.4^\circ\text{C}$  is  $\sim 16\%$  larger than the calculated bandwidth. The effective interaction length of the first DFG is estimated to be reduced by



16% from the physical length of 5 mm. A possible cause of the reduced effective interaction length was nonuniform temperature distribution over the length of the crystal. In our simple setup we placed the crystal on top of a MINCO HK5255R31.6L12D heater for temperature control. It was thus likely that different parts of the crystal did not have the same temperature. As mentioned in the previous chapter, there may also be a certain amount of random period errors in the domain-reversal profiles, especially that the domain-reversal profiles did not necessarily propagate straight down from the  $+z$  to the  $-z$  face. We did not measure the output power of the second DFG interaction as a function of temperature because we did not have an independent source at  $\lambda = 1596$  nm.

We also characterized the actual conversion efficiency of the first DFG interaction for the double-grating PPLN in order to estimate the expected rf beat signal power to be discussed in Section 6.3.4. We first derive expressions for the idler output power levels for the two DFG interactions. The expression for the output power for a DFG interaction is given by Eq. (2.23):

$$P_i = \frac{16\pi d_Q^2 P_p P_s \bar{h}_m(B, \zeta)}{c\epsilon_0 n_p n_s n_i \lambda_i^2 \left(\frac{1}{k_p} + \frac{1}{k_s}\right)} \text{sinc}^2 \left[ \frac{\Delta kl}{2} \right]. \quad (6.1)$$

Here  $P_p$  and  $P_s$  are the pump and signal powers,  $d_{eff}$  is the effective  $\chi^{(2)}$  nonlinear coefficient,  $l$  is the interaction length of the nonlinear medium,  $\bar{h}_m(B, \zeta)$  is the reduction factor due to non-optimal focusing [27], and  $\Delta kl$  is the amount of phase mismatch which acts to reduce conversion efficiency. For the first DFG interaction where  $\lambda_p = 532.2$  nm and  $\lambda_s = 798.3$  nm, we have  $d_{33} \sim 27$  pm/V and  $d_Q = \left(\frac{2}{3\pi}\right) d_{33} = 5.8$  pm/V for a 3rd-order interaction. For the second DFG interaction where  $\lambda_p = 798.3$  nm and  $\lambda_s = 1596.6$  nm, we have  $d_{33} \sim 24.3$  pm/V and  $d_Q = \left(\frac{2}{\pi}\right) d_{33} = 15.5$  pm/V for a 1st-order interaction. With an effective interaction length  $l$  of 4.25 mm, a confocal parameter of  $b = \frac{2\pi n}{\lambda} = 10$  mm, a reduction factor equal to  $\bar{h} = 0.402$ , and effective nonlinear coefficients of  $d_{Q1} = 5.8$  pm/V for DFG1 and  $d_{Q2} = 15.5$  pm/V for DFG2, one obtains

$$P_{i1} = 4.2 \times 10^{-4} P_p P_s. \quad (6.2)$$

The powers in the expression above refer to the power levels inside the PPLN crystal in  $W$ . Using expressions for the power levels outside the crystal, losses due to Fresnel reflections off the two uncoated crystal surfaces must be included. If we include the losses due to Fresnel reflections and the two long-wave-pass (LWP) filters at the output, the expression for the detected idler output from DFG1 becomes

$$P_{i1}(\text{det}) = 4.2 \times 10^{-4} P_p P_s T_{1p} T_{1s} T_{2i} T_f^2, \quad (6.3)$$

where  $T_{1p} = 0.854$  and  $T_{1s} = 0.863$  are the power transmissions for the pump (532 nm) and signal (798 nm) fields through the front surface of the PPLN,  $T_{2i} = 0.869$  is the power transmission for the idler field through the back facet, and  $T_f = 0.9$  is the transmission each of the two LWP filters at the idler wavelength.

The DFG idler power was measured by chopping the pump beam at 200 Hz and synchronously detecting the output on an InGaAs photodetector with a responsivity of 1.1 A/W and a transimpedance gain of  $10^4$  V/A. For input powers of  $P_p = 91$  mW at 532 nm and  $P_s = 160$  mW at 798 nm, we expect the detected idler output power to be  $P_{i1}(\text{det}) = 3.4 \mu\text{W}$ . The measured idler output power was  $2.3 \mu\text{W}$  at the peak phasematching temperature, which is  $\sim 67\%$  of the value calculated from theory. This implies a conversion efficiency that is also 67% of that obtained from theory, which yields an effective nonlinear coefficient of  $d_{Q1} = 4.7$  pm/V for the first DFG interaction. If we assume the second DFG interaction also has a conversion efficiency that is 67% of that calculated from theory, the effective nonlinearity for the second DFG interaction would be  $d_{Q2} = 12.6$  pm/V.

As mentioned above, based on measurements of the average and random duty cycle errors of the double-grating PPLN, we expect only  $\sim 2\%$  reduction in conversion efficiency for both DFG interactions compared to theory. The measured conversion efficiency was reduced by 33% compared to theory. This discrepancy can be attributed to two reasons. First, the actual domain-reversal profile is quite nonuniform from the

+z to the -z face and also along the width of the sample. The width of the domain reversal profile can vary by as much as  $\sim 2 \mu\text{m}$  along the 2-mm width of a given grating section. Thus the domain-reversal profile may not be quite uniform across the beam profile of the pump and signal beams. Second, the tapered amplifier pump output beam has significant astigmatism which also contributes to a lower conversion efficiency than expected.

## 6.3 Experimental Setup

This section describes the experimental setup for 3:1 optical frequency division of 532 nm using two successive DFG interactions.

### 6.3.1 532 nm laser system

The 532-nm pump laser source was a cw frequency-doubled Nd:YAG laser. The Nd:YAG laser was a Lightwave 122-1064-500-F diode-pumped solid-state non-planar-ring laser with a maximum output power of 500 mW. The laser frequency could be temperature-tuned over 30 GHz. The tuning characteristic of the laser exhibits several continuously-tunable stable regions separated by mode-hops. The tuning range across each continuously-tunable region is about 5 GHz with a tuning coefficient of  $-3.1\text{GHz}/^\circ\text{C}$ . The Nd:YAG laser could also be piezoelectrically tuned over a range of 30 MHz with a tuning coefficient of 2 MHz/volt. Figure 6-4 shows a schematic of the second-harmonic (SH) ring cavity which generates the frequency-doubled light at 532 nm [71]. The cavity length of the SH cavity was controlled and actively stabilized by a piezoelectric transducer (PZT) mounted to the end mirror of the cavity. Useful 532-nm output powers from the SH ring cavity were typically  $\sim 130$  mW.

### 6.3.2 798 nm laser system

As discussed in Chapter 5, the 798-nm laser system was a master-oscillator-power-amplifier (MOPA) system consisting of an extended-cavity diode-laser (ECDL) which

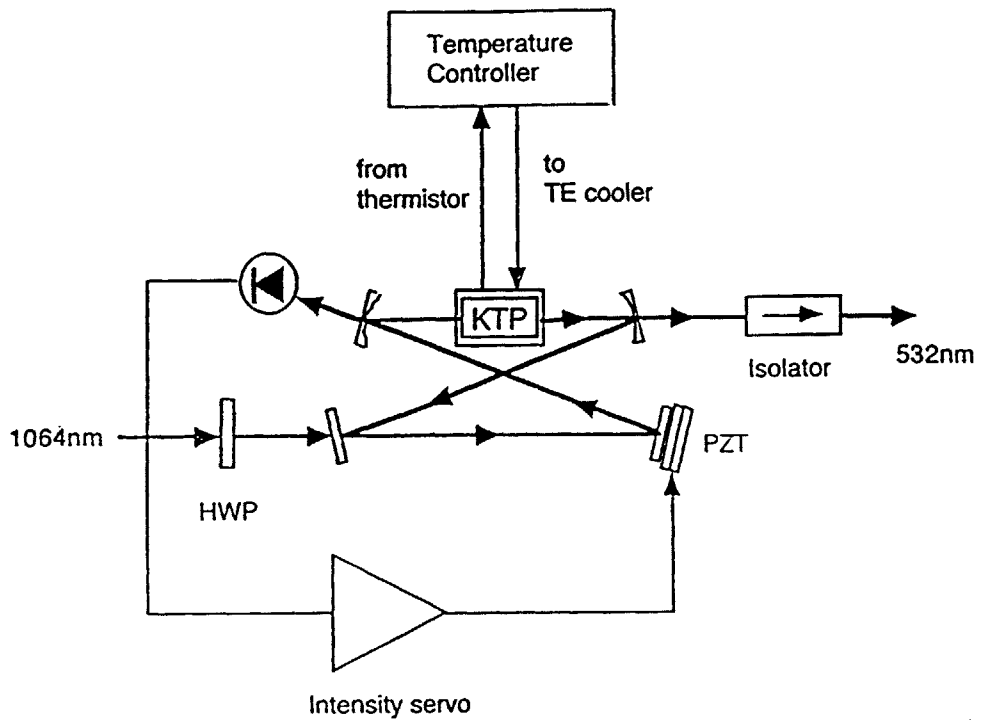


Figure 6-4: Schematic of harmonic ring cavity for frequency-doubling 1064 nm Nd:YAG laser. (E.J. Mason, Master's thesis, Massachusetts Institute of Technology, Cambridge, MA, June 1996)

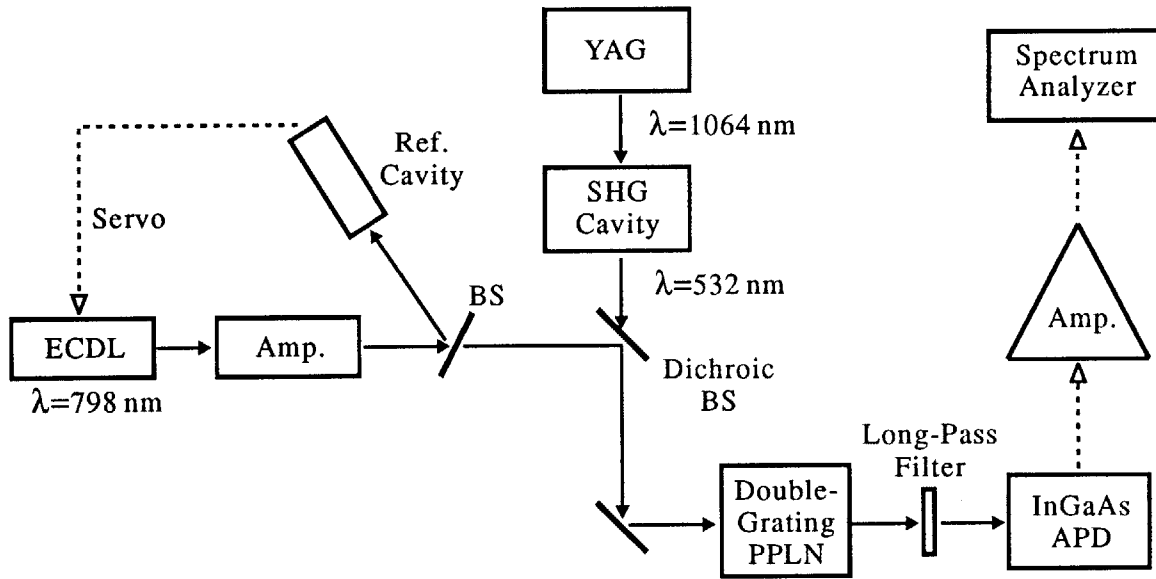


Figure 6-5: Experimental setup for 3-to-1 optical frequency divider using a double-grating PPLN crystal.

was used to injection-lock a SDL-8630-E tapered amplifier. Typical output power from the tapered amplifier was around 280 mW at 798 nm. The laser frequency could be continuously tuned by a PZT which controls the cavity length of the ECDL. Continuous tuning ranges were 100 MHz with approximately a 150-MHz separation between mode hops. The free-running 798-nm laser has a large frequency jitter on the order of a few MHz over a 1-s period.

### 6.3.3 Optics

The experimental setup is illustrated in Fig. 6-5. The frequency-doubled Nd:YAG laser and the MOPA outputs were combined via a dichroic beam splitter that reflected more than 99% of the 798-nm signal beam and transmitted 92% of the 532-nm pump beam. The 532-nm pump beam and the 798-nm signal beam were both focused to a confocal beam parameter of 10 mm inside the double-grating PPLN crystal. The incident beams at 532 nm and at 798 nm were filtered out after the PPLN using two long-wave-pass (LWP) filters, and the filtered outputs were collimated by a  $f = 10.0 \text{ cm}$  plano-convex lens and then focused via a  $f = 5.0 \text{ cm}$  lens into an InGaAs

avalanche photodiode (APD) detector to measure the beat signal between the idler outputs generated from the two DFG interactions. The signal from the APD detector was then amplified by an rf amplifier and sent to an rf spectrum analyzer for analysis.

The following paragraphs outline the steps taken to align the 532-nm frequency-doubled Nd:YAG pump laser and the 798-nm ECDL MOPA signal laser output beams into the PPLN crystal and to focus the output beams into the InGaAs APD.

(1) Steer the pump and signal beams using high reflectors such that the two beams line up approximately. Insert irises in the path of one of the beams and align the other beam through the same set of irises.

(2) Insert the focusing lens for each of the two beams. The lenses are each mounted on a 3-axis translation stage for fine adjustment. Move the lenses for each beam such that the beam waist locations are approximately matched.

(3) Mount the sample on a 5-axis translation stage. Set sample below the incident beams such that the beams pass above the sample and parallel to the edge of the sample. Move the sample longitudinally until the beam waists are roughly located close to the center of the sample. Move the sample up into the beams. Adjust the vertical and tilt knobs of the translation stage until the beam goes through the crystal with minimum clipping of the beam profiles.

(4) Set up the collimating lens approximately one focal length from the apparent beam waists. The transmitted pump and signal beams should be approximately collimated. Set up the long-wave pass (LWP) filters to extinguish the residual pump and signal. The focusing lens is placed at a distance from the detector roughly equal to its focal length at 1596 nm.

The above alignment procedure usually permitted detection of the idler output. A number of steps were then taken to optimize the output power. These steps are described in the following paragraphs.

(1) Adjust the sample vertically to ensure that the incident beams passes through the crystal without clipping.

(2) Adjust the tilt of the 5-axis translation stage for the sample in conjunction with the vertical translation to ensure that the incident beams propagate perpendicular to

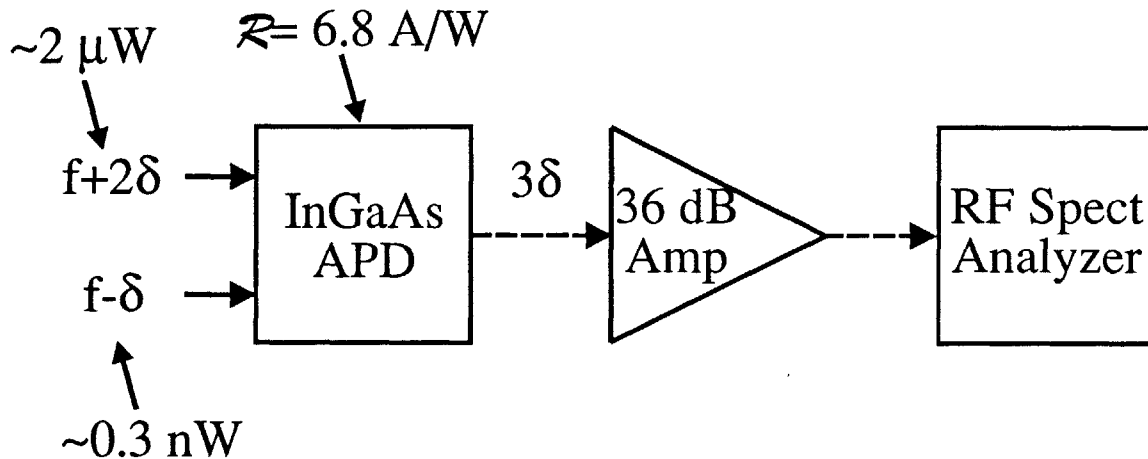


Figure 6-6: Schematic of detection system for  $3\delta$  beat signal.

the  $\pm z$  faces.

(3) Move the crystal longitudinally to center the beam waist at the center of the crystal.

(4) Move the beams relative to one another both horizontally and vertically to achieve optimum overlap between two beams inside the crystal.

(5) Steer the output beam with the mirror mount controls of the aluminum mirror to center the beam at the detector aperture.

(6) Move the final focusing lens along the direction of propagation to ensure that the beam is properly focused into the InGaAs detector aperture.

### 6.3.4 Detection system

The detection system of our 3:1 frequency division work is shown in Fig. 6-6. Our photodetector was an EG&G C30644E InGaAs avalanche-photodiode (APD), which was used to detect the beat signal between the two outputs at 1596 nm. An APD was required to amplify the very weak beat photocurrent of  $\sim 30 \text{ pA}$  in order to achieve a high signal-to-noise ratio and a wide detection bandwidth. The APD had a square aperture of  $50 \mu\text{m}$ . The 3-dB bandwidth of the APD was  $\sim 2 \text{ GHz}$ , and it was biased at -63 volts to yield a current gain of 8.2. At unity gain, the APD had a responsivity of  $0.84 \text{ A/W}$ . The output of the APD was connected to a 36 dB rf amplifier with a noise

figure of 2 dB. The amplified output was then split via a Mini-Circuits ZDC-10-1 10:1 rf coupler. The main output from the coupler was used for frequency stabilization of the beat signal to be discussed in Section 6.5. The coupled (-12 dB) output was sent to a HP 8563E rf spectrum analyzer to monitor the beat signal.

Based on the experimental parameters specified in Section 6.2, we outline the relevant expressions for estimating the detection sensitivity of the beat-note detection system. Eq. (6.1) provides the expression for the expected detected idler output from the first DFG stage. If we incorporate the assumption that our crystal had a conversion efficiency that was 67% of the theoretical value, then the expression for the detected idler output becomes

$$P_{i1}(\text{det}) = 2.8 \times 10^{-4} P_p P_s T_{1p} T_{1s} T_{2i} T_f^2. \quad (6.4)$$

where  $T_{1p} = 0.854$  and  $T_{1s} = 0.863$  are the power transmissions for the pump (532 nm) and signal (798 nm) fields through the front surface of the PPLN,  $T_{2i} = 0.869$  is the power transmission for the idler field through the back facet, and  $T_f = 0.9$  is the transmission of the LWP filters at the idler wavelength.

Likewise, the expression for the detector idler output power from DFG2 becomes

$$P_{i2}(\text{det}) = 3.1 \times 10^{-7} P_p P_s^2 T_{1p} T_{1s}^2 T_{2i} T_f^2. \quad (6.5)$$

where we have assumed again that the conversion efficiency is 67% of the theoretical value.

We now derive the expressions for the rf beat-note signal power as a function of the detected DFG idler output power levels. Consider an avalanche photodiode with a current gain  $M$  and a responsivity  $\mathcal{R}_0$  (for  $M = 1$ ) in units of A/W. It's overall responsivity is given by  $\mathcal{R} = \mathcal{R}_0 M$ . The photodiode output current can be expressed as  $I = \mathcal{R} P_{in}$  where  $P_{in}$  is the incident power. Let's consider the detection of the combined idler outputs from the two DFG interactions. The detected photocurrent is given by



$$I = \mathcal{R}[P_{di1} + P_{di2} + 2\sqrt{P_{di1}P_{di2}} \cos(\Delta\omega t + \phi)], \quad (6.6)$$

where  $\Delta\omega$  is the beat frequency between the two idler outputs. The corresponding rf power of the measured beat-note signal is

$$P_{\text{signal}} = 2\mathcal{R}^2 P_{di1} P_{di2} R G, \quad (6.7)$$

where  $R$  is the load impedance of the detector and  $G$  is the rf gain of any subsequent amplification.

We now derive expressions to estimate the noise of the detection system. The resistances inside the avalanche photodiode (APD) detection system contributes to the so-called Johnson noise. The  $4kT$  Johnson noise power density is equal to  $1.62 \times 10^{-20}$  W/Hz at room temperature. Subsequent amplification (with gain  $G$ ) adds amplifier noise which is specified by the noise figure ( $NF$ ) expressed in units of decibels (dB). The total output noise power in W/Hz is then

$$P_{\text{v,noise}} = 10^{NF/10} 1.62 \times 10^{-20} G \Delta f, \quad (6.8)$$

where  $NF$  is the noise figure of the rf amplifier and  $\Delta f$  is the detection bandwidth in units of Hz. The 36-dB rf amplifier we used had a noise figure of  $NF \sim 2$  dB.

The current noise of the system is due to the shot noise of the generated signal current as well as the leakage current  $I_D$  of the APD. In our system, the generated signal current is dominated by the detected idler power  $P_{di1}$  from DFG1. The total leakage current (dark current) is given as

$$I_D = I_{DS} + M I_{DB} \quad (6.9)$$

where  $M$  is the gain of the APD and  $I_{DS}$  and  $I_{DB}$  denote the surface and bulk leakage currents, respectively. Additionally, the avalanche process generates excess current with a noise factor  $F$  as compared to a regular PIN photodiode. The total current noise for the APD is thus given as

$$i_N = \sqrt{2q[I_{DS} + M^2F(I_{DB} + \mathcal{R}_0P_{di1})]\Delta f}, \quad (6.10)$$

where  $q = 1.6 \times 10^{-19}$  C is the electronic charge. In our case where  $M$  is reasonably large ( $M = 8.2$ ), the current noise contribution from  $I_{DS}$  can be neglected. For our APD (EG&G C30644E), typical specifications for the bulk dark current  $I_{DB}$  and the excess noise factor  $F$  are 1.5 nA and 5, respectively. With an APD gain of  $M = 8.2$  at a bias voltage of -63 V, the total responsivity  $\mathcal{R}$  is 6.8 A/W.

The total current noise power is

$$P_{i,\text{noise}} = i_N^2 R G \Delta f \quad (6.11)$$

The expected total noise power is then

$$P_{\text{noise}} = (i_N^2 R G + 10^{NF/10} 1.62 \times 10^{-20}) G \Delta f \quad (6.12)$$

The overall gain  $G$  between the APD and the spectrum analyzer was 21 dB. This included a gain of 36 dB from the rf amplifier, a 12-dB loss from the 10:1 coupler, and an additional 3-dB loss from the cables and connectors that connected the 10:1 coupler output to the spectrum analyzer.

For no input light we expected a total noise level of -100.1 dBm for a measurement bandwidth of 30 kHz. The measured noise level was -101 dBm, in good agreement with the calculated level given the uncertainty of the APD parameters. For input powers of 89 mW at 532 nm and 176 mW at 798 nm and  $d_Q$  values of 4.7 pm/V for the first DFG stage and 12.6 pm/V for the second DFG stage as measured in Section 6.2, we expected an rf beat signal power of -63 dBm and a total noise level of  $\sim$  -98.7 dBm. Our measured beat signal power was -65 dBm,  $\sim$ 2 dB below what we expect. The measured total noise level was -96 dBm,  $\sim$ 3 dB higher than expected. This suggests that the actual APD excess noise factor  $F$  was about twice the specified value of  $F = 5$ . The measured signal-to-noise ratio of the beat signal was  $\sim$ 30 dB.

Because of the limited bandwidths of the APD and the subsequent rf amplifiers, the effective bandwidth of our beat detection system was about 1 GHz. Furthermore,

because of the mode hops of the 798 nm laser and the frequency drift of the Nd:YAG laser, we often had to do a little frequency search in order to locate the beat signal. Once the beat signal was located, we could tune its frequency continuously for about 300 MHz before the 798 nm laser hops to another mode. By continuing to tune the laser frequency in the same direction using the PZT, one could recover the beat signal, located at about 450 MHz away from the point the mode-hop occurred. Without any external control of the frequency of the 798 nm diode laser, a particular mode was typically supported for a few minutes before modehopping occurs. Hence, any particular beat signal could stay on for only as long as a few minutes before disappearing. However, a slight tweak of the PZT controller of the ECDL laser was sufficient to recover the beat signal.

## 6.4 Frequency Stabilization

Because of the  $\sim 1$  MHz frequency jitter of the MOPA diode laser, the beat signal also suffered from a large frequency jitter on the order of a few MHz. As a first step to stabilize the beat signal frequency, we stabilized the frequency of the MOPA diode laser to a high-finesse reference cavity. Details of the frequency stabilization of the MOPA diode laser is provided in Section 5.4.

With the diode laser frequency stabilized we observed that the jitter of the beat signal was significantly reduced. The short-time peak-to-peak jitter was reduced from a few MHz to 260 kHz. There remained, however, a slow frequency drift on the order of 0.2 MHz/sec that could be attributed to 2 sources. First, the 532 nm frequency-doubled Nd:YAG laser was not frequency-stabilized. The YAG laser also contained a frequency drift that was specified to be  $\leq 0.8$  MHz/min. Second, the cavity length of the reference cavity for the 798 nm laser probably had a slow drift component due to slight temperature variations. Figure 6-7 shows the schematic for the frequency stabilization of the beat note frequency. As mentioned in Section 6.3.4, we used a Mini-Circuits ZDC-10-1 10:1 (-12 dB) rf coupler to split off a portion of the amplified (36 dB) beat-note signal for monitoring on the rf spectrum analyzer. The remaining

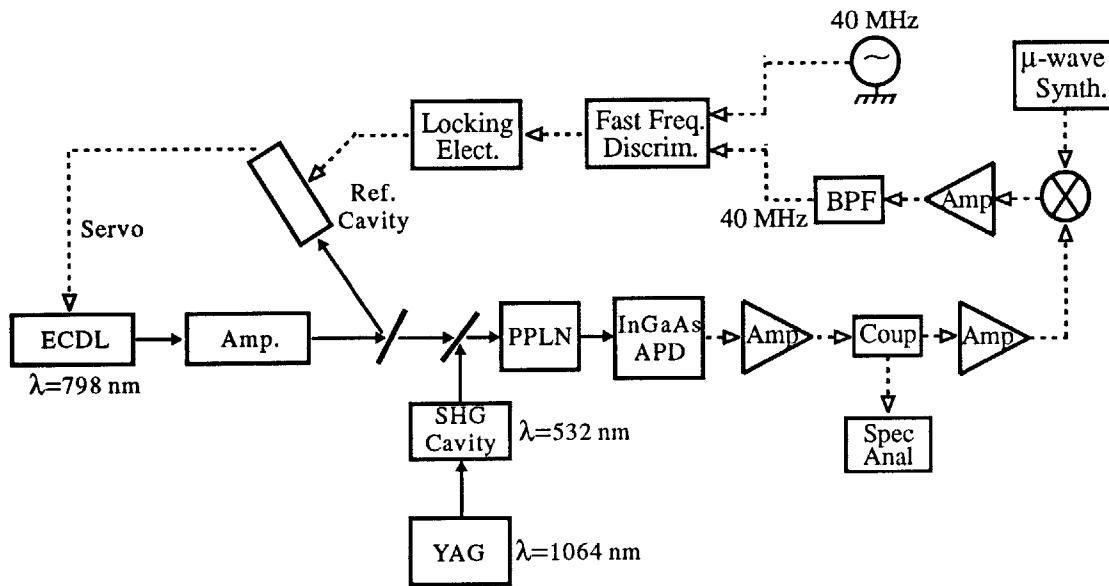


Figure 6-7: Frequency stabilization scheme for  $3\delta$  beat signal. BPF: band-pass filter.

beat-note signal output was amplified by a 21-dB (HP 8447E) rf amplifier and then down-converted to 40 MHz by mixing it with a microwave synthesizer. The down-converted signal was then amplified by another 21-dB (HP 8447E) rf amplifier. At this point we passed the beat signal through a bandpass filter centered at 40 MHz to remove excess white noise. The bandpass filter had a 3-dB bandwidth of 1.5 MHz which was adequate for the slow frequency drift and jitter of the beat note. The output of the bandpass filter was then compared with a 40 MHz local oscillator in a fast phase-frequency discriminator to yield an error signal. The output of the fast phase-frequency discriminator was proportional to the frequency difference between the LO and the beat note signal for two input signals with different frequencies. For two input signals with the same frequency, the discriminator output is proportional to the phase difference between the LO and the beat signal. The error signal was then amplified and sent to the PZT of the high-finesse reference cavity (for the 798-nm laser) to stabilize the cavity length. With the cavity length stabilized, the slow drift of the beat note signal was eliminated.

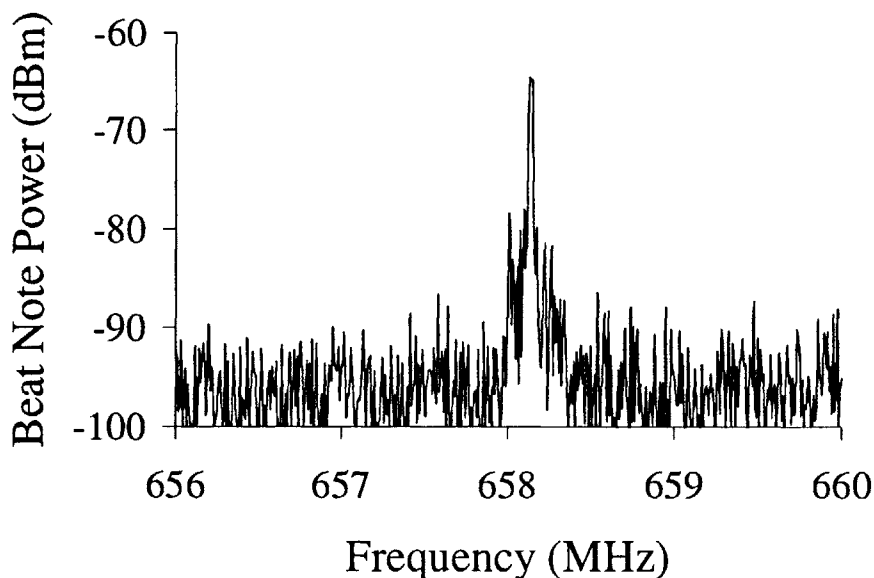


Figure 6-8: Single-shot trace of frequency-stabilized  $3\delta$  beat signal. Scan time = 50 ms. Detection bandwidth= 30 kHz.

## 6.5 Results

Figure 6-8 shows a single-shot trace of the frequency-stabilized beat signal taken over a time of 50 ms. The beat note had a peak-to-peak frequency jitter of 260 kHz. Figure 6-9 shows a plot of the average of 100 traces of the frequency-stabilized beat signal over a 5 sec time scale. On this 5 sec time scale the  $3\delta$  beat signal,  $\delta$  being the frequency deviation of the 798 nm laser from exactly  $2/3$  of the 532 nm laser frequency, was estimated to have a frequency uncertainty of  $\pm 25$  kHz. The corresponding fractional uncertainty, defined as the ratio between the uncertainty in  $\delta$ , which is  $\pm 8.3$  kHz, and the optical frequency of the 532-nm pump field, which is 564 THz, is  $\pm 1.5 \times 10^{-11}$ . The value of the center of the beat note frequency is  $3\delta = -658.14$  MHz. The sign was determined to be negative because increasing the extended cavity diode laser frequency results in a decrease in the frequency of the beat signal.

We have attempted to phase lock the beat signal to the 40-MHz reference LO of the phase-frequency discriminator by feeding the error signal to the drive current control of either laser. However, the 30 dB signal-to-noise ratio at a detection bandwidth of 30 kHz was insufficient because of the large beat frequency jitter and drift of the

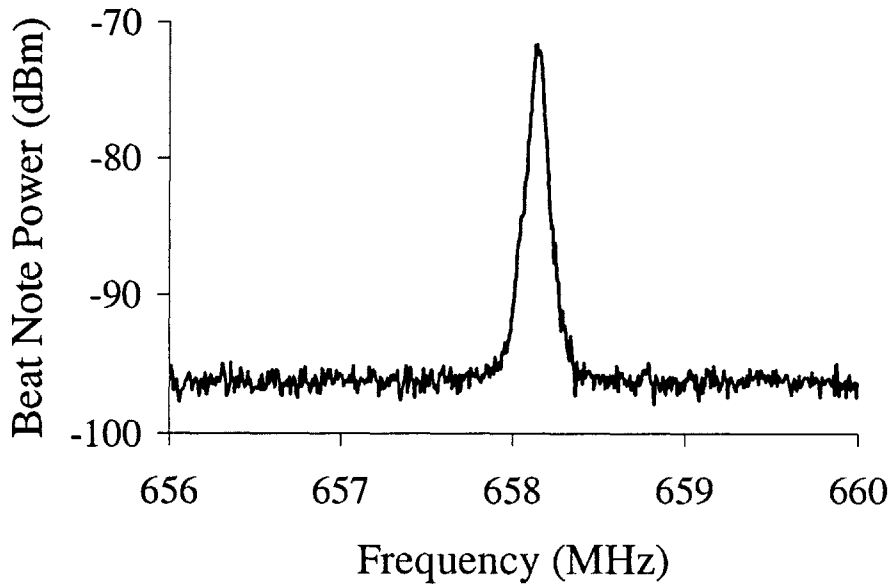


Figure 6-9: 100-trace average of frequency-stabilized  $3\delta$  beat signal. Total integration time is 5 s.

unstabilized beat signal. As a rule of thumb, the actual bandwidth of the phase-locked loop must be greater than the jitter linewidth of the beat signal. The jitter linewidth of the free-running  $3\delta$  beat signal was several MHz, which is much larger than the 10 kHz detection bandwidth for the frequency-stabilized  $3\delta$  beat signal. If we assume that the free-running beat signal has a 5-MHz jitter bandwidth and also that the phase-locked loop has the same 5 MHz bandwidth, the maximum SNR at the input to the phase-locked loop would be  $\sim 30 \text{ dB} - 10 \log_{10} (5 \text{ MHz}/30 \text{ kHz}) = 7 \text{ dB}$ , which could be insufficient for phaselocking since phaselocking typically requires at least 10 dB of SNR over the bandwidth of the phase-locked loop.

The signal-to-noise ratio can be improved in a number of ways. First, using a first-order grating period of  $7.2 \mu\text{m}$  for the first DFG interaction at an operating temperature of  $150^\circ\text{C}$  should yield a 9-fold improvement in the conversion efficiency in the first DFG stage. Second, at the time the double-grating PPLN was fabricated, the high voltage pulser we had was limited to 6 kV in output voltage. This limited the thickness of our PPLN sample to  $250\text{-}\mu\text{m}$  in thickness. Since then we have acquired a TREK Model 20/20 high voltage amplifier which can output high voltage pulses in excess of 20 kV. This allowed us to fabricate samples with thicknesses up to 0.75 mm.

With the increase in the thickness of the PPLN, we should be able to increase the length of future PPLN devices. By scaling the length of the PPLN crystal to 4 cm, we expect another 64-fold improvement in the beat signal rf power. Assuming Gaussian beam profiles for our laser beams, the beat signal rf power from the double-DFG interaction is proportional to  $l_1^2 l_2$  where  $l_1$  and  $l_2$  are the lengths of the first and the second DFG gratings, respectively. Instead of using the same grating length for the two DFG interactions, as was done for the work described in this thesis, one can also set  $l_1=2l_2$ , which would yield a slight 0.7 dB gain in the beat signal power. Hence, with a longer and thicker PPLN crystal composed of only first-order gratings, a total improvement of nearly 28 dB should be sufficient to phase lock the beat signal to an rf source.

## 6.6 Discussion

In this section a comparison is made between the 3-to-1 frequency division scheme described in this thesis with those reported by Pfister *et al.* [72] and Touahri *et al.* [12]. The fundamental difference lies in the fact that our 3-to-1 frequency division scheme employs input frequencies  $3f$  and  $2f$  in a dual-DFG scheme as shown in Fig. 6-1 (b), while in the schemes reported by Pfister *et al.* and Touahri *et al.*, the input frequencies were  $3f$  and  $f$  in a DFG-SHG process shown in Fig. 6-1 (a). Consider the DFG-SHG scheme with inputs at 532 nm ( $3f$ ) and 1596 nm ( $f$ ). Equation (2.16) gives an expression for the DFG output at 798 nm ( $2f$ ):

$$\frac{P_{2f}}{P_f P_{3f}} = \frac{16\pi d_{Q1}^2 L \bar{h}}{c\epsilon_o n_{3f} n_{2f} n_f \lambda_{2f}^2 (k_{3f}^{-1} + k_f^{-1})} = 1.4 \times 10^{-3}/W, \quad (6.13)$$

where we have assumed  $d_{Q1} = 5.8$  pm/V for a third-order QPM interaction,  $n_{3f} = 2.2370$ ,  $n_{2f} = 2.1783$ ,  $n_f = 2.1385$ ,  $L = 0.5$  cm, and  $\bar{h} = 0.463$ . The second QPM grating phasematches the second harmonic generation of 798 nm from 1596 nm. The second harmonic output power is given by

$$\frac{P'_{2f}}{P_f^2} = \frac{16\pi d^2_Q L \bar{h}}{c \epsilon_o n_{2f} n_f \lambda_f^3} = 1.8 \times 10^{-3}/W. \quad (6.14)$$

Here we assume  $d_Q = 15.5$  pm/V for the first-order QPM interaction. As discussed in Section 6.3 the beat-note rf power is proportional to the product of the output powers at frequency  $2f$ . That is,  $P_{beat} \propto P_{2f} P_f$ . From (6.13) and (6.14) we obtain

$$P_{2f} P'_{2f} = (2.5 \times 10^{-6}/W^2) P_{3f} P_f^3. \quad (6.15)$$

Now consider the dual-DFG scheme with inputs at 532 nm ( $3f$ ) and 798 nm ( $2f$ ). The DFG output at 1596 nm ( $f$ ) from the first DFG interaction is

$$\frac{P_f}{P_{2f} P_{3f}} = \frac{16\pi d^2_{Q1} L \bar{h}}{c \epsilon_o n_{3f} n_{2f} n_f \lambda_f^2 (k_{3f}^{-1} + k_{2f}^{-1})} = 5.7 \times 10^{-4}/W, \quad (6.16)$$

where we have again assumed the following:  $d_{Q1} = 5.8$  pm/V for the third-order QPM interaction,  $n_{3f} = 2.2370$ ,  $n_{2f} = 2.1783$ ,  $n_f = 2.1385$ ,  $L = 0.5$  cm, and  $\bar{h} = 0.4631$ . The DFG output at 1596 nm ( $f$ ) from the second DFG interaction is

$$\frac{P'_f}{P_f P_{2f}} = \frac{16\pi d^2_{Q2} L \bar{h}}{c \epsilon_o n_{2f} n_f^2 \lambda_f^2 (k_{2f}^{-1} + k_f^{-1})} = 2.3 \times 10^{-3}/W, \quad (6.17)$$

with  $d_{Q2} = 15.5$  pm/V. Here the beat note power is proportional to  $P_f P'_f$ . From (6.16) and (6.17) one obtains

$$P_f P'_f = 7.7 \times 10^{-10} P_{3f}^2 P_{2f}^2. \quad (6.18)$$

The ratio between the beat-note rf power for the two schemes is obtained by taking the ratio between (6.15) and (6.18):

$$\frac{P(3f, 2f)}{P(3f, f)} = \frac{7.7 \times 10^{-10} P_{3f}^2 P_{2f}^3}{2.5 \times 10^{-10} P_{3f} P_f^3} = 3.1 \times 10^{-4} P_{3f} \left( \frac{P_{2f}}{P_f} \right)^3. \quad (6.19)$$

where the powers are in units of W, and the same 1-cm-long PPLN used in our experiment is assumed for both cases. For  $P_{2f} = P_f$ , and  $P_{3f} = 75$  mW, as was the case for our experiment, the beat-note rf power for our scheme with input frequencies



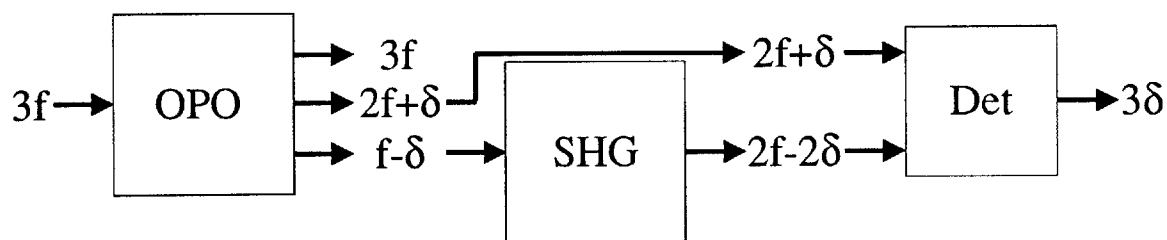


Figure 6-10: An OPO-based 3-to-1 optical frequency divider.

$3f$  and  $2f$  is smaller by a factor of 46 dB. The choice of the dual-DFG scheme with input frequencies  $3f$  and  $2f$  was dictated by the availability of input sources at  $3f$  (532 nm) and  $2f$  (798 nm) and also by our intention to build another 3-to-1 frequency divider pumped by the 798 nm source for use in the proposed optical-to-microwave frequency chain [23][24][25]. We should add that if we had used the DFG/SHG scheme for our 3:1 frequency divider (with the same input powers as the double-DFG scheme), the signal-to-noise ratio would be higher by 46 dB, which would be more than sufficient for phase-locking.

Furthermore, it is important to note that it is also possible to use an OPO for 3-to-1 optical frequency division, which would produce an even higher signal-to-noise ratio for the beat signal. Figure 6-10 illustrates a possible OPO-based 3-to-1 frequency division scheme.

Comparing the two ways of implementing a 3:1 optical frequency divider, one using an OPO and the other using DFG, one finds that using the OPO has the main advantage that the generated signal and idler outputs are both strong and in the 5 - 20 mW range for  $\sim 100$  mW of pump power. With the use of a double-grating PPLN, the SHG interaction can also be intra-cavity, thus yielding much higher efficiency ( $\sim 100$  times) than that for a single-pass SHG. This makes subsequent detection much easier because the signal-to-noise ratio is large. Furthermore, the OPO requires only one input pump source, while the double-DFG scheme requires two input sources in approximate 3:2 frequency ratios. The disadvantage of the OPO-based scheme is the complexity of operating the OPO in a highly stable manner. By contrast, the use of DFG greatly simplifies the frequency mixing process but at the expense of producing

a weak output at the idler frequency.

## 6.7 Summary

We have successfully implemented a frequency-stabilized three-to-one optical frequency divider of 532 nm based on consecutive DFG interactions in a double-grating PPLN crystal. By frequency-stabilizing the  $3\delta$  beat note signal to  $\pm 25$  kHz, we obtained a fractional uncertainty, defined as the ratio between the uncertainty in  $\delta$  and the optical frequency of the pump laser, of  $\pm 1.5 \times 10^{-11}$ . Our signal-to-noise ratio of 25-30 dB was not quite sufficient to implement a phase-coherent 3:1 frequency divider due to the noise of our input lasers. However, future improvements in conversion efficiency by the use of a longer PPLN sample with first-order QPM gratings or by the use of a PPLN OPO should allow us to achieve a phase-locked 3:1 optical frequency divider.

# Chapter 7

## Brewster-Angle PPLN OPO

This chapter describes the experiment which demonstrates a nearly degenerate doubly-resonant OPO with a Brewster-cut PPLN as the nonlinear medium. In Section 7.1, we provide the motivation for constructing a Brewster-cut PPLN OPO and compare our system with other works involved with doubly-resonant OPO's. The design and fabrication of the PPLN grating is discussed in Section 7.2, followed by a discussion of the design of the OPO cavity in Section 7.3. Characterization of the phasematching temperature and conversion efficiency with SHG and DFG is discussed in Section 7.4. Section 7.5 describes the experimental setup. The experimental results are discussed in Section 7.6, including a discussion of photorefractive effects which hampered the stability of our OPO system. Section 7.7 presents a discussion of our results and offers suggestions for future work.

### 7.1 Brewster-Cut-PPLN-Based OPO

As discussed in Chapters 1 and 2, OPO's are attractive sources of coherent radiation for their wide tuning range compared to traditional tunable lasers such as Ti:Sapphire and dye lasers. Numerous recent demonstrations of PPLN-based OPO's have been reviewed in Chapter 4. This chapter describes a PPLN-based doubly-resonant OPO with Brewster-cut facets. As discussed in Section 4.4, OPO's can be either singly resonant (SRO), in which only the signal field is resonant inside the resonator, or

doubly resonant (DRO), in which both the signal and idler fields are resonant. Doubly resonant OPO's have much lower threshold pump powers, typically on the order of a few mW to tens of mW for a 10-mm-long PPLN, compared to singly resonant OPO's whose threshold pump powers are typically 2 orders of magnitude higher. However, the trade-off for the lower threshold of doubly-resonant OPO's is the greater sensitivity of device performance on temperature, alignment, and mechanical and acoustical fluctuations since one needs to satisfy the resonance condition for both the signal and idler fields.

Our OPO work was motivated by the desire to implement a 3:1 optical frequency divider based on PPLN OPO's. As mentioned in Section 6.6, compared to the use of DFG interactions for 3:1 optical frequency division, an OPO requires only one laser input, and the signal-to-noise ratio of the beat is much higher due to substantially higher signal and idler output powers (typically 5-20 mW for a doubly-resonant OPO pumped at around 100 mW). A schematic of an OPO-based 3:1 frequency divider is shown in Fig. 6-11. Just like the DFG-based 3:1 divider, the 3:1 OPO-based divider can also be implemented with a double-grating PPLN designed to phasematch both the OPO as well as the SHG interactions. As discussed in Chapter 2, operation of a doubly-resonant OPO is over-constrained by the requirement of double resonance for the signal and idler fields. One way to relax this constraint is to construct separate cavities for the signal and idler fields, the so-called dual-cavity OPO. Dual-cavity OPO's have been demonstrated in type II OPO's in which the signal/idler output fields are orthogonally polarized and are separated by a polarizing beam splitter (PBS) [73][74]. Separation of the signal/idler fields cannot be accomplished with PBS for type I OPO's, whose signal/idler outputs are co-polarized, as is the case for our PPLN OPO. Instead, since the signal and idler output wavelengths are widely separated in a 3:1 optical frequency divider, we can utilize dispersion in  $\text{LiNbO}_3$  to construct a dual-cavity 3:1 PPLN OPO with Brewster-cut facets. The Brewster-cut facets serve the dual purpose of minimizing the reflection losses at the facets as well as physically separating the signal and idler fields, whose angles of incidence differ by  $\sim 2^\circ$  near Brewster angle for a 798-nm-pumped OPO with a signal/idler wavelengths at 1197

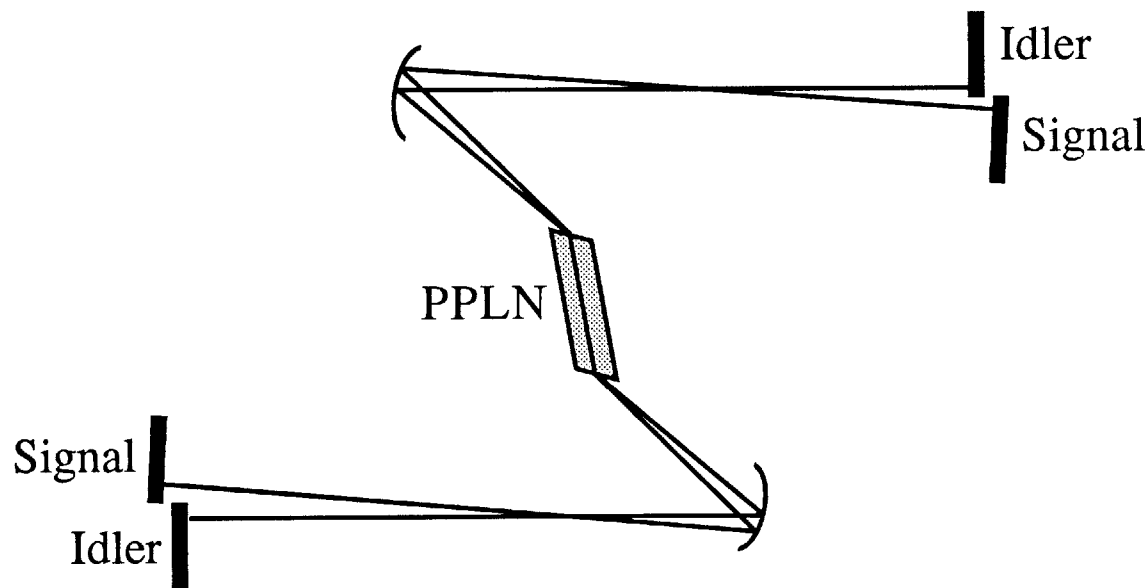


Figure 7-1: A Brewster-angle-cut-PPLN-based dual-cavity OPO. For widely separated signal/idler output wavelengths, the dispersion of  $\text{LiNbO}_3$  is utilized to separate the signal and idler beams to form a dual-cavity OPO.

nm and 2394 nm. Figure 7-1 illustrates a possible cavity configuration for such a 3:1 frequency divider.

To obtain low round-trip cavity losses, the nonlinear crystals in cw OPO's are typically AR-coated at the signal and idler wavelengths, with typical reflection losses of  $\sim 0.2\%$  per surface. The use of Brewster-cut facets eliminates the need for the typically expensive AR coatings. It can be calculated the facet losses at angles near the Brewster angle can be quite low, with a full-width angle acceptance of  $\sim 3^\circ$  for reflection losses below 0.1%. However, initially it was not clear to us whether scattering losses at the Brewster-polished surface was low enough to provide comparable or better performance than the use of AR coatings. The nearly degenerate OPO described in this chapter serves as a precursor to the aforementioned 3:1 Brewster-cut OPO, demonstrating successful operation of an Brewster-cut PPLN OPO. Furthermore, the nearly degenerate Brewster-cut PPLN OPO is interesting for the possibility of self-phase-locking at degeneracy. Self-phase-locking of the signal/idler output was observed by Nabors *et al.* in a birefringently phasematched  $\text{LiNbO}_3$  OPO in 1990 [69]. A PPLN-based self-phase-locked OPO, in principle, offers better stability with

respect to temperature fluctuations due to the fact that PPLN has a much wider temperature bandwidth ( $\sim 10$  K vs.  $\sim 1$  K) in the parametric gain than that for a birefringently phasematched  $\text{LiNbO}_3$ .

As noted in Chapter 4, cw PPLN DRO's have been demonstrated in 1995 by Myers *et al.* with a MOPA diode laser [50]. Nearly degenerate outputs at 1955 nm were detected. The work described in this chapter also demonstrates a nearly degenerate DRO, but differs from the work by Myers *et al.* in that the facets were polished at Brewster angle as opposed to the use of AR coatings, as was done in Myer's work [50]. However, the use of a Brewster-cut crystal also has drawbacks versus the conventional flat-polished geometry. Chief among them is the fact that the Brewster-angle facets introduces astigmatism between the tangential and sagittal components of each interacting field. Without any astigmatism compensation this results in the tangential component having a much larger beam size ( $\sim 3$ -4 times) and confocal parameter than the sagittal component inside the crystal. With a highly anisotropic spatial mode, one expects a higher threshold compared to an OPO with a circular resonator mode. Furthermore, without astigmatism compensation there is concern that the tangential component of the signal/idler field will be clipped by the 0.5-mm-thick crystal and thus incur excessive losses. For these reasons, we have constructed a 4-mirror folded resonator with 2 curve mirrors with non-normal incident angles for the purpose of astigmatism compensation. The specific cavity design will be presented in Section 7.3. Our work also differs from the work by Myers *et al.* in that the pump lasers are at different wavelengths. Our OPO was pumped at 798 nm while the OPO from Myers *et al.* was pumped at 978 nm [50].

## 7.2 Grating Design and Fabrication

Our PPLN crystal was 10-mm-long, 9-mm-wide, and 0.5-mm thick. The grating period was  $20.2 \mu\text{m}$ , designed for 1st-order QPM for a degenerate OPO pumped at 798 nm. The grating itself was 10 mm long and 8 mm wide, divided into 4 subsections with electrode widths designed to compensate for 2-5  $\mu\text{m}$  of domain spreading. For

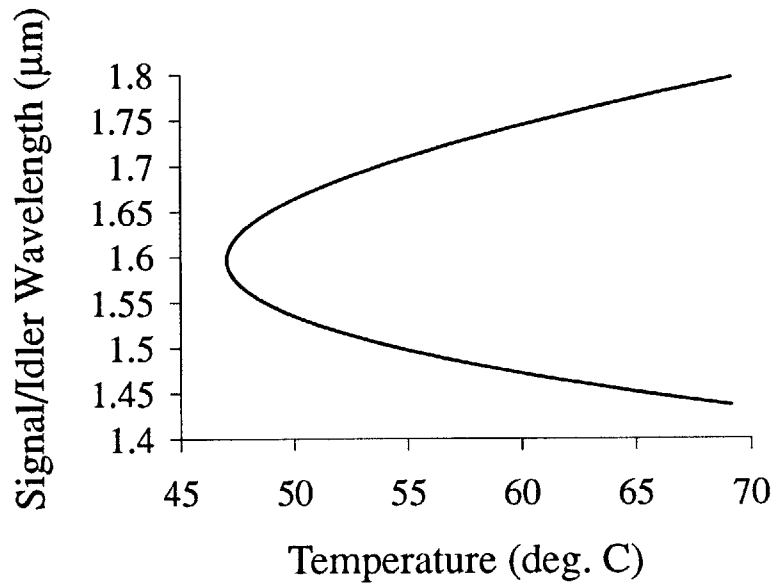


Figure 7-2: Temperature turning curve of a nearly degenerate PPLN-based OPO pumped at 798.4 nm with a 20.2  $\mu\text{m}$  grating period. The tuning curve is calculated from Sellmeier's equations.

a pump wavelength of 798.4 nm, the phasematching temperature at degeneracy ( $\lambda_s = \lambda_i = 1596.8$  nm) is calculated to be 47.0°C based on Sellmeier's equations by Edwards [30]. Figure 7-2 shows the calculated temperature tuning curve of the OPO. The spectral bandwidth of the PPLN OPO near degeneracy is calculated to be  $\sim 150$  nm assuming a 10-mm interaction length. The corresponding temperature acceptance bandwidth at degeneracy is  $\sim 8.4^\circ\text{C}$ . Our PPLN was fabricated using standard procedures described in Chapter 3. Following E-field poling the PPLN sample was diced to a length of 10 mm and a width of 9 mm (8 mm of grating width + 0.5 mm additional single-domain LN on each side). The sample was then sent to Optics Ltd. for Brewster-angle polishing. Figure 7-3 shows plots of the reflection coefficient for the air-LiNbO<sub>3</sub> interface at the degenerate signal/idler wavelength of 1596 nm. In Fig. 7-3 we have assumed that the  $z$ -axis of the LiNbO<sub>3</sub> crystal lies in the plane of incidence. The dashed and solid curves refer to the ordinary and extraordinary polarized fields, respectively. The Brewster angle corresponding to the  $e$ -wave of LiNbO<sub>3</sub> is 64.9°, which yields a refracted angle of 25.1°. Figure 7-4 illustrates the geometry of the Brewster-cut crystal. For OPO applications we demand that the power loss at

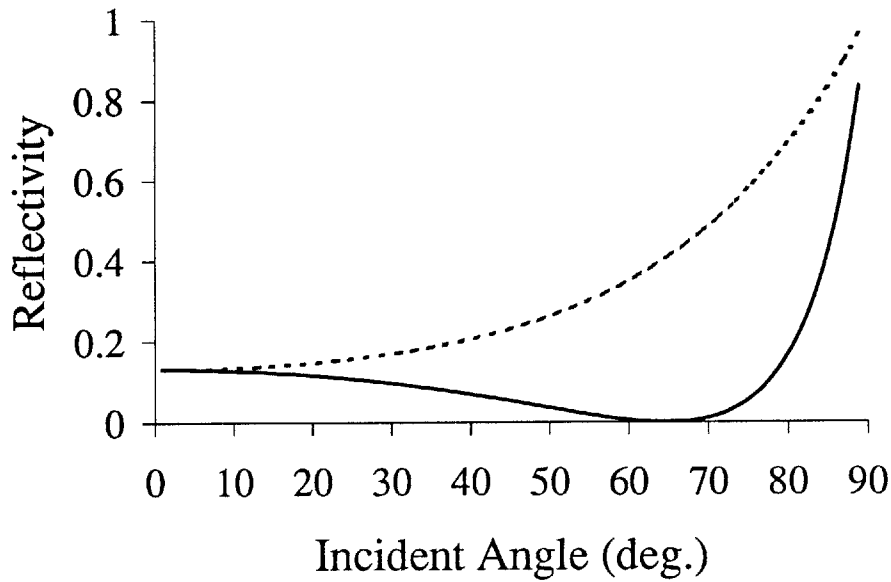


Figure 7-3: Reflectivity of air-LiNbO<sub>3</sub> interface as a function of angle of incidence for ordinary-polarized (dashed curve) and extraordinary-polarized (solid curve) fields. The orientation of the LiNbO<sub>3</sub> is such that the crystal z axis is in the plane of incidence.

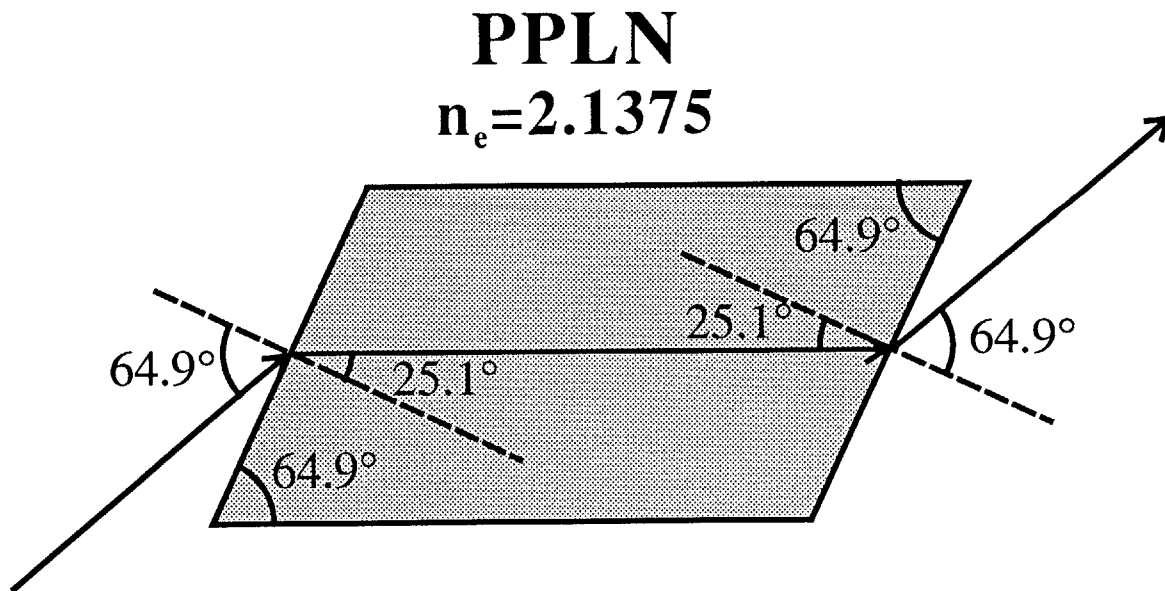


Figure 7-4: Brewster-angle refraction at the air-LiNbO<sub>3</sub> interface for  $\lambda = 1596$  nm.



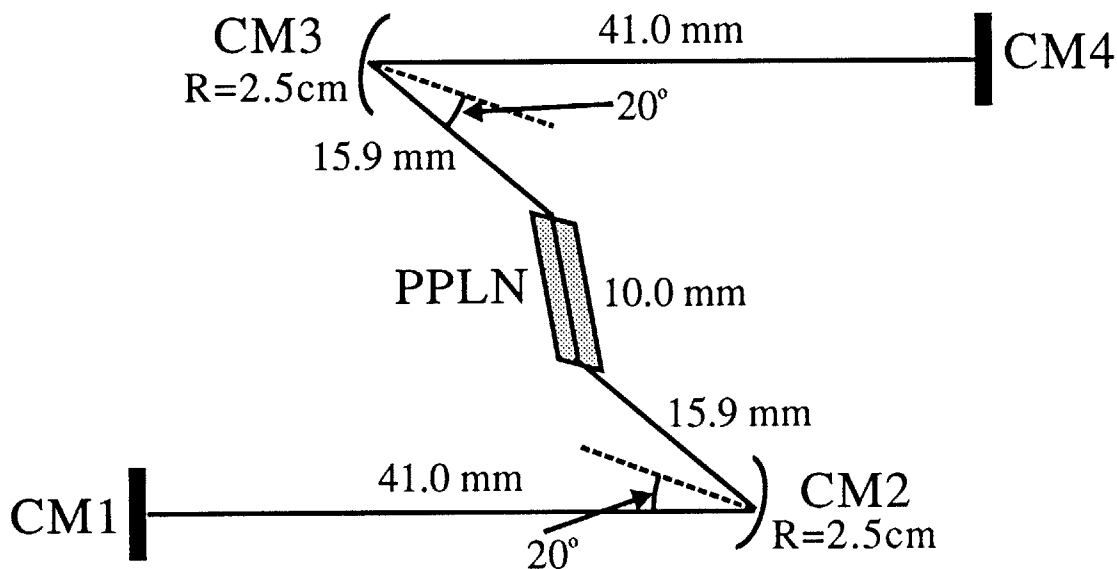


Figure 7-5: Cavity design for nearly degenerate Brewster-angle-cut PPLN OPO. The curve mirrors CM2 and CM3 are used to compensate for the astigmatism introduced at the Brewster-cut surface.

each facet be 0.1% or less. This corresponds to a tolerance of  $3.6^\circ$  in the Brewster angle, and a corresponding tolerance of  $0.78^\circ$  in the refracted angle.

### 7.3 OPO Cavity Design

Figure 7-5 shows a schematic of the 4-mirror OPO cavity with the 10-mm-long Brewster-cut PPLN. Mirrors CM1 and CM4 were 25.4-mm-diameter 9-mm-thick flat high reflectors at the signal/idler wavelength of 1596 nm. Mirrors CM2 and CM3 were 7.75-mm-diameter 4-mm-thick high reflectors at 1596 nm with a 25-mm radius of curvature. The two curved mirrors had incident angles of  $20^\circ$  to compensate for astigmatism introduced at the Brewster-angle facets of the crystal. In our cavity design CM2 and CM3 were spaced 15.9-mm from the PPLN Brewster-angle facets and 41.0 mm from the flat mirrors CM1 and CM4, respectively. The beam waist was located at the center of the PPLN crystal with a confocal parameter of 11.5 mm inside the crystal at  $\lambda = 1596$  nm. Two additional beam waists at CM1 and CM4 had confocal parameters of  $b(\tan) = 7.5$  mm and  $b(\text{sag}) = 30.4$  mm. The pump laser

at 798 nm entered the cavity from CM3 with an angle of incidence of  $17.5^\circ$  and was focused into the cavity with apparent confocal parameters of  $b(\tan)= 0.55$  mm and  $b(\text{sag})= 3.0$  mm, located at 14.8 mm and 16.3 mm, respectively, beyond the front facet (flat side) of CM3. The input coupler CM3 transmitted  $\sim 96\%$  of the incident pump power. In order to aid our alignment of the 4-mirror cavity and to measure the round-trip cavity losses at the signal/idler wavelength, we also mode-matched the output of a probe laser at 1596 nm into the cavity from CM1.

## 7.4 Experimental Setup

This section describes the experimental setup for the 798-nm-pumped nearly-degenerate DRO with a Brewster-cut PPLN.

### 7.4.1 798 nm laser system

Details to the 798 nm pump laser system has been described in Chapter 5 and will not be elaborated here.

### 7.4.2 1596 nm laser system

As mentioned in Section 7.3, to assist us in aligning the 4-mirror DRO cavity and characterize the cavity losses at the signal/idler wavelength, we mode-matched the output of a probe laser near  $1.6 \mu\text{m}$  into the DRO cavity. The probe laser was a New Focus Model 6263 external-cavity tunable diode laser with outputs tunable from 1570 nm to 1630 nm. Typical maximum output power was 3.7 mW around 1593 nm. The laser could be coarse-tuned from 1570 nm to 1630 nm at intervals of 0.01 nm and also fine-tuned with a piezo-electric transducer (PZT). Slight tuning of the laser frequency is also possible by changing the temperature of the laser diode, but we typically kept the temperature fixed at  $20^\circ\text{C}$ , as recommended by the manufacturer.

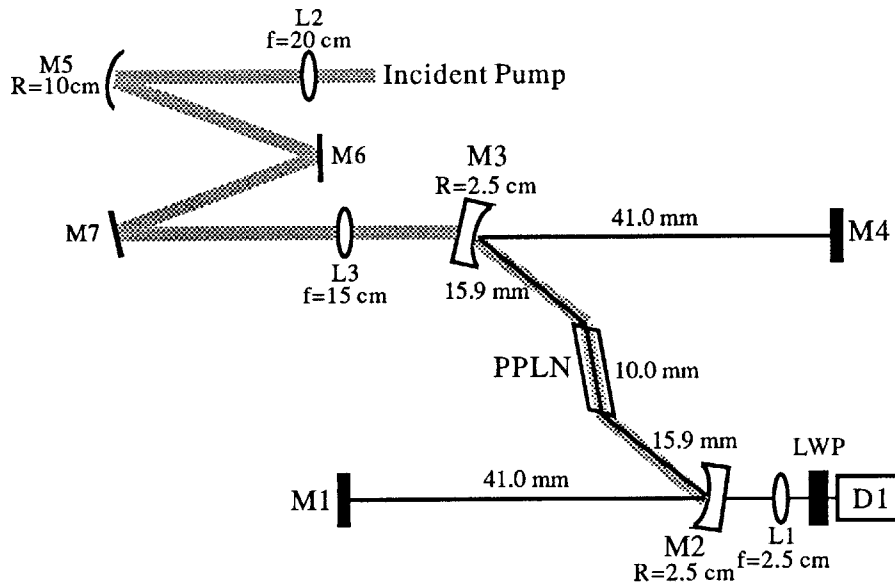


Figure 7-6: Experimental setup for nearly degenerate OPO based on Brewster-cut PPLN.

### 7.4.3 Optics for pump laser system

Shown in Fig. 7-6 is a schematic for the optics used for mode-matching the 798 nm pump laser into the DRO cavity. In order to mode-match to the DRO cavity with a circular beam profile with confocal parameter of  $b=11.5$  mm at the center of the crystal, the pump laser must be astigmatic at the input coupler CM3. Recall from Chapter 5 that the output of the tapered amplifier is slightly astigmatic, even after correction with a cylindrical lens. For this experiment we first corrected for the astigmatism with a curve mirror with a 25 mm radius of curvature (not shown in Fig. 7-6) and then used another curve mirror (AM1) with a 100 mm radius of curvature to generate the desired amount of astigmatism. The astigmatic pump beam was focused by a  $f=150$  mm plano-convex lens into the input coupler CM3 at an incident angle of  $17.5^\circ$ . The refracted angle (in air) at the opposite side of CM3 is  $19.2^\circ$ . The input coupler CM3 transmitted  $\sim 96\%$  of the pump power at 798 nm. Because of dispersion, the incident angle at the crystal facet was  $67.3^\circ$  for the pump beam, which was  $2.4^\circ$  larger than the  $64.9^\circ$  incident angle at the signal/idler wavelength. This also implies a theoretical power loss of  $1.4\%$  at the crystal facet due to Fresnel reflection for the

pump. The transmitted pump beam from the crystal was mostly transmitted through the curve mirror CM2 and then blocked by the mirror mount which housed CM2. A small portion of the pump was reflected from mirror CM2 and exited the cavity from the flat mirror CM1.

#### 7.4.4 Optics for probe laser system

Although the probe laser output was not directly involved in the OPO interaction, it served 3 important functions in our experiment. First, it was used to align the complicated 4-mirror DRO cavity that would be very difficult to align otherwise. Second, by scanning the cavity length with a PZT and measuring the finesse, we could determine the round-trip cavity losses at the signal/idler wavelength. This information is essential for estimating the threshold pump power. Third, in order for the OPO to reach threshold, the nonlinear gain provided by the pump must exceed the total cavity loss over 1 round-trip inside the cavity. With sufficient nonlinear gain at the signal/idler wavelength, it was possible to amplify a signal significantly at that wavelength with a pump power that is below threshold. By injecting the probe laser into the OPO cavity and scanning the cavity length, one would look for amplification of the probe resonance as a precursor to optical parametric oscillation.

Figure 7-7 shows a schematic of the optics for the probe laser system. The probe laser was first circularized and collimated (not shown) and then focused into the input coupler CM1 by a  $f=150$  mm plano-convex lens. Prior to the focusing lens a 1-mm-thick glass slide was inserted as a beam splitter to direct a fraction of the reflected probe laser beam into an InGaAs photodetector (D2) for monitoring and measurement purposes which will be explained later. The cavity mirrors CM1 through CM4 were each mounted on LEES mirror mounts. CM2 was mounted directly on a 4-stack PZT (Piezo Kinetics Model SR0.400-0.225-0.050-552) with an overall scanning rate of 4 nm/volt. A fraction ( $\sim 0.2\%$ ) of the circulating power inside the cavity was coupled out from CM2 and focused into another InGaAs detector (D1) by a  $f=25$  mm plano-convex lens. The InGaAs detector D1 had a responsivity of 1.1 A/W and a transimpedance gain of either  $10^4$  or  $10^5$  V/A (selectable by a switch).

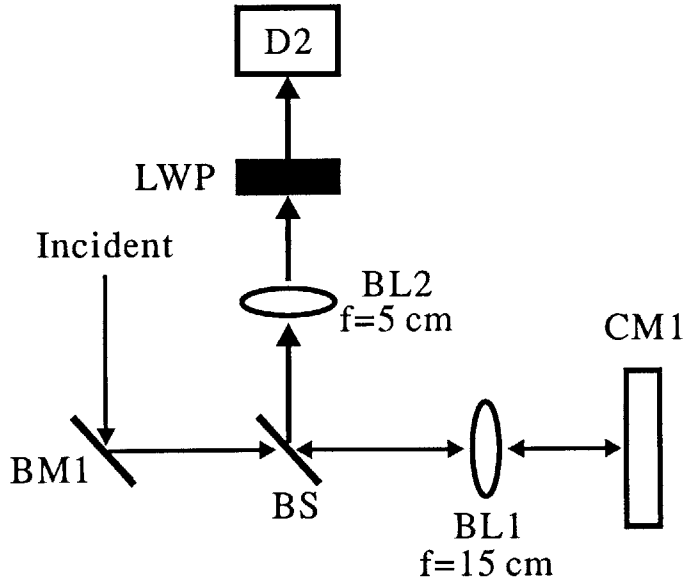


Figure 7-7: Optics for probe laser system. D2: InGaAs photodetector with responsivity of 0.68 A/W. CM1: input coupler for 4-mirror OPO cavity.

#### 7.4.5 Finesse measurements

We measured the finesse of the DRO cavity by scanning the cavity length over 1 free spectral range (FSR),  $\lambda/2 \sim 800$  nm, and observing the cavity transmission at detector D1. The finesse  $F$  of the cavity is defined as the ratio between the free spectral range and the FWHM linewidth of the cavity resonance. The round-trip cavity loss of the cavity can be approximated as  $a \sim 2\pi/F$ . Based on measurements of the finesse of the empty cavity (cavity without the PPLN crystal) and direct transmission measurements of the cavity mirrors, the reflectivities of each of the 4 cavity mirrors were determined and listed in Table 7.1. The total round-trip loss of the cavity is the sum of losses due to the cavity mirrors and residual losses at the crystal facets. Over one round-trip the probe beam makes 1 reflection each off CM1 and CM4, 2 reflections each off CM2 and CM3, and 2 passes through the PPLN crystal (4 incidences at the crystal facets). By adding up the mirror losses, we obtained a total round-trip cavity loss of  $\sim 0.8\%$ . We typically measured finesse of 420 to 480 for our cavity, which implies a round-trip cavity losses of 1.3% to 1.5%. This suggests that the reflection losses at each of the PPLN crystal facet were about 0.13% to 0.18%.

Mirror	Reflectivity
M1	$\geq 99.99$ %
M2	99.8 %
M3	99.8 %
M4	$\geq 99.99$ %

Table 7.1: Mirror reflectivities of the OPO cavity mirrors at 1593 nm

### 7.4.6 Single-pass DFG measurement

To properly align the pump laser beam to the OPO cavity we first performed a single-pass DFG measurement between the pump laser and the probe laser, to which the 4-mirror DRO cavity was aligned. By maximizing the DFG output signal we achieved the best overlap between the pump and the probe beams. In principle the signal/idler beam path should be identical to the probe beam path inside the cavity when the cavity was optimally aligned. Therefore, the single-pass DFG measurement provided a good starting point for aligning the pump beam to the signal/idler beam path. As discussed in Section 7.3, the single-pass DFG measurement was also useful in characterizing the effective interaction length of the PPLN crystal, which could be used to estimate the threshold of the DRO. The DFG interaction took place between the transmitted pump beam and the retro-reflected probe beam that was transmitted back through the crystal. We removed the front mirror (CM1) such that the full power of the probe beam could be used in the single-pass DFG interaction. The generated DFG output was then reflected by mirror CM2 to the glass slide (BS) (see Fig. 7-7) where a fraction ( $\sim 6\%$ ) was reflected and then focused by a  $f=50$  mm plano-convex lens into detector D2. A long-wave-pass (LWP) filter which transmits  $\sim 90\%$  of the probe beam power was positioned before the detector to filter out the residual 798-nm light. Typically we walked the mirror AM1 and the focusing lens AL1 of the pump laser system (see Fig. 7-6) both horizontally and vertically to peak up the DFG output signal. In addition we also maximized the DFG signal by moving lens AL1 along the direction of propagation. To detect the single-pass DFG we chopped the pump laser beam at 350 Hz using a mechanical chopper. The synchronously detected output signal was then amplified by a factor of 33 times and high-pass-filtered at 20 Hz. The

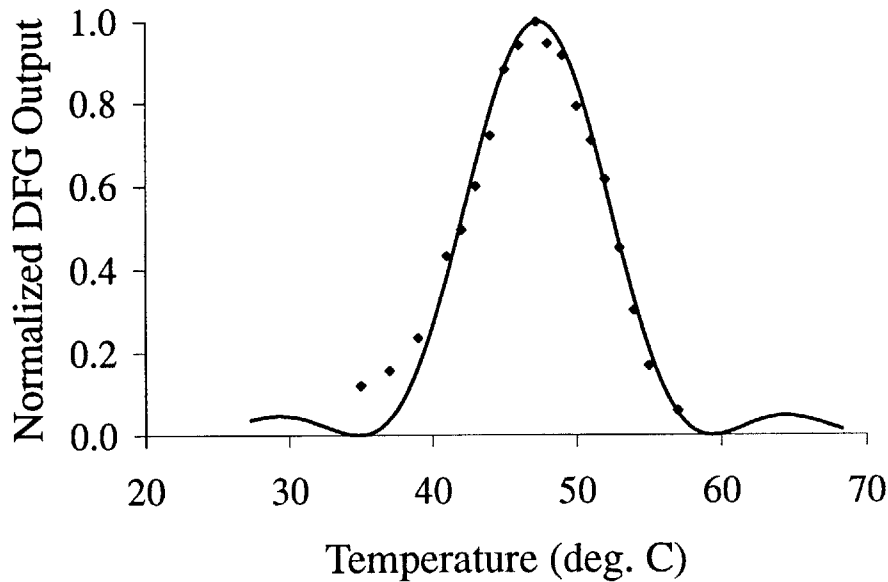


Figure 7-8: Temperature tuning of single-pass DFG efficiency between the pump laser at 798 nm and probe laser output at 1596 nm. The solid curve is calculated from the Sellmeier's equations.

detector D2 had a responsivity of 0.68 A/W and a transimpedance gain of  $10^4$  V/A.

For an input pump power of 110 mW (at the input coupler CM1) and probe input power of 2.6 mW, we expected a DFG output power of  $1.3 \mu\text{W}$  based on an effective nonlinear coefficient of  $d_Q = (\frac{2}{\pi}d_{33}) = 15.5 \text{ pm/V}$  and an effective length of 7.7 mm determined by the temperature tuning measurements to be discussed below. We measured an output power of  $0.80 \mu\text{W}$ . The measured efficiency is  $\sim 7\%$  less than that based on an effective nonlinear coefficient of  $d_Q = 12.6 \text{ pm/V}$  determined for the 20.1- $\mu\text{m}$  grating section of the double-grating PPLN in Chapter 6. The discrepancy was probably due to the fact that the 1.6  $\mu\text{m}$  probe beam was not astigmatically compensated and thus was not well mode-matched to the signal/idler cavity mode. Figure 7-8 shows the measured temperature tuning of the DFG output power for a pump wavelength of 798.4 nm and a signal wavelength of 1593.0 nm. Based on calculations using the Sellmeier's equations, we expected a peak phasematching temperature of  $47.0^\circ\text{C}$  and a FWHM bandwidth of  $8.4^\circ\text{C}$ . The measured peak phasematching temperature was  $47.2^\circ\text{C}$ , with a FWHM bandwidth of  $10.9^\circ\text{C}$ . The effective interaction length based on the DFG measurement was  $\sim 77\%$  of the physical length of 10 mm.

Part of the reduced interaction length was due to the fact that the aluminum blocks which sandwiched the PPLN were only 9 mm long, and therefore, only the central 9-mm portion of the PPLN crystal was in good thermal contact with the TE cooler. Therefore, the effective interaction length of 7.7 mm is  $\sim 85\%$  of the 9-mm thermally contacted region of the PPLN, which is consistent with results from the single-pass DFG measurement for the double-grating PPLN discussed in Chapter 6.

## 7.5 Results

We present the results in this section, demonstrating stable DRO output. We also discuss evidence of optical damage to the PPLN sample that prevented cw OPO from lasing for extended periods of time.

### 7.5.1 OPO threshold estimate

We estimate the pump threshold for the 4-mirror PPLN DRO based on our knowledge of cavity losses derived from the finesse measurements, our estimate of the focusing parameters of the pump, signal, and idler beams. From Eq. (2.52) the expression for the OPO threshold is given by

$$P_{th} = \frac{c\epsilon_o n_p n_s n_i \lambda_s \lambda_i (1/k_s + 1/k_i)}{64\pi d_{eff}^2 L \bar{h}_m} \quad (7.1)$$

The round-trip cavity losses  $a_s$ ,  $a_i$  were obtained from the cavity finesse measurements. We typically measured finesse values from 420 to 480 for a damage-free PPLN sample. Assuming a finesse of 420,

$$a_s = a_i \sim \frac{2\pi}{F} = 0.015$$

Based on results from the single-pass DFG measurements, the effective interaction length of our PPLN was  $\sim 7.7$  mm, and based on our cavity design, the confocal parameters of the signal and idler beams were  $b_s = b_i = 11.5$  mm. The estimated reduction factor  $\bar{h}$  is then  $\bar{h} \sim 0.59$ . Substituting these number into Eq. (7.18), and



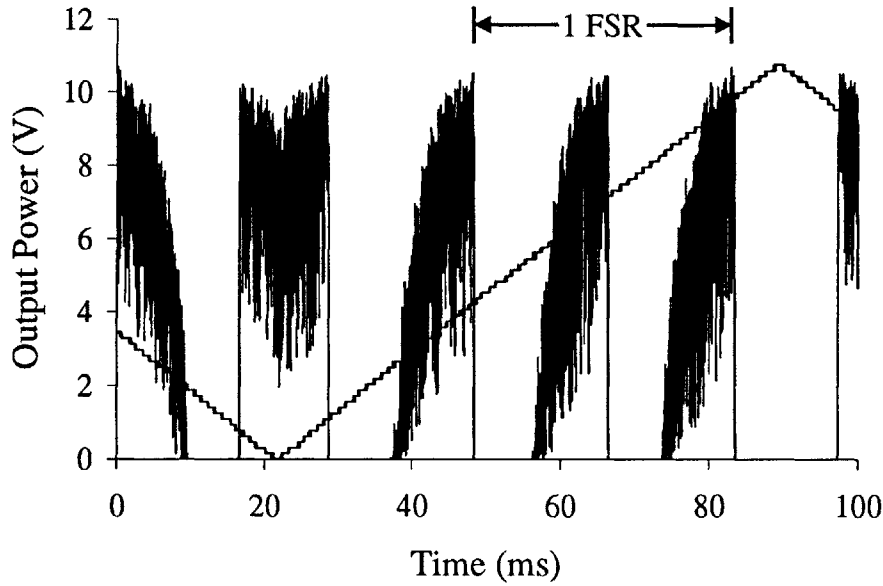


Figure 7-9: Trace of OPO output vs. scanned cavity length. D1 detector setting:  $10^4$  V/A. FSR: free spectral range. Scanning voltage and its digitizing noise is also shown.

assuming an effective nonlinearity of 12.6 pm/V from (6.83), the threshold pump power was estimated to be 25 mW.

### 7.5.2 OPO threshold/output

We were successful in obtaining above-threshold OPO operation for a pump wavelength of 798.35 nm. Figure 7-9 shows a trace of the DRO outputs with a pump power of  $\sim 145$  mW and a crystal temperature of  $48.3^\circ\text{C}$ . The threshold pump power was measured to be  $\sim 105$  mW for the trace shown in Fig. 7-9. The minimum threshold was 90 mW inside the crystal, which took into account the pump transmission losses at the input coupler and at the front facet of the PPLN crystal. The OPO outputs could be observed between  $46.5^\circ\text{C}$  and  $52.5^\circ\text{C}$ , suggesting that the signal and idler outputs could be tuned from degeneracy at 1596.7 nm to  $\sim 1695$  nm for the signal and to  $\sim 1510$  nm for the idler. In order to observe the DRO outputs, we typically had to start from the optimized alignment for the single-pass DFG measurement and then walked the pump beam a little both vertically and horizontally before the DRO outputs were observed. To peak up the DRO output power, we adjusted the 4 cavity

mirrors and tuned the cavity length slightly by adjusting the end mirrors. In a typical run, we could leave the OPO alone and observe the lasing continuously (while scanning the cavity with the PZT) for up to  $\sim 10$  minutes. However, over time the DRO output would decrease and even disappear momentarily. At this point we needed to adjust the cavity mirrors and/or translate the pump along the  $z$ -direction to recover the DRO outputs. By making periodic adjustments we were sometimes, but not always, able to sustain the DRO outputs for longer periods of time. At a pump power of 145 mW and a threshold of 105 mW (as shown in Fig. 7-9), the measured DRO output power coupled from the curve mirror CM2 was  $\sim 1$  mW. We expect an equal amount of signal/idler output to be coupled from the curve mirror CM3 which has the same transmission as CM2. The transmission from the flat mirrors CM1 and CM4 are about 2 orders of magnitude lower and are thus negligible. The total coupled output power is thus approximately 2 mW. The circulating signal/idler power was estimated to be  $\sim 560$  mW. Figure 7-9 shows two sets of the OPO signal/idler outputs over 1 cavity free spectral range. Each set of OPO outputs corresponds to OPO frequency clusters with integral and half-integral values of the total cavity mode number  $m = m_s + m_s$ . The OPO output peaks within each set correspond to the individual signal/idler axial modes. The individual axial modes seen in Fig. 7-9 do not necessarily belong to the same frequency cluster since the gain bandwidth of our degenerate PPLN OPO ( $\sim 175$  nm) is wide enough to encompass more than one frequency cluster.

The OPO clusters shown in Fig. 7-9 exhibit the well-known thermal hysteresis effect for doubly-resonant OPO's in which the clusters exhibit asymmetric intensity profiles as a function of the cavity length. Ideally, in the absence of thermal effects, one expects a symmetric cluster intensity profile centered around the optimum phase-matched condition as the cavity length is scanned at a uniform rate. As the cavity length is scanned, the OPO output intensity increases at first as the signal/idler output frequencies approach the optimal phasematching condition. The peak intensity corresponds to the mode pair under optimal phasematching. As the cavity length is scanned past the point corresponding to optimal phasematching, the OPO output

intensity begins to decrease.

The asymmetry of the OPO output intensity profile shown in Fig. 7-9 can be explained by incorporating the effects of thermal expansion (and contraction) of the PPLN crystal under above-threshold OPO operation. For our OPO cavity, an increase in the PZT voltage (up ramp shown in Fig. 7-9) increases the OPO cavity length via contraction of the PZT mounted on the cavity mirror CM2. The buildup of the circulating intensity of the signal/idler fields results in a slight temperature increase of the crystal because of crystal absorption. As a result, the crystal expands, which in turn decreases the optical path length of the OPO cavity. This effectively reduces the rate of expansion of the cavity length during the phase where the OPO output intensity increases as a function of increasing cavity length. The thermal effects thus produces a more gradual increase in the OPO output intensity as a function of increasing PZT voltage (or time) compared to the ideal case where thermal effects are neglected. After the peak intensity is reached, however, the OPO output intensity begins to decrease as the cavity length is scanned away from the optimum phase-matched condition. In this second phase the thermal effect acts instead to increase the optical path length of the OPO cavity and thus accelerate the rate of expansion of the cavity length. Consequently, one expects to see a more precipitous decrease in the OPO output intensity as a function of increasing PZT voltage (or time).

Attempts were made to stabilize the OPO outputs by stabilizing the cavity length with a PZT, but our efforts were hampered by the presence of photorefractive damage which limited the duration of the OPO to only a few minutes at a time. We routinely observed a steady decrease in the OPO output power until the OPO ceased to operate altogether. Typically we could sustain continuous OPO operation for 5-12 minutes. We typically measured an increase in the round-trip cavity losses at  $\sim 1.6 \mu\text{m}$  of  $\sim 0.4\%$  to  $1\%$  after the OPO ceased to operate. Each time after we have induced "damage" following operation of the OPO, we would translate the crystal by a few hundred  $\mu\text{m}$ 's to operate at a fresh spot. However, this typically required realignment of the cavity mirrors. Our efforts to characterize the photorefractive damage are discussed in the next section.

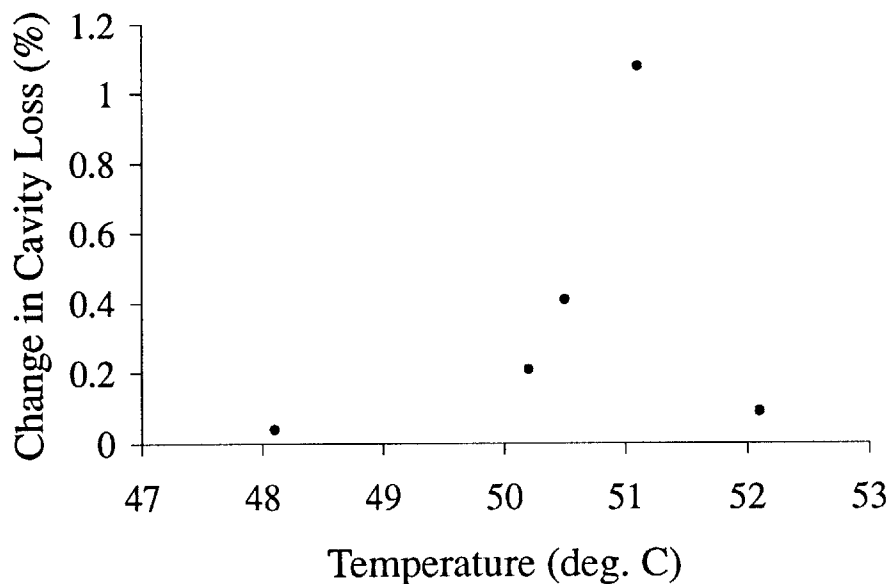


Figure 7-10: Increase in round-trip cavity loss vs. temperature at 1596 nm after 15-minute illumination with 150 mW of pump.

### 7.5.3 Optical damage

We have observed evidence of UV generation due to second harmonic generation by the pump beam. The UV generation was observed by placing a white piece of paper next to the facet where the pump beam exited the PPLN and observing a fluorescent blue spot. For a pump wavelength of 798.4 nm, we observed that the intensity of the UV was maximized at  $\sim 51^\circ\text{C}$ . The blue spot could be observed between  $49.8^\circ\text{C}$  and  $52.0^\circ\text{C}$ . We attempted to correlate the intensity of the UV generation with photorefractive damage by sending the pump beam through the PPLN crystal at a few temperature settings between  $50^\circ\text{C}$  and  $52^\circ\text{C}$  for 15 minutes and then measuring the increase in the round-trip cavity loss by comparing the cavity finesse before and after the pump illumination. Figure 7-10 shows a plot of the increase in cavity loss as a function of temperature. The round-trip cavity loss did indeed have a strong correlation with the generated UV intensity. We also performed some simulations on the amount of UV that would be generated for our PPLN sample. The coherence length for frequency doubling 798.4 nm in PPLN is  $\sim 1.27 \mu\text{m}$ ,  $\sim 1/8$  of the designed domain length of  $10.1 \mu\text{m}$ . Under the ideal case of zero random duty cycle error, we

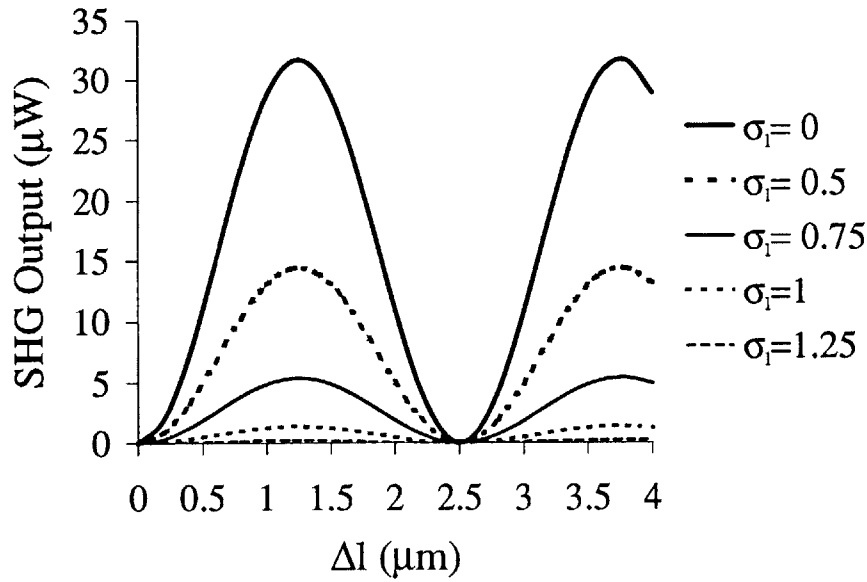


Figure 7-11: 8th-order QPM SHG of 798.4 nm as a function of  $\Delta l$ , the deviation from the ideal 50/50 duty cycle, for 5 different values of  $\sigma_l$  ( $\mu\text{m}$ ), the standard deviation of the random duty cycle error.

would expect to generate insignificant amounts of UV, which was confirmed by our simulation. However, it was unclear to us as to whether this remains true when there exists random duty cycle error, especially when the standard deviation of the domain length variation is large compared to the coherence length.

The 1st-order QPM grating period for frequency doubling 798.4 nm in PPLN is  $\sim 2.525 \mu\text{m}$ , exactly 1/8 of the  $20.2 \mu\text{m}$  grating period for our PPLN crystal. The 8:1 ratio suggests that the UV generation could be due to 8th-order QPM-SHG of the pump at 798.4 nm, even though under the ideal case of 50/50 duty cycle and zero random duty cycle there would be no conversion from an even-order QPM interaction. Figure 7-11 shows a theoretical plot of an 8th-order QPM SHG of 798.4 nm as a function of  $\Delta l$ , the deviation from the ideal 50/50 duty cycle, for different values of  $\sigma_l$ , the random duty cycle standard deviation. The plot is based on Eqs (2.94) and (2.97) in Chapter 2. In Fig. 7-11, we've also assumed a pump power of 150 mW. From Fig. 7-11, the deviation  $\Delta l$  from the ideal 50/50 duty cycle needed to phasematch the 8th-order QPM interaction is  $\Delta l = 1.2625 \mu\text{m}$ , which is precisely the coherence length of the SHG interaction. The corresponding duty cycle is 56.25% (or 43.75%)

Section	$\Delta l$ ( $\mu$ m)	$\sigma_l$ ( $\mu$ m)
1	2.57	1.10
2	1.19	0.35
3	1.16	0.34
4	2.75	0.47
5	2.44	0.78

Table 7.2: Measured average duty cycle error  $\Delta l$  and random duty cycle error  $\sigma_l$  for different sections along the length of the 10-mm PPLN sample with  $\Lambda = 20.2 \mu\text{m}$ . Each section is 2-mm long.

for the  $20.2 \mu\text{m}$  grating period of our PPLN. The effective nonlinearity  $d_Q$  of a QPM interaction is given by Eq. (2.93) as

$$d_Q = \sum d_{eff} \sin(\pi m D) \quad (7.2)$$

For  $m = 8$  we find that  $d_Q$  is maximized when the duty cycle  $D$  takes on the following values:  $1/16, 3/16, \dots, 15/16$ .

We measured the duty cycle and random duty cycle error for different parts of our PPLN crystal by sampling 5 evenly spaced regions along the length of the grating. In each region we sampled  $\sim 15$ -25 grating periods and measured the duty cycles for each period. Table 7.2 shows the results of our duty cycle and random duty cycle error measurements. There is significant non-uniformities in the poled domains for our PPLN sample. The spreading  $\Delta l$  of the domain lengths beyond the 50/50 cycle ratio ranges from  $1.2 \mu\text{m}$  to  $2.7 \mu\text{m}$ . The random duty cycle error  $\sigma_l$  also varied significantly, ranging from  $0.34 \mu\text{m}$  near the middle of the sample to  $1.1 \mu\text{m}$  at one of the ends.

In our simulation we modeled our PPLN as divided into 5 2-mm-long sections, with each section having a constant  $\Delta l$  and duty cycle error  $\sigma_l$  given by Table 7.2. For the random duty cycle errors  $\sigma_l$  we used a normal distribution with zero mean and standard deviation  $\sigma_l$  given in Table 7.2. Figure 7-12 shows a plot of the simulated UV output power as a function of temperature deviation from the peak phasematching temperature for a pump power of 150 mW at 798.4 nm. From Fig. 7-12 one sees that the peak UV output power could be a few  $\mu\text{W}$ . The peak phasematching temperature

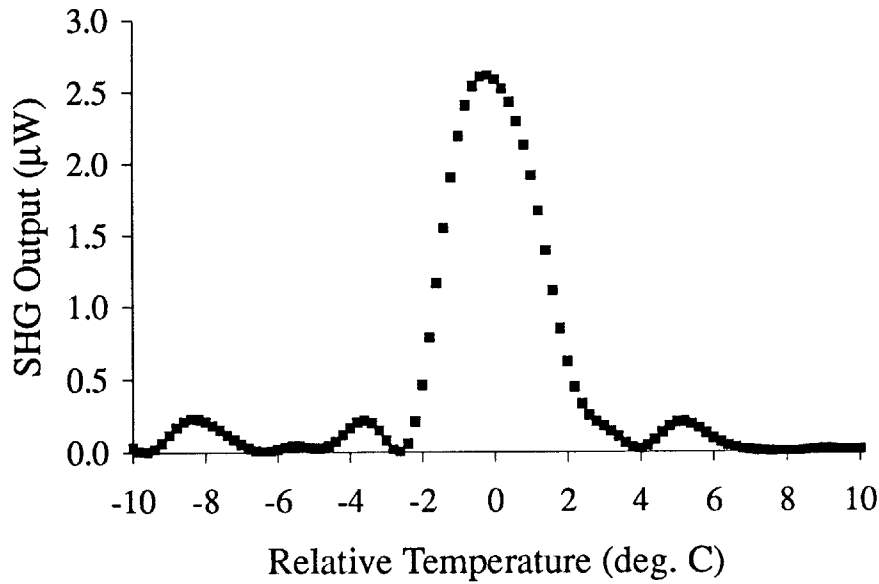


Figure 7-12: Simulated second harmonic output power as a function of temperature deviation from the peak phasematching temperature for 150 mW of fundamental input power at 798.4 nm. Secondary intensity peaks are spaced a few degrees C from the main intensity peak.  $\sigma_l$  and  $\Delta l$  of Table 7.2 are used.

calculated from our simulation is  $74^\circ\text{C}$ , which is  $\sim 23^\circ\text{C}$  larger than the observed peak at  $51^\circ\text{C}$ . We attributed the discrepancy to the accuracy of the Sellmeier's equations which were used to calculate the coherence lengths for the QPM. Figure 7-12 also shows the existence of secondary intensity peaks spaced a few  $^\circ\text{C}$  from the main peak. This also matched our visual observations of the temperature tuning behavior of the UV generation. The FWHM bandwidth of the UV intensity is  $\sim 3^\circ\text{C}$ , which is consistent with our observation. By using a different set of random numbers with the same values for  $\sigma_l$ , we obtained different values for the peak UV intensity, but the general qualitative behavior of the temperature tuning does not change. That is, the FWHM BW remains  $\sim 3^\circ\text{C}$  and there exists secondary intensity peaks spaced a few degrees away from the main intensity peak.

We also performed a series of 500 simulations of UV generation at the peak phase-matched condition ( $l_c = 1.2526 \mu\text{m}$ ,  $m = 8$ ). In each simulation a different set of random numbers is used. Results of the simulations produced peak UV intensities which varied from  $1.7 \mu\text{W}$  to  $3.8 \mu\text{W}$  with a mean of  $2.6 \mu\text{W}$  and a standard deviation of 0.3

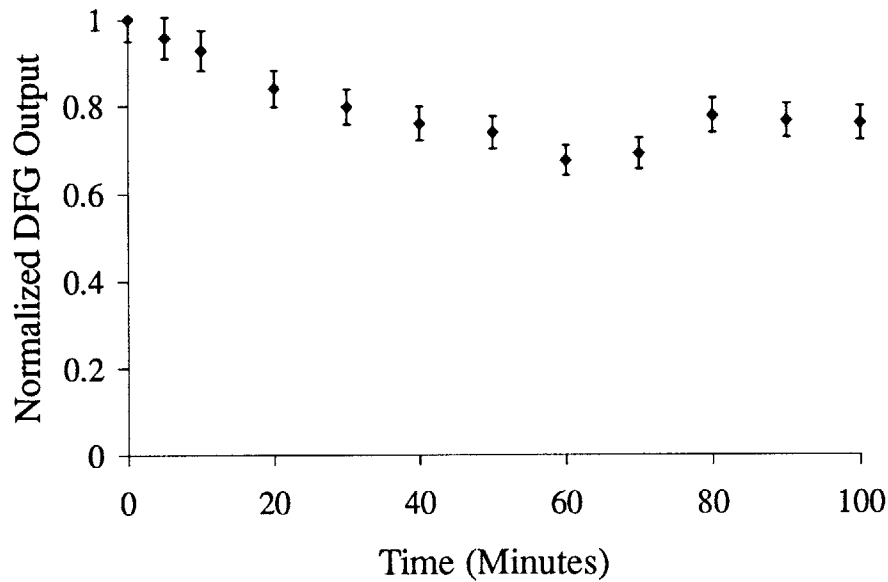


Figure 7-13: Degradation of single-pass DFG output vs. time for 110 mW of constant illumination with pump laser. The accuracy of the power measurements is  $\pm 5\%$ , as indicated by the error bars.

$\mu\text{W}$ .

The results of our simulation verified that the UV light we observed from the PPLN crystal was the 8th-order QPM SHG of our pump beam at 798.4 nm. Based on our simulation we estimated the peak UV intensity to be  $\sim 1\text{-}3 \mu\text{W}$ . Our cavity loss measurements shown in Fig. 7-10 suggested that generation of  $\mu\text{W}$ -level of UV from SHG is sufficient to cause significant photorefractive damage.

We also measured the single-pass DFG output power as a function of time at the peak phasematching temperature of  $47^\circ\text{C}$  to see if there is a reduction in the nonlinearity due to the photorefractive effects. Figure 7-13 shows the DFG output power as a function of time at a crystal temperature of  $47.2^\circ\text{C}$ , which is  $4^\circ\text{C}$  from the peak UV generation temperature.. From Fig. 7-13, it is evident that there is noticeable degradation in the DFG output power, although the DFG output power level stabilizes after  $\sim 40$  minutes. In the particular measurement shown in Fig. 7-13, the DFG output stabilized to  $\sim 76\%$  of the initial level.

We have also observed evidence of additional photorefractive damage that comes as a result of the OPO operation. Recall from the previous section that the OPO



typically ceased to operate after several minutes. Finesse measurements indicated substantial amounts of cavity losses (0.4-1%) that are significantly greater than those due to the SHG of the pump light alone. For instance, at 48.3°C, we measured an increase of round-trip cavity loss of  $\sim 0.1\%$  after sending the pump beam through the PPLN crystal for 15 minutes. However, we also had the OPO operating for 13 minutes at the same temperature and measured an increase of 1.1% in the round-trip cavity loss. We believe that the additional photorefractive damage is due to the sum frequency generation between the 798 nm pump and the signal/idler outputs around 1.6  $\mu\text{m}$ .

To get a sense of how much green radiation might be generated from the SFG process, we simulated the green SFG output using the same model for the PPLN duty cycle and random duty cycle errors as that for simulation of the UV generation. We assumed a SFG interaction between degenerate signal/idler outputs at 1596.6 nm and the pump at 798.4 nm with 150 mW at 798.4 nm and 0.56 W at 1596.6 nm (the amount of circulating signal/idler power in the OPO.) The temperature we used in our simulation was 48°C. We performed a series of 500 simulations, with each simulation having a different set of randomly generated numbers for the random duty cycle error  $\sigma_l$ . The generated green output power at 532 nm ranges from 0 to 700 nW with a mean of  $\sim 120$  nW and a standard deviation of 120 nW. We also repeated simulations for SFG between the pump at 798 nm and non-degenerate signal/idler outputs with wavelengths ranging from 1593 nm to 1600 nm, but the results were not significantly different from the degenerate case.

Results of our simulation showed that up to a few hundred nW of green may be generated from the SFG between the pump and the circulating signal/idler outputs in the OPO cavity. Although the generated green power levels were quite low ( $< 1\mu\text{W}$ ), they were sufficient to result in additional photorefractive damage, as indicated by our cavity finesse measurements before and after above-threshold OPO operation.

In principle, one could avoid the photorefractive damage by increasing the pump wavelength such that the DRO interaction is phasematched at a higher temperature. Unfortunately, our ECDL could not be tuned much beyond our operating wavelength

of 798.3 nm (the ECDL could be tuned to  $\sim 799$  nm but with a much lower output power).

## 7.6 Summary

We have demonstrated a nearly degenerate doubly-resonant OPO with a Brewster-cut PPLN as the nonlinear medium. We measured a minimum threshold pump power of  $\sim 90$  mW, compared to an estimated threshold of 25 mW. The high threshold was probably due to the non-optimal mode-matching of the pump beam to the OPO cavity, despite our best efforts at astigmatically compensating the pump beam to produce the proper mode-matching.

The DRO outputs could be temperature tuned from degeneracy near  $46.5^\circ\text{C}$  to  $52.5^\circ\text{C}$ , indicating a minimum signal/idler output span from 1510 nm to 1695 nm. Stable operation of the OPO was limited to a few minutes at a time as a result of photorefractive damage. Measurements of the cavity finesse indicate that the photorefractive damage was induced mainly by the sum-frequency generation of 532 nm radiation between the pump and the circulating signal/idler fields inside the cavity, and, to a lesser extent, by the second harmonic generation of the pump which produced UV radiation at 399 nm.

Nevertheless, we have demonstrated the feasibility of using a Brewster-cut PPLN crystal in a nearly degenerate cw OPO. In the future we expect to extend the use of Brewster-cut PPLN to an OPO-based 3-to-1 frequency divider with the grating periods designed for operation at elevated temperatures to avoid photorefractive effects. It is worth noting that one could also construct a 3:1 PPLN-OPO with one facet of the PPLN polished at Brewster angle but with the other facet flat polished and AR coated at the signal/idler wavelengths. With such a design the dual-cavity OPO configuration is preserved without the need to generate an astigmatic pump beam. Note that in this case it is still necessary to compensate for the astigmatism of the signal and idler beams on the side with the Brewster-polished facet. A variant of such a hybrid OPO design is a semi-monolithic configuration in which the flat-polished

facet of the PPLN is HR (high reflection)-coated at the signal/idler wavelengths and HT (high transmission)-coated at the pump wavelength. This eliminates the input coupler and further reduces the overall cavity losses.

# Chapter 8

## Conclusion

### 8.1 Summary

We have demonstrated 3-to-1 optical frequency division of 532 nm based on a double-grating PPLN crystal in which we utilized the engineerable phasematching properties of PPLN to phasematch two consecutive DFG interactions using two separate gratings. We achieved a frequency lock between the input lasers at 532 nm and 798 nm with a fractional uncertainty of  $1.5 \times 10^{-11}$ .

We have also demonstrated operation of a nearly degenerate cw PPLN OPO based on a novel configuration in which the crystal facets are polished at Brewster angle as opposed to the conventional way of using AR coatings on flat-polished facets to minimize cavity loss. Robust operation of the OPO was hampered by photorefractive damage near the phasematching temperature of 47°C.

### 8.2 Future Work

The ultimate goal of this research is to complete the building blocks of the frequency chain proposed by Wong [23][24][25]. This requires demonstration of 3-to-2 optical frequency divisions of 532 nm and 798 nm to generate an output at 4/9 the frequency of 532 nm. The preferred way of accomplishing the frequency division is through the use of OPO's. To operate a 3-to-1 PPLN OPO pumped at 532 nm requires a grating

period of  $7.4 \mu\text{m}$ , which is beyond our current fabrication capability. One area of future work lies in the improvement of our fabrication techniques to pole samples with shorter grating periods.

This research has demonstrated the feasibility of operating an OPO with a Brewster-cut PPLN. A natural extension of this work is to construct 3-to-1 optical frequency dividers based on Brewster-cut dual-cavity PPLN OPO's for both 532 nm and 798 nm. The presence of photorefractive damage in our nearly degenerate OPO work suggests that the grating periods of future PPLN devices should be designed to operate at an elevated temperature  $\sim 200^\circ\text{C}$  where photorefractive damage can be avoided. An alternative is to use periodically-poled lithium tantalate (PPLT) which is more resistant to photorefractive damage but has a nonlinearity that is only about 1/2 of that for PPLN.

# Bibliography

- [1] J.A. Armstrong, N. Bloembergen, J. Ducuing, and P.S. Pershan. Interactions between light waves in a nonlinear dielectric. *Physical Review*, 127:1918–1939, 1962.
- [2] P.A. Franken and J.F. Ward. Optical harmonics and nonlinear phenomena. *Review of Modern Physics*, 35:23–39, 1963.
- [3] D.E. Thompson, J.D. McMullen, and D.B. Anderson. Second-harmonic generation in GaAs stack of plates using high-power CO<sub>2</sub> laser radiation. *Applied Physics Letters*, 29:113–115, 1976.
- [4] M.S. Piltch, C.D. Cantrell, and R.C. Sze. Infrared second-harmonic generation in nonbirefringent cadmium telluride. *Journal of Applied Physics*, 47:3514–3517, 1976.
- [5] A. Szilagy, A. Hordvik, and H. Schlossberg. A quasi-phasematching technique for efficient optical mixing and frequency doubling. *Journal of Applied Physics*, 47:2025–2032, 1976.
- [6] M. Okada, K. Takizawa, and S. Ieiri. Second harmonic generation by periodic laminar structure of nonlinear optical crystal. *Optics Communications*, 18:331–334, 1976.
- [7] Y.H. Xue, N.B. Ming, J.S. Zhu, and D. Feng. Second harmonic generation in LiNbO<sub>3</sub> crystals with period laminar ferroelectric domains. *Chinese Physics*, 4:554–564, 1984.

- [8] V. Pruneri, R. Koch, P.G. Kazansky, W.A. Clarkson, P.St.J. Russel, and D.C. Hanna. 49 mW of cw blue light generated by first-order quasi-phase-matched frequency doubling of a diode-pumped 946-nm Nd:YAG laser. *Optics Letters*, 20(23):2375–2377, 1995.
- [9] L.E. Myers, W.R. Rosenberg, G.D. Miller, R.C. Eckardt, M.M. Fejer, and R.L. Byer. Quasi-phase-matched 1.064- $\mu\text{m}$ -pumped optical parametric oscillator in bulk periodically poled LiNbO<sub>3</sub>. *Optics Letters*, 20(1):52–54, 1995.
- [10] K. Schneider, P. Kramper, S. Schiller, and J. Mlynek. Toward an optical synthesizer: a single-frequency parametric oscillator using periodically poled LiNbO<sub>3</sub>. *Optics Letters*, 22(17):1293–1295, 1997.
- [11] G.A. Turnbull, T.J. Edwards, M.H. Dunn, and M Ebrahimzadeh. Continuous-wave singly-resonant intracavity optical parametric oscillator based on periodically-poled LiNbO<sub>3</sub>. *Electronics Letters*, 33(21):1817–1818, 1997.
- [12] D. Touahri, O. Acef, A. Alairon, J.J. Zondy, R. Felder, L. Hilico, B. de Beauvoir, F. Biraben, and F. Nez. Frequency measurement of the  $5s_{1/2}$  ( $f=3$ ) -  $5d_{1/2}$  ( $f+5$ ) two-photon transition in rubidium. *Optics Communications*, 133:471–478, 1997.
- [13] H. Lehmitz, J. Hattendorf-Ledwoch, R. Blatt, and H. Harde. Population trapping in excited Yb ions. *Physical Review Letters*, 62(18):2108–2111, 1989.
- [14] B.G. Whitford, K.J. Siemsen, A.A. Madej, and J.D. Sankey. Absolute frequency measurement of the narrow-linewidth 24-THz D-D transition of a single laser-cooled barium ion. *Optics Letters*, 19(5):356–358, 1994.
- [15] E. Peik, G. Hollemann, and H. Walther. Laser cooling and quantum jumps of a single indium ion. *Physical Review A*, 49(1):49–119, 1994.
- [16] G.P. Barwood, C.S. Edwards, P. Gill, G. Huang, H.A. Klein, and W.R.C. Rowley. Precision interferometric frequency measurement of the 674 nm  $^2S_{1/2}$  -  $^2D_{1/2}$  transition in a single cold Sr<sup>+</sup> ion. *IEEE Transactions on Instrumentation and Measurement*, 44(2):117–119, 1995.

- [17] H. Schnatz, B. Lipphardt, J. Helmcke, and G. Zinner. First phase-coherent frequency measurement of visible radiation. *Physical Review Letters*, 76(1):18–21, 1996.
- [18] P. Fritschel and R. Weiss. Frequency match of the Nd:YAG laser at  $1.064\mu\text{m}$  with a line in  $\text{CO}_2$ . *Applied Optics*, 31(12):1910–1912, 1992.
- [19] K. Nakagawa, T. Katsuda, A.S. Shelkovnikov, M. de Labachellerie, and M. Ohtsu. Highly selective detection of molecular absorption using a high finesse optical cavity. *Optics Communications*, 107:369–372, 1994.
- [20] P. Jungner, S. Swartz, M. Eickhoff, J. Ye, J.L. Hall, and S. Waltman. Absolute frequency of the molecular iodine transition R(56)32-0 near 532 nm. *IEEE Transactions on Instrumentation and Measurement*, 44(2):151–154, 1995.
- [21] J. Ye, L.S. Ma, and J.L. Hall. Sub-doppler optical frequency reference at  $1.064\mu\text{m}$  by means of ultrasensitive cavity-enhanced frequency modulation spectroscopy of a  $\text{C}_2\text{HP}$  overtone transition. *Optics Letters*, 21(13):1000–1002, 1996.
- [22] H.R. Telle, D. Meschede, and T.W. Hänsch. Realization of a new concept for visible frequency division: phase locking of harmonic and sum frequencies. *Optics Letters*, 15(8):532–534, 1990.
- [23] N.C. Wong. Optical frequency counting from the UV to the near IR. *Optics Letters*, 17(16):1155–1157, 1992.
- [24] N.C. Wong. Optical-to-microwave frequency chain utilizing a two-laser-based optical parametric oscillator network. *Applied Physics B*, 61:143–149, 1995.
- [25] N.C. Wong, B. Lai, P. Nee, and E. Mason. Experimental progress toward realizing a 3:1 optical frequency divider. In *Fifth Symposium on Frequency Standards and Metrology*, Woods Hole, MA, October 1995.
- [26] M.M. Fejer, G.A. Magel, D.H. Jundt, and R.L. Byer. Quasi-phase-matched second harmonic generation: tuning and tolerances. *IEEE Journal of Quantum Electronics*, 28(11):2631–2653, 1992.



- [27] G.D. Boyd and D.A. Kleinman. Parametric interaction of focused gaussian light beams. *Journal of Applied Physics*, 39:3596–3639, 1968.
- [28] R.C. Eckardt, C.D. Nabors, W.J. Kozlovsky, and R.L. Byer. Optical parametric oscillator frequency tuning and control. *Journal of Optical Society of America B*, 8(3):646–667, 1991.
- [29] D. Lee and N.C. Wong. Stabilization and tuning of a doubly-resonant optical parametric oscillator. *Journal of Optical Society of America B*, 10(9):1659–1667, 1993.
- [30] G.J. Edwards and M. Lawrence. A temperature-dependent dispersion equation for congruently grown lithium niobate. *Opt. Quantum Electronics*, 16:373–374, 1984.
- [31] L. E. Myers, W. R. Rosenberg, J. W. Pierce, R. C. Eckardt, M. M. Fejer, and R. L. Byer. Quasi-phase-matched optical parametric oscillators in bulk periodically poled  $\text{LiNbO}_3$ . *Journal of Optical Society of America B*, 12(11):2102–2116, 1995.
- [32] L.E. Myers, W.R. Rosenberg, R.C. Eckardt, M.M. Fejer, and R.L. Byer. Multi-grating quasi-phase-matched optical parametric oscillator in periodically poled  $\text{LiNbO}_3$ . *Optics Letters*, 21(8):591–593, 1996.
- [33] P.E. Powers, T.J. Pulp, and S.E. Bisson. Continuous tuning of a continuous-wave periodically poled lithium niobate optical parametric oscillator by use of a fan-out grating design. *Optics Letters*, 23(3):159–161, 1998.
- [34] M.A. Arbore and M.M. Fejer. Pulse compression during second-harmonic generation in aperiodic quasi-phase-matching gratings. *Optics Letters*, 22(12):865–867, 1997.
- [35] M.A. Arbore, A. Galvanauskas, D. Harter, M.H. Chou, and M.M. Fejer. Engineerable compression of ultrashort pulses by use of second-harmonic generation in chirped-period-poled lithium niobate. *Optics Letters*, 22(17):1341–1343, 1997.

- [36] G. Imeshev, M. Proctor, and M.M. Fejer. Lateral patterning of nonlinear frequency conversion with transversely varying quasi-phase-matching gratings. *Optics Letters*, 23(9):673–675, 1998.
- [37] F. Armani, D. Delacourt, E. Lallier, M. Papuchon, Q. He, M. De Micheli, and D.B. Ostrowsky. First order quasi-phase-matching in LiNbO<sub>3</sub>. *Electronics Letters*, 28(2):139–140, 1992.
- [38] E.J. Lim, M.M. Fejer, and R.L. Byer. Second-harmonic generation of green light in periodically poled planar lithium niobate wave-guide. *Electronics Letters*, 25:174–175, 1989.
- [39] M. Yamada and K. Kishima. Fabrication of periodically reversed domain structure for SHG in LiNbO<sub>3</sub> by direct electron beam lithography at room temperature. *Electronics Letters*, 27:828–829, 1991.
- [40] M. Yamada, N. Nada, M. Saitoh, and K. Watanabe. First-order quasi-phase-matched LiNbO<sub>3</sub> waveguide periodically poled by applying an external field for efficient blue second-harmonic generation. *Applied Physics Letters*, 62(5):435–436, 1993.
- [41] A. Räuber. Chemistry and physics of lithium niobate. In E. Kaldis, editor, *Current Topics in Materials Science*. North-Holland, Amsterdam, 1978.
- [42] W.K. Burns, W. McElhanon, and L Goldberg. Second harmonic generation in field poled, quasi-phase-matched, bulk LiNbO<sub>3</sub>. *Photonics Technology Letters*, 6(2):252–254, 1994.
- [43] J. Webjörn, V. Pruneri, P.St.J. Russel, J.R.M. Barr, and D.C. Hanna. Quasi-phase-matched blue light generation in bulk lithium niobate, electrically poled via periodic liquid electrodes. *Electronics Letters*, 30(11):894–895, 1994.
- [44] J. Webjörn, V. Pruneri, P.St.J. Russel, and D.C. Hanna. 55% conversion efficiency to green in bulk quasi-phaseshifting lithium niobate. *Electronics Letters*, 31(21):1869–1870, 1995.

- [45] L. Goldberg, R. W. McElhanon, and W. K. Burns. Blue light generation in bulk periodically field poled LiNbO<sub>3</sub>. *Electronics Letters*, 31(18):1576–1577, 1995.
- [46] G.W. Ross, M. Pollnau, P.G.R. Smith, W.A. Clarkson, P.E. Britton, and D.C. Hanna. Generation of high-power blue light in periodically poled LiNbO<sub>3</sub>. *Optics Letters*, 23(3):171–173, 1998.
- [47] G.D. Miller, R.G. Batchko, W.M. Tullock, D.R. Weise, M.M. Fejer, and R.L. Byer. 42%-efficient single-pass cw second-harmonic generation in periodically poled lithium niobate. *Optics Letters*, 22(24):1834–1836, 1997.
- [48] L. Goldberg, R. W. McElhanon, and W. K. Burns. Difference-frequency generation of tunable mid-infrared radiation in bulk periodically poled LiNbO<sub>3</sub>. *Optics Letters*, 20(11):1280–1282, 1995.
- [49] S. Sanders, R.L. Lang, L.E. Myers, and R.L. Byer. Broadly tunable mid-IR radiation source based on difference frequency mixing of high power wavelength-tunable laser diodes in bulk periodically poled LiNbO<sub>3</sub>. *Electronics Letters*, 32(3):218–219, 1996.
- [50] L.E. Myers, R.C. Eckardt, M.M. Fejer, R.L. Byer, and J.W. Pierce. CW diode-pumped optical parametric oscillator in bulk periodically poled LiNbO<sub>3</sub>. *Electronics Letters*, 42(1):556–559, 1995.
- [51] L.E. Myers, W.R. Rosenberg, A. Drobshoff, J.I. Alexander, and R.L. Byer. Continuous-wave singly resonant optical parametric oscillator based on periodically posed LiNbO<sub>3</sub>. *Optics Letters*, 21(10):713–715, 1996.
- [52] L.E. Myers, W.R. Rosenberg, A. Drobshoff, J.I. Alexander, and R.L. Byer. 93% pump depletion, 3.5-W continuous-wave, singly resonant optical parametric oscillator. *Optics Letters*, 21(17):1336–1338, 1996.
- [53] R.G. Batchko, D.R. Weise, T. Plettner, G.D. Miller, M.M. Fejer, and R.L. Byer. Continuous-wave 532-nm-pumped singly resonant optical parametric oscillator based on periodically poled lithium niobate. *Optics Letters*, 23(3):168–170, 1998.

- [54] M.L. Bortz, M.A. Arbore, and M.M. Fejer. An introduction to methods of periodic poling for second-harmonic generation. *Journal of Physics D, Applied Physics*, 28:1747–1763, 1995.
- [55] M.J. Missey, Dominic V., L.E. Myers, and R.C. Eckardt. Diffusion-bonded stacks of periodically poled lithium niobate. *Optics Letters*, 23(9):664–666, 1998.
- [56] J.P. Meyn and M.M. Fejer. Tunable ultraviolet radiation by second-harmonic generation in periodically poled lithium tantalate. *Optics Letters*, 22(16):1214–1216, 1997.
- [57] K. Mizuuchi, K. Yamamoto, and M. Kato. Generation of ultraviolet light by frequency doubling of a red laser diode in a first-order periodically poled bulk LiTaO<sub>3</sub>. *Applied Physics Letters*, 70(10):1201–1203, 1997.
- [58] K. Mizuuchi and K. Yamamoto. Harmonic blue light generation in bulk periodically poled LiTaO<sub>3</sub>. *Applied Physics Letters*, 66(22):2943–2945, 1995.
- [59] M.E. Klein, D.H. Lee, J.P. Meyn, B. Beier, K.J. Boller, and R Wallenstein. Diode-pumped continuous-wave widely tunable optical parametric oscillator based on periodically poled lithium tantalate. *Optics Letters*, 23(11):831–833, 1998.
- [60] Q. Chen and W.P. Risk. Periodic poling of KTiOPO<sub>4</sub> using an applied electric field. *Electronics Letters*, 30(18):1516–1517, 1994.
- [61] Q. Chen and W.P. Risk. High efficiency quasi-phasematched frequency doubling waveguides in KTiOPO<sub>4</sub> fabricated by electric field poling. *Electronics Letters*, 32(2):107–108, 1996.
- [62] K. Mizuuchi, K. Yamamoto, and M. Kato. highly efficient blue light generation in flux grown KTiOPO<sub>4</sub> periodically poled by an electric field. *Electronics Letters*, 33(9):807–808, 1997.

- [63] H. Karlsson, F. Laurell, P. Henriksson, and G. Arvidsson. Frequency doubling in periodically poled RbTiOAsO<sub>4</sub>. *Electronics Letters*, 32(6):556–557, 1996.
- [64] D.T. Reid, Z. Penman, M. Ebrahimzadeh, and W. Sibbett. Broadly tunable infrared femtosecond optical parametric oscillator based on periodically poled RbTiOAsO<sub>4</sub>. *Optics Letters*, 22(18):1397–1399, 1997.
- [65] T.J. Edwards, G.A. Turnbull, M.H. Dunn, M. Ebrahimzadeh, H. Karlsson, G. Arvidsson, and Laurell F. Continuous-wave singly resonant optical parametry oscillator based on periodically poled RbTiOAsO<sub>4</sub>. *Optics Letters*, 23(11):837–839, 1998.
- [66] R.W. Fox, A.S. Zibrov, and L. Hollberg. Semiconductor diode lasers. In F.B. Dunning and R.G. Hulet, editors, *Atomic, Molecular, and Optical Physics*, volume 3. Academic Press, Cambridge, MA, 1995.
- [67] K. Liu and M.G. Littmann. Novel geometry for single-mode scanning of tunable lasers. *Optics Letters*, 6(3):117–118, 1981.
- [68] L.R. Brothers, D. Lee, and N.C. Wong. Terahertz optical frequency comb generation and phase locking of an optical parametric oscillator at 665 GHz. *Optics Letters*, 19:245–247, 1994.
- [69] C.D. Nabors, S.T. Yang, and R.L. Byer. Coherence properties of a doubly resonant monolithic optical parametric oscillator. *Journal of Optical Society of America B*, 7(5):815–820, 1990.
- [70] D. Lee and N.C. Wong. Tunable optical frequency division using a phaselocked optical parametric oscillator. *Optics Letters*, 17(1):13–15, 1992.
- [71] E.J. Mason. Self-phase locking in a Type-II phase-matched optical parametric oscillator. Master’s thesis, Massachusetts Institute of Technology, Cambridge, MA, June 1996.

- [72] O. Pfister, M. Murtz, J.S. Wells, L. Hollberg, and J.T. Murray. Division by 3 of optical frequencies by use of difference-frequency generation in noncritically phase-matched RbTiOAsO<sub>4</sub>. *Optics Letters*, 21:1387–1389, 1996.
- [73] F.G. Colville, M.J. Padgett, and M.H. Dunn. Continuous-wave, dual-cavity, doubly resonant, optical parametric oscillator. *Applied Physics Letters*, 64(133):1490–1492, 1994.
- [74] D. Lee and N.C. Wong. Tuning characteristics of a cw dual-cavity KTP optical parametric oscillator. *Applied Physics B*, 66(2):133–143, 1998.